Polymorphism and Solid State Miscibility of Triacylglycerols. Application to Food Authentication

Laura Bayés-García

Universitat de Barcelona

Departament de Cristal·lografia, Mineralogia i Dipòsits Minerals

Polymorphism and Solid State Miscibility of Triacylglycerols. Application to Food Authentication

Laura Bayés-García

PhD thesis 2013

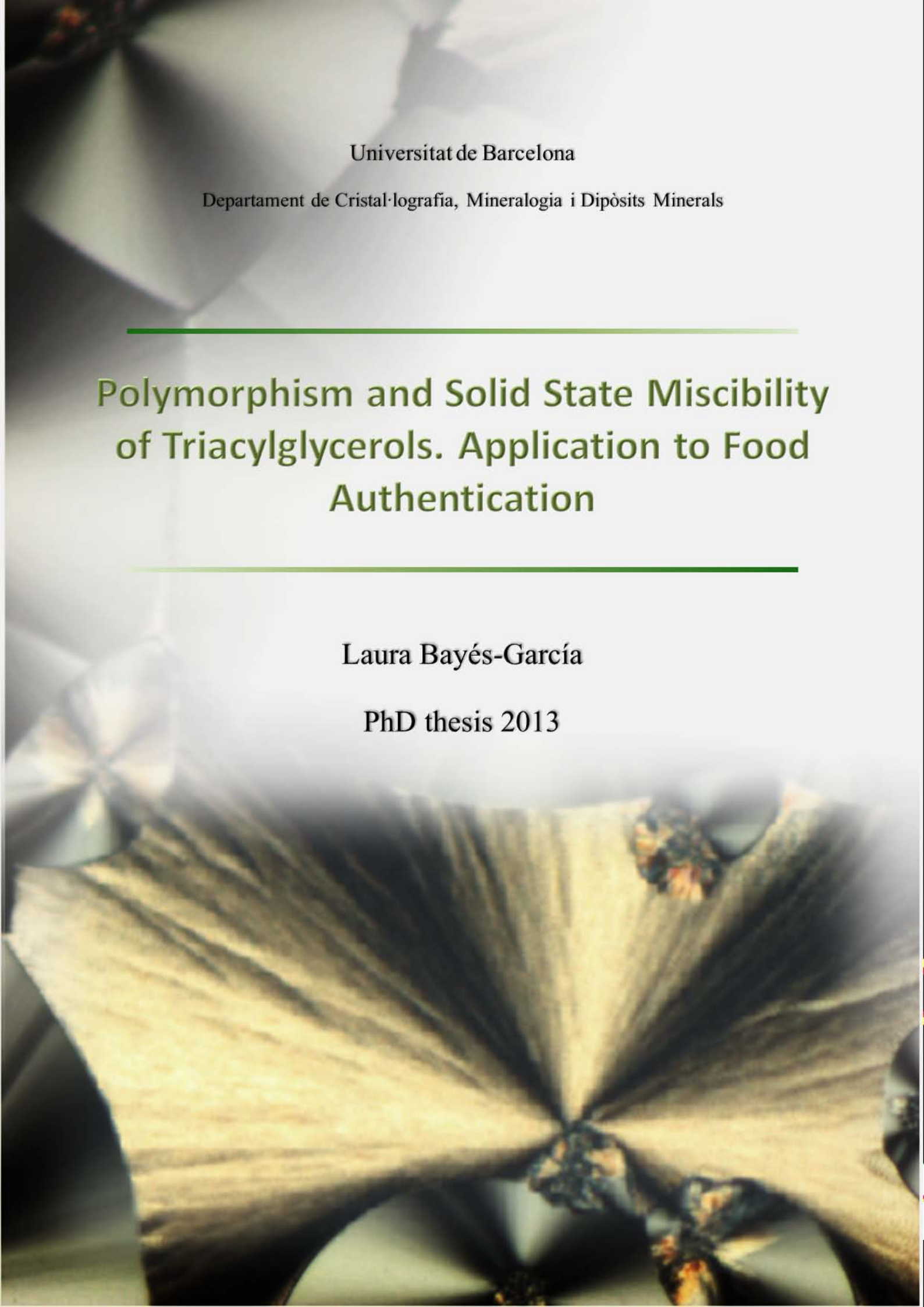

UNIVERSITAT DE BARCELONA

Departament de Cristal·lografia, Mineralogia i Dipòsits Minerals

Grup d'Aliatges Moleculars

Polymorphism and Solid State Miscibility of Triacylglycerols. Application to Food Authentication

-2013-

Memòria presentada per **Laura Bayés-García** per aspirar al títol de doctora per la Universitat de Barcelona. Aquesta tesi s'ha realitzat dins el **Programa de Doctorat de Ciències de la Terra**, sota la co-direcció del **Dr. Miquel Àngel Cuevas-Diarte** i la **Dra. Teresa Calvet i Pallàs**.

La doctoranda,

Laura Bayés-García
Dpt. Cristal·lografia, Mineralogia
i Dipòsits Minerals
Universitat de Barcelona

La tutora,

Dra. Teresa Calvet i Pallàs
Dpt. Cristal·lografia,Mineralogia
i Dipòsits Minerals
Universitat de Barcelona

Els directors,

Dr. Miquel Àngel Cuevas-Diarte
Dpt. Cristal·lografia, Mineralogia
i Dipòsits Minerals
Universitat de Barcelona

Dra. Teresa Calvet i Pallàs
Dpt. Cristal·lografia,Mineralogia
i Dipòsits Minerals
Universitat de Barcelona

Per als meus pares,

Para Enric y Belén,

Per a Carlos,

"Non enim paranda nobis solum, sed fruenda sapientia est"
(No només hem de buscar la sabiesa, sinó gaudir-la)

Ciceró (106 a.C.- 43 a.C.)
De finibus, I, 3

Acknowledgements (Agraïments)

Al final d'aquesta etapa, sento la satisfacció d'haver assolit tots els objectius que m'havia plantejat abans de començar la tesi. He après, m'he desenvolupat tant a nivell científic com a nivell personal, he tingut l'oportunitat de conèixer altres móns i persones molt diverses, ampliant els meus coneixements i horitzons. No obstant això, a l'hora sento certa tristesa. Tristesa perquè ja s'ha acabat una de les etapes més enriquidores de la meva vida, durant la que tant he gaudit i he tingut total llibertat per fer allò que sempre he somiat: recerca. Em sento francament afortunada per haver estat, en tot moment, rodejada i recolzada per tantíssima gent que m'ha facilitat tot aquest procés i m'han ajudat a adquirir unes aptituds que, d'altra manera, potser no les hauria tingut mai.

En primer lloc, vull agrair als meus directors de tesi, Prof. Miquel Àngel Cuevas-Diarte i Dra. Teresa Calvet Pallàs, la vostra dedicació, paciència, recolzament i confiança que m'heu donat durant tots aquests anys. Recordo com si fos ahir, i ja fa més de deu anys, el dia que ens vau proposar, al Raúl i a mi, que col·laboréssim per al Grup d'Aliatges Moleculars. Em vau fer sentir realment privilegiada. Miquel Àngel, gràcies per ensenyar-me, fer-me partícip i contagiar-me aquesta gran passió que sents per la Cristal·lografia. Teresa, gràcies per la teva contínua comprensió i el teu gran positivisme. He après moltíssim de tots dos, tant des del punt de vista científic com humà, i podria dir que, després de tants anys, el Grup d'Aliatges Moleculars ja és com una segona gran família per a mi, on m'he sentit àmpliament apreciada.

Quiero mostrar un especial agradecimiento a Mercedes Aguilar, una de las piezas clave del Grup d'Aliatges Moleculars. Mercedillas, ya sabes que te considero mi ángel de la guarda. Siempre me has ayudado en todo. Me has apoyado, me has aconsejado y has estado a mi lado, hasta en los más pequeños detalles. Gracias. També vull agrair profundament tot el suport donat per la Dra. Mercè Font. Mercè, gràcies per oferir-te sempre que una et necessita. Gràcies per tots els teus consells i les teves grans idees. Gràcies per confiar en mi. Quiero agradecer a mi "compi" Raquel Cordobilla la paciencia que ha tenido conmigo en muchos momentos. Muchas gracias, Raquelilla, por

apoyarme siempre, ser capaz de tranquilizarme, relativizar y hacerme ver qué es lo realmente importante. Gracias por nuestras numerosas “terapias”, que han sido tan efectivas. También quiero dar las gracias a mi compañero Raúl Benages: ¡suerte con tu tesis! Entramos juntos al Grup y ya van más de diez años juntos. Gracias. No m’oblido d’altres persones que han passat pel Grup d’Aliatges: Francisco, Evelyn, Xabier,… gracias por todos los buenos momentos compartidos.

I would like to acknowledge all the members of the Laboratory of Food Biophysics of the Faculty of Applied Biological Science of the Hiroshima University (Japan), especially to Prof. Kiyotaka Sato, Prof. Satoru Ueno and Dr. Hironori Hondoh. You welcomed me so warmly in your lab, where I stayed for nine months. You taught me so many things about fats crystallography and you gave me the possibility of visiting several times the synchrotron radiation facility Photon Factory (PF) at the High-Energy Accelerator Research Organization (KEK) in Tsukuba, where I could perform many experiments by using synchrotron radiation source. I don’t know how to express all my gratitude, so let us try in Japanese:

お礼の申しようがありませんが、大変お世話になりました。

先生方が私を研究室に暖かく歓迎してくださり、様々なことを教えてくださいました。私の "小さな世界" を拡大し、私に多くの新しい道や可能性を見せてくださいました。

心から感謝しています。

However, apart from the scientific point of view, you made me feel like another member of your lab. Thank you, Prof. Sato, for all our highly interesting scientific (and non-scientific) discussions (still continuing through *Skype*). I will never forget those loud conversations between a “typhoon man” and a “volcano lady”, which started in 2009 in Granada. I would also like to thank Prof. Sato’s wife (Mrs. Michiyo Sato) for welcoming me in her home and preparing such delicious dinners. Thank you, Prof. Ueno, for always taking care of me. Thank you. Thanks to all Japanese students for all their unconditional help, especially to Lakmali, my Sri Lanka friend, Hato, Ika, Kamin,

Giko, Waki, Mari, Long, Kaya, Kenji, Ampan, Zabi, Saya, Soft, China, Mokko and Sanx. I wish you all the best. Thank you Sofya (you know you are like another member of this lab), my Indonesian-Japanese friend, for being my Japanese translator and confidant. Thank you to other students of Hirodai: Kabo, Vivi and Suu Myat. Gracias a ti también, Ione, por todos los buenos momentos que compartimos en Japolandia.

I would like to acknowledge all the members of the jury and the referees for accepting to judge and revise this PhD thesis. Thanks to Prof. Dino Aquilano (Università degli Studi di Torino) for your kindness. Grazie Mille.

Agraeixo al Prof. Josep Boatella, al Dr. Francesc Guardiola i la Dra. Alba Tres (Departament de Nutrició i Bromatologia, Facultat de Farmàcia, UB) tota l'ajuda que m'heu donat tant punt l'he necessitat. Moltíssimes gràcies per les vostres brillants idees i per la fructífera col·laboració que mantenim. Josep, al final et vaig fer cas! Gràcies.

Merci au Dr Philippe Négrier et la Dr Denise Mondieig (Centre de Physique Moléculaire Optique et Hertzienne de l'Université Bordeaux I, France) pour votre aide dans la tentative de résoudre des structures moléculaires à partir de données de diffraction des rayons X de poudre.

I would also like to acknowledge Dr. Gianfranco Mazzanti (Dalhousie University, Canada), Dr. Kevin Smith (Fat Science Consulting, UK), and Dr. Rila Ristic (University of Sheffield, UK) for the fruitful and valuable scientific discussions we held.

També vull expressar un afectuós agraïment a la Dra. Maite Garcia Vallès. Gràcies, Maite, pels teus fantàstics consells i bones idees.

Vull agrair a la resta de membres del Departament de Cristal·lografia, Mineralogia i Dipòsits Minerals, sense oblidar al personal administratiu (Eladi, Yolanda, Dolors i Montse) per tota la seva ajuda i efectivitat a l'hora de dur a terme i resoldre tràmits.

Gràcies a la Dra. Immaculada Rafecas, de la Unitat de Protecció Radiològica dels Centres Científics i Tecnològics de la UB (CCiTUB), per la teva flexibilitat i disponibilitat a l'hora de facilitar-me les estàncies al sincrotró de Tsukuba (Japó).

Gràcies al Dr. Xavier Alcobé i a Jordi Jutglar de la Unitat de Difracció de Raigs X dels Centres Científics i Tecnològics de la UB per tota l'ajuda i paciència que heu mostrat durant quasi dos anys, en el llarg i complex procés de mesures de RX dels sistemes binaris incubats.

Gràcies al Dr. Javier Veigas de la Unitat de Microscòpia Electrònica de Rastreig dels Centres Científics i Tecnològics de la UB, per ajudar-nos a intentar observar esferulites a baixa temperatura. Estic segura que aviat ho aconseguirem.

M'agradaria també agrair tot el recolzament, ànims i suport que he rebut per part de molts dels meus amics. Gràcies Sergi, Álex, Costa, Carol, Albert, Mireia, Dani, David, Núria, Marta, Gisela, Sílvia, Núria, Josep, Anna,.. Gràcies per animar-me quan més ho necessitava. Gràcies als "Ewing" per les seves fantàstiques barbacoes!

Finalment vull expressar el meu més emotiu agraïment a la meva família, pel seu infinit recolzament. En especial, vull agrair als meus pares, Fina i Joaquim, l'incansable orgull que sempre heu mostrat. Sempre heu estat al meu costat, educant-me, animant-me, comprenent-me, motivant-me, aconsellant-me i respectant totes les meves decisions. Sense vosaltres, per descomptat que no hauria arribat fins aquí. També vull agrair al meu germà, Enric, i a la meva "cunyi", Belén, la comprensión que habéis mostrado en todo momento y todo lo que me habéis animado para seguir adelante con mis sueños.

I per últim, només em queda donar-te les gràcies a tu, Carlos, per la infinita paciència que has tingut, des que ens vam conèixer fins a l'última etapa d'aquest llarg procés. Gràcies pel teu optimisme i els teus incansables ànims. Gràcies per cuidar-me i escoltar-me sempre.

"Per bé que podríem ser savis amb la saviesa d'altres persones, només podem ser prudents amb la nostra pròpia prudència" (Michel de Montaigne, 1533-1592)

Background

The present work was carried out in the *Grup d'Aliatges Moleculars* of the *Departament de Cristal·lografia, Mineralogia i Dipòsits Minerals* of the *Facultat de Geologia* of the *Universitat de Barcelona*, under the direction of Prof. Miquel Àngel Cuevas-Diarte and Dr. Teresa Calvet Pallàs. Through its history, the research developed by the *Grup d'Aliatges Moleculars* has been mainly focused on the polymorphic characterization and solid state miscibility of benzenes, naphthalenes, and long aliphatic chain compounds, such as alkanes, alcohols, mono-carboxylic and di-carboxylic acids with odd and even carbon atoms number. This PhD thesis rose from the earliest stage of a collaboration with the research group of Prof. Josep Boatella and Dr. Francesc Guardiola of the *Departament de Nutrició i Bromatologia* of the *Facultat de Farmàcia* of the *Universitat de Barcelona*. Moreover, the study on the polymorphic characterization and mixing behavior of triacylglycerols permitted enriching our scientific knowledge and experience on the crystallographic behavior of long chain compounds. This thesis was funded by a *Formación de Profesorado Universitario (FPU)* scholarship from the Spanish Government (*Ministerio de Educación, Cultura y Deporte*).

The polymorphic characterization and mixing behavior of triacylglycerols were carried out in collaboration with Prof. Kiyotaka Sato, Prof. Satoru Ueno and Dr. Hironori Hondoh of the Laboratory of Food Biophysics of the Faculty of Applied Biological Science of the Hiroshima University (Higashi-Hiroshima, Japan). The research group leaded by Prof. Sato and Prof. Ueno is recognized worldwide and becomes a reference in the lipids crystallization field. A total of nine months of stay in the Laboratory of Food Biophysics permitted acquiring the required knowledge to understand the highly complex subject studied, and developing fruitful scientific discussions with its members. Furthermore, several stays in the synchrotron radiation facility Photon Factory (PF) at the High-Energy Accelerator Research Organization (KEK) in Tsukuba (Japan) permitted using different beamlines and performing many experiments with synchrotron radiation source. Thus, a solid collaboration arose

between the two groups and some original papers were published and some others are in preparation.

We also started trying to solve the molecular structure of some monounsaturated triacylglycerols by using powder x-ray diffraction data, in collaboration with Dr. Philippe Négrier and Dr. Denise Mondieig of the *Centre de Physique Moléculaire Optique et Hertzienne* of the *Université Bordeaux 1* (Bordeaux, France). These studies started at the last stage of this thesis and no definitive results have been obtained until now, as the corresponding calculations are still in process and will continue in the near future. Moreover, very recently we also started to perform theoretical calculations on the structure and molecular interactions of the same monounsaturated triacylglycerols, in collaboration with Dr. Santiago Álvarez of the *Departament de Química Inorgànica* of the *Facultat de Química* of the *Universitat de Barcelona*.

The last section of the present thesis, corresponding to the polymorphic characterization of edible fats and oils for food authentication, was performed in collaboration with Prof. Josep Boatella, Dr. Francesc Guardiola and Dr. Alba Tres of the *Departament de Nutrició i Bromatologia* of *the Facultat de Farmàcia* of the *Universitat de Barcelona*.

This PhD thesis is based on the study of the *in situ* polymorphic characterization of the main triacylglycerols of some vegetable and animal fats and oils, some of their mixtures and its application to food products authentication. It is structured in the following five chapters.

Chapter 1 consists of a general introduction to the triacylglycerols polymorphism and mixing behavior. Initially, a synthesized first approach to the foods crystallography field is included, in order to set the reader in the lipids crystallization background. Later, the main polymorphic forms, packing and molecular interactions of tricylglycerols are described. Moreover, a brief overview of some studies reported on molecular structures resolutions by single crystal and powder x-ray diffraction data is given, and some general comments about crystallization of triacylglycerols and mixing behavior are also included.

Chapter 2 describes the *in situ* polymorphic characterization of the main triacylgycerols present in some vegetable and animal fats and oils, such as olive oil or Iberian ham fat. Thus, the polymorphic occurrence and transformation pathways of POP, OPO, POO, SOO, POL, OOO and OOL were analyzed as a function of some kinetic

factors (variations of the cooling and heating rates applied to the samples). Polymorphic crystallization and transformations were dynamically monitored by mainly using synchrotron radiation x-ray diffraction, with SAXD and WAXD simultaneous measurements.

Not only characterizing the pure compounds but also their mixtures acquires special importance for its application. In particular, studies on binary mixture systems provide quite valuable information about the molecular interactions among different triacylglycerols. For this reason, **Chapter 3** deals with the determination of the phase behavior of binary mixtures of mixed-acid triacylglycerols containing palmitic and oleic fatty acid moieties: PPO:OPO, PPO:POO and POO:OPO. Thus, also considering the already reported work, the whole mixing behavior among all mixed-acid TAGs constituted by palmitic and oleic fatty acids could be determined, enabling the extrapolation to other systems formed by other saturated/unsaturated mixed-acid triacylglycerols. Furthermore, the morphology and microstructure of spherulites of POP:OPO mixtures were analyzed by using synchrotron radiation microbeam x-ray diffraction (SR-μ-XRD) to determine the relative nucleation rates and crystal growth of the component materials, which have a direct application to lipid fractionation processes.

In an attempt to make an approach to complex natural fatty samples, the polymorphism of multicomponent mixtures (from 3 to 6 triacylglycerol components) was analyzed and discussed, and the results are shown in **Chapter 4**. This chapter also focuses on an application of the characterization of fat polymorphism to natural products: the foods authentication. Hence, we used polymorphism as a tool to detect fraudulent additions of hazelnut oil in virgin and extra virgin olive oil, but also to discriminate among Iberian hams produced with different fattening systems (*cebo* and *bellota*).

Finally, **Chapter 5** summarizes the main results and conclusions derived from this thesis, and points out some open questions and future work.

CONTENTS

CHAPTER 3

Solid state miscibility of triacylglycerols containing palmitic and oleic fatty acids

CHAPTER 1

General introduction

1.1.

Overview of the Foods Crystallography field within the period 2000-2010

Foods represent a very important and active productive sector, which relies on both fundamental and applied scientific research. Along with such traditional sectors, like the chocolate one, every day new food products, intended for industry or the consumption, are developed, and new regulations governing them from the legal and health point of view arise.

As Roos stated in his book *Phase Transitions in Foods*, published in 1995, foods become complicated systems, but their physical state is usually governed by phase transitions of the main components, i.e., carbohydrates, lipids, proteins, and water. Temperature, time, and water content have enormous effects on the physical state and quality of food and biological materials. These materials are often metastable and they undergo phase and state transitions in various processes and during storage. Kinetics of various changes is related to these transitions and, therefore, to molecular mobility. Understanding phase transitions and the relationships between molecular mobility and stability is often the basis of proper control of food processing and storage conditions.
Carbohydrates are present in almost all foods. Phase transitions of low molecular weight sugars, as well as those of carbohydrate polymers, are extremely important and determining for food properties. The phase behavior of sugars is relevant in manufacturing of various sweet foods including candies, confectionery, bakery products, and almost all food materials that contain sugar (Dhonsi et al., 2006). Starch, which is obtained from cereal and legume seed endosperm, potato tuber and others, is the most common carbohydrate polymer found in foods.

Lipids as food components significantly differ from carbohydrates. Represented by triacylglycerols (TAGs), they become materials of great importance from both the fundamental and applied point of view. In biological tissues, fats are present in the complex lipids of membranes, lipoproteins and lipid deposits, where their physical properties in liquid, liquid crystals and solid states play dominant roles in biological functionality, together with other constituents such as proteins, carbohydrates, etc. To cope with current diversified market demand for production of fats and oils, elucidation

for quality control of end products has been attempted by physical, chemical, biochemical, biotechnological and chemical engineering approaches. Among them, physical methods are critically important for improving functionality of end products under processing, storage and consuming conditions. The physical properties of the food fats are primarily influenced by three main factors: fat crystal structure, solidification and transformation behavior, and rheological and textural properties exhibited by the fat crystal networks (Marangoni et al., 2002). Crystallization and transformation of polymorphic triacylglycerols constitutes an important body in the research of the physical properties of fats (Sato et al., 2001a).

The objective of this section was to provide a general overview of the scientific production on crystallography of foods within the period 2000-2010, mainly focusing on lipids and carbohydrates. Crystallography is understood here in a broad sense, including the physicochemical aspects. With this purpose, we used the Thomson Reuters database by the way of the Web of Knowledge in the Science Citation Index Expanded, Conference Proceedings Citation Index-Science, and Book Citation Index-Science. When keywords were introduced, the search process was performed by considering the title, abstract, keywords of the authors and keywords of the journal. As to the interrogation procedure, the following keywords were used: crystal growth, nucleation, crystal morphology, crystal size, crystallinity, crystallization, recrystallization, crystal structure, microstructure, nanostructure, nanocrystals, nanocomposites, phase transitions, polymorphism, transformation, liquid crystals, kinetics, tempering, cooling rate, phase diagrams, miscibility, binary mixtures or phase behavior, and rheological properties. Simultaneously, another set of keywords related to a series of materials, which are involved in the food industry, were used: oils, fats, milk, chocolate, butter, polyols, triacylglycerols, starch, lipids, ice-cream, carbohydrates, corn, sodium chloride, and snacks. Obviously, it is very difficult to be exhaustive, but in our opinion this set of keywords may provide a large vision of the main topics of fundamental and applied research in the foods crystallography field. However, in this section we only show some general or global results, as the whole review work is in preparation for being published.

The overall results of the interrogation process consisted of almost 8000 citations. From this set, a manual selection and analysis of the data allowed to remove papers out of the scope of our goal.

Analyzed scientific production considerably grew from 2000 to 2010. About 150 articles were published in 2000, and more than the double (more than 350 papers) were produced in 2010. There is a stable scientific community with established groups, which before 2010 was already publishing, and that recurs in a systematic way. The major production is located in USA, which duplicates the articles of France (second country in the production ranking), although there are other highly productive areas, such as Asia. Noteworthy is the quantitative contribution of other countries, like Spain.

The disciplines distribution is illustrated in Figure 1.1. Obviously, *food science and technology* becomes the most productive field, with a 44.6%, whereas *crystallography* only occupies a 1.6%. The considerable dispersion between areas evidences the significantly interdisciplinary nature of the subject.

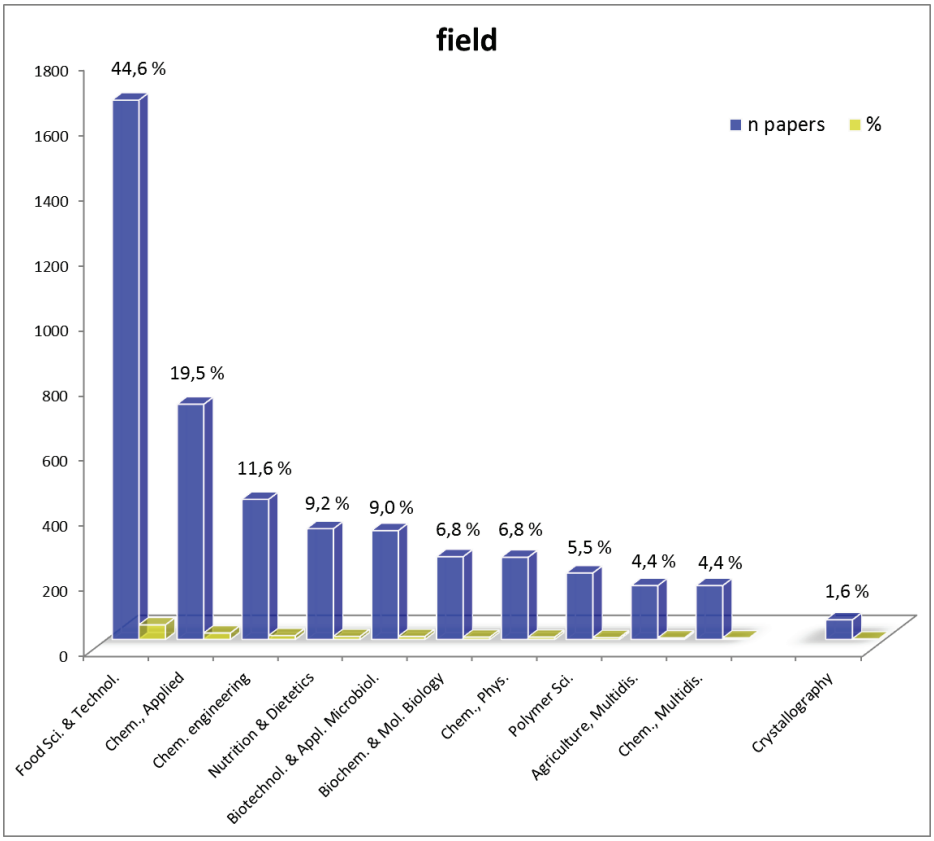

Figure 1.1. Number and percentage of articles as a function of the disciplinary area.

Figure 1.2 shows the distribution as a function of the studied materials. Oils represent the major 17.9% of the productivity. Other food products, such as milk, chocolate and butter have been also widely studied. It should be pointed out that the fats

and triacylglycerols groups are referred to articles in which the keywords did not note a specific application.

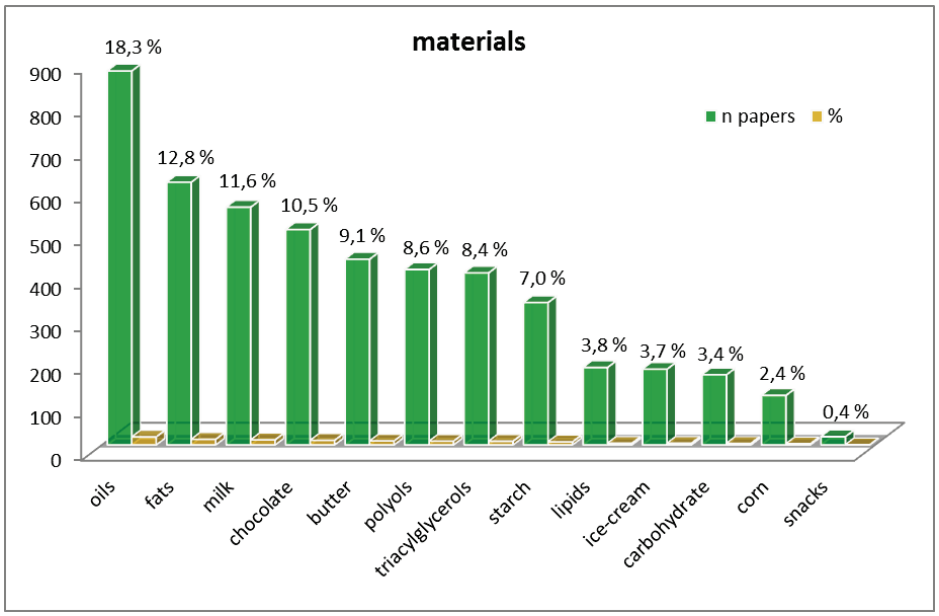

Figure 1.2. Number and percentage of articles as a function of the studied materials.

As previously stated, the *crystallography* area, which is of our interest, becomes relatively unimportant. However, the areas classification is based on the scientific journals belonging to each field and, at this point, the fact that many authors conducted crystallographic studies in journals of other areas should be taken into account. Therefore, we preferred to consider some relevant crystallographic terms in order to determine those works somehow related to *crystallography of foods* and classify them into different crystallographic aspects (i.e. influence of some kinetic factors on the polymorphic behavior of a food product), as depicted in Figure 1.3.

After a series of refinements carried out through the database, 2859 contributions were taken into account. However, it should be considered that a certain number of studies may be present in more than one category, as they made contributions to more than one of the established topics. Some categories have been grouped to simplify: e.g. crystal growth includes crystal growth, nucleation, crystal morphology, crystal size, crystallinity, crystallization and recrystallization.

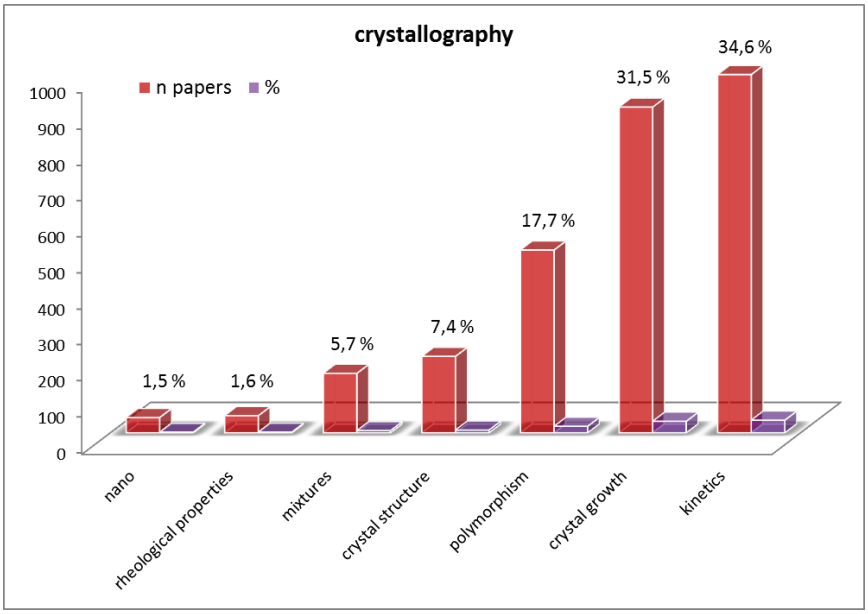

Figure 1.3. Number and percentage of articles related to crystallography.

As shown in Figure 1.3, major contributions are those related to kinetics (34.6%) and crystal growth (31.5%), followed by those focused on polymorphism (17.7%). However, a more detailed analysis would reveal that the three categories are closely related. Crystal structures and mixtures categories should be also understood in their broad sense and acquire less importance, representing a 7.4% and 5.7%, respectively. The rest of the selected topics account for around the 3% of the total.

1.2.

Introduction to triacylglycerols

Lipids, together with proteins and carbohydrates are major nutrients and also employed as lipophilic materials in food, cosmetic and pharmaceutical industries (Larsson et.al., 2006). Alimentary and industrial fats and oils (such as vegetable oils, margarine, chocolate and confectionery fats) mainly consist of triacylglycerols (TAGs), whose molecules involve different types of fatty acid moieties. Thus, a TAG molecule consists of a triester of a glycerol structure and three fatty acids, as illustrated in Figure 1.4.

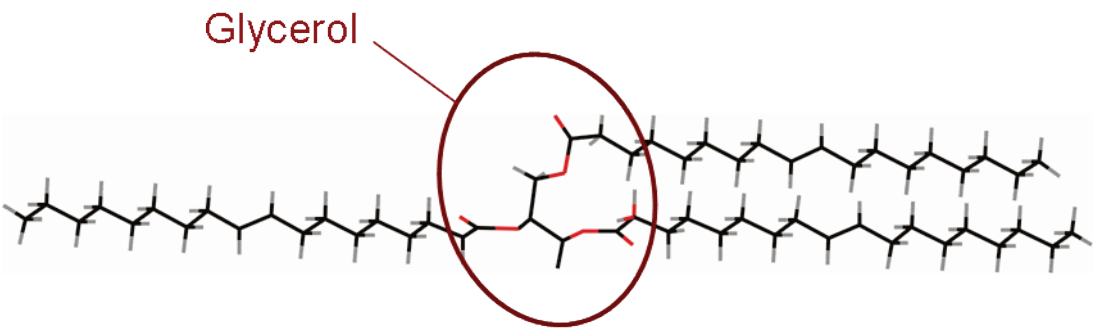

Figure 1.4. Triacylgycerol molecule, consisting of a triester of a glycerol molecule with three fatty acids.

Fatty acid compositions (e.g. saturated/unsaturated acyl chains, unsaturated acyl chains with cis- or trans- double bonds, acyl chain length, and so on) determine the physical properties of TAGs, such as melting, morphology, rheology, and texture (Marangoni et al., 2002). Those TAGs containing identical acyl chains in all positions are called *mono-acid* or *simple* TAGs, whereas those containing different acyl chains are named *mixed-acid* TAGs.

Moreover, the physical chemistry of TAGs is complicated by the fact that the middle carbon (carbon-2 of glycerol) is potentially asymmetrical as different substitutions at carbons-1 and -3 generate stereoisomers of the glycerol derivatives. The isolation and determination of the *sn*-specificity of TAGs becomes a difficult chemical

task. Moreover, the synthesis of TAGs is also complex, and great care must be taken in producing the proper *sn*-configurations with different fatty acids (Small, 1986). Hence, for a given asymmetric TAG, racemic mixtures are more often produced. As an example, for the TAG POO, containing one palmitic and two oleic fatty acid chains, the corresponding racemic mixture may contain some *sn*-POO (~50%) and the rest *sn*-OOP. For the reasons explained above, the asymmetric TAGs examined in the present thesis consisted of their racemic mixtures (coexistence of R and S entantiomers). In order to specify the racemic nature of asymmetric TAGs, the *(rac)* notation can be included or, as an alternative, more saturated fatty acids and/or with the shortest chain length should be named first. In the previous example, the racemic mixture of POO and OOP may be named POO (with no need of specifying the *(rac)* notation), as palmitic is a saturated fatty acid containing 16 carbon atoms (C16:0) and oleic acid contains 18 carbon atoms and one double bond (C18:1). When the synthesis or analysis has been specifically carried out to determine the *sn*- positions, the prefix *sn* is used.

1.3.

Basic terms on triacilglycerols polymorphism

TAGs show a complicated crystallization behavior. The physico-chemical properties of a TAG molecule are determined by the nature and compositions of the three fatty acid moieties. The three most commonly encountered polymorphs of TAGs are α, β' and β forms (Lutton, 1950).

These polymorphic forms are defined according to their subcell structures, which correspond to cross-sectional packing modes of the zigzag aliphatic chain, as shown in Figure 1.5 (Larsson, 1966).

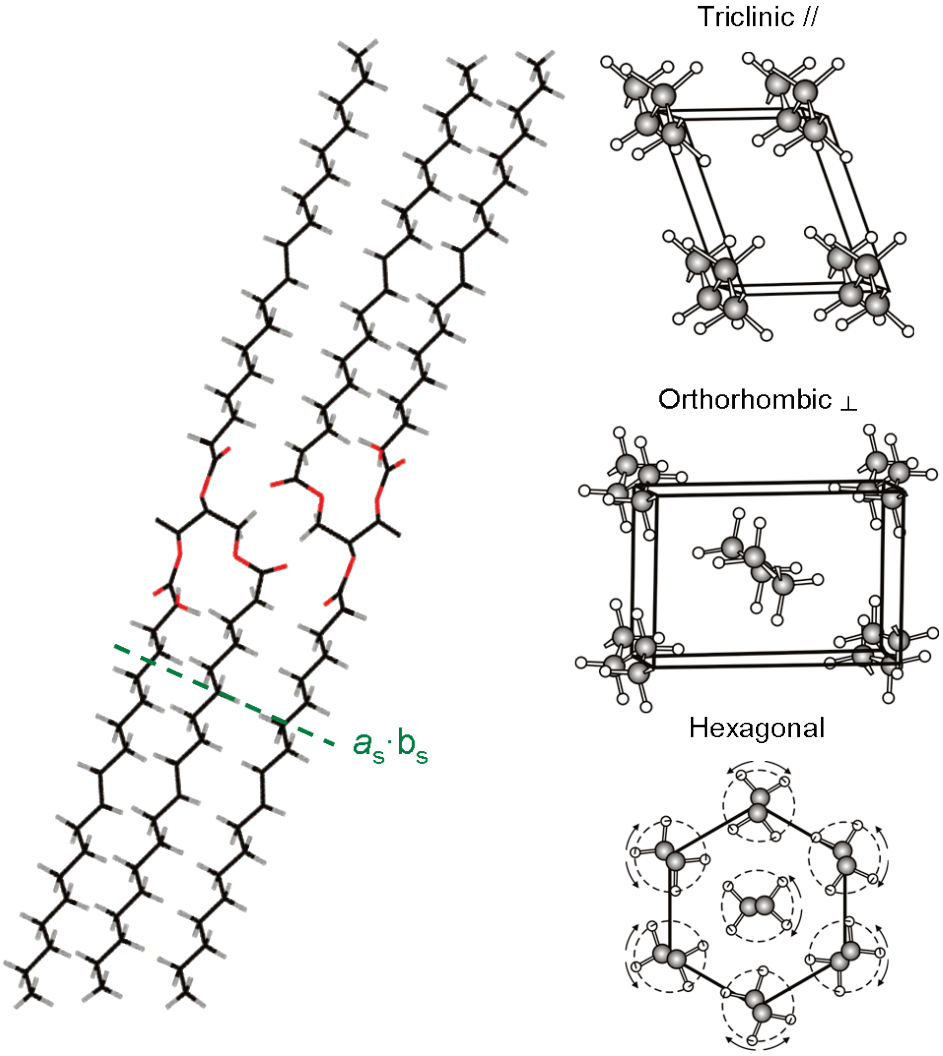

Figure 1.5. Typical subcell structures of TAG polymorphs.

Thus, α form is defined by a hexagonal subcell (H), β' has an orthorhombic perpendicular subcell (O⊥), and the subcell of β form is triclinic parallel (T//).

The subcell concept is often used to define hydrocarbon packing modes for lipids. Three axes (c_s for the translation between equivalent positions within a chain, and a_s and b_s for the lateral translations) and three interaxial angles define the three-dimensional subcell. Two possibilities exist in the mutual orientation of zig-zag planes defined by neighbouring hydrocarbon chains: parallel (//), like in the triclinic parallel subcell ($T_{//}$) associated to β form, or perpendicular (⊥), as in the orthorhombic perpendicular (O⊥) subcell of β' form. α form exhibits an hexagonal (H) packing, where the hydrocarbon chains freely rotate about their long axis, similarly to rotator phases of paraffins (Small, 1986).

Referring to their relative stability, the β form is the most stable, while β' is metastable and α is the least stable, having the lowest melting temperature (T_m). As the TAGs polymorphism becomes monotropic, the Gibbs free energy (G) values are largest for α, intermediate for β' and smallest for β, as shown in Figure 1.6.

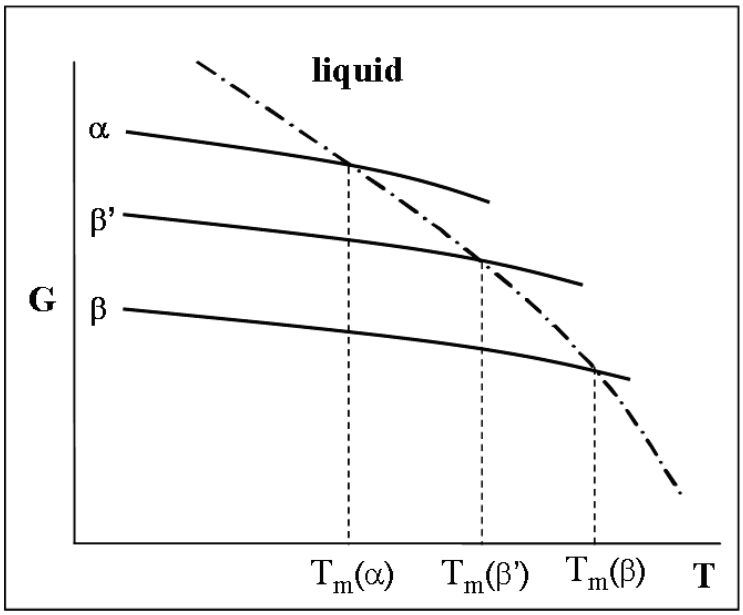

Figure 1.6. Gibbs energy (G)-Temperature (T) relationship of the three basic polymorphs of TAGs.

These basic polymorphic forms, however, can be modified depending on the fatty acid compositions and some of them can be absent or new forms can occur. Depending on the acyl chain composition, other metastable forms, called γ and δ, and

several β' and β forms occur in mixed-acid TAGs, which are the most common in nature (Sato, 1996).

As to the packing of TAG molecules, the chain length structure generates a repetitive sequence of the acyl chains involved in a unit cell lamella along the long-chain axis, where each unit layer formed by one acyl chain is named *leaflet* (Figure 1.7).

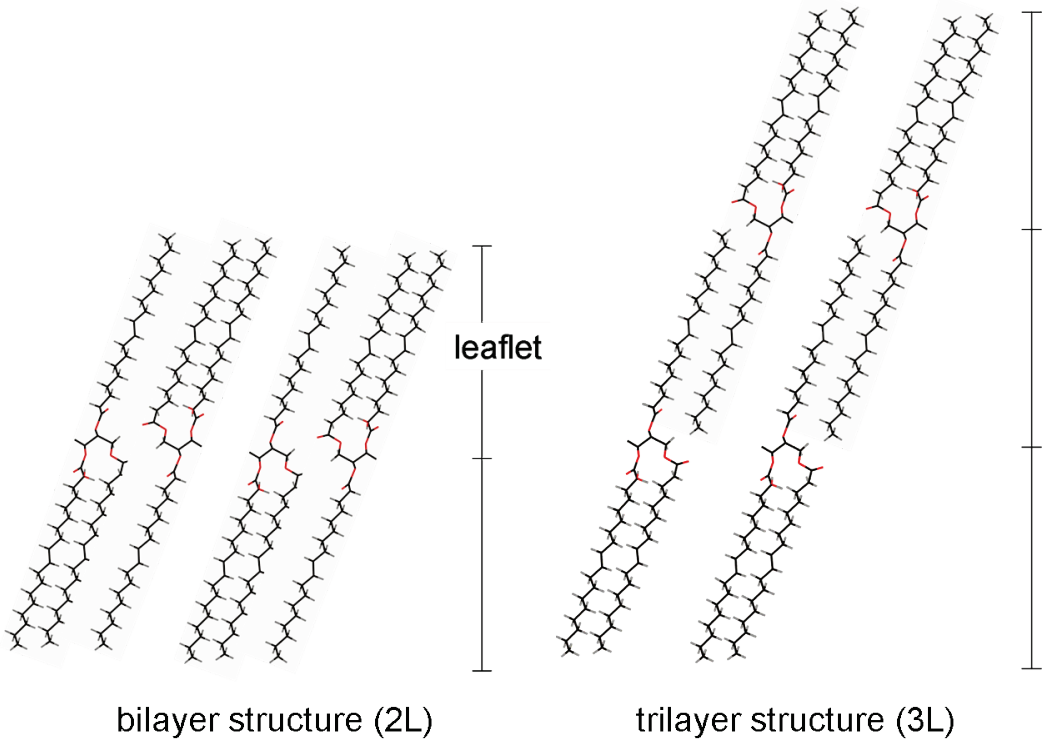

Figure 1.7. Triacylgycerols packing in bilayer (2L) and trilayer (3L) structures.

When the chemical properties of the three fatty acid moieties are identical or very similar, a double chain length or bilayer structure is obtained. On the contrary, a triple chain length or trilayer structure is formed when the chemical properties of one or two fatty acid moieties are largely different from the others, due to chain sorting (Goto et al., 1992). Two factors are determinant for the layer thickness or long spacing, which are the length of the acyl chains and the tilt angle between the chain axes and the lamellar plane. As an example, in γ form of 1,3-distearoyl-2-oleoyl glycerol (SOS), the long chains are arranged almost normal to the lamellar interface, whereas the inclination angle is about 70º in β' form, and about 52º in β form (Sato et al., 1999).

The major interactions which are thought to be most influential in exhibiting the polymorphic structures of TAGs are depicted in Figure 1.8, where such interactions are shown for a mixed TAG (1,3-dipalmitoyl-2-oleoyl glycerol, POP).

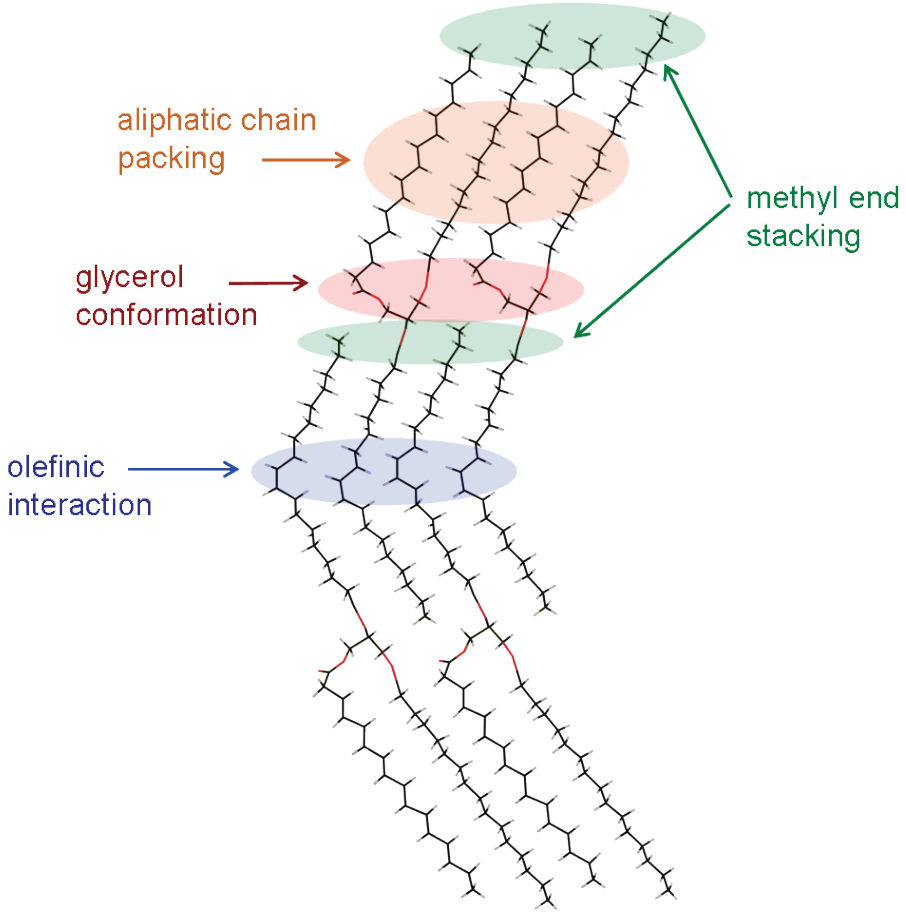

Figure 1.8. Major molecular interactions for the structural stabilization of TAGs (Sato, 2001b).

Thus, the main interactions for the structural stabilization of TAG crystals are the following: (i) aliphatic chain packing due to hydrocarbon chain-chain interactions, (ii) glycerol conformation whose influences may act through dipole-dipole interactions of the glycerol groups, (iii) methyl end stacking which may mostly determine the organization of different chain length structures, (iv) olefinic interactions which may predominate in the polymorphic occurrence of mixed acid TAGs that contain unsaturated fatty acid moieties. In the case of mixed-acid TAGs, the molecular interactions through the main body of the aliphatic chains, methyl end packing, and glycerol groups are modified compared to those of the monoacid TAGs. Therefore,

multiplicity and relative stability of the polymorphic forms and their lattice energies are modified (Sato, 2001b).

As an example of the diversified polymorphic forms that occur in TAGs, depending on the fatty acid compositions, Table 1.1 presents the polymorphs that have been described for tristearoyl glycerol (SSS), trioleoyl glycerol (OOO) and mixed-acid TAGs containing stearic and oleic fatty acids (1,3-distearoyl-2-oleoyl glycerol or SOS, 1,3-dioleoyl-2-stearoyl glycerol or OSO, 1,2-distearoyl-3-oleoyl glycerol or SSO and 1-stearoyl-2,3-dioleoyl glycerol or SOO). In the data shown, the chain length of each polymorphic form is specified. As already stated above, mixed-acid TAGs, which are more common in nature, often exhibit a more complex polymorphic behavior, with multiple β' or β forms or additional γ and δ forms.

Table 1.1. Occurrence of polymorphic forms of triacylglycerols containing stearic and oleic fatty acids.

TAG					
SSS	**SOS**	**OSO**	**SSO**	**SOO**	**OOO**
α-2L	α-2L	α-2L	α-3L	α-n.d.	α-2L
	γ-3L				
β'-2L	β'-3L	β'-2L	β'-3L	β'_2-3L	β'-2L
				β'_1-3L	
β-2L	β_2-3L	β-3L			β-2L
	β_1-3L				

n.d. Not determined

Chapman (1962) reported the polymorphism of some trisaturated, triunsaturated and mixed-acid TAGs. The author described three different polymorphic forms (α, β' and β) for tristearin and other trisaturated TAGs, such as tripalmitin or trimyristin, all having a double chain length structure (2L). The same polymorphic forms were described for the triunsaturated TAG trioleoyl glycerol, also having a double chain length structure (Chapman, 1962; Akita et al., 2006). However, Hagemann et al. (1972) described three different β' forms for OOO. Both SSS and OOO exhibit a 2L structure in their polymorphic forms due to the identical chemical properties of the three fatty acid moieties. As to the mixed-acid TAGs containing stearic and oleic fatty acids, triple

chain length structures were also detected (see Table 1.1). SOS exhibits five different polymorphic forms: α-2L form, an additional γ-3L form, β'-3L, and most stable β_2-3L and β_1-3L forms (Sato et al., 1989). As to the chain length structures, the one of least stable α form is double, whereas γ, β' and two β forms exhibit a triple chain length structure. On the contrary, OSO only shows the three main polymorphs α, β' (both having a double chain length structure) and β (with a triple chain length structure) (Kodali et al., 1987). As to asymmetric SSO and SOO TAGs, in disaturated SSO only two polymorphic forms occur, both having a triple chain length structure (α-3L and β'-3L) (Takeuchi et al., 2002), whereas three polymorphs appear in SOO (α, β'_2-3L and β'_1 -3L) (Zhang et al., 2009).

Thus, no β forms are present in SSO and SOO, and the most stable polymorph is β'. This result was also observed in other asymmetric mixed-acid TAGs, such as 1,2-dipalmitoyl-3-myristoyl-*sn*-glycerol (PPM) (Kodali et al., 1990), 1,2-dipalmitoyl-3-oleoyl-*rac*-glycerol (PPO) (Minato et al., 1997a) and 1-palmitoyl-2,3-oleoyl-*rac*-glycerol (POO) (Zhang et al., 2007).

It is possible to crystallize the different polymorphs from the liquid state (e.g. by changing the rates of cooling), where kinetic factors play an important role as it will be discussed through this thesis. Transformations from one polymorph to another can occur in the solid state or through melt mediation (melting of a less stable form followed by the re-crystallization of a more stable form). Furthermore, occurrence of liquid crystalline phases can occur before the crystallization of the polymorphic crystals or during the melt-mediated transformation of a metastable phase (Sato, 2001a).

Controlling polymorphism of TAGs becomes an important challenge for industrial fields, such as the pharmaceutical, biomedical or food areas, with the aim of obtaining the desired product characteristics. Therefore, recently, many studies have focused on the influences of external factors on the polymorphic behavior of TAGs and more complex lipid samples, such as the cooling and heating rate variations (Campos et al., 2002), encapsulation, additives (Smith et al., 2011), shear (Mazzanti et al., 2011), and sonication (Ueno et al., 2003).

1.4.

Structural studies and polymorphic characterization of triacylglycerols

Structural determination of TAG crystals at an atomic level may have important implications in understanding the structure-function relationships of lipids, lipoproteins, biomembrane lipids and so on. Few crystal structures have been determined for triacylglycerols. As to some examples of single crystal determination, molecular structures have been solved for most stable forms of 1,2,3-tridecanoyl glycerol or tricaprin (10.10.10) (Jensen et al., 1966), 1,2,3-tridodecanoyl glycerol or trilaurin (LaLaLa) (Vand et al., 1951; Larsson, 1964), the triacylglycerol of 11-bromoundecanoic acid (Larsson, 1963), 1,2-dipalmitoyl-3-acetyl-*sn*-glycerol (PP2) (Goto et al., 1992) and 1,2-dipalmitoyl-3-myristoyl-*sn*-glycerol (PPM) (Sato et al., 2001c). However, many difficulties arise when trying to grow TAG single crystals of good quality, due to influences of complicated polymorphism, presence of impurities, etc. Moreover, most of the TAGs which are found in nature are liquid at room temperature. Therefore, recently some work focused on the structure resolution by using powder x-ray diffraction data. Van Langevelde et al. (2000) solved the crystal structure of the β' phase of 1,3-didecanoyl-2-dodecanoyl (10La10) glycerol and 1,3-ditetradecanoyl-2-hexadecanoyl glycerol (MMP) from single crystal X-ray diffraction and high resolution X-ray powder diffraction data, respectively. The same research group determined the molecular structure of β form of 1,2,3-tritetradecanoyl glycerol or trimiristin (MMM), 1,2,3-trioctadecanoyl glycerol or tristearin (SSS) (Van Langevelde et al, 2001a), and 1,2,3-tris(tridecanoyl glycerol) (10.10.10) (Van Langevelde et al., 2001b) by also using high-resolution X-ray powder diffraction data. As to monounsaturated TAGs, Van Mechelen et al. (2006a) determined several crystalline structures from synchrotron powder diffraction measurements, such as the β_1 form of 1,3-dimyristoyl-2-oleoyl glycerol (MOM); 1,3-dipalmitoyl-2-oleoyl glycerol (POP); 1,3-distearoyl-2-oleoyl glycerol (SOS); 1-dipalmitoyl-2-oleoyl-3-stearoyl glycerol (POS); 1-stearoyl-2-oleoyl-2-arachidoyl glycerol (SOA); cocrystallized SOS:POP (in a 50:50 concentration ratio); and two cocoa butters from Bahia and Ivory Coast. Soon after, the same authors reported on the crystal structure of the β_2 polymorphs of POP,

SOS, POS, SOA, and the equivalent β_2-V polymorph of Ivory Coast cocoa butter (Van Mechelen et al., 2006b). They also used powder diffraction data to solve the crystalline structure of polymorphs of a series of mixed saturated and trans-monounsaturated TAGs, comprising symmetric and asymmetric even numbered TAGs (SES, PEP, PSP, PPE, SSE, PPS, PSS, MMP, LaLaM and LaMM; being S stearic acid, P palmitic acid, E elaidic acid, M miristic acid, and La lauric acid) (Van Mechelen et al., 2008a; Van Mechelen et al., 2008b). Following the same methodology, they determined the structure of several polymorphic forms of another monounsaturated TAG (1,3-dilauroyl-2-oleoyl glycerol, LaOLa) (Van Mechelen et al., 2008c).

However, the use of X-ray diffraction techniques, with both laboratory-scale and synchrotron radiation, are mainly focused on the identification of the polymorphic forms and the study of the polymorphic occurrence when different thermal treatments are applied to fat samples. This becomes one of the main objectives of this thesis. It is important to determine the most efficient cooling, heating or isothermal processes that should be employed in order to obtain the polymorphic form with the desired characteristics, which will give the appropriate texture and rheological properties to the final product. To give some examples, it should be mentioned that the preferred polymorphic form of cocoa butter in chocolate is β_2 (or form V) (MacMillan et al., 2002; Hodge et al., 2002), whereas small β' crystals result in good plasticity and gives proper softness to fat products, such as margarine and shortenings (Miskandar et al., 2004).

In the X-ray diffraction pattern of TAGs, long spacing values provide information about the chain length structure (bilayered or trilayered structures), whereas short spacings give some evidence of the kind of subcell present (polymorphic identification). For instance, a triclinic parallel subcell gives a strong and sharp spacing at 0.46 nm, while an orthorhombic perpendicular subcell gives strong spacings at about 0.42 nm and 0.38 nm. In the hexagonal packing, a single strong spacing is present at about 0.41-0.42 nm. Nevertheless, a large variety of intermediate forms often occur, especially in mixed TAGs, giving rise to a range of different subcells (M//, O//, O'//) (Small, 1986).

As to the other techniques used to investigate the complicated polymorphism of TAGs, vibrational spectroscopy should be highlighted. Some research has been done on the use of FT-IR (Fourier-transform infra-red) to analyze the molecular conformations

of polymorphic forms of fatty acids and TAGs, on the basis of the vibrational analysis of the polymethylene chains (Kaneko, 2001). Thus, relationships between the molecular structures and the infrared spectral features of TAGs have been established (Yano et al., 1997). Moreover, polymorphic transformation of some saturated-unsaturated mixed TAGs were monitored by FT-IR spectroscopy using deuterated specimens in which stearoyl chains were fully deuterated (Yano et al., 1999). A combination of Raman and FT-IR spectroscopy also clarified the polymorphic behavior of cis-unsaturated TAGs, such as 1,2,3-trioleoyl glycerol or triolein (OOO) (Akita et al., 2006).

Through this thesis, the polymorphic identification of TAG samples and their mixtures was mainly carried out by using X-ray diffraction with laboratory-scale and synchrotron radiation. Moreover, Raman spectroscopy was also applied in some case. The use of synchrotron radiation X-ray diffraction techniques enabled the dynamic characterization of the polymorphic crystallization and transformation of TAGs and their mixtures. Dynamic properties of fats become more relevant to real systems of industrial fat productions compared to the static properties (Sato, 2001a).

1.5.

Crystal growth and crystallization of triacylglycerols

Few works have focused on the fundamental study of crystal growth and crystallization mechanisms of TAGs. In the present PhD we did not work on crystal growth aspects, although it is worthy to note some of the reported works belonging to this field.

Bennema et al. (2004), in a general paper form 2004, reviewed 200 years of modeling crystal growth and morphology. From the discovery of the law of rational indices, the interplanar distance law of Bravais, Friedel, Donnay, and Harker, to more structural theories such as the Hartman-Perdok theory, as well as statistical mechanical cell models, we arrive at the modern growth theories supported by Monte Carlo growth simulations. Their new insights were applied to β form of some trisaturated TAGs, such as tripalmitoyl glycerol (PPP), to illustrate their scope and applicability.

Taking β' form of a trisaturated TAG as an example, Boerrigter et al. (2002) described a method to explain the morphology of TAG needle-shaped crystals by analyzing the growth mechanisms for the various crystal faces, the relevant parameter being the edge free energy of a two-dimensional nucleus on a surface. The results obtained were compared with Monte Carlo simulations.

The morphology of β form of tripalmitoyl glycerol (PPP) and β' forms of 1,3-dicaproyl-2-lauroyl glycerol (10La10) and 1,2-dipalmitoyl-3-myristoyl glycerol (PPM) were described by Hollander et al. (2003) on the basis of a connected net analysis taking into account the edge energies of a 2D nucleation growth mechanism. The morphology of the three fats ranged from long needles in spherulitic growth forms to lozenge shaped single crystals. It was shown that the elongated growth habit of β' of 10La10 fat crystals having fast growing top faces was a result of a very small edge free energy of 2D nuclei on these faces. In contrast, for the less symmetric β' PPM crystals, the corresponding edge energies became much higher, resulting in lozenge shaped crystals.

Crystallization regimes found in nature, as well as those used in food and pharmaceutical processing, are normally non-isothermal. Therefore, as to the nucleation stage, a probabilistic approach to model non-isothermal nucleation of TAG melts was developed by Marangoni et al. (2006). It consisted of defining a new parameter to

characterize the driving force of nucleation, the supercooling-time exposure (β), which not only depends on the difference between the melting temperature and the onset temperature of nucleation, but also on the induction time of nucleation and, therefore, the cooling rate. The energy of activation for the nucleation process in palm oil, milk fat, and other palm oil based fats were estimated.

As to some crystallization processes of TAGs mixtures, Acevedo et al. (2010a) reported on the characterization of the nanoscale in triacylglycerol crystal networks of edible fats. Blends of trioleoyl glycerol (OOO) and tristearoyl glycerol (SSS) were prepared in different proportions in order to achieve a wide range of supersaturations. Cryogenic Transmission Electron Microcopy (cryo-TEM) permitted the visualization of primary crystals consisting of nanoplatelets, where the bimolecular triacylglycerol lamellae within the cross-section of nanoplatelets could be observed.

The crystallization of multicomponent triglyceride mixtures from the melt was studied by Marangoni et al. (2007). The polycrystalline clusters, or spherulites, formed under low undercooling were analyzed by using polarized light microscopy and image analysis. The results suggested that the internal spatial distribution of mass within these spherulites is fractal in nature. They also derived a relationship between spherulite diameter and the free energy of nucleation.

As to crystallization properties applied to final food products characteristics, Vereecken et al. (2007) investigated the different structure levels (crystallization, microstructure, macrostructure, etc.) that lead to good technological functionality of filling fats. Differential Scanning Calorimetry and microscopy techniques were applied to characterize the isothermal crystallization behavior of trans-containing and trans-free filling fats. Furthermore, the hardness of the samples was examined after cooling at different temperatures and at different storage times. The results obtained indicated that trans-containing filling fat crystallized faster and in smaller crystals as compared to the trans-free filling fat. The filling matrix components seemed to have a pronounced influence on the microstructure and thus on the macroscopic properties. Rousseau et al. (2008) reported on the influence of dispersed particulates present in chocolate on the microstructural development and fat crystal growth of cocoa butter (CB) during storage. Atomic force microscopy of both chocolate and cocoa butter revealed that surface crystal growth on both materials was similar during isothermal storage. During the

crystal growth, gradual increases in the proportion of the form VI polymorph, solid fat, and whiteness occurred over time.

Thus, crystal growth studies have been performed not only for pure TAG samples, but also for their mixtures and more complex lipid samples. However, more research needs to be carried out in this sense, in order to fully understand the growth mechanisms of such compounds and apply this knowledge to end food products.

1.6.

Phase behavior of triacylglycerols mixtures

As natural fats present in real systems in biotissues or food materials become mixtures of different types of TAGs, one must pay attention to the complicated behavior of melting, crystallization and transformations of natural fats by examining the mixing behavior of binary, ternary or more multiple phases of specific TAG components. In other words, the physicochemical properties of lipids must be studied not only in their pure systems but also in mixed systems. In particular, studies on binary mixture systems provide valuable information about molecular interactions among different lipid materials. Moreover, the phase behavior of TAG mixtures has critical implications in fat blending and separation of component TAGs from natural fats and oil resources (Sato, 2001a).

Diversified molecular interactions among TAGs are found in polymorphism and mixing behavior. For the binary mixing behavior of TAGs, three different phases may occur: solid solution phase, eutectic phase, and molecular compound formation (also called molecular complex or cocrystal). Solid solution phase occurs when the two component TAG molecules exhibit structural similarity and affinitive molecular interactions. On the contrary, when two component molecules are immiscible due to steric hindrance, the eutectic behavior takes place (Kitaigorodsky, 1984). A molecular compound is formed through specific molecular interactions between two component molecules. Figure 1.9 illustrates the three main kinds of mixing behavior for an A-B system.

Primary factors determining the phase behavior are the differences in chain length and chemical structures of the fatty acid moieties (Rossel, 1967). Further complexity is caused by both polymorphism and acyl chain compositions attached to the glycerol group. In principle, the phase behavior of pure TAGs is relatively simple (the most stable crystalline form, which is β form in most cases, will melt directly to the liquid state at the transition temperature). In practice, however, phase behavior become extremely complicated due to the formation of metastable polymorphic phases (other β, β' and α forms) occurring below the true melting point of the most stable β form. Furthermore, in some mixed-acid TAGs, and certainly in mixtures of TAGs, β' form

apparently becomes the most stable form (Small, 1986). For these reason, to determine the phase behavior of most stable phases, TAG mixtures are often subjected to thermodynamical stabilization through isothermal incubation periods, which become so long in some cases.

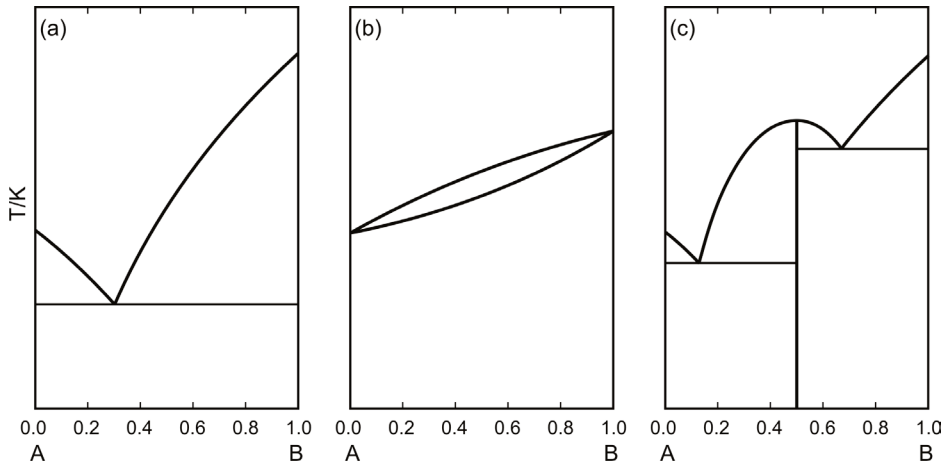

Figure 1.9. Three main kinds of binary molecular systems A-B. a) Eutectic system. b) Systems with random molecular alloys $A_{1-x}B_x$ (total miscibility). c) Molecular compound formation at a 50:50 concentration ratio.

Regarding the three typical mixing behaviors described above (see Figure 1.9), some examples can be cited as follows.

In his PhD thesis, L. H. Wesdorp (1990) developed some reliable methods to predict the melting range and solid phase composition of fats from their overall composition. Thus, he compared the experimental and theoretical results obtained concerning the phase behavior of binary and ternary mixtures of different trisaturated, triunsaturated and saturated-unsaturated mixed acid TAGs.

In mixtures of saturated monoacid TAGs whose chain length differences is not larger than two carbon atoms (i.e. SSS-PPP binary mixtures), the eutectic phase with a limited region of solid solution is formed for the stable β form, yet the miscible phases are obtained in the metastable α and β' forms (Kellens et al., 1990). At this point, Takeuchi et al. (2003) analyzed three types of binary mixtures of saturated monoacid TAGs: trilaurin-trimiristin (LaLaLa-MMM), trilaurin-tripalmitin (LaLaLa-PPP) and trilaurin-tristearin (LaLaLa-SSS), by using synchrotron radiation with small and wide angle X-ray scattering (SAXD/WAXD). The carbon atoms numbers for the fatty acid chains of the three TAGS are 12 (LLL), 14 (MMM), 16 (PPP), and 18 (SSS). In the LLL-MMM system, miscible phase behavior occurred in metastable α and β' forms,

whereas the most stable β form exhibited an eutectic phase. On the other hand, LLL-PPP and LLL-SSS mixtures showed immiscible phases for α, β', and β forms. Therefore, they confirmed that TAG binary mixtures were miscible in metastable polymorphs of α and β' forms when the carbon atoms number differed by two, whereas the immiscible mixtures were constructed in all polymorphic forms when the carbon atoms number differed by four and six.

In the mixtures between the saturated monoacid TAGs and unsaturated monoacid TAGs, neither miscible nor molecular compound forming systems were observed (Rossel, 1967). As to binary systems of saturated-unsaturated mixed-acid TAGs, Rousset et al. (1998) determined the miscible behavior of major components of cocoa butter (POS-SOS). However, recent studies have shown the molecular compound crystals formation in various combinations of saturated-unsaturated mixed-acid TAGs, such as SOS-SSO (Engstrom, 1992; Takeuchi et al., 2002), SOS-OSO (Koyano et al., 1992), POP-PPO (Minato et al., 1997a), and POP-OPO both in neat liquid (Minato et al., 1997b) and n-dodecane solution system (Ikeda et al., 2010). It should be noted that the mixing behaviors of TAGs containing stearic and oleic fatty acids become the same to their equivalent TAGs containing palmitic instead of stearic acid, as both become saturated fatty acids only differing by two carbon atoms. The combined usage of synchrotron radiation X-ray diffraction and DSC has clarified thermodynamic (for most stable states) and kinetic (for metastable states) properties of the phase behavior of the molecular compound forming systems. Moreover, FT-IR experiments permitted characterizing the molecular structures of POP-PPO and POP-OPO molecular compounds, and indicated that steric hindrance and glycerol interactions play important roles in the formation of the molecular compound crystals (Minato et al., 1997c).

As to some immiscible systems of saturated-unsaturated mixed-acid TAGs, Zhang et al. (2009) conducted thermal and X-ray diffraction experiments on binary mixtures of symmetric stearic-oleic mixed-acid TAG SOS and asymmetric OOS, in which optically active *sn*-OOS was employed. The authors found that SOS-OOS mixtures exhibited immiscible monotectic or peritectic mixing behavior. This result was consistent with previous work on binary mixtures of POP and OOP (Zhang et al., 2007), in which racemic OOP molecules were employed. The differences between the SOS-OOS and POP-OOP mixtures were in the polymorphic behavior of the fractions of POP and SOS. No effect was found from using an optically active (*sn*-OOS) or racemic

mixture (*rac*-OOP) as an asymmetric oleic-oleic-saturated acid TAG. From the two results, they concluded that an immiscible phase was formed in the binary mixtures of symmetric saturated-oleic-saturated TAGs and asymmetric oleic-oleic-saturated TAGs, of both racemic and optically active types.

As typical examples, in this thesis we present the results obtained for the phase behavior of binary mixtures of saturated-unsaturated mixed-acid TAGs containing palmitic and oleic acid moieties: PPO-OPO, PPO-POO and POO-OPO. The determination of these binary systems permits completing the mixing behavior among all mixed-acid TAGs containing palmitic and oleic fatty acids, and extrapolating the results obtained to other mixed-acid TAGs constituted by other saturated and unsaturated fatty acids. Moreover, synchrotron radiation microbeam X-ray diffraction (SR-μ-XRD) experiments were carried out to determine the crystallization kinetics of POP-OPO mixtures through the analysis of the morphology and microstructure of the heterogeneous spherulites formed during the crystallization process. Thus, microstructures of spherulites of mixture samples were determined by relative rates of nucleation and crystal growth of component materials, which are directly related to fractionation processes.

Next step in understanding the polymorphic behavior of natural fats and oils is the characterization of more complex or multicomponent mixtures, as will be discussed through this study.

CHAPTER 2

In situ polymorphic study of main triacylglycerols of some vegetable and animal fats and oils

"Don't pay much attention to the rice grain at the corner of the bowl.
First, eat the whole dish and, afterwards, think about that grain"

Prof. Kiyotaka Sato, Higashi-Hiroshima, 2010

2.1.

Introduction

Many crystals exhibit polymorphism, in which structural determination and thermodynamic stabilization of the polymorphic modifications are of primary significance to determining the overall polymorphic nature of every substance (Bernstein, 2002). In addition, the kinetic properties of crystallization and structural transformation are important, particularly for the application of polymorphic crystal systems in pharmaceutical, biomedical, food technology, and other applications (Widlak et al., 2001). As for the crystallization of different polymorphic forms, the Ostwald step rule (Ostwald, 1897; Threlfall, 2003; Aquilano et al., 2001; Aree et al. 2008) has been used for macroscopic estimation of the behavior of multiple polymorphic forms when they are crystallized from vapour, solution, and melt phases. This rule dictates that less stable polymorphic forms crystallize much faster than more stable forms when the driving force for crystallization takes place under certain values of supersaturation and supercooling and less stables forms transform to more stable forms after the crystallization. Actually, the kinetics of polymorphic nucleation of various systems often follows this rule. For example, a metastable vaterite form crystallizes faster than the more stable calcite in $CaCO_3$ (Zhao et al., 2010; Falini et al., 1998). However, more detailed studies are needed to examine the effects of supercooling, additives, etc. and become necessary to establish some rules of behavior of the influence of kinetics on the polymorphic crystallization and study the situations where the Ostwald step rule may be complemented.

Complicated polymorphism is observed in almost all TAGs. The number of individual polymorphic forms and their molecular structures are strongly related to the chemical nature of the fatty acid components (chain length, saturated or unsaturated) (Larsson et al., 2006). To control the physical properties of fats, many researchers have focused on (i) the determination of molecular and crystal structures, (ii) the influence of external factors on the transformation mechanisms, (iii) the formation mechanisms of fat crystal networks from nano-scale primary fat crystals to meso-scale and macro-scale structures, and (iv) the rheological and texture properties, which are basically determined by fat crystal networks (Sato et al., 2011). In these four areas, the influence

of external factors can be categorized as dynamic temperature variation (cooling, heating, thermal cycle, etc.; see below), additives (Smith et al., 2011), shear (Mazzanti et a., 2003; Mazzanti et al., 2011), ultrasonication (Ueno et al., 2003; Martini et al., 2008), and emulsification (Wassell et al., 2012; Arima et al., 2009; McClements, 2012).

The metastable and more stable polymorphic forms of TAGs are largely influenced by dynamic temperature variations such as the rates of heating and cooling. These effects are highly significant for applications in the pharmaceutical, biomedical, and food areas, since specific polymorphic forms should be crystallized by tailoring the most efficient thermal treatments, and such forms should be maintained over long periods by preventing their conversion into other less functional polymorphic forms.

Therefore, many studies have focused on the role of thermal treatments in the polymorphic crystallization and transformation of TAGs in pure TAGs and their binary mixtures (Koyano et al., 1991; Miura et al., 2001; Bouzidi et al., 2010; Bouzidi et al., 2012; Himawan et al., 2006; Boodhoo et al., 2008; Smith et al., 2005; Rousset et al., 1998) as well as natural fats such as palm oil (Foubert et al., 2008; Chong et al., 2007; Vuillequez et al., 2010), palm stearin in sesame oil (Toro-Vazquez et al., 2002), milk fat (Lopez et al., 2005a; Campos et al., 2002), cheese (Gliguem et al., 2009), pork and lard (Campos et al., 2002; Svenstrup et al., 2005), and cocoa butter (Foubert et al., 2008; Campos et al., 2010; Humphrey et al., 2007; Perez-Martinez et al., 2007).

For example, Foubert et al. (2008) describes a stop-and-return DSC method used in different fat samples, which consists of stopping the crystallization at different moments during the isothermal crystallization and raising the temperature of the sample. Koyano et al. (1991) studied the crystallization kinetics of the polymorphic forms of POP (1,3-dipalmitoyl-2-oleoyl glycerol). Miura et al. (2001) examined the crystallization behavior of POP, POO (1-palmitoyl-2,3-dioleoyl glycerol) and their mixtures, by using the information obtained from the granular crystals of a model margarine. Smith et al. (2005) examined the influence of the cooling rate on the width of the metastable zone of the crystallization of POP in acetone solution. Rousset et al. (1998) analyzed the crystallization of a binary system of POS (1,3-palmitoyl-stearoyl-2-oleoyl glycerol) and SOS (1,3-stearoyl-stearoyl-2-oleoyl glycerol), both of which are main component TAGs of cocoa butter. They constructed time-temperature-transformation diagrams to illustrate the kinetics of isothermal crystallization as a

function of temperature. They found that increasing the amount of the POS molecule induced a lower growth rate in the mixtures.

Toro-Vazquez et al. (2002) studied the quantitative evolution of crystallization of natural fats such as palm stearin in sesame oil, using different crystallization temperatures attained at several cooling rates. Campos et al. (2010) examined the crystallization kinetics, crystal structure, microstructure, and mechanical strength of blends of cocoa butter and small amounts of other TAGs.

In this chapter, the polymorphic crystallization and transformation of POP (1,3-dipalmitoyl-2-oleoyl glycerol), OPO (1,3-dioleoyl-2-palmitoyl glycerol), POO (1-palmitoyl-2,3-dioleoyl glycerol), SOO (1-stearoyl-2,3-dioleoyl glycerol), POL (1- palmitoyl-2-oleoyl-3-linoleoyl glycerol), OOO (trioleoyl glycerol) and OOL (1,2- dioleoyl-3-linoleoyl glycerol) are reported. These TAGs become the major components of some vegetable and animal oils and fats, such as palm oil, olive oil and Iberian ham. The saturated/unsaturated nature of their fatty acid components has an important influence on their melting point (as the number of unsaturations increases, the melting point decreases), which has to be considered for fractionation processes of fats and oils (see below).

Samples were cooled from the melt and, afterwards, heated at different rates of cooling/heating. To avoid oxidation, samples were kept in purged (N_2) dark vials, which were stored in the freezer.

In order to follow and characterize the polymorphic crystallization and transformation of such components, Differential Scanning Calorimetry (DSC), Thermo-Optical Microscopy (TOM), Raman spectroscopy, laboratory-scale powder X-Ray Diffraction (XRD) and Synchrotron Radiation X-Ray Diffraction (SR-XRD) with Small-Angle X-Ray Diffraction (SAXD) and Wide-Angle X-Ray Diffraction (WAXD) were used. Using SR-XRD enabled us to monitor the occurrence and transformation behavior *in-situ* at high rates, which are very close to the actual rates in real applications in factories and cannot be attained with traditional laboratory-scale XRD techniques. Therefore, using this technique and a DSC coupled to the beamline, enables rapid thermal programs to provide highly accurate structural information. Few studies using SR-XRD have been conducted to determine the relative occurrence of the polymorphic forms of TAGs, since most work has been performed with an optical microscope, DSC, and *ex-situ* (not on-line) XRD measurements with laboratory equipment after

crystallization ceased. SR-XRD can facilitate fast cooling rate measurements because of its high-intensity X-ray beam.

2.2.

Materials and methods

POP, OOO, OOL, POO, SOO and POL were all purchased from Tsukishima Foods Industry (Tokyo, Japan) and used without further purification (purity >99%). The OPO used for thermal analysis (DSC and TOM) (99% pure without further purification) was purchased from Larodan Fine Chemicals (Malmö, Sweden). The OPO used for SR-XRD was also 99% pure and it was obtained from Tsukishima Foods Industry (Tokyo, Japan). The DSC profiles for both compounds were completely identical. It should be noted that samples of asymmetric TAGs (OOL, POO, SOO and POL) were not enantipure compounds, as they consisted of the racemic mixture of the corresponding enantiomers (R and S).

DSC experiments were conducted at atmospheric pressure using both a Perkin-Elmer DSC-7 and a Perkin-Elmer DSC Diamond. The DSC thermograms obtained by the two calorimeters were completely comparable. Samples (9.0 to 9.4mg) were weighted into 50 μl aluminium pans, and covers were sealed into place. Both instruments were calibrated with reference to the enthalpy and the melting points of indium (melting temperature: 156.6ºC; ΔH: 28.45 J/g) and decane (melting temperature: -29.7ºC; ΔH: 202.1 J/g) standards. As reference, an empty pan was used. Dry nitrogen was used as purge gas in the DSC cell (at 23cm^3/min in the Perkin-Elmer DSC-7 and at 20cm^3/min in the Perkin-Elmer DSC Diamond). Thermograms were analyzed with Pyris Software to obtain the enthalpy (J/g, integration of the DSC signals), T_{onset} and T_{end} of the transitions (ºC, intersections of the baseline and the initial and final tangents at the transition). Although both T_{onset} and T_{end} were determined, in the present study only T_{onset} values are shown. At least three independent measurements were made for each experiment (n=3). Random uncertainty was estimated with a 95% threshold of reliability using the Student's t-distribution, which enables estimating the mean of a normally distributed population when it is small (Mortimer, 2005). A correction was applied for analyses with cooling or heating rates different from 2ºC·min^{-1}, since both calorimeters were calibrated at the mentioned rate. The following expression was applied at each value (Perkin Elmer, 1982):

$$T_{true} = T_{obs} - C \cdot (dT/dt)_a + C \cdot (dT/dt)_b$$

where C is a constant value (0.085), $(dT/dt)_a$ is the rate of the analysis, and $(dT/dt)_b$ is the calibration rate (2ºC·min^{-1}).

Several DSC tests were performed, by cooling and heating some TAGs at different rates (50ºC·min^{-1}, 20ºC·min^{-1}, 15ºC·min^{-1}, 10ºC·min^{-1}, 5ºC·min^{-1}, 2ºC·min^{-1}, 1ºC·min^{-1}, 0.5ºC·min^{-1} and 0.1ºC·min^{-1}), until the final experimental conditions were selected.

TOM images were obtained on a Linkam THMSG-600 stage mounted to a Nikon Eclipse 50iPol Microscope. The sample was placed on a quartz sample cell and covered with a glass cover slip to ensure a thin sample layer. An LNP liquid nitrogen cooling system and a TMS94 temperature controller were used. Images were captured with a Nikon Digital Camera DXM1200F and NIS-Elements Software.

SR-XRD experiments were performed at two different beamlines (BL-15A and BL-9C) of the synchrotron radiation facility Photon Factory (PF) at the High-Energy Accelerator Research Organization (KEK) in Tsukuba (Japan). In both beamlines, a double-focusing camera operated at a wavelength of 0.15 nm. In BL-9C, the X-ray scattering data were simultaneously collected by Position Sensitive Proportional Counters (PSPCs, Rigaku Co., PSPC-10) for the small (SAXD) and wide-angles (WAXD). In BL-15A, a CCD camera was used for small-angle data, and a PSPC for wide-angle data. The SAXD pattern was used for determining the chain length structure of the triacylglycerol and the WAXD pattern permitted us to identify the polymorphic forms (Lopez et al., 2005b). Each temperature program was controlled by a Mettler DSC-FP84 (Mettler Instrument Corp., Greifensee, Switzerland) with FP99 software. However, in some cases, thermal treatments were controlled by a Linkam stage LK-600. A 2mm-thick sample was placed in an aluminium sample cell with Kapton film windows. SR-XRD spectra were acquired at 30 or 60s intervals, depending on the rates of cooling/heating used and the complexity of the thermal profile.

Laboratory-scale powder XRD was used for some experimental conditions using a PANalytical X'Pert Pro MPD powder diffractometer equipped with a Hybrid Monochromator and an X'Celerator Detector. The equipment also included an Oxford Cryostream Plus 220V (temperature 80 to 500K). This diffractometer operated with Debye-Scherrer transmission. The sample was introduced in a 1mm-diameter

Lindemann glass capillary. The latter was rotated about its axis during the experiment to minimize preferential orientations of the crystallites. The step size was 0.013º from 1.004º to 28º 2θ and the measuring time was 2.5 minutes per pattern.

Micro-Raman spectra were determined for some experimental condition. They were measured with a dispersive Jobin-Yvon Lab Ram HR 800 spetrometer, with a 532 nm line as the excitation source. The laser power was 6 mW at the sample point. The detector was a charge-coupled device (CCD), which was cooled at -70ºC. The spectrometer was coupled to an optic microscope Olympus BXFM (50x). A Linkam THMG600/720 stage, with a PE95/T95 temperature controller and an LNP liquid nitrogen cooling system, was installed on the microscope. Samples were put on an aluminium sample cell in the Linkam stage. Raman spectra were obtained for an exposure time of 15 s. The coupling of the Linkam stage and the micro-Raman equipment permitted us to strictly follow thermal treatments, controlling the cooling and heating rates in a wide temperature range.

2.3.

A Saturated-Unsaturated-Saturated (SUS) triacylglycerol: 1,3-dipalmitoyl-2-oleoyl glycerol (POP)

POP is a main TAG of vegetable and animal fats such as cocoa butter, palm oil, and pork fat (Timms, 2005). POP exhibits polymorphic forms α, γ, δ, β'_2, β'_1, β_2, and β_1 that cause a complicated behavior. As mentioned above, Koyano et al. (1991) examined the crystallization kinetics of POP using optical microscopy, DSC, and X-ray diffraction. They observed that metastable forms α and γ occurred with decreasing crystallization temperatures (T_c) when the molten samples were quenched to different T_c. However, they did not perform *in-situ* observation of the crystallization of POP polymorphs at different cooling rates. Cebula et al. (1991) applied DSC to the crystallization of POP, POS, and SOS and demonstrated the effects of variations in the cooling and heating rates. They observed that the number of DSC peaks depended on the rates of cooling and heating, as well as the fatty-acid composition of the analyzed TAGs. When samples were cooled rapidly, progressive polymorphic transformations occurred during reheating. The degree of transformation was greater when low heating rates were applied. However, details about the polymorphic structures were not given, since an XRD analysis was not performed.

In this section, we applied DSC and SR-XRD to monitor the crystallization and transformation kinetics of POP polymorphs *in-situ*. A combination of two techniques permits us to observe *in-situ* the transformation pathways during cooling and heating. Melted samples were cooled from 40ºC to -80ºC and heated afterwards. They were subjected to cooling rates of 15, 2, 1, and 0.5ºC·min^{-1} and heating rates of 15, 2, 1, 0.5, and 0.1ºC·min^{-1} in the following patterns: (1) Cooled at 15ºC·min^{-1} and heated at 15ºC·min^{-1} and 0.1ºC·min^{-1}, (2) Cooled at 2ºC·min^{-1} and heated at 15ºC·min^{-1}, 2ºC·min^{-1} and 1ºC·min^{-1}, (3) Cooled at 1ºC·min^{-1} and heated at 15ºC·min^{-1}, 2ºC·min^{-1}, 0.5 ºC·min^{-1} and 0.1ºC·min^{-1}, and (4) Cooled at 0.5ºC·min^{-1} and heated at 15ºC·min^{-1}. The reasons for choosing the above temperature variations will be explained below. As complementary data, we used conventional XRD methods to observe *in-situ* the transformation behavior during heating at rates of 0.5 and 0.1ºC·min^{-1} after crystallization.

Table 2.1 summarizes the melting temperatures (T_m) and the long and short spacing of the POP polymorphs studied in this work. The results agree well with those of previous literature data (Sato et al., 1989). Chain-length structures of the seven polymorphs are double for α form and two β' forms and triple for γ, δ, and two β forms. We could not identify the two β forms in the present study because of subtle differences in short and long spacing values. Therefore, we will simply refer to β form.

Table 2.1. Melting temperatures (T_m), long and short spacing values of the POP polymorphs. (A) Previous work (Sato et al., 1989) and (B) present study.

Polymorph		α	γ	δ	β'_2	β'_1	β_2	β_1
A	T_m (ºC)	15.2	27.0	29.2	30.3	33.5	35.1	36.7
	Long spacing/nm	4.65	6.54	6.25	4.24	4.24	6.10	6.10
	Short spacing/nm	0.42	0.47 0.45 0.39 0.36	0.43 0.41 0.38	0.44 0.42 0.40	0.43 0.41 0.40	0.46 0.41 0.39 0.38 0.37	0.46 0.41 0.39 0.37
B	T_m (ºC)	16	26	30	27*	32	35	36
	Long spacing/nm	4.7	7.5	6.5	4.2	4.2	6.1	
	Short spacing/nm	0.42	0.48 0.47 0.45 0.40 0.39	0.42 0.40 0.38	0.43 0.42 0.39	0.43 0.40	0.46 0.41 0.38 0.37	

* This melting temperature corresponds to the peak top value, not to the T_{onset}.

2.3.1. Cooling rates of 15ºC·min^{-1} and 2ºC·min^{-1}

α form was crystallized when the cooling rate was 15ºC·min^{-1}. However, the transformation from α to more stable forms was quite different when we changed the heating rate, as indicated in Table 2.2A. Heating at a rate of 15ºC·min^{-1} caused the melt-mediated transformation of α→liquid→β'_2 and the melting of β'_2 form, whereas heating at 0.1ºC·min^{-1} caused α→γ→δ→liquid→β→liquid transformations. We will present the typical experimental data showing the above results.

Table 2.2. DSC data of crystallization and transformation of POP polymorphs obtained by cooling rates of (A) 15ºC·min^{-1} and (B) 2ºC·min^{-1} and different heating rates. The letters, *c*, *s* and *m*, in parentheses noting polymorphic forms mean crystallization, solid-state transformation and melting.

A	**Cooling**	**Heating**				
	(15ºC·min^{-1})	**(15ºC·min^{-1})**				
	α (c)	*α (m)*	*β′$_2$ (c)*	*β′$_2$ (m)*		
T_{onset} (ºC)	10.4 ± 0.5	15.5 ± 0.5	20.5 ± 0.8	22.5 ± 0.5		
ΔH (J/g)	-87 ± 2	79 ± 3	-2 ± 1	11 ± 2		
		(0.1ºC·min^{-1})				
		α → γ (s)	*γ → δ (s)*	*δ (m)*	*β (c)*	*β (m)*
T_{onset} (ºC)		12.0 ± 0.6	24.7 ± 0.4	31.7 ± 0.5	32.6 ± 0.3	35.6 ± 0.4
ΔH (J/g)		-23 ± 4	-17 ± 3	148 ± 15	-58 ± 14	73 ± 15
B	**Cooling**	**Heating**				
	(2ºC·min^{-1})	**(15ºC·min^{-1})**				
	α (c)	*α (m)*	*β′$_2$ (c)*	*β′$_2$ (m)*		
T_{onset} (ºC)	13.6 ± 0.3	15.7 ± 0.3	20.6 ± 0.8	22.6 ± 0.6		
ΔH (J/g)	-88 ± 4	77 ± 5	-2 ± <1	18 ± 6		
		(2ºC·min^{-1})				
		α (m)	*γ (c)*	*γ (m)*	*β (c)*	*β (m)*
T_{onset} (ºC)		15.7 ± 0.4	16.7 ± 0.3	26.1 ± 0.4	28.5 ± 0.3	30.9 ± 0.3
ΔH (J/g)		21 ± 2	-38 ± 2	122 ± 9	-21 ± 3	29 ± 3
		(1ºC·min^{-1})				
		α → γ	*γ (m)*	*β(c)*	*β (m)*	
T_{onset} (ºC)		14.9 ± 0.5	26.1 ± 0.6	28.3 ± 0.5	31.1 ± 0.5	
ΔH (J/g)		-25 ± 1	113 ± 5	-55 ± 4	67 ± 4	

Figure 2.1 depicts the DSC thermograms and the SR-SAXD and SR-WAXD patterns obtained after cooling the sample from the melt at 15ºC·min^{-1} and heating it afterwards at 15ºC·min^{-1}.

α form was crystallized when POP was cooled at 15ºC·min^{-1}, as a long spacing of 4.7 nm and a short spacing of 0.42 nm were observed. After this crystallization, a melt-mediated transition from α form to β'$_2$ form occurred on heating at 15ºC·min^{-1}, as confirmed by an endothermic peak at T_{onset}=15.5ºC, an exothermic peak at T_{onset}=20.5ºC, and an endothermic peak at T_{onset}=22.5ºC in DSC. In addition, the SAXD peak shifted from 4.7 nm to 4.2 nm, and three new WAXD short spacing peaks of 0.43, 0.42, and 0.39 nm appeared in the SR-XRD data taken during heating at 15ºC·min^{-1}. This form finally melted around 22ºC. Table 2.2A summarizes the onset temperatures (T_{onset}) and enthalpy (ΔH) of crystallization of α form and the transformations into more stable forms.

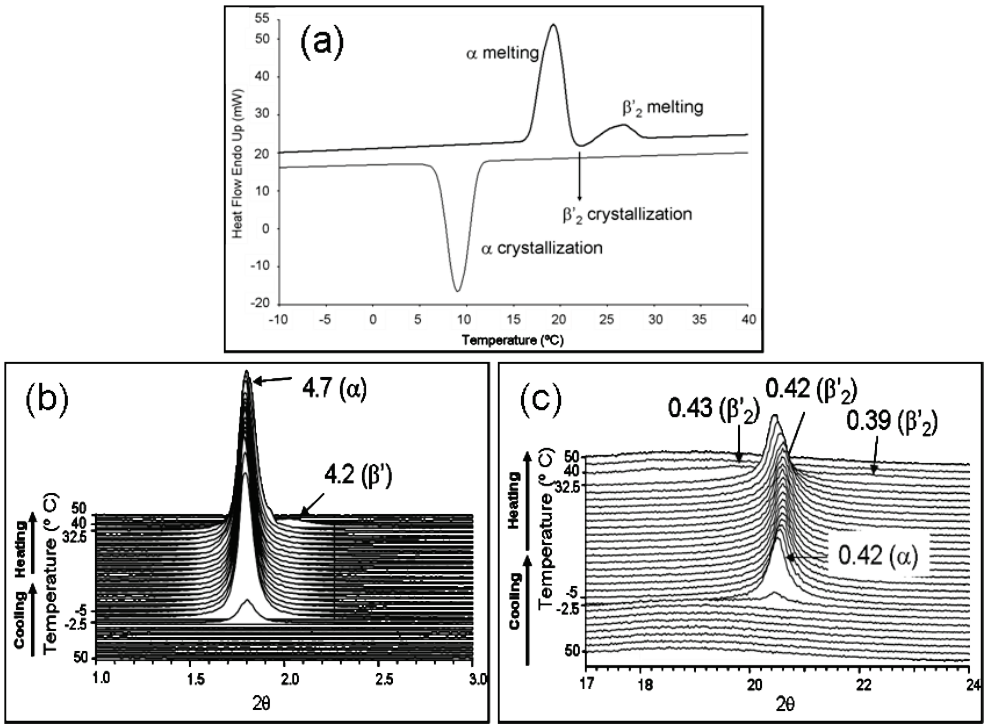

Figure 2.1. Polymorphic behavior of POP when cooled at 15ºC·min^{-1} (α crystallization) and heated at 15ºC·min^{-1}. (a) DSC thermogram. (b) SR-SAXD pattern. (c) SR-WAXD pattern.

The heating rate was decreased to 0.1ºC·min^{-1} after crystallization at 15ºC·min^{-1} to observe the more stable forms from α (Figure 2.2). The heating DSC patterns between 12ºC and 38ºC were enlarged because the DSC heating thermopeaks acquired at the rate of 0.1 ºC·min^{-1} were so weak compared to those acquired by heating at 15 ºC·min^{-1}, and are presented in Figure 2.2(a).

Two consecutive solid-state transitions took place, from α form to γ form at T_{onset}=12.0 ºC and from γ form to δ form at T_{onset}=24.7 ºC, as indicated by the two exothermic DSC peaks. On further heating, a melt-mediated transformation from δ form to β form occurred, and β form eventually melted. The T_{onset} values of these transformations are given in Table 2.2A.

The solid-state α→γ transition can be clearly confirmed in the XRD patterns using conventional XRD apparatus (Figure 2.2(b)). The change from a double-chain-length (4.6 nm) to a triple-chain-length structure (3.5 nm of the 002 reflection) and the changes in the WAXD from a short spacing of 0.42 nm to 0.47 nm, 0.45 nm, and 0.39 nm correspond to the α→γ transition. The solid-state γ→δ transformation is clearly indicated by the presence of strong WAXD peaks at 0.42 nm, 0.40 nm, and 0.38 nm. The XRD patterns of δ form disappear around 31ºC because of the melting of δ form,

and new XRD peaks of β form occur around 33ºC and disappear around 36ºC. Although conventional XRD patterns cannot distinguish between the two β forms, the double melting peaks in the DSC profile probably correspond to the melting of β_2 and β_1 forms.

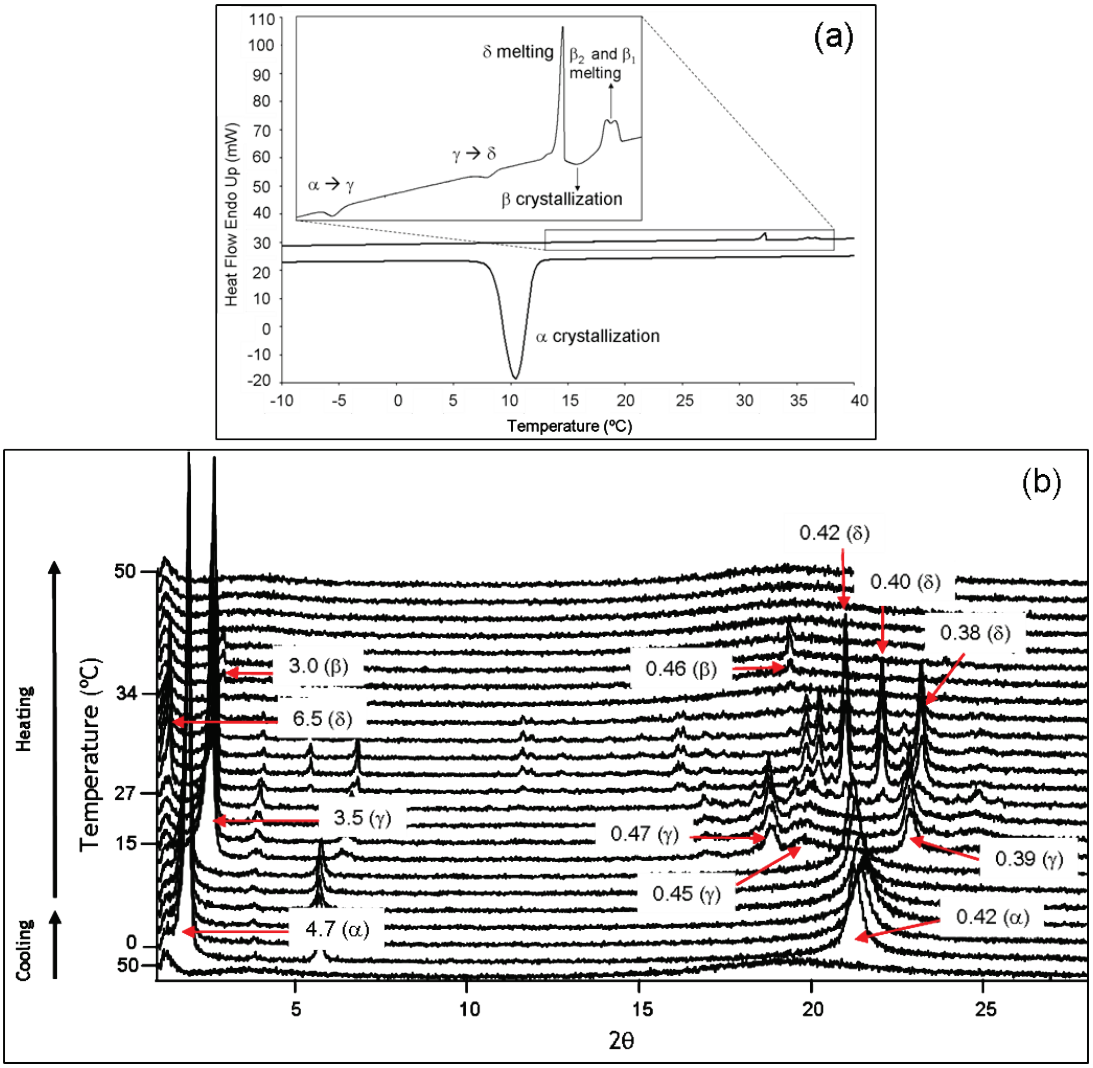

Figure 2.2. Polymorphic behavior of POP when cooled at 15ºC·min^{-1} (α crystallization) and heated at 0.1ºC·min^{-1}. (a) DSC thermogram. (b) Conventional XRD patterns.

In all of the above cases, some hysteresis was observed between the crystallization and melting processes (Table 2.2). Some crystallization enthalpies may be underestimated due to the peaks overlapping or more complex phenomena. The enthalpy corresponding to the δ form melting becomes particularly high compared to the melting enthalpy of the other forms.

α form was crystallized when the cooling rate was 2ºC·min^{-1}, similarly to cooling at 15ºC·min^{-1}. DSC and XRD experiments were performed at heating rates of 15, 2, and 1ºC·min^{-1} (Table 2.2B). The results obtained for cooling at 2ºC·min^{-1} and heating at 15ºC·min^{-1} were the same than those of cooling and heating at 15ºC·min^{-1}: melt-mediated α-β' transformation and melting of β'form. Figure 2.3(a) presents the DSC and XRD data for cooling and heating at 2ºC·min^{-1}.

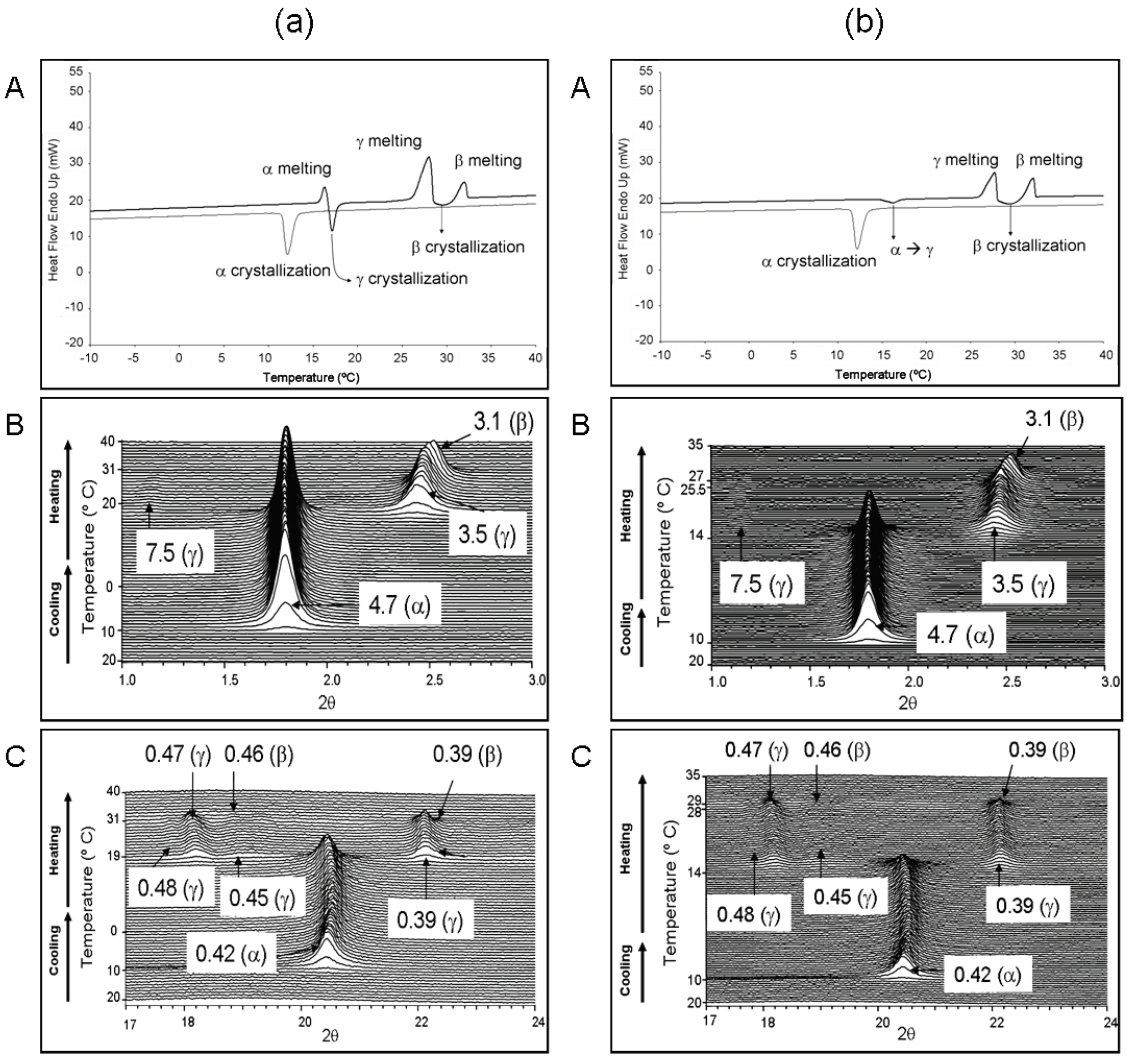

Figure 2.3. Polymorphic behavior of POP. (a) Cooling at 2ºC·min^{-1} and heating at 2ºC·min^{-1}. A. DSC thermogram. B. SR-SAXD pattern. C. SR-WAXD pattern. (b) Cooling at 2ºC·min^{-1} and heating at 1ºC·min^{-1}. A. DSC thermogram. B. SR-SAXD pattern. C. SR-WAXD pattern.

Melt-mediated transformations from α form to γ form (γ to β) occurred around 15 to 16ºC (26 to 28ºC), and the β form melted at 35ºC. These results are indicated by the successive appearance of endothermic and exothermic DSC peaks and the

corresponding occurrence and disappearance of SAXD and WAXD patterns. By contrast, heating at 1ºC·min^{-1} (Figure 2.3(b)) caused a solid-state transformation from α form to γ form at 15ºC , as indicated by the exothermic DSC peak. Similarly to heating at 2ºC·min^{-1}, melt-mediated transformations from γ form to β form occurred at 26 to 28ºC, and the β form melted at 31ºC.

The main results of the transformation pathways from α form obtained with cooling rates of 15ºC·min^{-1} and 2ºC·min^{-1} and different heating rates can be summarized as follows. (a) Melt-mediated transformations occurred at heating rates of 15ºC·min^{-1} (α-liquid-β'$_2$-liquid) and 2ºC·min^{-1} (α-liquid-γ-liquid-β-liquid). (b) Solid-state α→γ transformation occurred at a heating rate of 1ºC·min^{-1}. (c) The most stable β form occurred when the heating rate was decreased to 2ºC·min^{-1} or less. These properties were basically the same as those observed with cooling at 15ºC·min^{-1} and heating at 15ºC·min^{-1} and 0.1ºC·min^{-1} (Figures 2.1 and 2.2).

2.3.2. Cooling rates of 1ºC·min^{-1} and 0.5ºC·min^{-1}

γ form was always crystallized when the cooling rate was 1ºC·min^{-1} or 0.5ºC·min^{-1}. The transformation from γ form to more stable forms became very complicated when we changed the rates of heating to 15, 2, 0.5, and finally 0.1ºC·min^{-1} (Table 2.3).

The transformation pathways observed during heating after crystallization at a cooling rate of 1ºC·min^{-1} are listed in Table 2.3A. Heating at rates of 15ºC·min^{-1} and 2ºC·min^{-1} caused melting of γ form without transformation into other forms. By contrast, melt-mediated transformation into β' form and its melting occurred at a heating rate of 0.5ºC·min^{-1}, whereas successive transformations of γ→liquid→β'+δ→liquid→β→ liquid occurred at a heating rate of 0.1ºC·min^{-1}. The experiments with cooling at 0.5ºC·min^{-1} and heating at 15ºC·min^{-1} suggested simple melting of γ form (Table 2.3B).

Here, we provide typical data for the XRD and DSC experiments in Table 2.3.

Table 2.3. DSC data of crystallization and transformation of POP polymorphs obtained by cooling rates of 1ºC·min^{-1} and 0.5ºC·min^{-1}, and different heating rates. In each column noting polymorph, *c*, *s* and *m* in parentheses mean crystallization, solid-state transformation and melting.

A	**Cooling**	**Heating**					
	(1ºC·min^{-1})	**(15ºC·min^{-1})**					
	γ (c)	*γ (m)*					
T_{onset} (ºC)	17.7 ± 0.4	25.5 ± 0.4					
ΔH (J/g)	-112 ± 3	116 ± 4					
		(2ºC·min^{-1})					
		γ (m)					
T_{onset} (ºC)		26.4 ± 0.9					
ΔH (J/g)		118 ± 3					
		(0.5ºC·min^{-1})					
		γ (m)	*β′$_1$ (m)*				
T_{onset} (ºC)		26.6 ± 0.5	31.5 ± 0.5				
ΔH (J/g)		127 ± 3	3 ± 2				
		(0.1ºC·min^{-1})					
		γ (m)	*δ+β′$_1$ (c)*	*δ (m)*	*β′$_1$ (m)*	*β (c)*	*β$_2$ + β$_1$(m)*	
T_{onset} (ºC)		26.9 ± 0.4	28.0 ± 0.4	30.4 ± 0.6	31.6 ± 0.5	32.1 ± 0.5	34.9 ± 0.5	35.7 ± 0.6
ΔH (J/g)		*	-84 ± 9	~ 1	3 ± 2	-6 ± 4	170 ± 11	
B	**Cooling**	**Heating**					
	(0.5ºC·min^{-1})	**(15ºC·min^{-1})**					
	γ (c)	*γ (m)*					
T_{onset} (ºC)	19.9 ± 0.7	25.6 ± 0.4					
ΔH (J/g)	-116 ± 5	120 ± 4					

***** It was not possible to determine this value due to phenomena overlapping.

Figure 2.4 presents the results of cooling at 1ºC·min^{-1} and heating at 15ºC·min^{-1}. The crystallization (melting) of γ form are indicated by DSC exothermic (endothermic) peaks on cooling (heating). The corresponding SAXD and WAXD patterns are also presented in Figure 2.4. Although not shown here, the same results were observed for cooling at 1ºC·min^{-1} and heating at 2ºC·min^{-1}, and for cooling at 0.5ºC·min^{-1} and heating at 15ºC·min^{-1}.

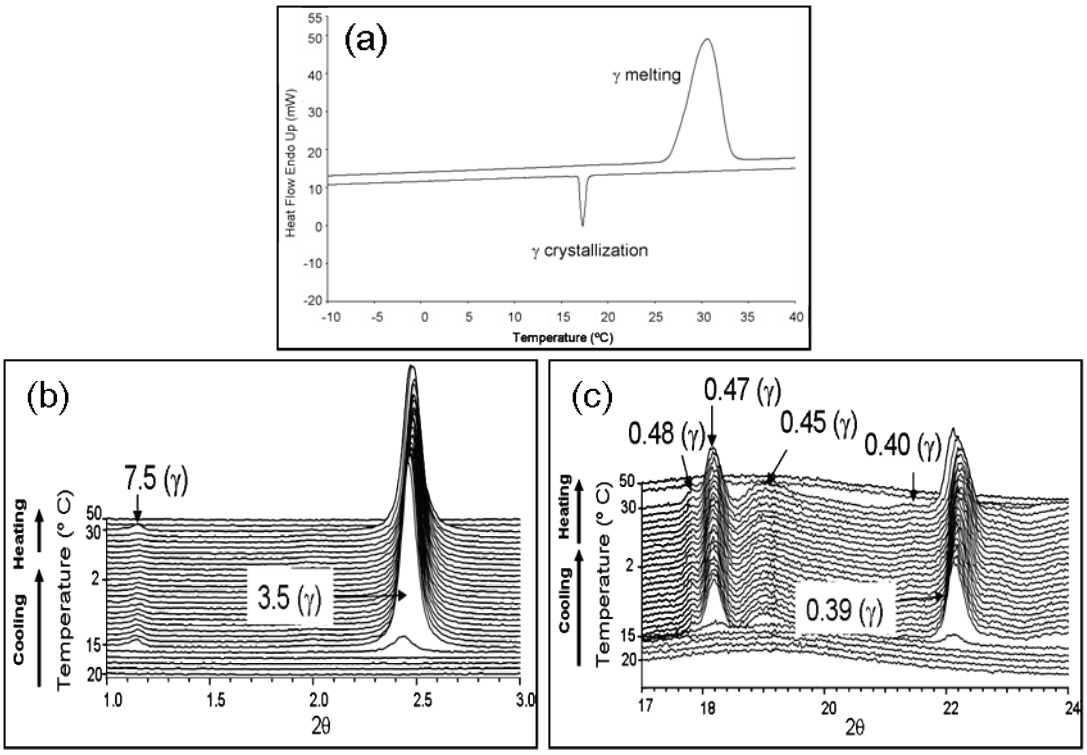

Figure 2.4. Polymorphic behavior of POP when cooled at 1ºC·min^{-1} (γ crystallization) and heated at 15ºC·min^{-1}. (a) DSC thermogram. (b) SR-SAXD pattern. (c) SR-WAXD pattern.

Reducing the heating rates, however, affected the transformation pathways from γ to more stable forms. Figure 2.5 presents the results of cooling at 1ºC·min^{-1} and heating at 0.5ºC·min^{-1}.

The DSC heating profile has two endothermic peaks, an intense peak corresponding to the melting of γ form and a very small peak due to the melting of β' form. The conventional XRD experiments indicated that the characteristic diffraction peaks of δ and β'_2 forms also appeared before β'_1 form. Moreover, the typical diffraction peaks of the β form (6.1 nm and 0.46 nm) were also identified by heating to 40ºC. These transformation pathways were not detectable by DSC, probably due to the subtle thermal energies associated with the transformations.

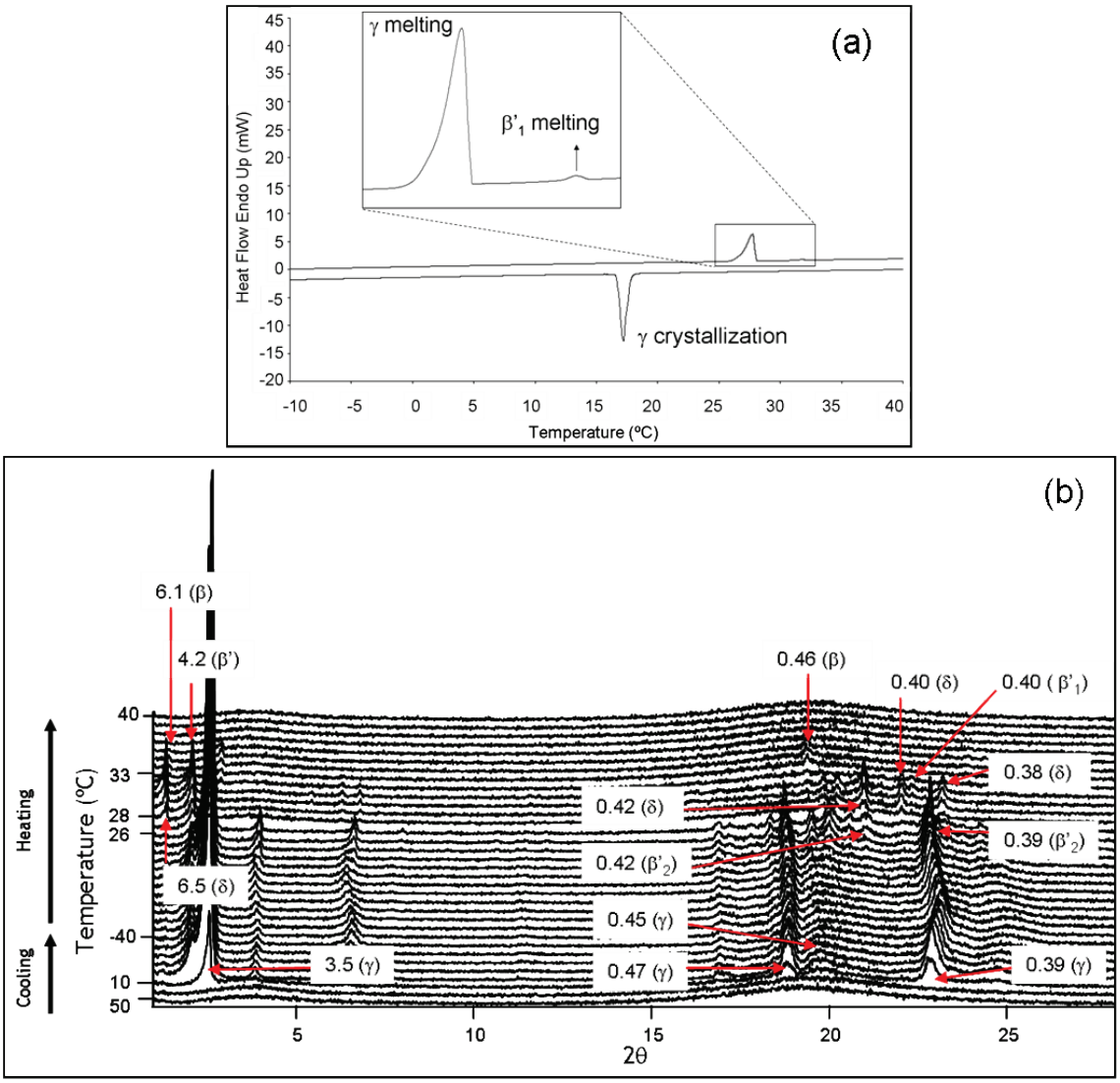

Figure 2.5. Polymorphic behavior of POP when cooled at 1ºC·min^{-1} (γ crystallization) and heated at 0.5ºC·min^{-1}. (a) DSC thermogram. (b) Conventional XRD pattern.

Additional polymorphic pathways were observed for cooling at 1ºC·min^{-1} and heating at 0.1ºC·min^{-1} (Figure 2.6). Quite complicated DSC heating thermopeaks were observed after γ form crystallized (see the inserts in Figure 2.6(a)). The conventional XRD study clarified that these DSC peaks correspond to successive melt-mediated transformations from γ to β forms through various intermediate forms (Figure 2.6(b)).

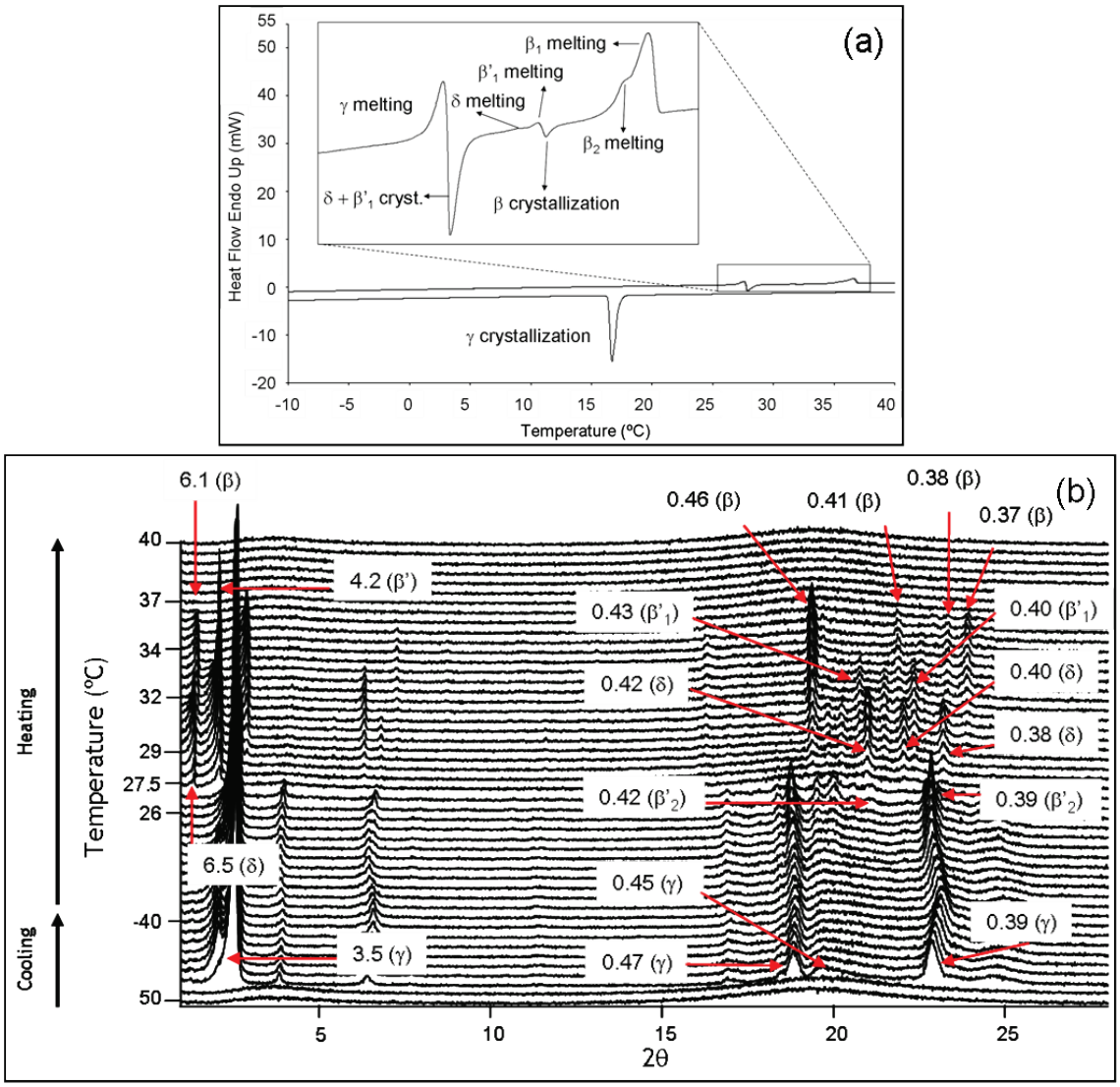

Figure 2.6. Polymorphic behavior of POP when cooled at 1ºC·min^{-1} (γ crystallization) and heated at 0.1ºC·min^{-1}. (a) DSC thermogram. (b) Conventional XRD pattern.

The melting of γ form caused concurrent crystallization of δ and β'$_1$ forms. On further heating, δ and β'$_1$ forms melted around 30 to 31ºC and β form crystallized at 32ºC. Two melting peaks were observed, probably corresponding to the two β forms. Although not seen in the DSC profile, β'$_2$ form (with short spacing of 0.42 nm and 0.39 nm) appeared before the δ form, according to the conventional XRD data.

Looking at the temperatures in Table 2.3, there is also hysteresis between the crystallization and melting processes for γ crystallization.

The main results of the transformation pathways from γ form obtained by cooling rates of 1ºC·min^{-1} and 0.5ºC·min^{-1} with different heating rates can be summarized as follows:

(a) Samples did not transform into more stable forms at heating rates of 15ºC·min^{-1} and 2ºC·min^{-1}; instead, the γ form simply melted. This clearly contrasts with the results from the transformation pathways starting from α to more stable forms, even at a heating rate of 15ºC·min^{-1} (Table 2.2).

(b) Melt-mediated transformations occurred at heating rates below 0.5ºC·min^{-1} (γ-liquid-β'$_2$-liquid) and 0.1ºC·min^{-1} (γ-liquid-β'+δ-liquid-β-liquid).

(c) No particular solid-state transformation occurred at any heating rate examined.

(d) The most stable β form occurred when the heating rate was 0.1ºC·min^{-1}.

Figure 2.7 summarizes all of the transformation pathways examined in the present study.

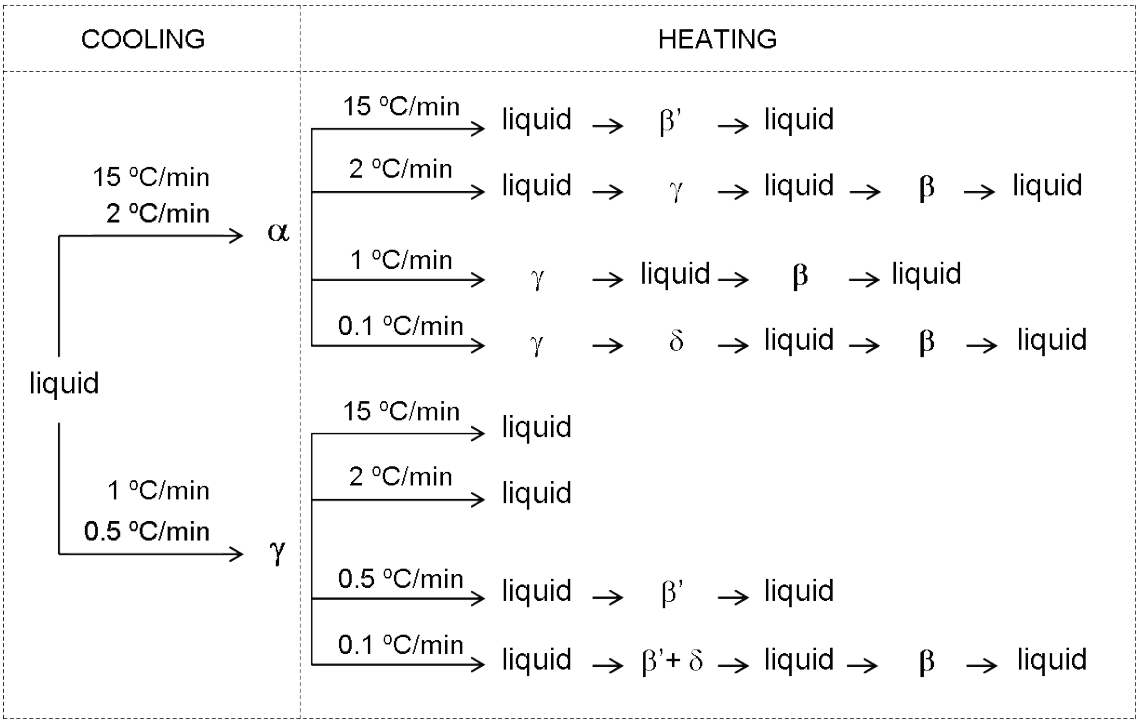

Figure 2.7. Diagrams of polymorphic pathways of POP under different cooling and heating conditions.

The following properties of the very complicated phenomena observed in the crystallization and polymorphic transformations must be discussed.

(a) Polymorphic crystallization depending on different cooling rates.

(b) The causes for the different pathways of polymorphic transformations, namely simple melting, melt-mediated transformation, and solid-state transformation,

which are influenced by the rate of heating and the first-occurring polymorph, α or γ forms.

(c) The causes for the most stable form of β with decreased rates of heating.

2.3.3. Cooling rates and polymorphic crystallization

The Ostwald step rule (Ostwald, 1897) should be discussed for polymorphic crystallization. This rule predicts that the first solid phase appearing from liquid should be a stable phase, such as amorphous phase or a less stable polymorph, which then transforms to more stable phases during stabilization. However, it must be pointed out that other factors such as the cooling rate may modify this "rule."

Figure 2.8 illustrates the relationships between the polymorphic crystallization of α, γ, and β' forms of POP and the cooling rate**,** which are depicted based on the present work.

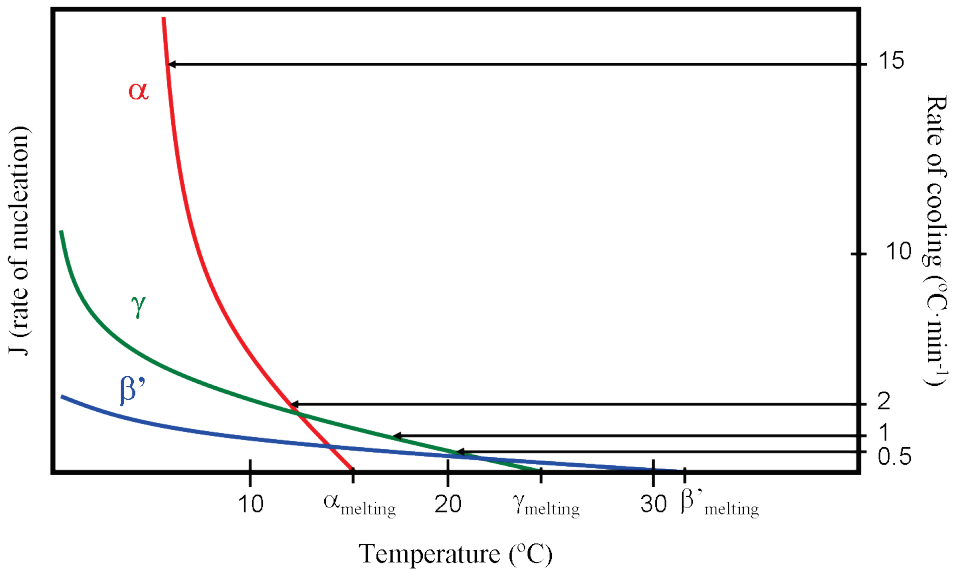

Figure 2.8. Relationship between different cooling rates and crystallization behavior of POP polymorphs.

We assumed that the rate of nucleation (J) of α form rapidly increases with decreasing crystallization temperature (T_c) (increasing supercooling: T_m-T_c) because of the higher α nucleation rate. By contrast, the increase in J with decreasing T_c in the more stable γ and β' forms is less than that of α form because of their lower nucleation

rates. Figure 2.8 indicates that preferentially nucleating polymorph may vary with different T_c as follows: α form in a low-temperature T_c region (α-dominating region), γ form in an intermediate T_c region (γ-dominating region), and β' form in the highest T_c region (β'-dominating region). Considering this, we may expect that cooling rates of 15 and 2ºC·min^{-1} may reach the α-dominating region, and that cooling rates of 1 and 0.5ºC·min^{-1} may reach the γ-dominating region. More stable polymorphs of the β' and β forms could only be obtained by cooling POP at rates much lower than 0.5ºC·min^{-1}, and therefore we could not obtain these forms in the present study.

In previous work, Koyano et al. (1991) reported that they observed the crystallization of β' and β forms of POP**,** in addition to α and γ forms, by performing isothermal crystallization after rapidly cooling the liquid to different T_c and observing the crystallization at that temperature. The range in which β' form crystallized at a T_c of 23 to 27ºC, and the induction times for β' occurrence were quite long. The β form was only crystallized from γ-melt-mediated transformation. β' and β forms of POP should thus be crystallized at very low rates of cooling, as our present study has demonstrated.

2.3.4. Heating rates and polymorphic transformation pathways

The Ostwald step rule predicts that the first-occurring metastable forms are followed by other forms of increasing stability. This phenomenon was observed in the heating experiments in the present study, as phase transitions from α or γ forms to more stable forms were observed during the heating processes. A peculiar feature observed in this study is that the transformations pathways were markedly and in a very complex way influenced by the rate of heating, as summarized in Figure 2.7.

As an example, α crystals transformed into β' through the liquid state (melt-mediated transformation) at a heating rate of 15ºC·min^{-1}. When the heating rate was 2ºC·min^{-1}, the α→γ transformation also occurred through the liquid state, but at 1ºC·min^{-1} the same transition took place in the solid state. Moreover, there were two consecutive solid-solid transitions of α→γ and γ→δ followed by a melt-mediated transformation of δ→β at a heating rate of 0.1ºC·min^{-1}.

We should also consider the different behavior at the same rate of heating when we change the starting polymorph from α to γ. When α crystals were heated at 15ºC·min^{-1}, β' crystals were obtained through a melt-mediated transformation. In contrast, no further polymorphic transformation occurred when the same heating rate was applied to transformations starting from γ crystals, and the γ crystals simply melted.

Comparing the polymorphic transformations from α and γ to other forms during heating at 0.1ºC·min^{-1}, it seems that a greater amount of the most stable forms is obtained when the heating process starts from γ rather than α form. As an example, we can compare the ΔH values of melting of the β form, having different starting polymorphs, α form (Table 2.2) or γ form (Table 2.3). ΔH for β(m) was 73 ± 15 J·g^{-1} when starting from α form, but it was 170 ± 11 J·g^{-1} when starting from γ form. This difference was also observed in the XRD peaks corresponding to the β form: they became more intense when starting with γ form.

We can understand the above complex transformation pathways by taking into account the activation free-energy diagrams of solid-state and melt-mediated transformations. Figure 2.9 illustrates two typical transformations that take place from a less stable form (A) to a more stable form (B), in addition to simple melting of form A without transformation to form B.

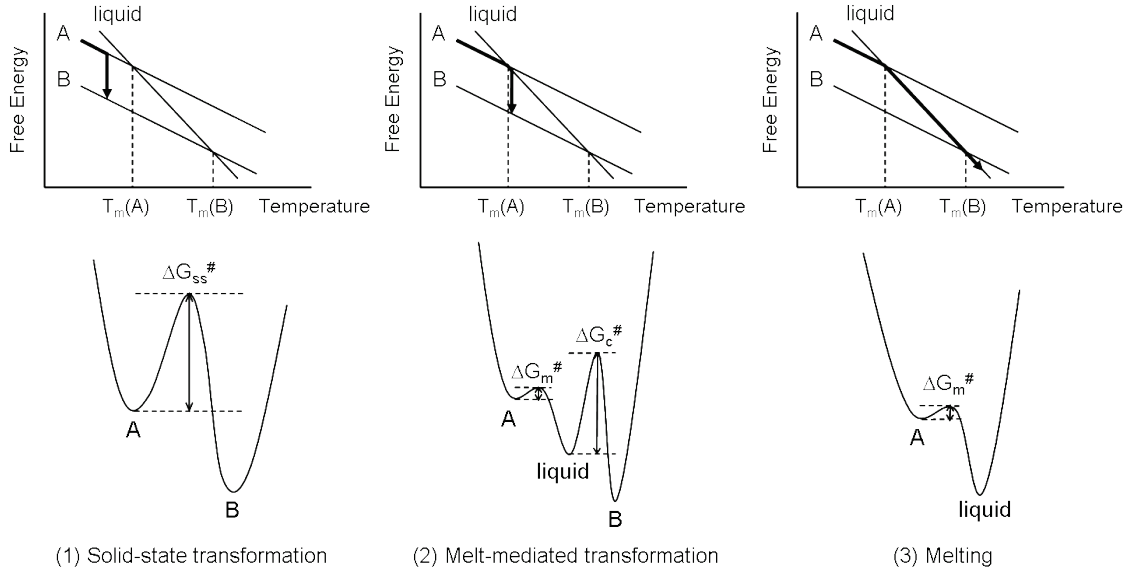

Figure 2.9. Relative stability of two polymorphic forms showing typical transformation pathways. (1) Solid-state transformation (2) melt-mediated transformation and (3) simple melting.

These transformations are basically determined by the magnitude of the activation free energies involved in each process (Kashchiev et al., 1998). In a solid-state transformation, the transition rate is determined by $\Delta G_{ss}^{\#}$, which may include excess energy to enable structural changes (subcell structure, chain-length structure, etc.) needed to cause the transformation from form A to form B. The rate of the melt-mediated transformation is determined by the magnitude of the activation free-energy barriers of the melting ($\Delta G_m^{\#}$) of form A and the subsequent crystallization ($\Delta G_c^{\#}$) of form B.

Whether a transformation pathway results in solid-state or melt-mediated transformations or simple melting at different rates of heating may be understood by comparing the induction time for the transformation pathways with the time allocated to the samples for transformation (transformation time) at a defined heating rate. We may assume that a higher heating rate yields a shorter transformation time.

The induction time (τ) can be defined for solid-state transformation (τ_{ss}), melt-mediated transformation (τ_{mm}), and melting (τ_m) as follows.

$$\tau_{ss} = A_1 \exp(\Delta G_{ss}^{\#}/RT)$$

$$\tau_{mm} = A_2 \exp(\Delta G_{mm}^{\#}/RT) = A_2 \exp[(\Delta G_m^{\#} + \Delta G_c^{\#})/RT]$$

$$\tau_m = A_3 \exp(\Delta G_m^{\#}/RT)$$

Here A_1 to A_3 are coefficients, R and T are the gas constant and temperature, $\Delta G_{ss}^{\#}$ is the activation Gibbs free energy for solid-state transformation, $\Delta G_{mm}^{\#} = \Delta G_m^{\#} + \Delta G_c^{\#}$ is that for melt-mediated transformation including melting of less stable forms and crystallization of more stable forms, and $\Delta G_m^{\#}$ is that for melting (Figure 2.9). Obviously, the induction time for the transformation increases as $\Delta G^{\#}$ increases. It is reasonable that $\Delta G_m^{\#}$ is much smaller than the others, and that the values of $\Delta G_{ss}^{\#}$ and $\Delta G_c^{\#}$ increase when the polymorphic form becomes more stable, as the crystal packing of the more stable form is more stabilized than that of less stable forms. This may apply to the present cases of α, γ, β', and δ forms such that $\Delta G_{ss}^{\#}$ for $\gamma \rightarrow \beta'$, $\gamma \rightarrow \delta$, and $\delta \rightarrow \beta$ may be greater than that of $\alpha \rightarrow \gamma$. $\Delta G_c^{\#}$ is evidently greater for β' and γ forms than for α form, based on the present study (Figure 2.8). Therefore, the following relations can be obtained.

τ_{ss} ($\alpha \rightarrow \gamma$) < τ_{ss} ($\gamma \rightarrow \delta$) < τ_{ss} ($\gamma \rightarrow \beta'$) < τ_{ss} ($\delta \rightarrow \beta$)

τ_{mm} ($\alpha \rightarrow \gamma$) < τ_{mm} ($\gamma \rightarrow \beta'$) < τ_{mm} ($\gamma \rightarrow \delta$) < τ_{mm} ($\delta \rightarrow \beta$) < τ_{mm} ($\beta' \rightarrow \beta$)

If the heating rate is increased, the time for the polymorphic form to transform into more stable forms is decreased, as expressed in r^{-1}, in which r is the heating rate. There are three typical relationships between the heating rates and the induction times for the transformations, corresponding to the experiment results (Figure 2.7).

Case 1. $r^{-1} < \tau_{mm} < \tau_{ss}$

This is applied to simple melting of γ form at heating rates of 15 and 2ºC·min^{-1}, since solid-state and melt-mediated transformations cannot occur due to large values of $\Delta G_{ss}^{\#}$ and $\Delta G_{mm}^{\#}$ from γ to other stable forms.

Case 2. $\tau_{mm} < r^{-1} < \tau_{ss}$

This is applied to the melt-mediated transformation pathways of $\alpha \rightarrow \beta$' (15ºC·min^{-1}) and $\alpha \rightarrow \gamma$ (2ºC·min^{-1}), $\gamma \rightarrow \beta$ (2ºC·min^{-1} and 1ºC·min^{-1}), $\gamma \rightarrow \beta'$ (0.5ºC·min^{-1}), $\gamma \rightarrow \beta'+\delta$ (0.1ºC·min^{-1}), and $\beta'+\delta \rightarrow \beta$ (0.1ºC·min^{-1}).

Case 3. $\tau_{ss} < r^{-1}$

This is applied to the cases with very low heating rates of $\alpha \rightarrow \gamma$ (1ºC·min^{-1} and 0.1ºC·min^{-1}) and $\gamma \rightarrow \delta$ (0.1ºC·min^{-1}).

Some results are complex, there is a clear tendency in which the transformation pathways changed from solid-state to melt-mediated and simple melting when the starting polymorph changed from α to γ and the heating rate was increased.

As to the formation of the most stable form of β, the values of τ_{ss} for $\alpha \rightarrow \beta$ and $\gamma \rightarrow \beta$ are too long to be reached by the heating rate of 0.1ºC·min^{-1}. Instead, τ_{mm} can be reached by decreasing the heating rate below 1ºC·min^{-1}. This may be ascribed to the most dense subcell packing ($T_{//}$) and the triple-chain-length structure of the β form of POP.

This section examined the relationships between the cooling and heating rates and the complicated polymorphic crystallization and transformation pathways of POP. The results were discussed in terms of activation free energies ($\Delta G^{\#}$) for crystallization and transformation, which vary greatly among the polymorphic forms. The results obtained in the present study are closely related to actual crystallization processes of edible fats such as tempering of chocolate and fat spreads, in which most functional polymorphic forms can be attained by applying tailored temperature variations. Thus it is necessary to precisely analyze actual fat systems using the experimental framework presented in this study. This study, based on the polymorphic crystallization and transformation of POP, was published as a research paper (Bayés-García et al., 2013).

2.4.

An Unsaturated-Saturated-Unsaturated (USU) triacylglycerol: 1,3-dioleoyl-2-palmitoyl glycerol (OPO)

OPO is important in palm oil fractionation (Timms, 2005; Calliauw et al., 2007; Smith, 2001), as it belongs to low-melting temperature fractions. Palm oil is often modified to improve its applicability as an edible oil. Due to its heterogeneous composition, well-defined fractions with a high added value are obtained through fractionation. Basically, dry fractionation consists of separating successively different crystal fractions obtained by controlled cooling from the melt. As the temperature decreases during fractionation, fractions richer in high levels of monounsaturated TAGs are separated. Minato et al. (1997b) studied the thermodynamic and polymorphic behavior of OPO and POP and their binary mixtures. However, the present work is focused on the influence of a kinetic parameter (cooling rate) on the polymorphic crystallization of 1,3-dioleoyl-2-palmitoyl glycerol (OPO). Moreover, the relationship between this behavior and the Ostwald step rule is examined. For characterizing the polymorphism of this TAG, no variations in the heating rate were performed, as the present study is entirely focused on the polymorphic crystallization of OPO from the melt.

Therefore, several techniques, such as DSC, TOM and SR-XRD as a function of kinetics (variation of the cooling rates), were used.

Samples were cooled from the melt at different rates (15ºC·min^{-1}, 2ºC·min^{-1}, 1ºC·min^{-1} and 0.5ºC·min^{-1}) from 35ºC to -80ºC and heated at 15ºC·min^{-1}.

Figure 2.10 depicts the OPO DSC thermograms (cooling and heating) obtained by changing the cooling rate and keeping the same heating rate of 15ºC·min^{-1}. Crystal forms were identified by the SR-XRD patterns of simultaneous SAXD and WAXD measurements following the same DSC programs (Figure 2.11). Long spacing values of α, β', β_1, and β_2 forms are known from the work of Minato et al. (1997b).

Table 2.4 specifies T_{onset} for each transition observed in the DSC thermal profiles.

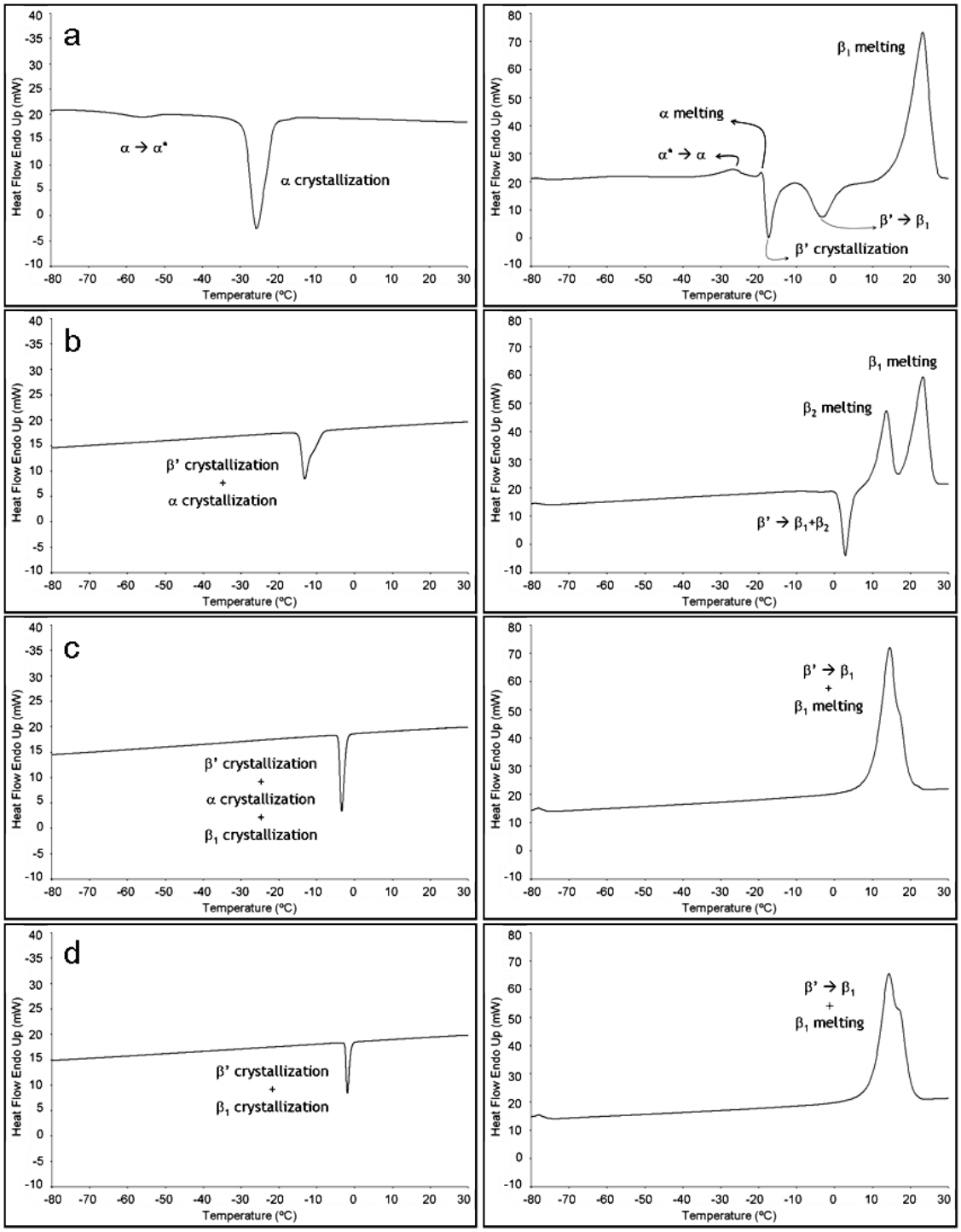

Figure 2.10. DSC thermograms of OPO obtained by changing the cooling rate and keeping a heating rate of 15ºC·min^{-1}. a) Cooling profile at a rate of 15ºC·min^{-1} and heating profile. b) Cooling profile at a rate of 2ºC·min^{-1} and heating profile. c) Cooling profile at a rate of 1ºC·min^{-1} and heating profile. d) Cooling profile at a rate of 0.5ºC·min^{-1} and heating profile.

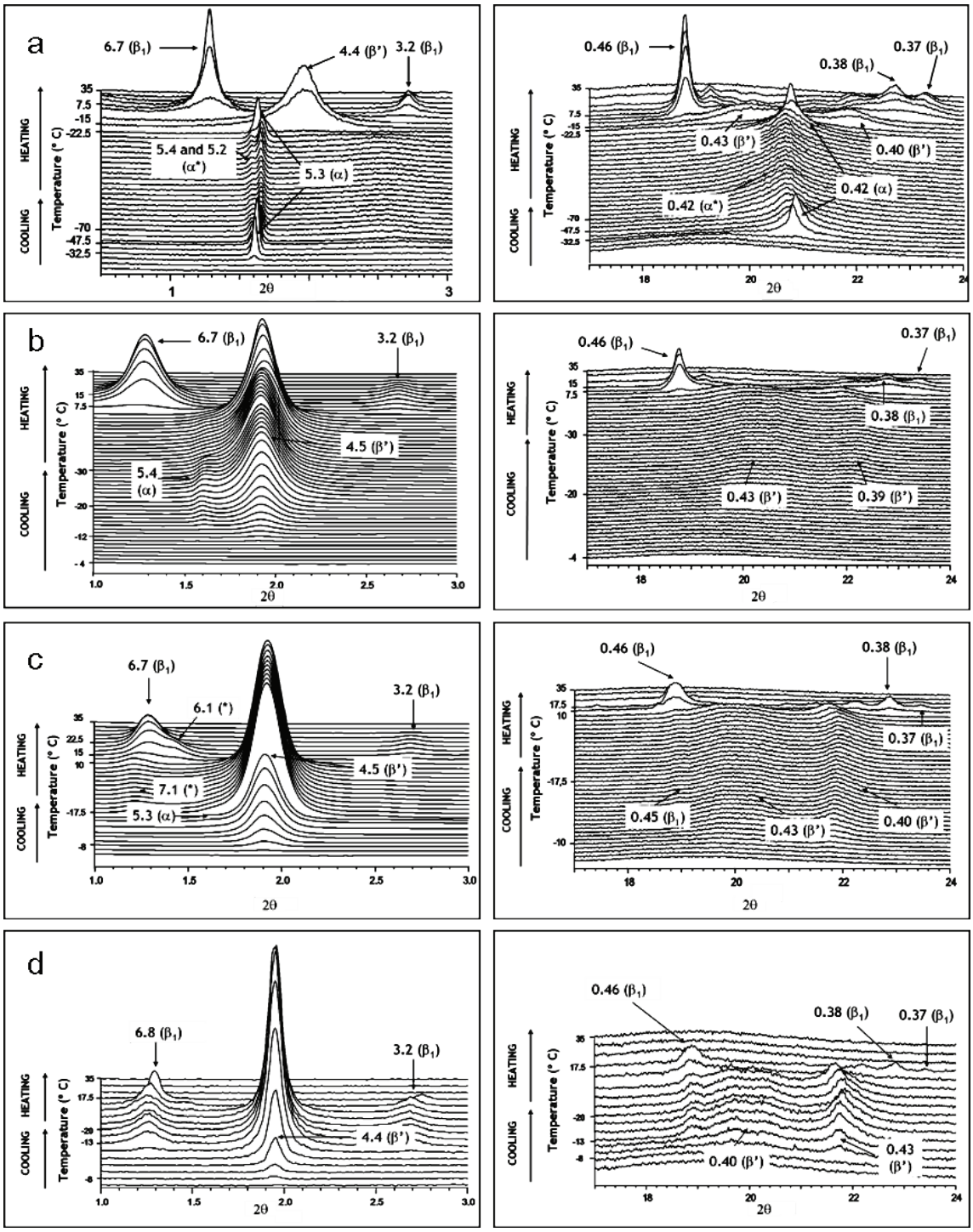

Figure 2.11. SR-XRD SAXD (left) and WAXD (right) patterns of OPO corresponding to the respective DSC programs. d-Spacing values (nm) are shown for the most representative peaks. a) Cooling rate: 15ºC·min^{-1}. b) Cooling rate: 2ºC·min^{-1}: (*) long spacing values for some intermediate forms. c) Cooling rate: 1ºC·min^{-1}. d) Cooling rate: 0.5ºC·min^{-1}.

Table 2.4. T_{onset} for each transition, obtained from the DSC data for OPO when the sample was cooled down at different cooling rates and heated at 15ºC·min^{-1}. In each column noting polymorph, *c*, *s* and *m* in parentheses mean crystallization, solid-state transformation and melting.

	Cooling (15ºC·min^{-1})		**Heating (15ºC·min^{-1})**				
	α (c)	*α→α*(s)*	*α*→ α (s)*	*α (m)*	*β' (c)*	*β'→β$_1$(s)*	*β$_1$ (m)*
T_{onset} (ºC)	-21.7±0.3	-50.8±1.6	-37.3±0.4	-21.5±0.3	-20.1±0.3	-9.5±0.3	13.6±0.6
	Cooling (2ºC·min^{-1})		**Heating (15ºC·min^{-1})**				
	α + β' (c)		*β'→β$_1$ + β$_2$ (s)*	*β$_2$ (m)*	*β$_1$ (m)*		
T_{onset} (ºC)	-7.6±0.5	-10.4±0.7	-0.4±0.3	6.9±1	15.8±0.7		
	Cooling (1ºC·min^{-1})		**Heating (15ºC·min^{-1})**				
	α + β' + β$_1$ (c)		*β'→β$_1$ and β$_1$ (m)*				
T_{onset} (ºC)	-1.6±0.6		7.2±0.7				
	Cooling (0.5ºC·min^{-1})		**Heating (15ºC·min^{-1})**				
	β' + β$_1$ (c)		*β' → β$_1$ and β$_1$ (m)*				
T_{onset} (ºC)	-0.4±0.5		6.9±0.4				

2.4.1. Cooling rate: 15ºC·min^{-1}

On cooling, the polymorphic form that crystallized was α form (less stable). Afterwards, a solid-solid transition took place at -50.8 ± 1.6ºC (Table 2.4) to obtain another α form (α*), characterized by an appreciable double peak in the SAXD pattern (5.4 and 5.2 nm) and a broad peak in the WAXD pattern (0.42 nm). Ueno et al.(1997) reported an α form for SOS (1,3-distearoyl-2-oleoyl glycerol), characterized by a double peak in the SAXD pattern and they explained the transformation from the double SAXD peak into a single peak (characteristic of α) as a relaxation process of the α form. In the present work, we have called this form, characterized by the double SAXD peak, α*.

During the heating process, the α* form transformed into α and melted. Then, β' form crystallized (identified by two peaks in the WAXD pattern, with d-spacings of 0.43 and 0.40 nm) and was transformed into the β_1 form (exothermic transition, see Figure 2.10). Finally, the β_1 form, which is the most stable one, melted. These results are in agreement with those of Minato et al. (1997b), who

studied the polymorphism of POP-OPO binary mixtures and observed the same behavior for pure OPO.

2.4.2. Cooling rate: 2ºC·min^{-1}

When OPO was cooled at 2ºC·min^{-1}, concurrent crystallization of α and β' forms was observed in the SAXD pattern. However, on heating, the intensity of α peaks decreased, while those of β' peaks increased, probably due to an α→β' transition. Nevertheless, in the WAXD pattern, only β' crystallization was clearly noticeable. However, the first β' peak (0.43 nm) was broader than when the cooling rate was 15ºC·min^{-1}, probably due to an overlapping of the β' first peak and a smooth α peak.

According to the DSC thermogram, on heating, a transition from β' form to β_1 and β_2 forms must have occurred simultaneously, as two melting endothermic peaks were present. Nevertheless, in both the SAXD and the WAXD patterns, only the β_1 polymorphic form could be observed.

Figure 2.12 illustrates a thermo-optical polarized microscopy experiment using the same DSC program.

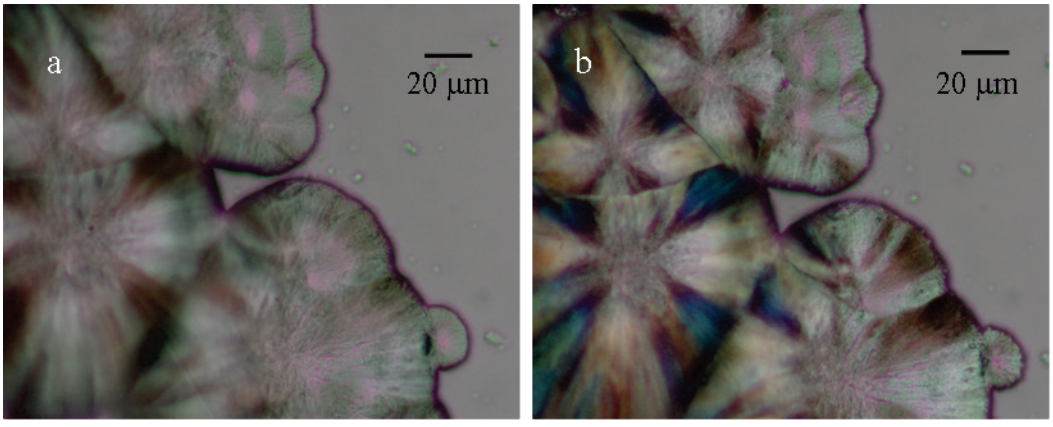

Figure 2.12. Thermo-optical polarized microscopy images obtained when OPO was cooled down at 2ºC·min^{-1} and heated at 15ºC·min^{-1}. The temperature range corresponds to the β'→β_1+β_2 phase transition. The colour changes became clearly noticeable. a) -14.3ºC. b) 4.5ºC.

In the temperature range of the solid-solid transition $\beta' \rightarrow \beta_1+\beta_2$, the sample, crystallized as spherulites, exhibited clear color changes, due to the solid-solid transition: before the transition it was possible to appreciate some brown and green colors (Figure 2.12a) and there were some changes to obtain some blue, yellow and brown tonalities (Figure 2.12b). However, it was not possible to distinguish between the newly formed β_1 and β_2 forms by using this technique.

2.4.3. Cooling rate: 1ºC·min^{-1}

On the one hand, the SAXD pattern exhibited concurrent crystallization of α and β' forms in the cooling process, although the α peak did not become important and disappeared immediately. On the other hand, the crystallization of β' form was also present in the WAXD pattern, but it was accompanied by some β_1 crystallization. Therefore, both SAXD and WAXD results indicated concurrent crystallization of α, β' and β_1 forms.

When the sample was heated, all β' form was transformed into β_1 form, but before this transition, some peaks of possible intermediate forms could be seen in the SAXD profile (7.1 and 6.1 nm). We must point out that only one endothermic peak with a shoulder was observed in the DSC heating thermogram, whereas the $\beta' \rightarrow \beta_1$ transition should have been exothermic. This may be because the β_1 melting process was so energetic that the convolution of both phenomena ($\beta' \rightarrow \beta_1$ transition and β_1 melting) became a single endothermic peak in the DSC.

2.4.4. Cooling rate: 0.5ºC·min^{-1}

According to the SAXD and WAXD patterns, α form did not crystallize when cooling, and there was only a concurrent crystallization of β' and β_1 forms. Afterwards, β' form transformed into β_1 on heating and β_1 form melted. The DSC thermogram obtained was similar to that of cooling at 1ºC·min^{-1}.

In order to check the crystallization behavior at an intermediate cooling rate

between 15 and 2ºC·min^{-1}, DSC experiments at a cooling rate of 8ºC·min^{-1} and a heating rate of 15ºC·min^{-1} were carried out (not shown). The thermal profiles were similar to the one obtained by the cooling at 2ºC·min^{-1}, whose details are explained in Figure 2.10b.

Overall, as the cooling rate decreased, the DSC profiles became simpler. This fact is represented in the triangular shape of Table 2.4. Also, T_{end} and enthalpy values were determined for each transition, and some comparisons can be established. When the cooling rate was 15ºC·min^{-1}, α form crystallized, giving an energetic peak; however, the α→α* transition was less energetic and much broader. Afterwards, the energy of the α melting was low when heating, and the correspondent peak became very narrow. The energies for the following β' crystallization and β'→β_1 transition were about the same magnitude as for the α form crystallization. Finally, the β_1 melting was more energetic than all the previous phenomena, and the peaks became broader than those of the α form crystallization. With cooling rates of 2, 1, and 0.5ºC·min^{-1}, concurrent crystallizations took place, so the processes were more complex and energies were higher (100 J·g^{-1}), due to the overlapping of some phenomena, although the corresponding peaks were not so broad. The same happened during the heating step with 1 and 0.5ºC·min^{-1}: as the endothermic peak was, in fact, a convolution of the β'→β_1 transition and the β_1 melting, and energies became high. When the cooling rate was 2ºC·min^{-1}, the energy value for the transition β'→β_1 + β_2 (heating step) was similar to that of the β'→β_1 transition with a cooling rate of 15ºC·min^{-1}. Comparison of the two experiments also indicated that the energy value of the convolution of β_1 and β_2 forms melting (it was not possible to separate the two peaks) was the same as for β_1 melting. Therefore, it can be concluded that β_2 crystallization and melting were not as energetic as those of β_1 form, and the amount of β_2 crystallized was not as high. The T_{onset} of β_1 melting when the cooling rates were 15º and 2ºC·min^{-1} were slightly different due to the fact that, at 2ºC·min^{-1}, the β_1 melting peak was close to the β_2 melting peak, so the β_2 melting process made some influence to change somehow the β_1 melting value. However, at 15ºC·min^{-1}, the β_1 melting peak was completely isolated.

All the crystallographic data obtained in order to characterize each polymorph are summarized in Table 2.5, where a comparison with the Minato et al.

(1997b) results can also be found.

Table 2.5. Crystallographic data of the OPO polymorphic forms.

	Present work				Minato et al. work		
	α	α*	β'	β_1	α	β'	β_1
Short Spacing/nm	0.42	0.42	0.43 0.40	0.48 0.38 0.37	––	––	––
Long Spacing/nm	5.3	5.4 5.2	4.4	6.7	4.8	4.4	6.4
Chain Length Structure	Double	Double	Double	Triple	Double	Double	Triple

We have defined the chain length structure of α and α∗ as double, although the long spacing values are higher (from 5.2 to 5.4) than those of Minato et al. As other studies have confirmed (Ueno et al., 1997), sometimes α form can reach these high values, which can be understood as a more straight double chain structure.

Similarly to the POP case, the Ostwald step rule should be discussed. According to this rule for polymorphic nucleation, the solid first formed on crystallization of a melt or a solution would be the least stable polymorph, which is first produced by spontaneous crystallization. As Ostwald stated: "When leaving a given state and in transforming to another state, the state which is sought out is not the thermodynamically stable one, but the nearest in stability to the original state" and this must be the next least stable (the one with the smallest energy barrier expressed in kinetic/thermodynamic terms) (Threlfall, 2003). However, some factors (e.g., cooling rate) affect crystallization (Bouzidi et al., 2010; Lam et al., 2010) and polymorphic nucleation. In this work, we have shown the influence of kinetics, so that as the cooling rate decreases, more stable forms crystallize, not following the Ostwald step rule. In most cases, concurrent crystallizations of different polymorphs occurred, but the tendency becomes clear. Therefore, this becomes an example where kinetics, thermodynamics and structural factors are competing. However, the Ostwald's Rule also states that the polymorph first formed is followed successively by forms of increasing stability. This fact has been observed on the heating profiles

of the experiments performed in the present work, as the phase transitions follow a sequence by continuously increasing the stability of the forms obtained. Figure 2.13 summarizes the influence of cooling rate variation on the OPO polymorphism.

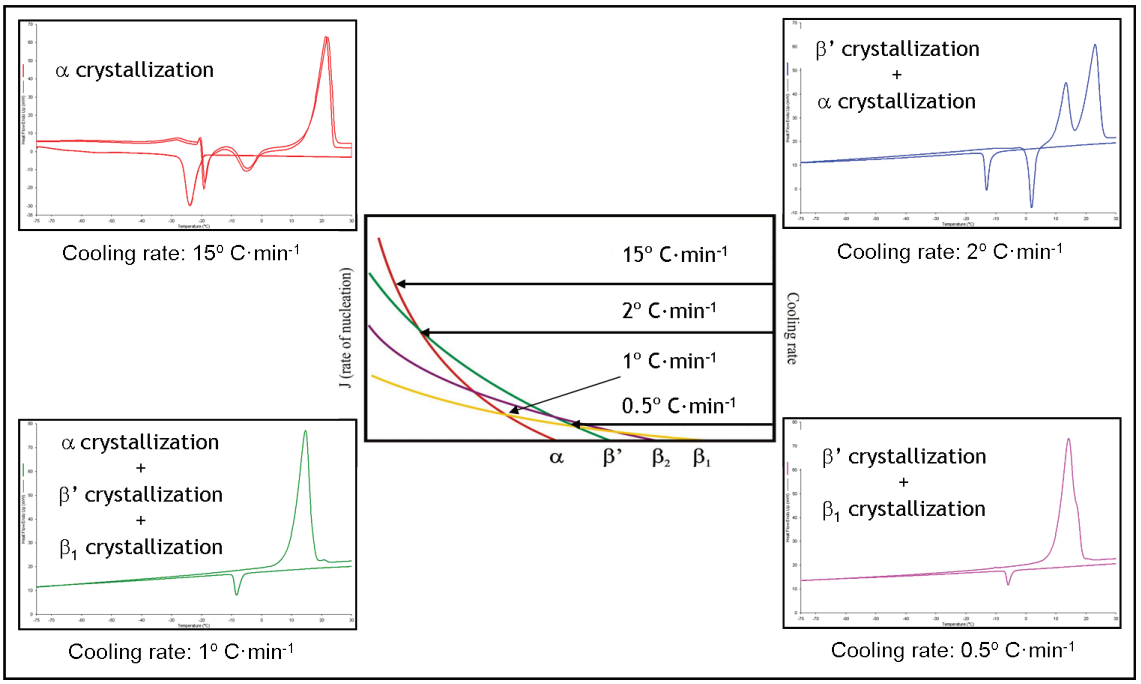

Figure 2.13. Diagram of the influence of changing the cooling rate on the OPO polymorphism.

The proposed diagram includes all the polymorphic sequences experimentally observed. As DSCs showed, a more simplified polymorphic behavior was obtained with a decreased cooling rate because the transformation sequence became shorter. If the polymorphic crystallization of POP and OPO are compared, one may easily notice that in the range of cooling rates used (from 15ºC·min^{-1} to 0.5ºC·min^{-1}), a higher number of polymorphic forms were directly obtained from the melt, having complex concurrent crystalization processes in most of cases. As to the heating steps, by heating OPO at a high rate (15ºC·min^{-1}), most stable polymorph (β_1) was always reached, independently from the starting polymorph. On the contrary, POP needed to be heated at low rates in order to obtain significative amounts of most stable forms.

Moreover, we studied the relation between the cooling and the crystallization rates of the β' form of OPO (Figure 2.14).

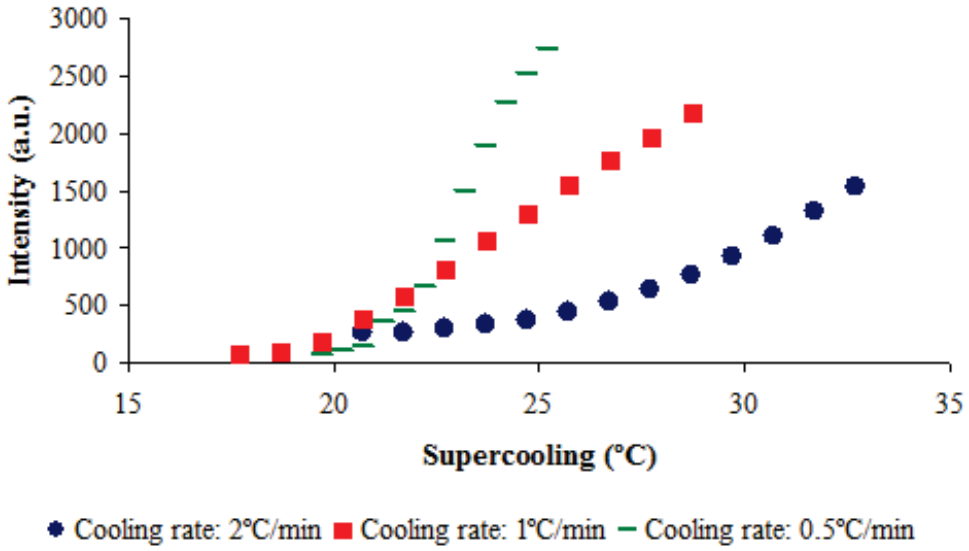

Figure 2.14. Graphs showing the relation cooling rate-crystallization rate for β'.

The variation of the SAXD peaks intensity of β' form (at 4.5 or 4.4 nm), present during the cooling process (at three rates of cooling), is represented in front of the supercooling ($\Delta T = T_m - T_c$), in which T_m is the melting temperature of β' form and T_c becomes the experimental temperature. It was evident that the SAXD peak intensity increased more rapidly as the cooling rate decreased above the ΔT values of 22°C. Although the degree of perfection of crystals or crystallinity may vary the corresponding XRD peaks in that less perfect crystal diffract less X-ray beams, the intensity of the XRD peaks basically depends on the concentration of crystals present in the growth medium that were subjected to XRD measurement. Therefore, the results (Figure 2.14) may be related to the amount of β' crystals formed during different rates of cooling. It appeared that the rate of crystallization decreased with increasing cooling rate, since the peak intensity of the SAXD pattern decreased with increasing ΔT. However, this was not the case. The amount of crystals is the summation of the crystallized materials in the supercooled liquid, resulting from both the rate of nucleation and the subsequent crystal growth. The rate of nucleation is defined as the increase in crystal numbers per unit of time and unit of volume of supercooled liquid, and the rate of crystal growth is defined as the increase in volume of crystals per unit time. As the rate of cooling decreases, the amount of time required for the growth medium to allow crystal nucleation and crystal growth

to occur increases; therefore, the integrated amount of crystals may increase with time. This phenomenon was clearly observed for the same polymorphic form of β' as depicted in Figure 2.14. For example, at a supercooling value of 24ºC, the intensity values of XRD peaks obtained at the cooling rates of 2ºC·min^{-1}, 1ºC·min^{-1} and 0.5ºC·min^{-1} are 335, 1065 and 1900, respectively. Then, the times allocated for crystallization during supercooled conditions are 12 minutes (2ºC·min^{-1}), 24 minutes (1ºC·min^{-1}) and 48 minutes (0.5ºC·min^{-1}). This result qualitatively shows the dependence of the cooling rate on the extent of crystallization due to the difference in crystallization time.

DSC and SR-XRD clarified the polymorphic behavior of OPO as a function of kinetics. As the cooling rate decreases, the polymorphic crystallization is directed to more stable forms, not following the Ostwald step rule. Nevertheless, concurrent crystallization often occurs in a complex phenomena. In more detail, when the cooling rate was 15ºC·min^{-1}, α form crystallized; at 2ºC·min^{-1}, α and β' were formed; at 1ºC·min^{-1} concurrent crystallization of α, β' and β_1 forms occurred; and when the controlled cooling rate was 0.5ºC·min^{-1}, β' and β_1 forms crystallized. Using SR-XRD coupled with DSC, rapid dynamic polymorphic transformations on the heating step could be identified. Also, intensities of the SAXD peaks have been related to supercooling for β' form, by comparing the slopes of the graphs obtained at each cooling rate. Results indicate that the nucleation rate of β' form tends to increase as the cooling rate decreases. The study of the polymorphic crystallization of OPO was published as a research paper (Bayés-García et al., 2011a).

2.5.

Saturated-Unsaturated-Unsaturated (SUU) triacylglycerols: 1-palmitoyl-2,3-dioleoyl glycerol (POO), 1-palmitoyl-2-oleoyl-3-linoleoyl glycerol (POL) and 1-stearoyl-2,3-dioleoyl glycerol (SOO)

POO, SOO and POL become the main Saturated-Unsaturated-Unsaturated (SUU) TAGs present in olive oil and Iberian ham fat, but they are also present in other edible fats and oils. Probably due to its asymmetric fatty acid composition, β forms are not present and β' form becomes the most stable polymorph. Miura et al. (2001) (see the Introduction part of the present chapter) studied the crystallization behavior of POO and some POO:POP mixtures, as they play an important role in the formation of granular crystals in margarine. In addition, Zhang et al. (2007), determined the eutectic binary phase behavior of POP:POO in metastable and stable conditions, due to its practical importance for dry fractionation of palm oil. In these previous studies, only two polymorphic forms (α and β') of POO were determined. Similarly, later on Zhang et al. (2009) reported on the immiscible phase behavior of the SOS:SOO binary mixtures, determining the presence of three SOO polymorphs (α, β'_2 and β'_1). In the present work, by studying the influence of varying the cooling and heating rates on the polymorphic behavior of POO and SOO, a higher number of polymorphs were characterized and liquid crystal (LC) phases were detected. Moreover, to the best of our knowledge, this is the first work where the POL polymorphism is being reported.

To dynamically follow the polymorphic crystallization and transformation kinetics of POO, SOO and POL polymorphs, the combination of SR-XRD and DSC was used. However, in some cases, due to the low rates applied to samples or the simplicity of the thermal profile, laboratory-scale XRD could also be applied.

Before the thermal treatments were selected, a screening of cooling and heating rate conditions was performed for POO, which could be extrapolated to the SOO and POL cases, due to their same Saturated-Unsaturated-Unsaturated (SUU) structure. Figure 2.15 depicts all the DSC thermograms obtained when several cooling and

heating rates were applied to POO. In each row a different cooling rate is shown and, in each column, a different rate of heating appears.

Thus, all the possible combinations by varying the rates of cooling/heating ($15ºC·min^{-1}$, $2ºC·min^{-1}$, $1ºC·min^{-1}$ and $0.5ºC·min^{-1}$) are represented. As already demonstrated for the other TAGs reported in this chapter, as the cooling rate decreases (moving down through a column, i.e. from Figure 2.15a to 2.15m), a more simplified DSC thermogram is obtained, as the polymorphic crystallization occurred from the melt is directed to more stable polymorphs. It should be considered that, in general, when high cooling/heating rates are applied to a sample, thermal peaks become stronger and sharper, whereas they are smother at low rates. Therefore, when moving through a line in Figure 2.15 (from higher to lower heating rates, i.e. from Figure 2.15a to 2.15d) it is more difficult to appreciate the polymorphic transformations that occur in the heating step. However, in general, as in other TAGs, a bigger amount of most stable polymorphs is obtained during heating when the rate is low.

From all these experimental conditions, only some of them were selected in order to characterize each thermal phenomenon by SR-XRD or laboratory-scale XRD (highlighted figures in red in Figure 2.15: Figure 2.15a, 2.15d, 2.15f and 2.15m). POL and SOO were subjected to the same thermal treatments. Therefore, samples were cooled from the melt (from 40ºC to -80ºC) and heated afterwards (from -80ºC to 40ºC) by using the following rates: (1) Cooling at $15ºC·min^{-1}$ and heating at $15ºC·min^{-1}$ and at $0.5ºC·min^{-1}$, (2) Cooling at $2ºC·min^{-1}$ and heating at $2ºC·min^{-1}$, and (3) Cooling at $0.5ºC·min^{-1}$ and heating at $15ºC·min^{-1}$. One may notice that the chosen conditions include high, intermediate and low rates of cooling/heating.

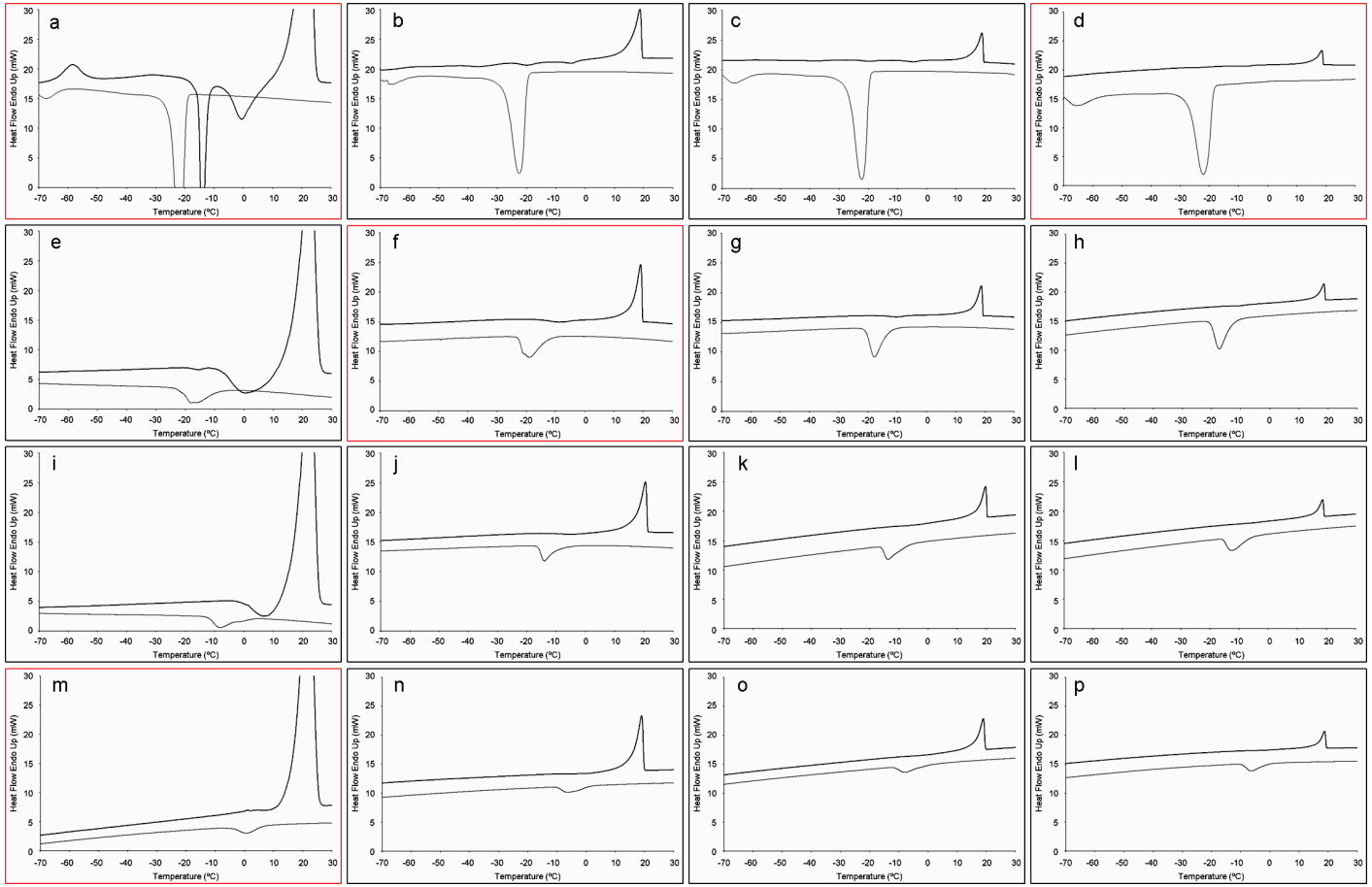

Figure 2.15. POO DSC thermograms under different cooling and heating rate conditions. a) Cooled at 15ºC·min^{-1} and heated at 15ºC·min^{-1}. b) Cooled at 15ºC·min^{-1} and heated at 2ºC·min^{-1}. c) Cooled at 15ºC·min^{-1} and heated at 1ºC·min^{-1}. d) Cooled at 15ºC·min^{-1} and heated at 0.5ºC·min^{-1}. e) Cooled at 2ºC·min^{-1} and heated at 15ºC·min^{-1}. f) Cooled at 2ºC·min^{-1} and heated at 2ºC·min^{-1}. g) Cooled at 2ºC·min^{-1} and heated at 1ºC·min^{-1}. h) Cooled at 2ºC·min^{-1} and heated at 0.5ºC·min^{-1}. i) Cooled at 1ºC·min^{-1} and heated at 15ºC·min^{-1}. j) Cooled at 1ºC·min^{-1} and heated at 2ºC·min^{-1}. k) Cooled at 1ºC·min^{-1} and heated at 1ºC·min^{-1}. l) Cooled at 1ºC·min^{-1} and heated at 0.5ºC·min^{-1}. m) Cooled at 0.5ºC·min^{-1} and heated at 15ºC·min^{-1}. n) Cooled at 0.5ºC·min^{-1} and heated at 2ºC·min^{-1}. o) Cooled at 0.5ºC·min^{-1} and heated at 1ºC·min^{-1}. p) Cooled at 0.5ºC·min^{-1} and heated at 0.5ºC·min^{-1}.

Table 2.6 summarizes the long and short spacing values of the POO, POL and SOO polymorphs studied in this work. The values shown are in good agreement with those of previous studies (Miura et al., 2001; Zhang et al., 2007; Zhang et al., 2009).

Table 2.6. Long and short spacing values of the POO, POL and SOO polymorphs.

POO		
	Long Spacing/nm	Short Spacing/nm
sub-α	5.8	0.42 0.38
α	5.7	0.41
LC	6.0	—
β'_2	6.7	0.43 0.41
β'_1	6.7	0.47 0.46 0.45 0.43 0.41 0.40 0.39
POL		
	Long Spacing/nm	Short Spacing/nm
sub-α	5.7	0.42 0.38
α	5.6	0.41
β'_2	6.3	0.42 0.38
β'_1	6.4	0.47 0.46 0.45 0.44 0.42 0.41 0.40 0.39
SOO		
	Long Spacing/nm	Short Spacing/nm
sub-α	6.2	0.42 0.38
α	6.0	0.41
LC	6.7	—
β'_2	7.1	0.43 0.41
β'_1	6.9	0.47 0.45 0.43 0.42 0.41 0.40 0.39

Chain-length structures of sub-α and α forms are double, and triple for the two β' forms. Long spacing values become much higher than those of POP and OPO, especially for double chain-length structures, as the inclination angles toward the lamellar interface should be relatively short. LC forms (of smectic type) were formed in POO and SOO and they were characterized by a single long spacing value (see below).

2.5.1. 1- palmitoyl-2,3-dioleoyl glycerol (POO)

DSC data (T_{onset} and ΔH) of all the thermal treatments applied to POO are shown in Table 2.7. At high (15ºC·min^{-1}) and intermediate (2ºC·min^{-1}) cooling rates, the

crystallizing polymorph was α, whereas low rates (0.5ºC·min^{-1}) leaded the crystallization to more stable forms (β'$_2$). On heating, most stable form (β'$_1$) was obtained in all cases, but through different pathways depending on the rate used.

Table 2.7. DSC data of crystallization and transformation of POO polymorphs obtained by cooling rates of (A) 15ºC·min^{-1}, (B) 2ºC·min^{-1}, and (C) 0.5ºC·min^{-1} and different heating rates. The letters, *c* and *m*, in parentheses noting polymorphic forms mean crystallization and melting.

A	**Cooling**		**Heating**				
	(15ºC·min^{-1})		**(15ºC·min^{-1})**				
	α (c)	*α → sub-α*	*sub-α → α*	*α (m)*	*β'$_2$ (c)*	*β'$_2$ → β'$_1$*	*β'$_1$ (m)*
T_{onset} (ºC)	-20.4 ± 0.4	-62.9 ± 0.5	-65.8 ± 0.5	-44.0 ± 2.1	-16.3 ± 0.4	-6.6 ± 0.6	12.5 ± 0.5
ΔH (J/g)	-44 ± 1	-5 ± 1	9 ± <1	4 ± 1	-29 ± 1	-17 ± 2	111 ± 3
			(0.5ºC·min^{-1})				
			sub-a⇒β'$_1$	*β'$_1$ (m)*			
T_{onset} (ºC)			3.5 ± 2.3 (T_{end})	12.4 ± 0.3			
ΔH (J/g)			___	106 ± 21			
B	**Cooling**		**Heating**				
	(2ºC·min^{-1})		**(2ºC·min^{-1})**				
	α (c)	*α → sub-α*	*sub-α⇒ β'$_1$*	*β'$_1$ (m)*			
T_{onset} (ºC)	-11.3 ± 1.6	___	-0.8 ± 3.7 (T_{end})	13.5 ± 0.9			
ΔH (J/g)	-78 ± 2	___	___	109 ± 8			
C	**Cooling**		**Heating**				
	(0.5ºC·min^{-1})		**(15ºC·min^{-1})**				
	β'$_2$+β'$_1$ (c)		*β'$_2$ (m) / β'$_2$ → β'$_1$*		*β'$_1$ (m)*		
T_{onset} (ºC)	7.3 ± 1.3		-4.5 ± 4	-1.7±2.2	14.4 ± 1.5		
ΔH (J/g)	-103 ± 4		1 ± <1		108 ± 5		

Figure 2.16 depicts the polymorphic behavior of POO when it was cooled at 15ºC·min^{-1} and heated at 15ºC·min^{-1} (Figure 2.16a) and 0.5ºC·min^{-1} (Figure 2.16b).

At cooling rates as high as 15ºC·min^{-1}, the crystallizing polymorph was α, having a long spacing value of 5.7 nm and a short spacing value of 0.41 nm. On further cooling, the SR-XRD peaks shifted from 5.7 to 5.8 nm (SAXD pattern) and from 0.41 to 0.42 nm (WAXD pattern), due to the α→sub-α transformation. The sub-α form is characterized by two WAXD peaks: a stronger one (i.e. at 0.42 nm for POO) accompanied by a weaker one (at 0.38 nm for POO), which couldn't be appreciated at this high cooling rate, but it could be determined at other experimental conditions (see WAXD pattern in Figure 2.16b). When POO was afterwards heated at 15ºC·min^{-1} (Figure 2.16a), a sub-α→α transformation occurred around -65.8ºC (see Table 2.7A) as, according to the SR-XRD, the SAXD peak at 5.8 moved to 5.7 nm and the WAXD peak at 0.42 nm shifted to 0.41 nm. α form melted at approximately -44.0ºC and β'$_2$ form

crystallized around -16.3ºC, appreciable by the presence of the SAXD peak at 6.7 nm and two broad WAXD peaks at 0.43 and 0.41 nm. Later on, the DSC profile showed an exothermic peak at -6.6ºC corresponding to a $\beta'_2 \rightarrow \beta'_1$ transition. Simultaneously, new WAXD peaks appeared at 0.47, 0.45, 0.43, 0.41 and 0.40 nm, although the SAXD peak at 6.7 nm did not experiment any change. Finally, according to the DSC data, the most stable form (β'_1) melted around 12.5ºC. The considerable width and, in addition, the high enthalpy value of the β'_1 melting peak (111 $J \cdot g^{-1}$) should be considered. Probably some concurrent melting of both β'_2 and β'_1 forms should have occurred.

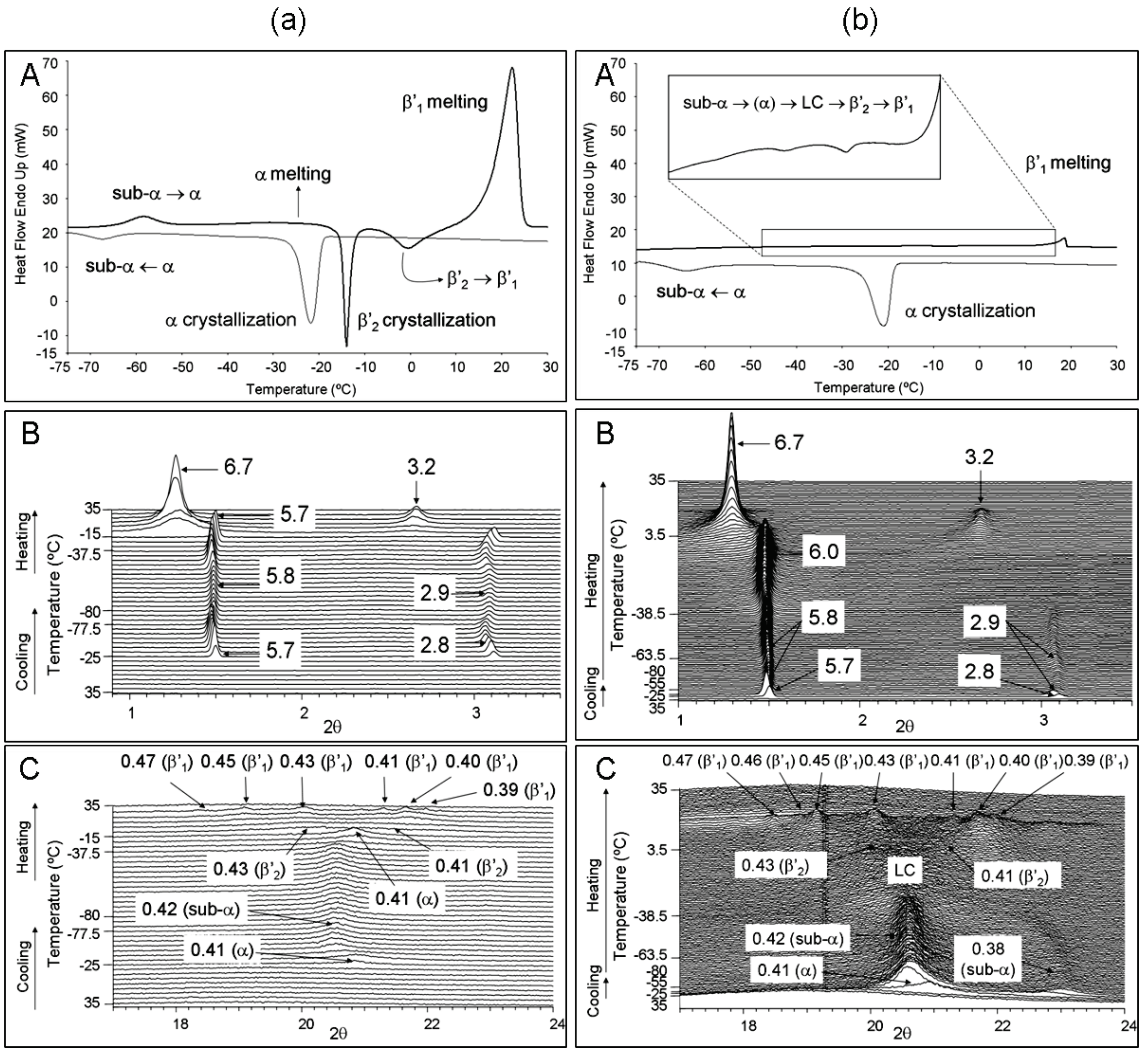

Figure 2.16. Polymorphic behavior of POO. a) Cooling at 15ºC·min^{-1} and heating at 15ºC·min^{-1}. A. DSC thermogram. B. SR-SAXD pattern. C. SR-WAXD pattern. b) Cooling at 15ºC·min^{-1} and heating at 0.5ºC·min^{-1}. A. DSC thermogram. B. SR-SAXD pattern. C. SR-WAXD pattern.

On the contrary, if the POO sub-α form was heated at a low rate (0.5ºC·min^{-1}, Figure 2.16b), a series of complex thermal phenomena could be observed in the DSC profile through a temperature range from around -50 to 3.5ºC (see enlarged figure in Figure 2.16b). The endothermic/exothermic nature of the DSC peaks couldn't be properly identified and, for this reason, only the T_{end} of this set of phenomena was determined (Table 2.7A, where the process is noted as sub-α⇒β'$_1$). Through all this large temperature range, the SR-XRD data revealed that the SAXD peak at 5.8 nm shifted to 6.0 nm and its corresponding (002) reflection did not appear. As to the WAXD pattern, the typical peak of the sub-α form at 0.42 nm vanished and no diffraction peak was present. We defined this phase, having a single long spacing value, a liquid crystal phase, tentatively called LC. This phase is, therefore, characterized by a structural periodicity of 6.0 nm of the lamellar distance, but with no definite periodicity in the lateral packing. Other works, which have reported the occurrence of liquid crystal phases in other TAGs, such as 1,3-distearoyl-2-oleoyl glycerol (SOS) (Ueno et al., 1997), defined them as of a smectic type. Many transitions were observed in the DSC long temperature range and, probably, the sequence passed through some α form before the formation of LC. Later on, LC transformed to β'$_2$ form (presence of a SAXD peak at 6.7 nm and two WAXD peaks at 0.43 and 0.41 nm) and, then, a β'$_2$→β'$_1$ transition occurred. Thus, the typical SR-XRD peaks of β'$_1$ form at 0.47, 0.46, 0.45, 0.43, 0.41, 0.40 and 0.39 nm were observed in the WAXD pattern. Finally, β'$_1$ form melted at 12.4ºC.

Intermediate rates of cooling and heating were also used (2ºC·min^{-1}). The polymorphic behavior observed was the same than that obtained by cooling at 15ºC·min^{-1} and heating at 0.5ºC·min^{-1}(Figure 2.17 and Table 2.7B).

Hence, on cooling at 2ºC·min^{-1}, the DSC thermogram showed an exothermic peak with a T_{onset} at -11.3ºC corresponding to the α form crystallization (identifiable by a SAXD peak at 5.7 nm and a WAXD peak at 0.41 nm). Further on, the SR-XRD data revealed a shifting from 5.7 to 5.8 nm in the SAXD pattern and from 0.41 to 0.42 nm in the WAXD pattern, due to the α→sub-α transformation, although the corresponding DSC thermal peak was not observed. After POO was cooled at 2ºC·min^{-1}, it was heated at the same rate. Again, a complicated transformation process appeared in the DSC heating curve through a wide temperature range (from -20 to -0.8ºC, in this case). The SAXD pattern showed again a single peak at 6.0 nm and no WAXD peak was detected,

corresponding to the LC phase described above. Right afterwards, the occurrence of β'_2 form could be identified by the presence of a SAXD peak at 6.7 nm and two peaks at 0.43 and 0.41 nm in the WAXD pattern. Finally, β'_2 form transformed to β'_1 form and the WAXD peaks shifted to 0.47, 0.45, 0.43, 0.41, 0.40, 0.39 nm. β'_1 form melted around 13.5ºC (see Table 2.7B), having a ΔH value of 109 $J \cdot g^{-1}$.

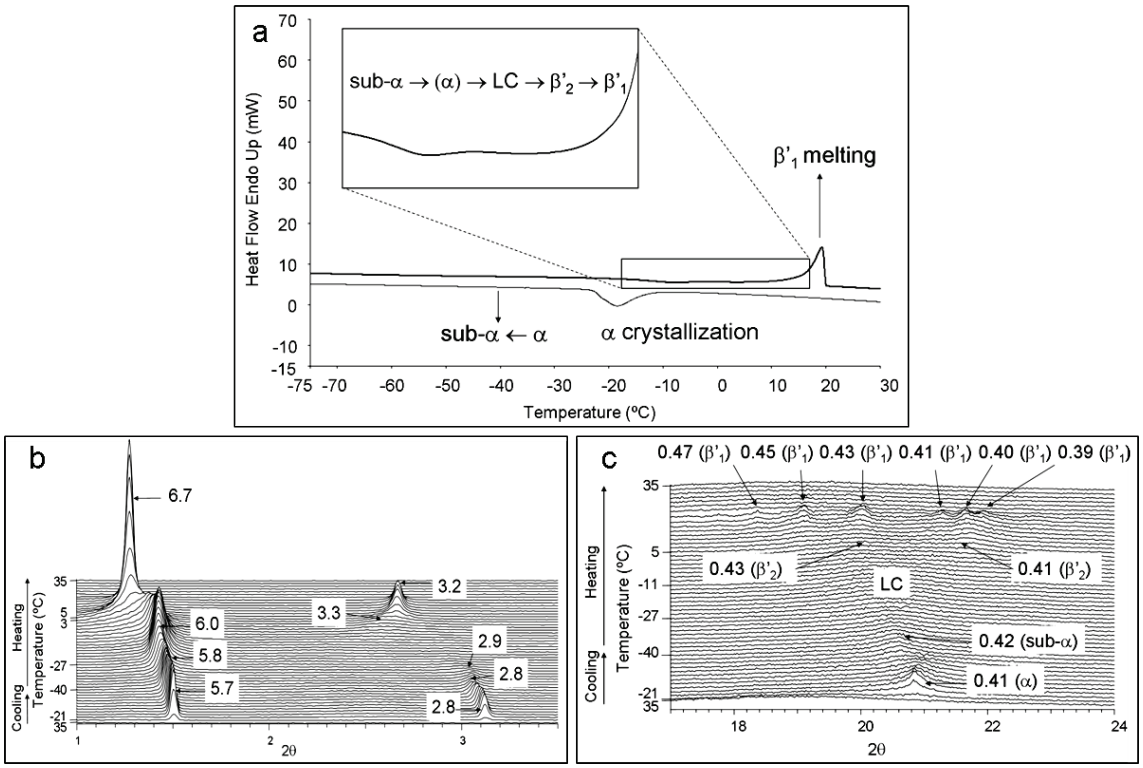

Figure 2.17. Polymorphic behavior of POO when cooled at 2ºC·min^{-1} (α crystallization) and heated at 2ºC·min^{-1}. a) DSC thermogram. b) SR-SAXD pattern. c) SR-WAXD pattern.

The polymorphic crystallization of POO was also studied under low rates of cooling. Thus, the melted sample was cooled at 0.5ºC·min^{-1} and heated at 15ºC·min^{-1} (Figure 2.18).

Conventional XRD could be carried out under these conditions, due to the simplicity observed in the DSC thermal profile. A concurrent crystallization of β'_2 and β'_1 forms took place at 7.3ºC (see Table 2.7C). The XRD pattern showed a peak at 6.7 nm in the Small-Angle region and three peaks in the Wide-Angle XRD region at 0.45 nm (corresponding to β'_1 form), and 0.43 and 0.41 nm (β'_2 form). On heating, the DSC curve showed a weak and broad melting peak with two T_{onset} at -4.5 and -1.7ºC. At the same temperature range, the XRD patterns revealed more defined β'_1 peaks (0.47, 0.45,

0.43, 0.41, 0.39 nm), so probably the broad DSC peak at -4.5ºC was due to some β'_2 melting, or some $\beta'_2 \rightarrow \beta'_1$ transition, or a combination of both. Finally, only β'_1 form was present and it melted at 14.4ºC.

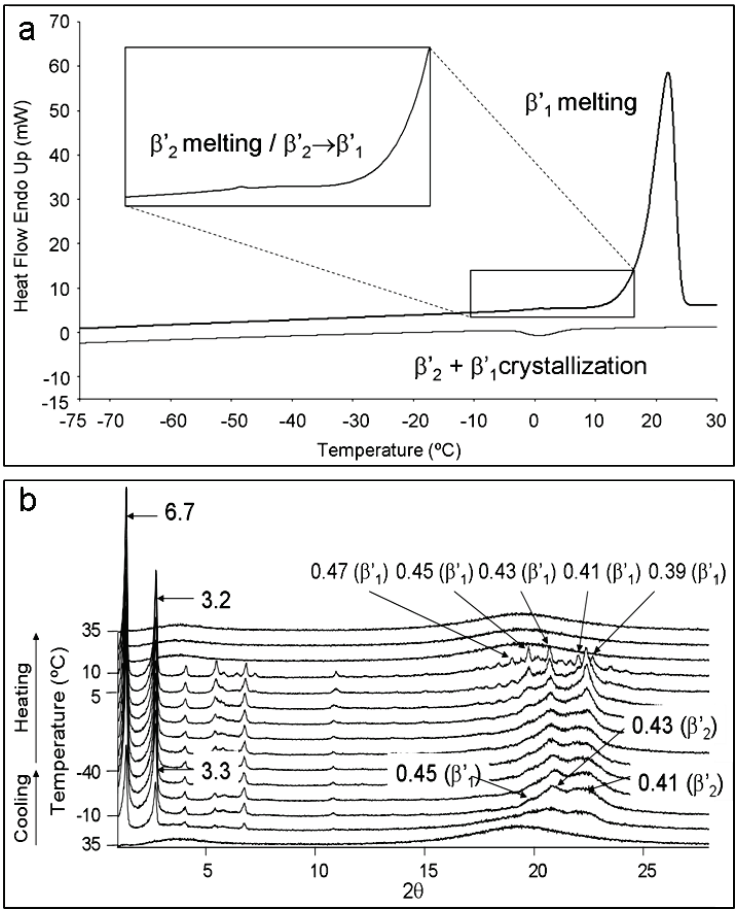

Figure 2.18. Polymorphic behavior of POO when cooled at 0.5ºC·min^{-1} (β'_2 + β'_1 crystallization) and heated at 15ºC·min^{-1}. a) DSC thermogram. b) Conventional XRD patterns.

2.5.2. 1- palmitoyl-2-oleoyl-3-linoleoyl glycerol (POL)

POL was subjected to the same thermal treatments and the polymorphic behavior was similar to that of POO. Table 2.8 shows T_{onset} and ΔH values of the phenomena observed in the corresponding DSC thermograms.

Not surprisingly, α form was crystallized from the melt at high and intermediate rates (15 and 2ºC·min^{-1}), whereas more stable β'_2 form was obtained at low cooling rates (0.5ºC·min^{-1}). The heating processes followed a polymorphic sequence of increasing stability, but no LC phase was detected, even when low heating rates were applied to POL.

Table 2.8. DSC data of crystallization and transformation of POL polymorphs obtained by cooling rates of (A) 15ºC·min^{-1}, (B) 2ºC·min^{-1}, and (C) 0.5ºC·min^{-1} and different heating rates. The letters, *c* and *m*, in parentheses noting polymorphiv forms mean crystallization and melting.

A	**Cooling (15ºC·min^{-1})**		**Heating (15ºC·min^{-1})**				
	α (c)	*α → sub-α*	*sub-α → α*	*α (m)*	*β'$_2$ (c)*	*β'$_2$ → β'$_1$*	*β'$_1$ (m)*
T_{onset} (ºC)	-20.6 ± 0.3	-41.3 ± 0.6 (peak top)	-31.8± 1.6 (peak top)	-16.1 ± 1.7	-12.6 ± 2.3	-5.6 ± 2	8.8 ± 2.2
ΔH (J/g)	-45 ± 2	-1 ± 1	2 ± 1	22 ± 4	-85 ± 18		97 ± 8
			(0.5ºC·min^{-1})				
			sub-α → α	*α → β'$_2$*	*β'$_2$ → β'$_1$*	*β'$_2$ (m)*	*β'$_1$ (m)*
T_{onset} (ºC)			-35.2 ± 2.5 (peak top)	-33.7 ± 1.2	-10.4 ±1.3	8.2 ± 0.5	9.6 ± 0.3
ΔH (J/g)			12 ± 2	-18 ± 2	-6 ± 2	14 ± 3	93 ± 4
B	**Cooling (2ºC·min^{-1})**		**Heating (2ºC·min^{-1})**				
	α (c)	*α → sub-α*	*α → β'$_2$*	*β'$_2$ → β'$_1$*	*β'$_2$ (m)*	*β'$_1$ (m)*	
T_{onset} (ºC)	-17.5 ± 0.6	-36.3 ± 0.6 (peak top)	-23.0 ± 0.7	-6.0 ± 1.1	7.5 ± 0.8	10.1 ± 0.8	
ΔH (J/g)	-45 ± 2	-1 ± 1	-24 ± 2	-12 ± 9	107 ± 9		
C	**Cooling (0.5ºC·min^{-1})**		**Heating (15ºC·min^{-1})**				
	β'$_2$ (c)		*β'$_2$ (m)*	*β'$_1$ (c)*	*β'$_1$ (m)*		
T_{onset} (ºC)	-12.8 ± 0.9		-1.5 ± 1.2	1.6 ± 1.6	8.0 ± 1.2		
ΔH (J/g)	-79 ± 10		3 ± 2	-17 ± 2	99 ± 5		

The polymorphic behavior of POL observed when it was cooled at 15ºC·min^{-1} and heated at 15 and 0.5ºC·min^{-1} is shown in Figure 2.19a and 2.19b, respectively.

SR-XRD data revealed the α form crystallization, which occurred at around -20.6ºC, through a SAXD peak at 5.6 nm and a WAXD peak at 0.41 nm. A shifting to 5.7 nm and 0.42 nm, respectively, showed the α→sub-α transformation, having a peak top in DSC profile at -41.3ºC. T_{onset} could not be determined in this case due to the flat appearance of the DSC peak. The opposite transformation (sub-α→α) occurred on heating at -31.8ºC (peak top) and, simultaneously, the SAXD peak at 5.7 nm moved to 5.6 nm again and, the WAXD peak, from 0.42 to 0.41 nm. A sharp endothermic DSC peak appeared at -16.1ºC, corresponding to the α melting and, further on, a crystallization process took place. Two exothermic peaks (with T_{onset} at -12.6ºC and -5.6ºC, respectively) appeared, but only the second one could be identified. SR-XRD showed the occurrence of β'$_1$ form through the peaks at 6.4 nm (SAXD) and 0.47 nm,

0.46 nm, 0.42 nm, 0.41 nm and 0.40 nm (WAXD). Most probably and similarly to the case of POO, the exothermic DSC peak with T_{onset} at -12.6ºC was due to the β'_2 crystallization, which, straightaway, transformed to β'_1 form at -5.6ºC. However, we could not distinguish the two processes by SR-XRD, as they were so close to each other and the heating rate used was so high. At the end, β'_1 form melted around 8.8ºC.

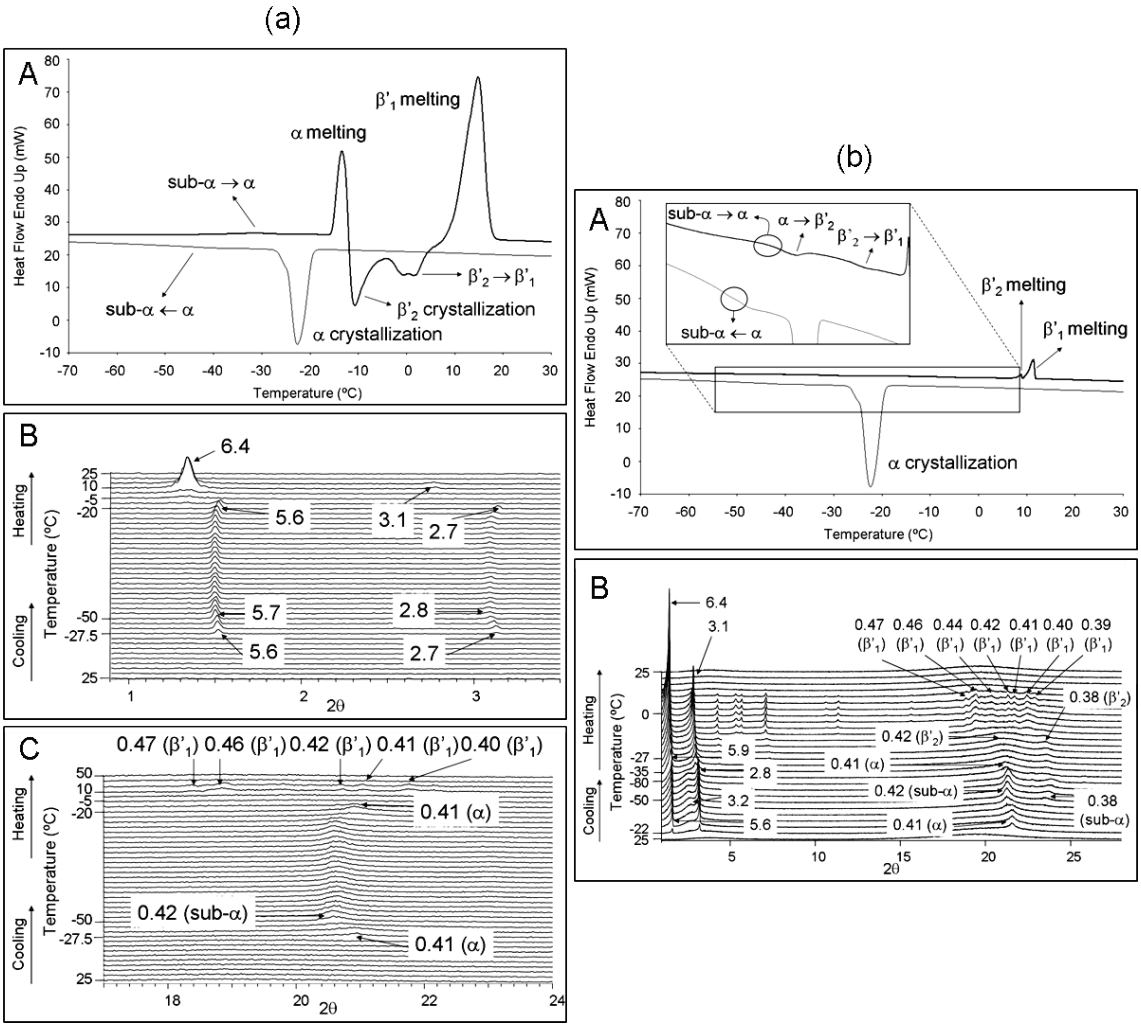

Figure 2.19. Polymorphic behavior of POL. a) Cooling at 15ºC·min^{-1} and heating at 15ºC·min^{-1}. A. DSC thermogram. B. SR-SAXD pattern. C. SR-WAXD pattern. b) Cooling at 15ºC·min^{-1} and heating at 0.5ºC·min^{-1}. A. DSC thermogram. B. Conventional XRD patterns.

Figure 2.19b depicts the DSC and laboratory-scale XRD results obtained when POL was cooled at 15ºC·min^{-1} and heated at 0.5ºC·min^{-1}. By heating at such a low rate, the sub-α form obtained during cooling transformed to α form at -35.2ºC (peak top temperature, see Table 2.8a), which soon after passed to β'_2 form through a solid-state

transformation at -33.7ºC. β'_2 form was identified by its Wide-Angle region peaks at 0.42 and 0.38 nm, as the laboratory-scale XRD data showed. Again, the most stable polymorph of POL (β'_1) was reached on further heating, when, at -10.4ºC, an exothermic peak, corresponding to the $\beta'_2 \rightarrow \beta'_1$ transition, appeared in the DSC profile. The XRD peaks at 6.4 nm (Small-Angle) and 0.47 nm, 0.46nm, 0.44 nm, 0.42 nm, 0.41 nm, 0.40 nm and 0.39 nm (Wide-Angle region) revealed the presence of β'_1 form. At the end, two consecutive melting peaks were observed in the DSC heating curve, corresponding to both meltings of some remaining β'_2 (T_{onset}=8.2ºC) and β'_1 (T_{onset}=9.6ºC) forms. Hence, not all the existing β'_2 form was transformed to β'_1 at -10.4ºC.

By applying intermediate rates of cooling/heating (2ºC·min^{-1}) to the sample, the polymorphic behavior of POL did not experiment significant variations.

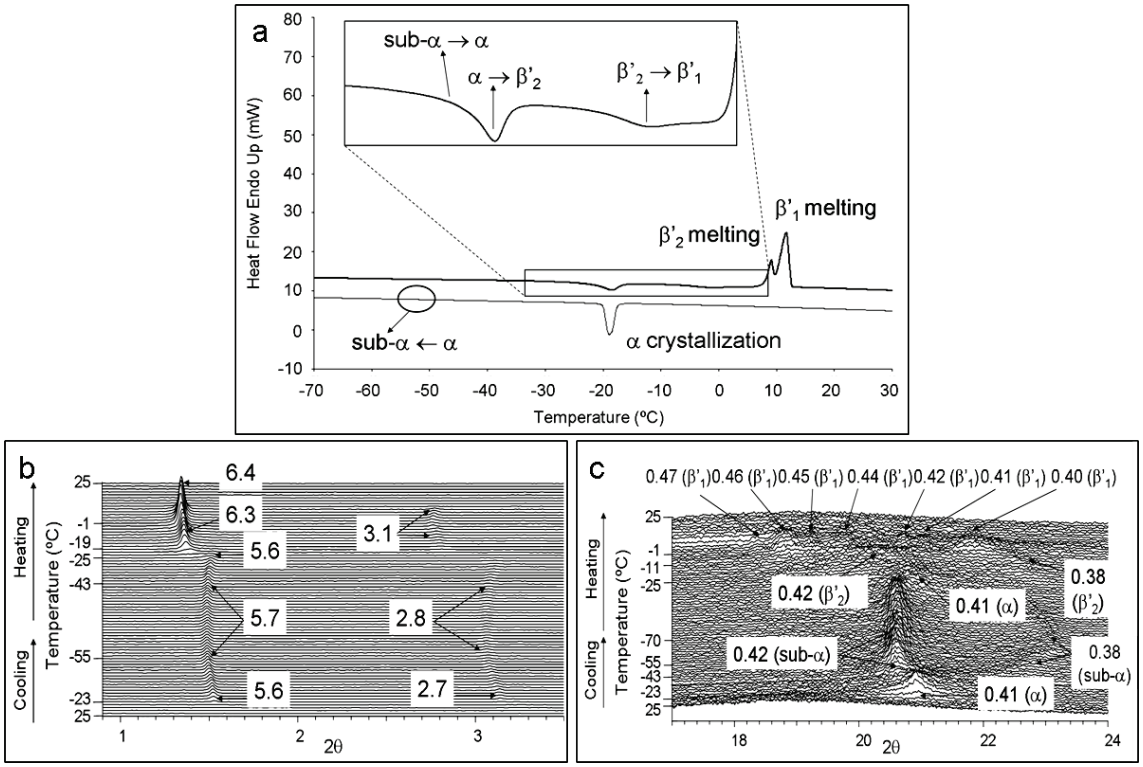

Figure 2.20. Polymorphic behavior of POL when cooled at 2ºC·min^{-1} (α crystallization) and heated at 2ºC·min^{-1}. a) DSC thermogram. b) SR-SAXD pattern. c) SR-WAXD pattern.

As shown in Figure 2.20, α crystals were also obtained by cooling the melted sample at 2ºC·min^{-1}, which transformed to sub-α form at -36.3ºC, as shown in Table 2.8b. This transition was identified in the SR-XRD pattern by the shifting from 5.6 to

5.7 nm (SAXD) and from 0.41 to 0.42 and 0.38 nm. On heating, although the corresponding DSC peak was not observed, sub-α transformed to α form (the SAXD peak at 5.6 nm and the WAXD peak at 0.41 appeared again at the expense of the α peaks). Soon after, at -23.0ºC, a SAXD peak at 6.3 nm and two WAXD peaks at 0.42 nm and 0.38 nm appeared, showing a solid-state transformation from α to β'_2 form. Part of this β'_2 transformed to β'_1 form at -6.0ºC, which was allocated by the SAXD peak at 6.4 nm and typical WAXD peaks at 0.47 nm, 0.46 nm, 0.45 nm, 0.44 nm, 0.42 nm, 0.41 nm and 0.40 nm. Finally, both β'_2 and β'_1 forms melted at 7.5ºC and 10.1ºC, respectively. Unlike the results obtained by applying low heating rates (0.5ºC·min^{-1}) to POL, both endothermic melting peaks were not completely separated at 2ºC·min^{-1}, and the enthalpy of melting (107 J·g^{-1}) had to be determined as a whole (as the sum of both melting processes).

More stable β'_2 crystallization occurred when melted POL was cooled at 0.5ºC·min^{-1}. Figure 2.21 presents the DSC and SR-XRD data for cooling at 0.5ºC·min^{-1} and heating at 15ºC·min^{-1}.

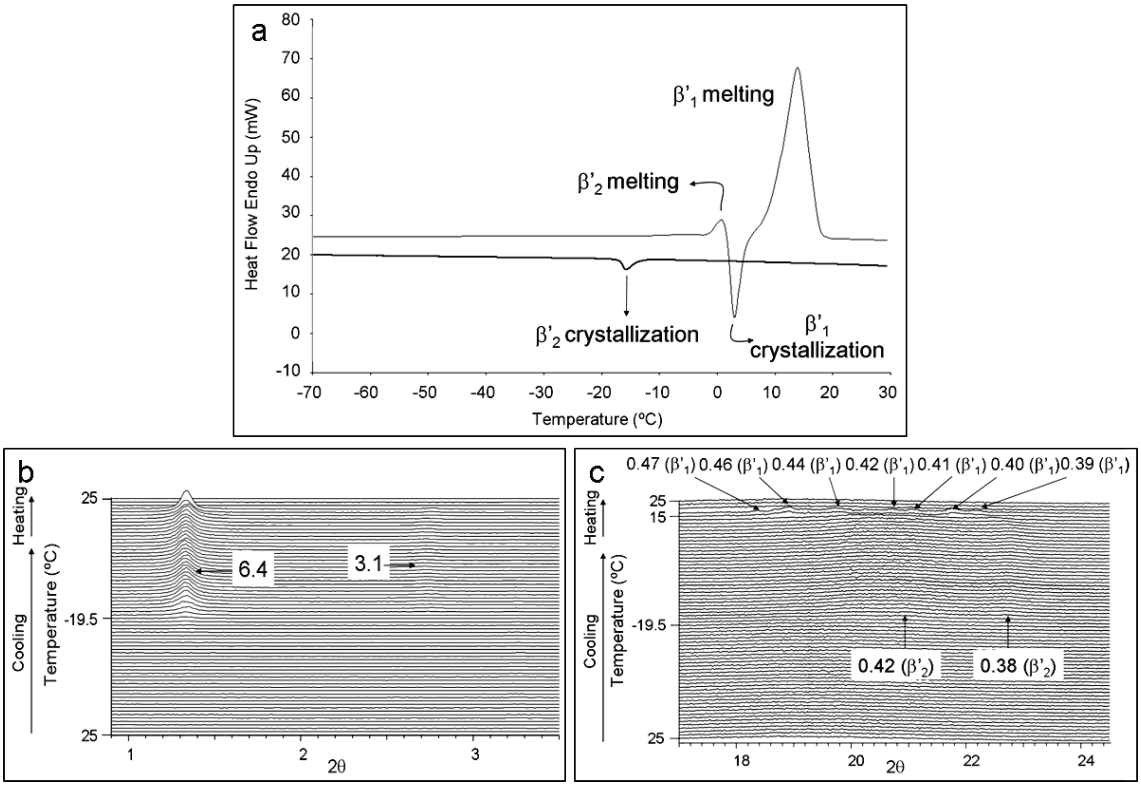

Figure 2.21. Polymorphic behavior of POL when cooled at 0.5ºC·min^{-1} (β'_2 crystallization) and heated at 15ºC·min^{-1}. a) DSC thermogram. b) SR-SAXD pattern. c) SR-WAXD pattern.

β'$_2$ form was identified by a triple chain length SAXD peak at 6.4 and two broad WAXD peaks at 0.42 nm and 0.38 nm. When the sample was quickly heated at 15ºC·min^{-1}, a melt-mediated transition from β'$_2$ to β'$_1$ form happened, consisting of the β'$_2$ melting with a T_{onset} at -1.5ºC and the β'$_1$ crystallization at 1.6ºC (see Table 2.8c). During this transformation, the SAXD peak didn't experiment any change, whereas WAXD peaks appeared at 0.47 nm, 0.46 nm, 0.44 nm, 0.42 nm, 0.41 nm, 0.40 nm and 0.39 nm, at the expense of β'$_2$ peaks. Most stable β'$_1$ form melted at 8ºC. Probably, the considerable width of the endothermic peak may be due to some concurrent β'$_2$ and β'$_1$ melting.

2.5.3. 1- stearoyl-2,3-dioleoyl glycerol (SOO)

The influence of varying the rates of cooling and heating was also analyzed for SOO. The DSC data of all the thermal peaks observed are shown in Table 2.9.

Table 2.9. DSC data of crystallization and transformation of SOO polymorphs obtained by cooling rates of (A) 15ºC·min^{-1}, (B) 2ºC·min^{-1}, and (C) 0.5ºC·min^{-1} and different heating rates. The letters, *c* and *m*, in parentheses noting polymorphic forms mean crystallization and melting.

A	**Cooling (15ºC·min^{-1})**		**Heating (15ºC·min^{-1})**				
	α (c)	*α → sub-α*	*sub-α → α*	*α (m)*	*β'$_2$ (c)*	*β'$_2$ →β'$_1$*	*β'$_1$ (m)*
T_{onset} (ºC)	-9.0 ± 0.4	-25.0 ± 0.3	-22.4 ± 0.8	-6.2 ± 0.9	-3.3 ± 0.6	2.7 ± 0.8	19.8 ± 0.5
ΔH (J/g)	-48 ± 1	-1 ± <1	1 ± 1	7 ± 2	-74 ± 16		109 ± 9
			(0.5ºC·min^{-1})				
			sub-α → α	*α → β'$_2$*	*β'$_2$ → β'$_1$*	*β'$_1$ (m)*	
			-62.2 ± 1.4	-26.6 ± 0.7	-4.5 ± 0.6	22.0 ± 0.6	
			9 ± 8	-18 ± 4	-3 ± 1	136 ± 18	
B	**Cooling (2ºC·min^{-1})**		**Heating (2ºC·min^{-1})**				
	α + β'$_2$(c)	*α → sub-α*	*LC → β'$_2$*	*β'$_2$ → β'$_1$*	*β'$_1$ (m)*		
T_{onset} (ºC)	-5.4 ± 0.3	-21.8 ± 0.6	-18.9 ± 0.9	-2.4 ± 0.4	20.9 ± 0.4		
ΔH (J/g)	-49 ± 3	-1 ± <1	-21 ± 1	-15 ± 2	122 ± 4		
C	**Cooling (0.5ºC·min^{-1})**		**Heating (15ºC·min^{-1})**				
	β'$_2$ (c)		*β'$_2$ → β'$_1$*	*β'$_1$ (m)*			
T_{onset} (ºC)	5.5 ± 1.8		6.5 ± 1.6	21.1 ± 1.0			
ΔH (J/g)	-96 ± 4		-15 ± 6	111 ± 10			

Following the same tendency than POO and POL, metastable α form crystallized at high cooling rates, while a concurrent crystallization of α and β'$_2$ forms took place at intermediate rates, and β'$_2$ crystals were obtained at low rates. Forms of increasing stability were reached while heating and a LC phase was identified in some experimental conditions.

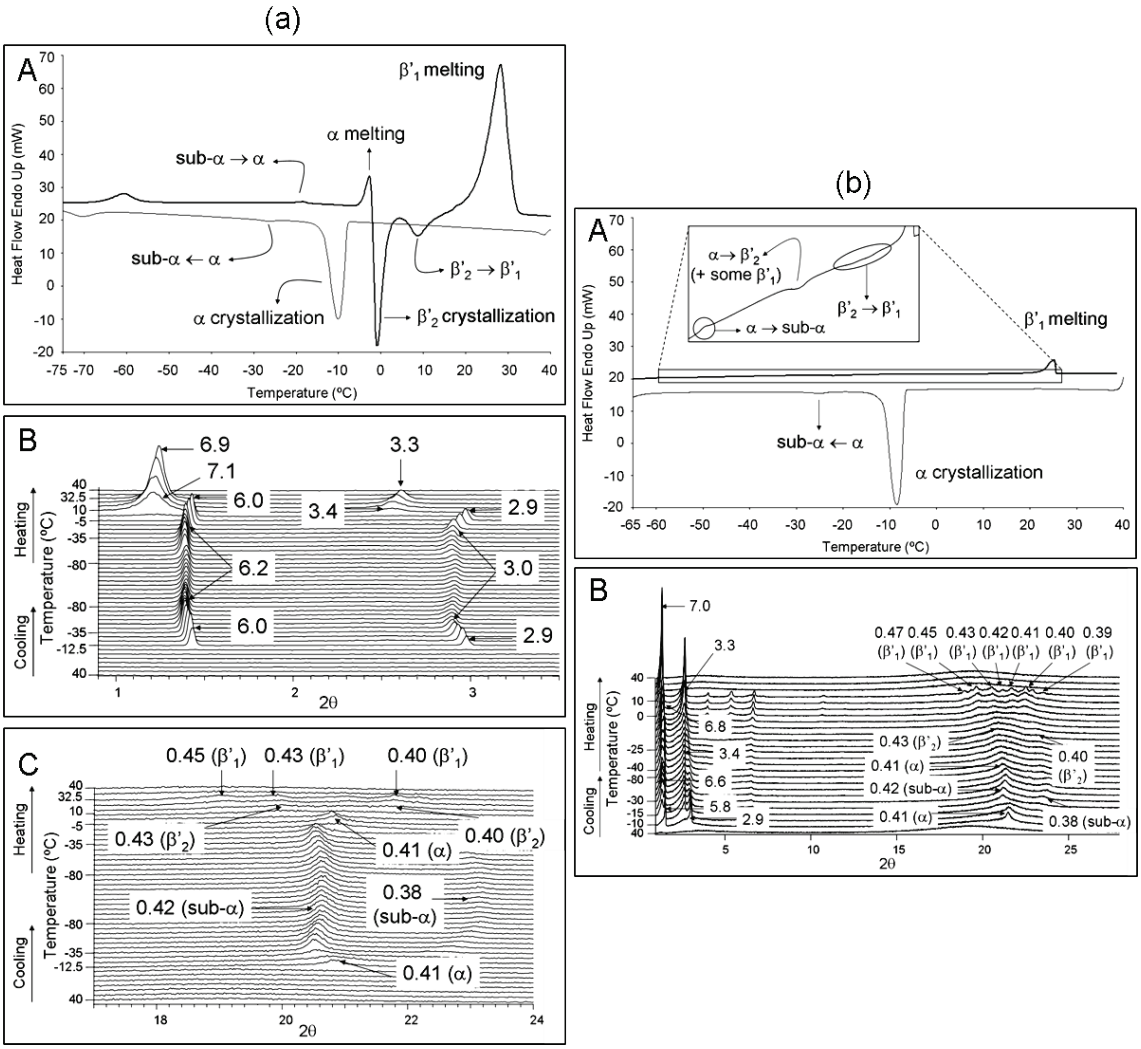

Figure 2.22. Polymorphic behavior of SOO. a) Cooling at 15ºC·min^{-1} and heating at 15ºC·min^{-1}. A. DSC thermogram. B. SR-SAXD pattern. C. SR-WAXD pattern. b) Cooling at 15ºC·min^{-1} and heating at 0.5ºC·min^{-1}. A. DSC thermogram. B. Conventional XRD patterns.

By cooling SOO at 15ºC·min^{-1}, the exothermic crystallization of α form occurred at around -9.0ºC, which transformed to sub-α form at -25.0ºC. Thus, the SAXD peak moved from 6.0 nm (α) to 6.2 nm (sub-α) and the α WAXD peak at 0.41 nm changed to the two sub-α peaks at 0.42 nm and 0.38 nm. Around -70ºC and at the

beginning of the heating step at 15ºC·min^{-1} (approximately at -60ºC, see Figure 2.22a) an exothermic and an endothermic peak were observed, respectively, in the DSC profile. However, they could not be identified by the SR-XRD patterns, as no changes were appreciated in the mentioned temperature ranges. At -22.4ºC, sub-α form transformed to α form. Right after, a melt-mediated transition from α to β'$_2$ form took place, which consisted of the melting of α form (at approximately -6.2ºC) and the subsequent β'$_2$ crystallization (at -3.3ºC). Simultaneously, SR-XRD peaks became so flat, almost inexistent, due to the α melting and progressively, a triple chain length SAXD peak at 7.1 nm and two broad β'$_2$ WAXD peaks appeared at 0.43 nm and 0.40 nm, caused by the β'$_2$ crystallization. Afterwards, the peak at 7.1 nm, observable in the SAXD pattern, moved to 6.9 nm and new WAXD peaks at 0.45 nm, 0.43 nm and 0.40 nm identified a β'$_2$→β'$_1$ solid-state transformation, which occurred at 2.7ºC. β'$_1$ form melted at a T_{onset} of 19.8ºC.

Figure 2.22b depicts the DSC and laboratory-scale XRD data of cooling SOO at 15ºC·min^{-1} and heating it at 0.5ºC·min^{-1}. By heating sub-α form at such a low heating rate, it transformed to α form at -62.2ºC (see Table 2.9a and enlarged figure in Figure 2.22bA). At around -26.6ºC, a α→β'$_2$ transition happened, which could be identified by the occurrence of the two typical broad XRD peaks at 0.43 nm and 0.40 nm in the Wide-Angle region. Later on, another transformation (from β'$_2$ to β'$_1$ form, in this case) occurred at -4.5ºC. At this point, β'$_1$ XRD peaks appeared at 0.47nm, 0.45 nm, 0.43 nm, 0.42 nm, 0.41 nm, 0.40 nm and 0.39 nm. This most stable form finally melted, at 22.0ºC, having a melting enthalpy of 136 J·g^{-1}. This high value suggests that, logically, low heating rates permit obtaining higher amounts of most stable forms. However, taking into account the low enthalpy value associated to the β'$_2$→β'$_1$ transformation (-3 J·g^{-1}), one may reasonably think that some β'$_1$ form was formed in another step, for example in the α→β'$_2$ transition. Therefore, probably some β'$_1$ form may have formed concurrently to β'$_2$. By looking at the XRD patterns, one may notice that the β'$_2$ diffraction peaks became so broad, so they were probably overlapping some β'$_1$ peaks, which became more defined on further heating, when all SOO was converted to β'$_1$ form.

Intermediate rates of cooling and heating (2ºC·min^{-1}) were also applied to SOO, as shown in Figure 2.23.

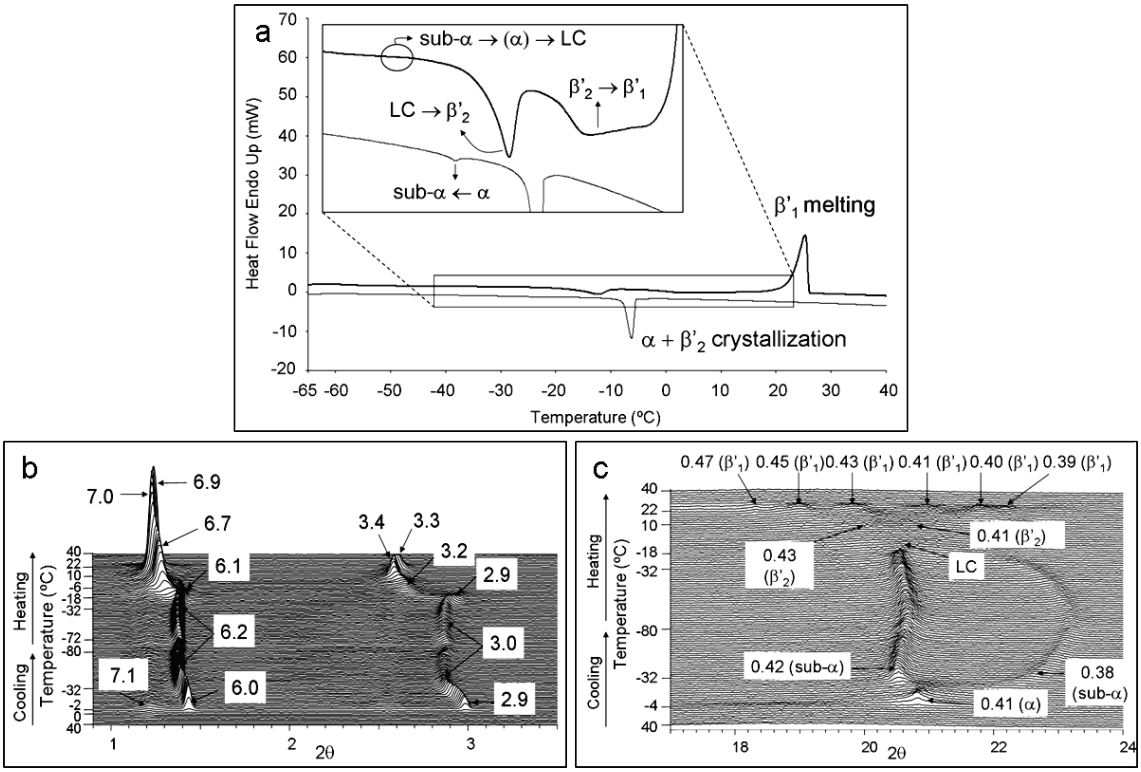

Figure 2.23. Polymorphic behavior of SOO when cooled at 2ºC·min^{-1} (α + β'$_2$ crystallization) and heated at 2ºC·min^{-1}. a) DSC thermogram. b) SR-SAXD pattern. c) SR-WAXD pattern.

Concurrently, α and β'$_2$ forms crystallized from the melt at -5.4ºC when the sample was cooled at 2ºC·min^{-1}. Thus, the SR-SAXD pattern revealed the presence of a weak peak at 7.1 nm (corresponding to β'$_2$ form) and another one at 6.0 nm (belonging to α form). However, the SR-WAXD pattern only showed the α peak at 0.41 nm. At -21.8ºC, the SAXD peak moved to 6.2 nm and the WAXD peak at 0.41 nm changed to two peaks at 0.42 nm and 0.38 nm, caused by the α→sub-α transformation. Later, when sub-α form was heated at 2ºC·min^{-1}, diffraction peaks disappeared in the WAXD pattern and a single SAXD peak was detected at 6.1 nm, meaning the occurrence of a LC phase, similarly to the case of POO. Nevertheless, this phenomenon could not be attributed to any thermal peak of the DSC curve. Judging from the long-spacing values, probably some α was formed before the occurrence of the LC phase, as a weak SAXD peak at 2.9 nm, corresponding to the 002 reflection of the α peak at 6.0 nm, could be observed. On further heating, the SAXD and WAXD peaks of β'$_2$ form appeared at 7.0 nm, and at 0.43 nm and 0.41 nm, respectively. The exothermic DSC peak at -18.9ºC could be attributed to this LC→β'$_2$ transition. According to the DSC data, β'$_2$ form transformed to β'$_1$ form at -2.4ºC. Then, the SR-XRD revealed a shifting from 7.0 nm to

6.9 nm and new WAXD peaks appeared at 0.47 nm, 0.45 nm, 0.43 nm, 0.41 nm, 0.40 nm, 0.39 nm. Soon after the β'_1 formation, it melted at around 20.9ºC.

Simpler polymorphic behavior was verified by cooling SOO at 0.5ºC·min^{-1} and heating it at 15ºC·min^{-1} (Figure 2.24).

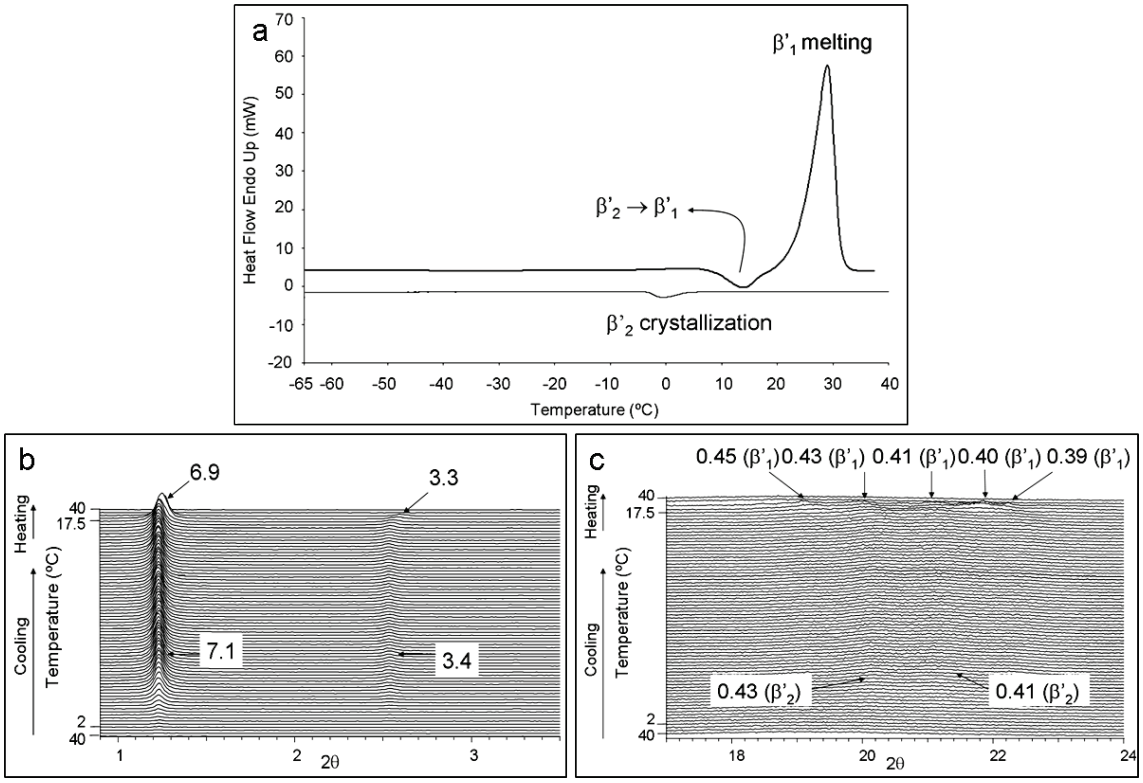

Figure 2.24. Polymorphic behavior of SOO when cooled at 0.5ºC·min^{-1} (β'_2 crystallization) and heated at 15ºC·min^{-1}. a) DSC thermogram. b) SR-SAXD pattern. c) SR-WAXD pattern.

Under this low cooling rate, β'_2 crystals were obtained from the melt at 5.5ºC (see Table 2.9c), as confirmed by the SR-XRD data, with a SAXD peak at 7.1 nm, and two WAXD peaks at 0.43 nm and 0.41 nm. On heating, the DSC curve exhibited an exothermic phenomenon corresponding to the $\beta'_2 \rightarrow \beta'_1$ transformation. SR-XRD data permitted us to identify the β'_1 form through the diffraction peaks at 6.9 nm (SAXD pattern), and 0.45 nm, 0.43 nm, 0.41 nm, 0.40 nm and 0.39 nm. According to the DSC results, β'_1 form straightaway melted at 21.1ºC.

The polymorphic crystallization and transformation of the three SUU (Saturated-Unsaturated-Unsaturated) TAGs described in the present chapter follow the same general tendencies, as described below.

Figure 2.25 depicts, as a summary, some schematic diagrams of the polymorphic pathways followed by the mentioned compounds.

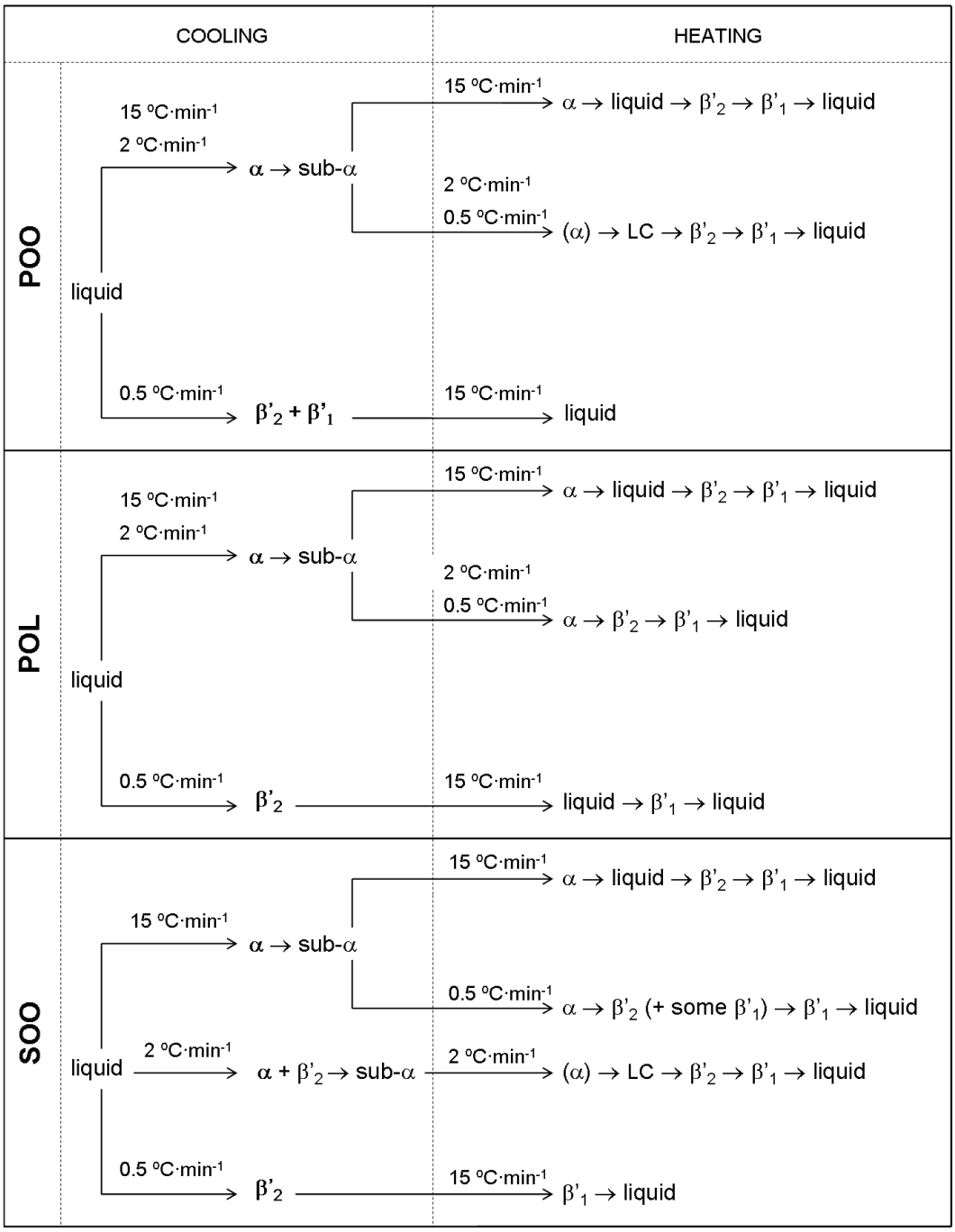

Figure 2.25. Diagrams of polymorphic pathways of POO, POL and SOO under different cooling and heating conditions.

One may realize that the polymorphic behavior of POO, POL and SOO when samples were cooled at 15ºC·min^{-1} and heated at 15ºC·min^{-1} is the same in the three cases. α crystals were directly obtained from the melt, and they transformed to sub-α

form on further cooling. Upon heating, the sequence of polymorphic transformations was as follows: sub-α→α→liquid→β'_2→β'_1→liquid. We should consider that, as already discussed above for the case of POP, when high heating rates are used, melt-mediated transitions more frequently occur. After cooling at 15ºC·min^{-1}, if the TAGs studied were heated at low rates (0.5ºC·min^{-1}), complex DSC curves were obtained in all cases, but the general pattern was: sub-α→α→β'_2→β'_1→liquid. No clear melt-mediated transformations were observed when the heating rate was decreased. However, a liquid crystal (LC) phase was obtained between sub-α and β'_2 forms in POO, but not for POL and SOO.

At intermediate rates of cooling/heating (both 2ºC·min^{-1}), the results obtained for POO and POL were the same than those of cooling at 15ºC·min^{-1} and heating at 0.5ºC·min^{-1}. On the contrary, a concurrent crystallization of α and β'_2 forms took place in SOO, instead of only α form. By heating it afterwards at 2ºC·min^{-1}, the sequence was: sub-α→(α)→LC→β'_2→β'_1→liquid. We specified α form between parentheses, as probably some α form was observed for a short time before the LC phase due to the occurrence of α 002 peak at 2.9 nm. Here we should point out the formation of the LC phase when POO was cooled at 15ºC·min^{-1} and heated at 0.5ºC·min^{-1}, and cooled and heated at 2ºC·min^{-1}. For SOO, the LC phase was only observed when it was cooled and heated at 2ºC·min^{-1}, but there was no evidence when it was cooled at 15ºC·min^{-1} and heated at 0.5ºC·min^{-1}. For these last thermal treatment, laboratory-scale XRD experiments were carried out, not SR-XRD. As the measuring time per temperature was longer in conventional XRD experiments, most probably the sample evolved more quickly than measurements, having not enough time to detect the presence of the LC phase.

Finally, the three samples were subjected to low cooling rate (0.5ºC·min^{-1}) and high heating rate (15ºC·min^{-1}). As expected, more stable forms than α crystallized from the melt, not following the Ostwald step rule of stages: β'_2 form in POL and SOO, and concurrent β'_2+β'_1 forms in POO. By heating at high rates, β'_2 form transformed to β'_1, which finally melted. However, the nature of this polymorphic transformation was different depending on the TAG. More concretely, it occurred through melt-mediation in POL and through the solid state in SOO. In the case of POO, no clear transformation appeared in the DSC heating curve.

As to the LC phases, two different lamellar structures, having the lamellar distance of 6.0 nm and 6.7 nm were identified in POO and SOO, respectively, with no definite periodicity in the lateral packing. This means that both LC correspond to liquid crystals of a smectic type (Ueno et al., 1997). This becomes the first work where LC phases are reported for POO and SOO. They were obtained at low or intermediate rates of heating, becoming intermediate phases between sub-α and β'_2 forms (although some α form could probably take place for a short time after the sub-α form and before LC). Ueno et al.(1997) reported on the liquid crystal formation in SOS. SOS was subjected to different thermal treatments, consisting of thermal annealing and temperature jumps, not using a dynamic temperature variation. However, they observed two types of liquid crystalline structures during the intermediate period after the α melting and before the occurrence of γ or β' forms. Also in the present study, the two liquid crystalline phases were less stable than β' forms, as they appeared before. Moreover, these LC phases could only be detected by SR-XRD experiments, not laboratory-scale XRD, due to their instability. In other words, reproducing the most dynamic XRD experiments, by using Synchrotron Radiation, permitted us to monitor their occurrence.

Concerning the LC forming TAGs studied in this section, one question may arise: taking into account that both POO and SOO revealed an LC phase, why a liquid crystalline phase did not occur in POL? May it be due to its more unsaturated structure? Further work is needed in order to get more information about the structure of these liquid crystalline phases (not only the lamellar distance) and, therefore, be able to know and understand the reasons why LC phases only appear in some TAGs.

High, intermediate and low cooling and heating rates were applied to the main SUU TAGs present in olive oil and Iberian ham fat (POO, POL and SOO). The same pattern was observed in the three cases: when the cooling rate was decreased, more stable polymorphs were directly crystallized from the melt, not following the Ostwald step rule. As to the heating step, higher amounts of β'_1 form (most stable) were obtained by decreasing the rate used. Furthermore, liquid crystalline phases were detected as intermediate forms when POO and SOO were moderately or slowly heated. The information given in this section may be useful for fractionation purposes.

2.6.

Triunsaturated (UUU) triacylglycerols: trioleoyl glycerol (OOO) and 1,2-dioleoyl-3-linoleoyl glycerol (OOL)

This section reports on the polymorphic characteristics of trioleoyl glycerol (OOO) and 1,2-dioleoyl-3-linoleoyl glycerol (OOL), which are the main triunsaturated TAGs present in vegetable oils (e.g., olive oil) (Chiavaro et al., 2010) and other edible oils, by dry fractionation of palm oil (Timms, 2005). The crystallization characteristics of these low-melting TAGs are important for the physical properties of foods employed at chilled temperatures (e.g., frozen foods).

Regarding the polymorphism of OOO, Wheeler et al. (1940) demonstrated the existence of "three crystalline or solid forms: Form I, Form II, and Form III" and presented their melting point data. Later, Ferguson et al. (1947) determined the long- and short-spacing values of three polymorphic forms of OOO: α, β', and β. More polymorphs were characterized by Hagemann et al. (1972), who reported that three β' forms (β'_1, β'_2, and β'_3) appeared when different thermal treatments were applied. They conducted DSC and IR experiments but provided no XRD data on the newly found β' forms. Sato and Ueno noted the presence of three β' forms and two β forms in OOO (Sato et al., 2005) but presented no details. Akita et al. (2006) recently reported the molecular conformations and crystal structures of α, β', and β forms using a combination of XRD, infra-red (IR), and Raman methods. However, few studies have focused on the kinetic properties of the crystallization and transformation of polymorphic forms of OOO.

In this study, we applied DSC, SR-XRD, and micro-Raman methods to *in-situ* observation of the crystallization and transformation kinetics of OOO and OOL. Conventional powder XRD was used for some intermediate cooling and heating rates.

In order to avoid the effects of impurities on polymorphic characteristics, we used highly pure samples of OOO and OOL. Different thermal treatments were applied to the samples by changing the cooling and heating rates. Long- and short-spacing values were determined for all the studied polymorphic forms of OOO (α, β'_2, β'_1, β_2,

and β_1) and OOL (α, β'_2, and β'_1). To the best of our knowledge, this study is the first to examine the polymorphic characteristics of OOL.

Samples were subjected to different cooling and heating rates in the following patterns. OOO was cooled at 15, 2, 1, and 0.5ºC·min^{-1}, and heated at 15ºC·min^{-1}; cooled at 2ºC·min^{-1} and heated at 2ºC·min^{-1}. OOL was cooled at 15ºC·min^{-1}, and heated at 15 and 0.5ºC·min^{-1}; cooled at 2ºC·min^{-1} and heated at 2ºC·min^{-1}; cooled at 0.5ºC·min^{-1} and heated at 15ºC·min^{-1}.

2.6.1. General polymorphic properties

Table 2.10 summarizes the melting points and long/short-spacing values of the polymorphs of OOO and OOL examined in the present section.

Table 2.10. Long and short spacing values of the polymorphic forms of OOO and OOL. Unit, nm.

OOO			
	Melting temperature (°C)	Long spacing	Short Spacing
α-2	-33	4.5	0.431 with shoulder
β'_2-2	---	4.5	0.434, 0.405
β'_1-2	-13	4.5	0.452, 0.436, 0.407, 0.393
β_2-2	-2	4.4	0.458 (0.456), 0.448, 0.398, 0.389, 0.378
β_1-2	2.9	4.4	0.458 (0.456), 0.448, 0.435, 0.405, 0.399, 0.387, 0.381, 0.377, 0.374, 0.368
OOL			
	Melting temperature (°C)	Long Spacing	Short Spacing
α-2	-60	4.4	0.421 with shoulder
β'_2-2	-25	4.4	0.433, 0.410
β'_1-2	-21	4.5	0.453, 0.438, 0.391

The XRD data of three forms of OOO (α, β', and β) have been determined in previous studies (Ferguson et al., 1947; Akita et al., 2006) whose data are in good

agreement with those reported in the present study. Additionally, we observed the long- and short-spacing values of two β' forms (β'_2 and β'_1) and two β forms (β_2 and β_1) of OOO. Previously, Hagemann et al. (1972) confirmed the existence of three β' forms (β'_3, β'_2, and β'_1). Using IR, they could determine the typical orthorhombic subcell structure of β' form and the DSC data permitted to differentiate three β' forms; however, no XRD data were given. Akita et al. (2006) reported only one form of β' and β, corresponding to β'_1 and β_1 of the present study in accordance with the melting points.

No β form was observed for OOL, since the short-spacing pattern of 0.458nm, which is typical of the triclinic subcell of β form, was not detectable. Instead, two β' forms were observed as the most stable polymorphs.

The chain-length structures of all the polymorphic forms of OOO and OOL are double (Table 2.10). From the long-spacing values observed, we can conclude that the inclination angles are relatively large even in the α phases. Compared with the long-spacing values of the corresponding trisaturated TAG (tristearin, SSS), the difference in the long-spacing values between polymorphs of OOO and OOL is much smaller. SSS exhibits long spacing at 5.06, 4.72, and 4.50nm for the corresponding polymorphs (α, β', and β) (Chapman, 1962). The large long-spacing value of α of SSS is due to the perpendicular orientation of the acyl chains against the lamellar surface, and the acyl chains are more inclined in the order of β' and β. Therefore, the smaller long-spacing value of α form for OOO and OOL than for SSS may indicate that the presence of *cis*-double bonds may shorten lamellar distance. The structure models of OOO and OOL will be discussed later.

2.6.2. Polymorphic characteristics of OOO

Figure 2.26 depicts the DSC thermograms of OOO taken by cooling from the melt at different rates (15ºC·min^{-1}, 2ºC·min^{-1}, 1ºC·min^{-1}, and 0.5ºC·min^{-1}) and heated at 15ºC·min^{-1}.

The DSC data, including the onset temperature (T_{onset}) and enthalpy (ΔH) associated with each transition, are presented in Table 2.11.

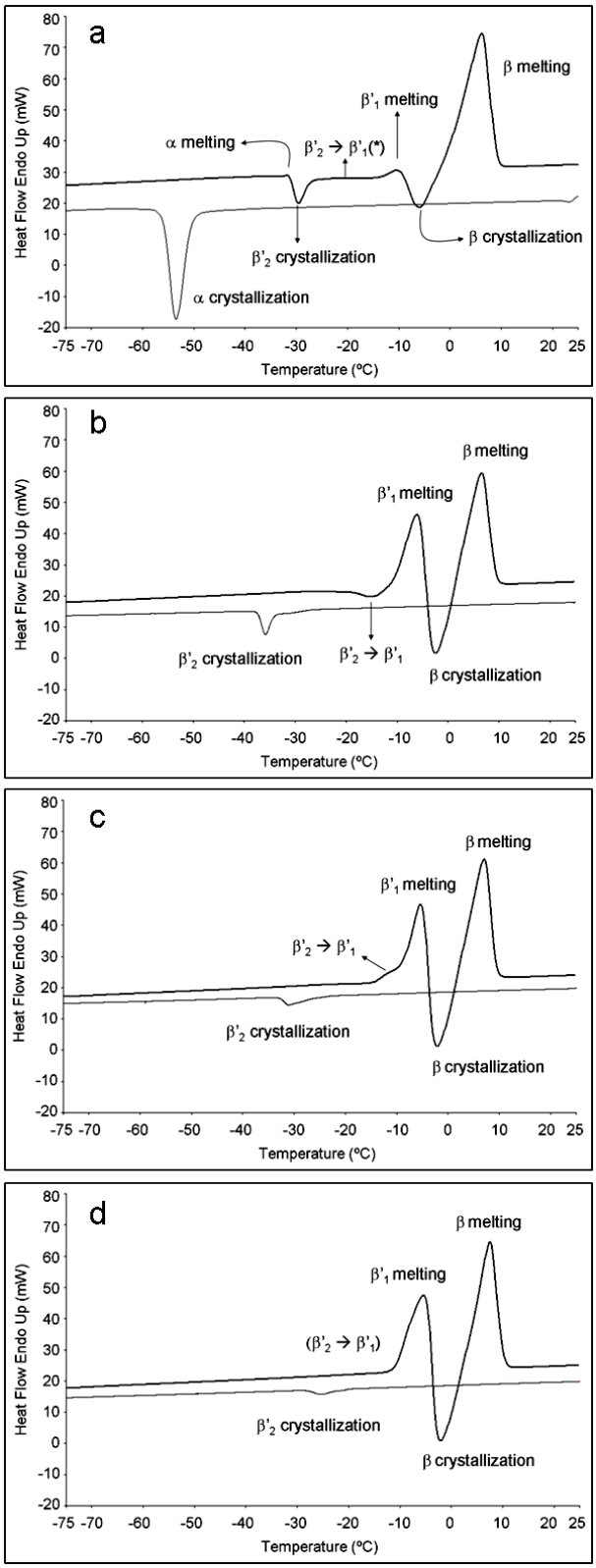

Figure 2.26. DSC thermograms of OOO obtained by applying different cooling rates (heating rate was always 15ºC·min^{-1}). (a) 15ºC·min^{-1}, (b) 2ºC·min^{-1}, (c) 1ºC·min^{-1} and (d) 0.5ºC·min^{-1}.

Table 2.11. DSC data of the polymorphic crystallization and transformation of OOO obtained when the sample was cooled and heated at different rates. The letters *c*, *s* and *m* mean crystallization, solid-state transformation and melting, respectively.

	Cooling		**Heating**				
	(15ºC·min^{-1})		**(15ºC·min^{-1})**				
Polymorph	*α (c)*		*α (m)*	*β′$_2$ (c)*	*β′$_1$ (m)*	*β (c)*	*β (m)*
T (ºC)	-51.1 ± 0.6		-34.1 ± 0.5	-32.3 ± 0.5	-14.4 ± 0.5	-10.2 ± 0.8	-3.3 ± 0.8
ΔH (J/g)	-54 ± 2		aprox. 0	-9 ± <1	2 ± 1	-16 ± 2	105 ± 17
	Cooling		**Heating**				
	(2ºC·min^{-1})		**(15ºC·min^{-1})**				
Polymorph	*β′$_2$ (c)*		*β′$_2$ → β′$_1$*	*β′$_1$ (m)*	*β (c)*	*β (m)*	
T (ºC)	-26.6 ± 1.2	-33.4 ± 0.7	-20.8 ± 1.3	-13.3 ± 0.6	-5.3 ± 0.4	0.4 ± 0.4	
ΔH (J/g)	-70 ± 1		-6 ± 3	41 ± 2	-33 ± 3	73 ± 3	
			(2º C·min^{-1})				
Polymorph			*β′$_2$ → β$_2$*	*β$_2$ → β$_1$*	*β$_2$ + β$_1$ (m)*		
T (ºC)			-25 ± 1.7	-11.3 ± 1.7	-2.2 ± 0.7	2.9 ± 1.3	
ΔH (J/g)			*	-27 ± 4	128 ± 5**		
	Cooling		**Heating**				
	(1ºC·min^{-1})		**(15ºC·min^{-1})**				
Polymorph	*β′$_2$ (c)*		*β′$_2$ → β′$_1$*	*β′$_1$ (m)*	*β (c)*	*β (m)*	
T (ºC)	-22.3 ± 0.7	26.3 ± 3.1	-15.7 ± 0.8	-11.2 ± 0.4	-5.0 ± 0.6	0.6 ± 0.5	
ΔH (J/g)	-76 ± 3		40 ± 2**		-31 ± 2	71 ± 2	
	Cooling		**Heating**				
	(0.5ºC·min^{-1})		**(15ºC·min^{-1})**				
Polymorph	*β′$_2$ (c)*		*β′$_1$ (m)*	*β (c)*	*β (m)*		
T (ºC)	-19.1 ± 1.5	21.5 ± 0.7	-12.2 ± 1.2	-4.5 ± 1.1	1.3 ± 1		
ΔH (J/g)	-83 ± 5		45 ± 4	-33 ± 6	73 ± 8		

* It was not possible to determine this value, as the nature of this transformation pathway is not clear (see text).
** These enthalpy values correspond to the global enthalpy of overlapped peaks.

To identify the crystallization and transformation processes of the polymorphic forms exhibited in exothermic and endothermic DSC peaks, we conducted SR-XRD experiments by applying the same thermal treatments as DSC (Figure 2.27).

When the cooling rate was 15ºC·min^{-1}, we observed the crystallization of α at -51.1ºC, indicated by the long-spacing peak of 4.5nm and short-spacing peak of 0.431 nm (Figure 2.27). However, the more stable β'$_2$ form crystallized with the decreased cooling rates of 2, 1, and 0.5ºC·min^{-1}. The transformation pathways to more stable forms differed when starting from α or β'$_2$ crystals, although β phase was reached as the most stable form in both cases. The details of the experiment results are explained below.

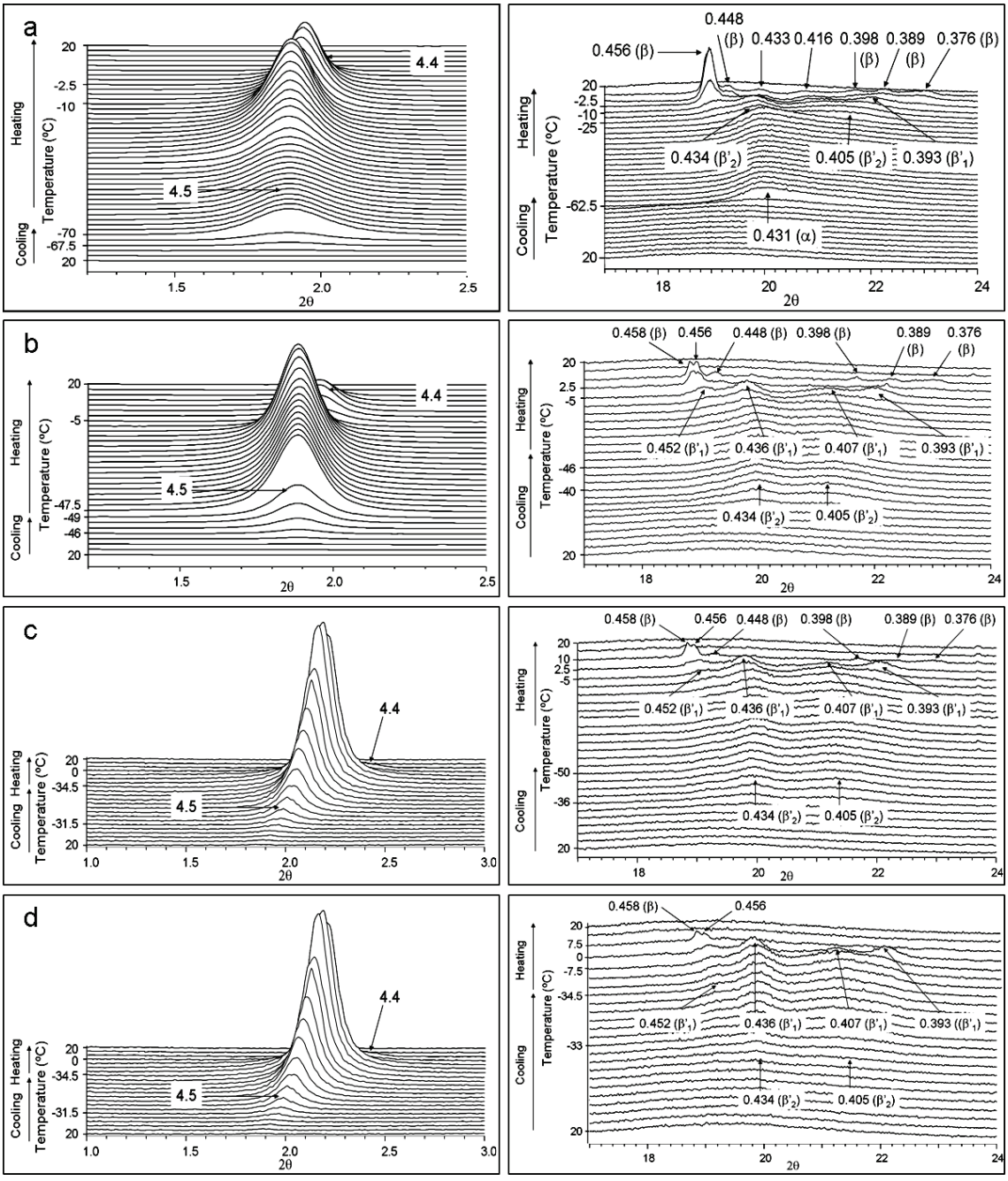

Figure 2.27. SR-XRD patterns of OOO obtained by applying different cooling rates (heating rate was always 15 ºC·min^{-1}). (a) 15ºC·min^{-1}, (b) 2ºC·min^{-1}, (c) 1ºC·min^{-1} and (d) 0.5ºC·min^{-1}. SAXD pattern (left) and SR-WAXD pattern (right).

After crystallization of α by cooling at 15ºC·min^{-1}, very complicated transformation processes occurred from α to β forms through intermediate forms during heating at 15ºC·min^{-1}, as demonstrated in a series of DSC endothermic and exothermic peaks (Figure 2.26a) and changes in the SR-XRD WAXD patterns (Figure 2.27a). First,

melt-mediated transition occurred from α (melting at -34.1ºC) to β'_2 (crystallization at -32.3ºC). Although not detected in DSC peaks, transformation from β'_2 to β'_1 was observed at -20ºC, as indicated in the SR-XRD patterns (Figure 2.27a). Another melt-mediated transformation then occurred from β'_1 (melting at -14.4ºC) to β (crystallization at -10.2ºC). Finally, β melted at -3.3ºC.

In the SR-XRD patterns, β'_2 form was identified by two new WAXD peaks with d-spacing values of 0.434 nm and 0.405 nm, although the SAXD peak was maintained with respect to that corresponding to α form. On further heating, a new peak at 0.393 nm of β'_1 was detected in the WAXD pattern, corresponding to transformation from β'_2 to β'_1. However, no transition was observed in the DSC thermogram in the same temperature range. β'_1 melted at -14.4ºC (T_{onset}); soon after, β form crystallized at -10.2ºC (melt-mediated transition). This was confirmed by a shift from 4.5 nm to 4.4 nm in the SAXD pattern and by the most representative WAXD peaks with d-spacing values of 0.456 nm, 0.448 nm, 0.398 nm, 0.389 nm, and 0.376 nm. This form finally melted at -3.3ºC (T_{onset}).

When the cooling rate was decreased to 2, 1, or 0.5ºC·min^{-1}, β'_2 form (instead of α) was obtained from the melt, as indicated by the SAXD peak at 4.5 nm and two WAXD peaks with d-spacing values of 0.434 nm and 0.405 nm (Figures 2.27b-d). The crystallization temperatures of β'_2 increased with decreasing cooling rates as follows: -26.6ºC at 2ºC·min^{-1}, -22.3ºC at 1ºC·min^{-1}, and -19.1ºC at 0.5ºC·min^{-1}. In these three cases, two onset temperatures were determined for the β'_2 crystallization peak (Table 2.11), as the complex DSC signal consisted of a main exothermic peak having a shoulder. Nevertheless, the beginning of the crystallization phenomenon corresponded to the first determined onset temperature. The transformation pathways from the starting polymorph β'_2 on heating were $\beta'_2 \rightarrow \beta'_1 \rightarrow$ liquid$\rightarrow\beta\rightarrow$liquid when the heating rate was 15ºC·min^{-1}. Transformation into β'_1 was indicated by XRD peaks at 0.452 nm, 0.436 nm, 0.407 nm, and 0.393 nm (WAXD pattern).

Even though the SR-XRD patterns exhibiting $\beta'_2 \rightarrow \beta'_1$ transformation on heating were quite similar to the three different cooling rates, the DSC patterns differed. When the cooling rate was 2ºC·min^{-1}, the $\beta'_2 \rightarrow \beta'_1$ transformation appeared as an exothermic DSC peak with an onset temperature of -20.8ºC. However, when the cooling rate was 1ºC·min^{-1}, this peak became endothermic (T_{onset}= -15.7ºC), and no peak was observed

when the cooling rate was 0.5ºC·min^{-1}. We assume that the transformation from β'$_2$ to β'$_1$ may partially occur even during cooling at 1ºC·min^{-1} and 0.5ºC·min^{-1}.

After the β'$_2$→β'$_1$ transition, melt-mediated transformation from β'$_1$ to β occurred on heating at a rate of 15ºC·min^{-1}. The DSC patterns clearly exhibited endothermic peaks of β'$_1$ melting at -11 to -13ºC, which is associated with exothermic peaks of β crystallization at -6 to -4ºC (Figure 2.26). Furthermore, β was easily identified by the shifting of the SAXD peak from 4.5 nm to 4.4 nm and the 0.458 nm, 0.448 nm, 0.398 nm, 0.389 nm, and 0.376 nm WAXD peaks (Figure 2.27). Finally, β form melted at 0.4ºC to 1.3ºC. The temperatures of melting of β'$_1$, crystallization, and melting of β somehow varied when the applied cooling rates changed from 2, 1, and 0.5ºC·min^{-1}. However, taking into account the error associated with the values given by the DSC data (see Table 2.11), we can assume that the temperatures at which each phenomenon occurred when different cooling rates were used are comparable.

It is noteworthy that the transformation characteristics from β'$_2$, which occurred after crystallization at the cooling rate of 2ºC·min^{-1}, changed when the heating rate was decreased from 15ºC·min^{-1} to 2ºC·min^{-1} (Figure 2.28).

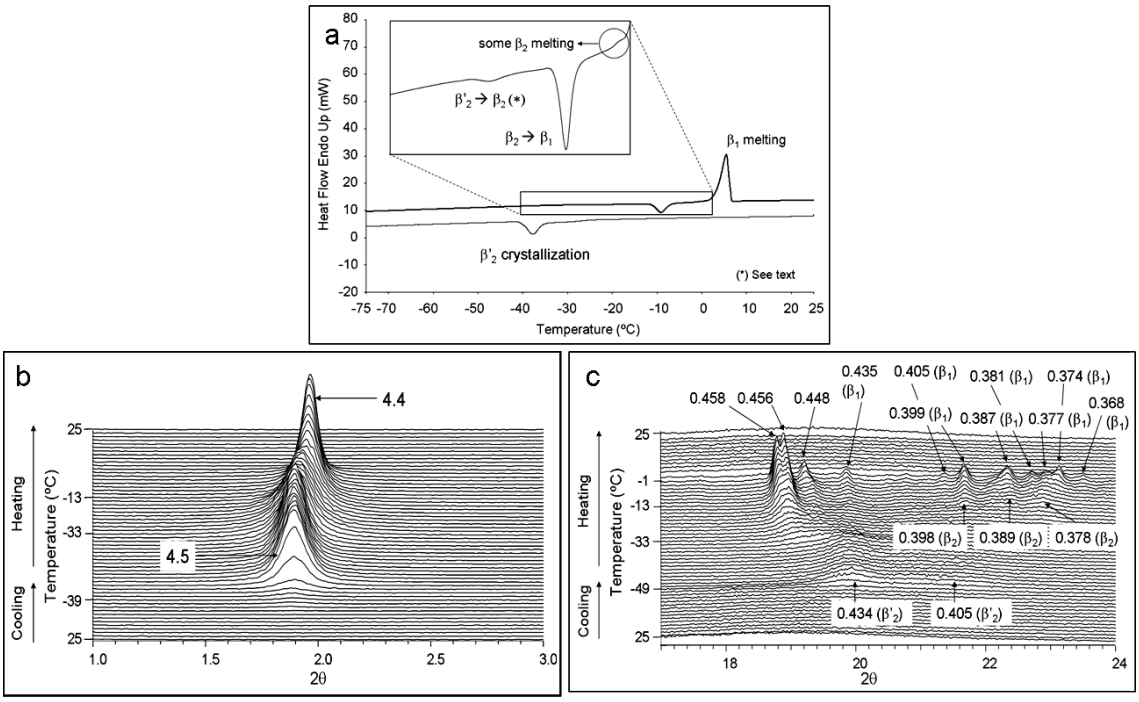

Figure 2.28. Polymorphic behavior of OOO when cooled at 2ºC·min^{-1} (β'$_2$ crystallization) and heated at 2ºC·min^{-1}. a) DSC thermogram. b) SR-SAXD pattern. c) SR-WAXD pattern.

Here, two β forms (β_2 and β_1) could be distinguished, as confirmed by the SR-XRD data and by the presence of a narrow melting peak with a shoulder at high temperatures in the DSC profile. Two consecutive transitions took place, from β'_2 to β_2 at T_{onset} of -25ºC and from β_2 to β_1 at T_{onset} of -11.3ºC (insert in Figure 2.28a). It was difficult to clearly define the nature of the transformation pathway from β'_2 to β_2. However, the shape of the DSC peak indicated that the transition might occur through melt-mediated transformation with a broad and flat melting peak. At -33ºC, some changes could be observed in the SR-XRD WAXD pattern (e.g., decreased peak intensity), possibly due to some melting. Nevertheless, the only phenomenon that was easy to identify in the DSC profile was the exothermic peak with an onset temperature of -25ºC. We could easily detect the β_2 form through the WAXD peaks at 0.458 nm, 0.398 nm, 0.389 nm, and 0.378 nm. On further heating, another transformation (with T_{onset}= -11.3ºC) occurred to obtain another β form (β_1). Hence, we could distinguish between two β forms in OOO, as the typical WAXD peaks of β were maintained but a clear change was observed when new WAXD peaks of β_1 appeared at 0.381 nm, 0.374 nm, and 0.368 nm. The melting curve of these two β forms appeared as a sharp melting peak (narrower than in the cases described above) with T_{onset} of 2.9ºC (due to β_1 melting) revealing a clear shoulder at -2.2ºC (β_2 melting). Therefore, as some β_2 melting was observed, we can conclude that not all β_2 transformed to β_1, as some melted at a higher temperature than that of the $\beta_2 \rightarrow \beta_1$ transformation. Comparison of the ΔH values associated with β melting when OOO was cooled at 2ºC·min^{-1} and heated at 15ºC·min^{-1} (melting ΔH of 73J/g) and 2ºC·min^{-1} (melting ΔH of 128J/g) indicates an increase in the amount of β obtained as the heating rate was decreased.

Two β forms of OOO were previously indicated (Sato et al., 2005), and the present study clearly confirmed it using SR-XRD data.

Micro-Raman experiments were carried out in order to study the polymorphic transformations that occurred when OOO was cooled and heated at 2ºC·min^{-1} (Figure 2.29). Clear differences were observed in the spectra corresponding to the liquid state, β' and β forms. However, it was not possible to identify the two β forms.

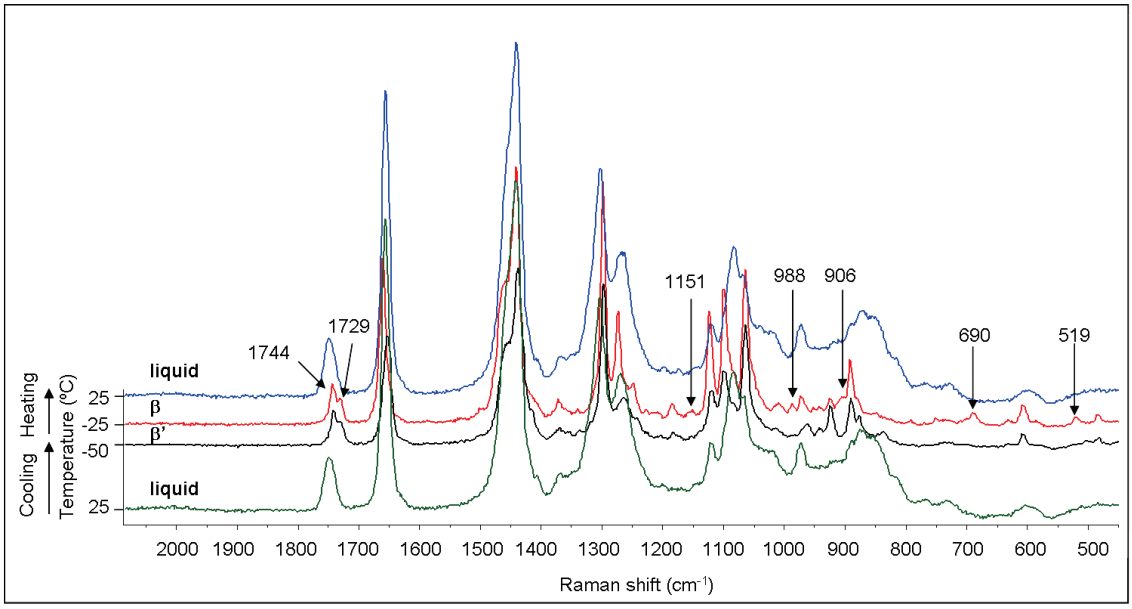

Figure 2.29. Raman spectra of OOO taken during cooling and heating processes at 2ºC·min^{-1}.

At -50ºC, β' form was detected; at -25ºC, it transformed to β form on heating. As Akita et al. (2006) reported, the carbonyl stretch [ν(C=O)] band at 1749cm^{-1} in the liquid state split into two bands at 1744 and 1729 cm^{-1} in β form. Subtle splitting could also be observed in the Raman spectrum corresponding to the β' form. According to Akita et al. (2006), the Raman C=C stretching band ν(C=C) is a good indicator of the conformation of the *cis*-olefin group. Thus, the band at 1653 cm^{-1} in β' form shifted to 1660 cm^{-1} in β form. Moreover, additional bands appeared at 1151, 988, 906, 690, and 519 cm^{-1} when β' transformed to β form.

Figure 2.30 summarizes the polymorphic crystallization and transformation pathways of OOO.

The α form was obtained by cooling OOO at 15ºC·min^{-1}. This α form did not exhibit the typical sharp WAXD peak of 0.41 nm, corresponding to the hexagonal (H) subcell structure that appears in saturated, mono-, and diunsaturated TAGs (Bayés-García et al., 2011; Bayés-García et al. 2013). Here, the α form exhibited a broad peak at 0.431 nm with a shoulder peak. This phenomenon has already been reported (Ferguson et al., 1947; Akita et al., 2006). For this result, Akita et al. (2006) indicated an anisotropic lateral packing of hydrocarbon chains and a distorted H subcell structure. It was evident that the first-occurring polymorph changed from α to β'_2 with decreasing rates of cooling from 15ºC·min^{-1} to 2, 1, and 0.5ºC·min^{-1}. We have already observed the

same results in OPO, POP, POO, POL and SOO, as described in previous sections of this chapter (Bayés-García et al., 2011; Bayés-García et al., 2013).

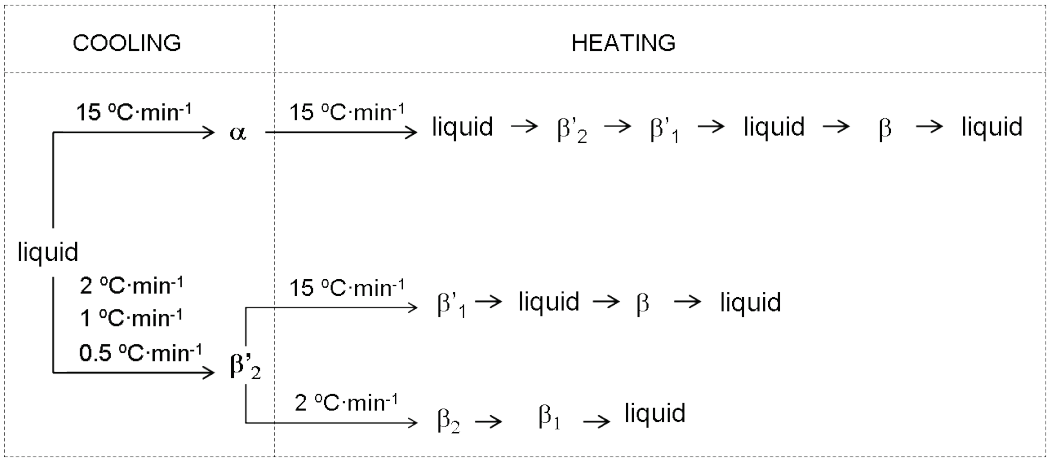

Figure 2.30. Polymorphic crystallization and transformation pathways of OOO under different cooling and heating conditions.

Regarding the transformation pathways on heating, the polymorphic pathways depended mainly on heating rate and, as the Ostwald step rule (Ostwald, 1897) predicts, the first-occurring metastable forms were successively followed by other forms of increasing stability. Thus, the most stable β form was always reached at the two heating rates used (15 and 2ºC·min^{-1}) through β'$_2$ and β'$_1$. Furthermore, when OOO was heated at the lower heating rate (2ºC·min^{-1}), it was possible to distinguish the two β forms (β$_2$ and β$_1$).

2.6.3. Polymorphic characteristics of OOL

OOL was also subjected to different thermal programs. Table 2.12 summarizes the melting temperatures and ΔH values when different rates of cooling (15, 2, and 0.5ºC·min^{-1}) and heating (15, 2 and 0.5º C·min^{-1}) were applied to the OOL samples.

Table 2.12. DSC data of the polymorphic crystallization and transformation of OOL obtained when the sample was cooled and heated at different rates. The letters *c*, *s* and *m* mean crystallization, solid-state transformation and melting, respectively. DSC onset temperatures were defined for crystallization and melting.

	Cooling	**Heating**			
	(15ºC·min^{-1})	**(15ºC·min^{-1})**			
Polymorph	*α (c)*	*α (m)*	*β′$_2$ (c)*	*β′$_2$ + β′$_1$ (m)*	
T_{onset} (ºC)	*	-65.5 ± 1.1	-57.8 ± 0.2	-25.4 ± 0.5	-24.0 ± 0.6
ΔH (J/g)		2 ± 1	-11 ± 2	72 ± 4**	
		(0.5ºC·min^{-1})			
Polymorph		*α → β′$_2$*	*β′$_1$ (m)*		
T_{onset} (ºC)		-65.2 ± 0.3	-20.9 ± 0.4		
ΔH (J/g)		-5 ± 2	79 ± 3		
	Cooling	**Heating**			
	(2ºC·min^{-1})	**(2ºC·min^{-1})**			
Polymorph	*β′$_1$ (c)*	*β′$_1$ (m)*			
T_{onset} (ºC)	-41.6 ± 0.4	-20.4 ± 0.8			
ΔH (J/g)	-61 ± 4	73 ± 3			
	Cooling	**Heating**			
	(0.5ºC·min^{-1})	**(15ºC·min^{-1})**			
Polymorph	*β′$_1$ (c)*	*β′$_1$ (m)*			
T_{onset} (ºC)	-33.4 ± 0.6	-21.9 ± 0.5			
ΔH (J/g)	-72 ± 4	80 ± 4			

* The α crystallization occurred during the isothermal and the beginning of the heating processes, so the DSC peak could not be interpreted as a function of temperature.
** These enthalpy values correspond to the global enthalpy of overlapped peaks.

No β forms were present, and the most stable polymorph was β'. This result was the same as for 1,2-dipalmitoyl-3-myristoyl-*sn*-glycerol (PPM) (Kodali et al., 1990), 1,2-dipalmitoyl-3-oleoyl-*rac*-glycerol (PPO) (Minato et al., 1997a), 1,2-distearoyl-3-oleoyl-*rac*-glycerol (SSO) (Takeuchi et al., 2002), 1-palmitoyl-2, 3-oleoyl-*rac*-glycerol (POO) (Zhang et al., 2007), and 1-stearoyl-2, 3-oleoyl-*rac*-glycerol (SOO) (Zhang et al., 2009), probably due to all these TAGs being asymmetric mixed-acid TAGs.

The least stable polymorph (α) was obtained when the cooling rate was high, whereas the most stable form (β'$_1$) crystallized from the melt at cooling rates of 2ºC·min^{-1} and 0.5ºC·min^{-1}. When the heating rate was varied, the most stable β'$_1$ form was obtained in all cases examined, similar to OOO.

Figure 2.31 depicts the polymorphic characteristics of OOL when it was cooled at a high rate (15ºC·min^{-1}) and heated at high (15ºC·min^{-1}) and low (0.5ºC·min^{-1}) rates.

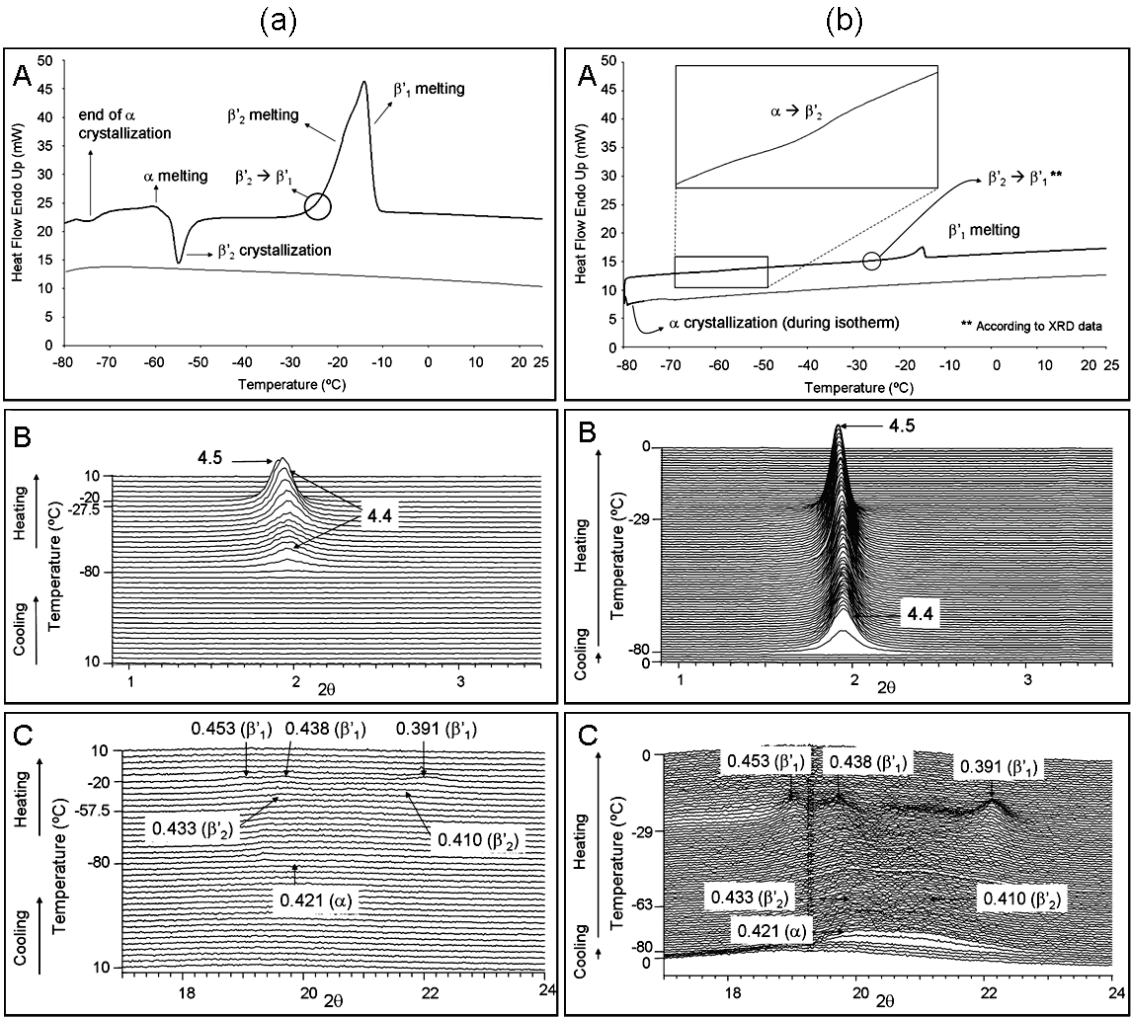

Figure 2.31. Polymorphic behavior of OOL (a) Cooling at 15ºC·min^{-1} and heating at 15ºC·min^{-1}. A. DSC thermogram. B. SR-SAXD pattern. C. SR-WAXD pattern. (b) Cooling at 15ºC·min^{-1} and heating at 0.5ºC·min^{-1}. A. DSC thermogram. B. SR-SAXD pattern. C. SR-WAXD pattern.

At 15ºC·min^{-1}, the α form, with a long-spacing of 4.4 nm and a single short-spacing of 0.421 nm, crystallized. Similar to OOO, the broad WAXD peak at 0.421 nm had a shoulder. No exothermic DSC peak corresponding to this crystallization was observed in the cooling thermal step, due to the low crystallization temperature of this polymorphic form and the high cooling rate used. The α crystallization started during the isotherm (1min long) that took place between the cooling and heating steps, and ended at the beginning of the heating process (Figure 2.31(a)A).

After α crystallization, melt-mediated transformation from α to β'$_2$ occurred when the sample was heated at 15ºC·min^{-1}, as observed in the melting of α at -65.5ºC and the crystallization of β'$_2$ at -57.8ºC, (Figure 2.31(a)A). This was clearly

demonstrated by the presence of the β'_2 WAXD broad peaks at 0.433 nm and 0.410 nm (Figure 2.31(a)B). Later, the SR-XRD data indicated that β'_2 transformed to β'_1 before β'_1 melted. During this transformation, the SAXD peak shifted from 4.4 nm to 4.5 nm, and new WAXD peaks of β'_1 appeared at 0.453 nm, 0.438 nm, and 0.391 nm. Apparently not all β'_2 transformed to β'_1, as the last melting peak seemed to be double, with clear onset temperatures of -25.4ºC (corresponding to β'_2 melting) and -24ºC (corresponding to β'_1 melting).

Solid-state $\alpha \rightarrow \beta'_2$ transformation occurred at a heating rate of 0.5ºC·min^{-1}, as indicated by an exothermic DSC peak (insert in Figure 2.31(b)A). This contrasts with the melt-mediated $\alpha \rightarrow \beta'_2$ transformation obtained by heating at 15ºC·min^{-1}. This solid-state transformation occurred at -65.2ºC; concurrently, β'_2 WAXD peaks of 0.433 nm and 0.410 nm appeared. Later, $\beta'_2 \rightarrow \beta'_1$ transformation occurred at -39ºC, as indicated by the SAXD peak shifting from 4.4 nm to 4.5 nm and WAXD peaks at 0.453 nm, 0.438 nm, and 0.391 nm, although no DSC thermopeaks were observed. The β'_1 form finally melted at -20.9ºC. As explained above, not all β'_2 transformed to β'_1 at the heating rate of 15ºC·min^{-1}, as β'_2 melting was observed together with the melting of β'_1. Not surprisingly, β'_2 had enough time to transform completely to β'_1, and β'_1 melted afterwards at a lower heating rate of 0.5ºC·min^{-1}.

The effects of the decreased cooling rate on the polymorphic crystallization of OOL were clearly observed. Figure 2.32 depicts the DSC and laboratory-scale XRD data of OOL when it was cooled and heated at 2ºC·min^{-1}. Figure 2.33 presents the results obtained for cooling at 0.5ºC·min^{-1} and heating at 15ºC·min^{-1}.

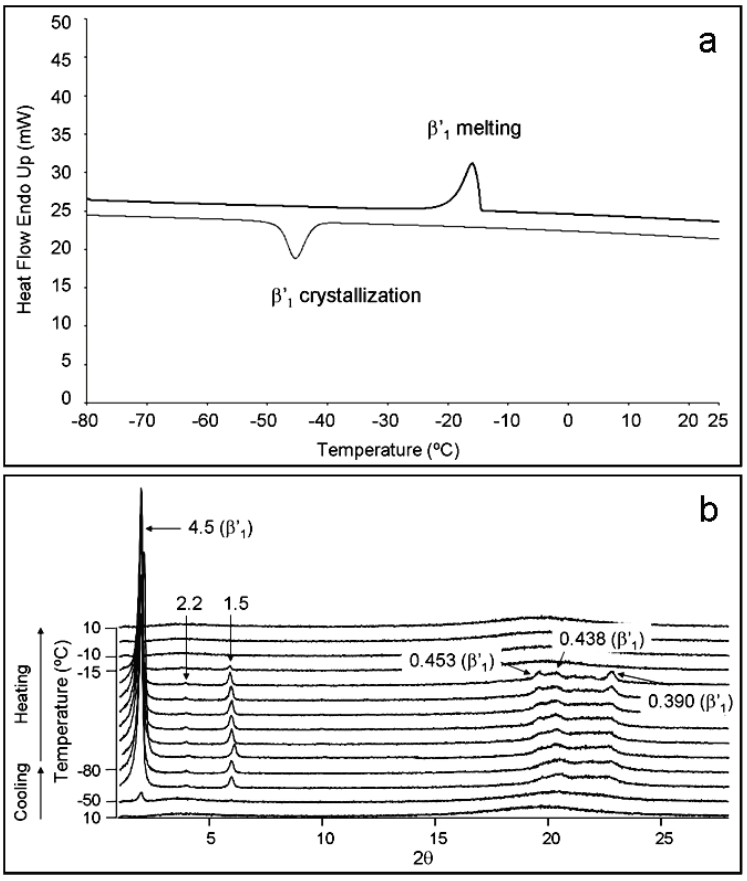

Figure 2.32. Polymorphic behavior of OOL when cooled at 2ºC·min^{-1} (β'$_1$ crystallization) and heated at 2ºC·min^{-1}. a) DSC thermogram. b) Laboratory-scale XRD pattern.

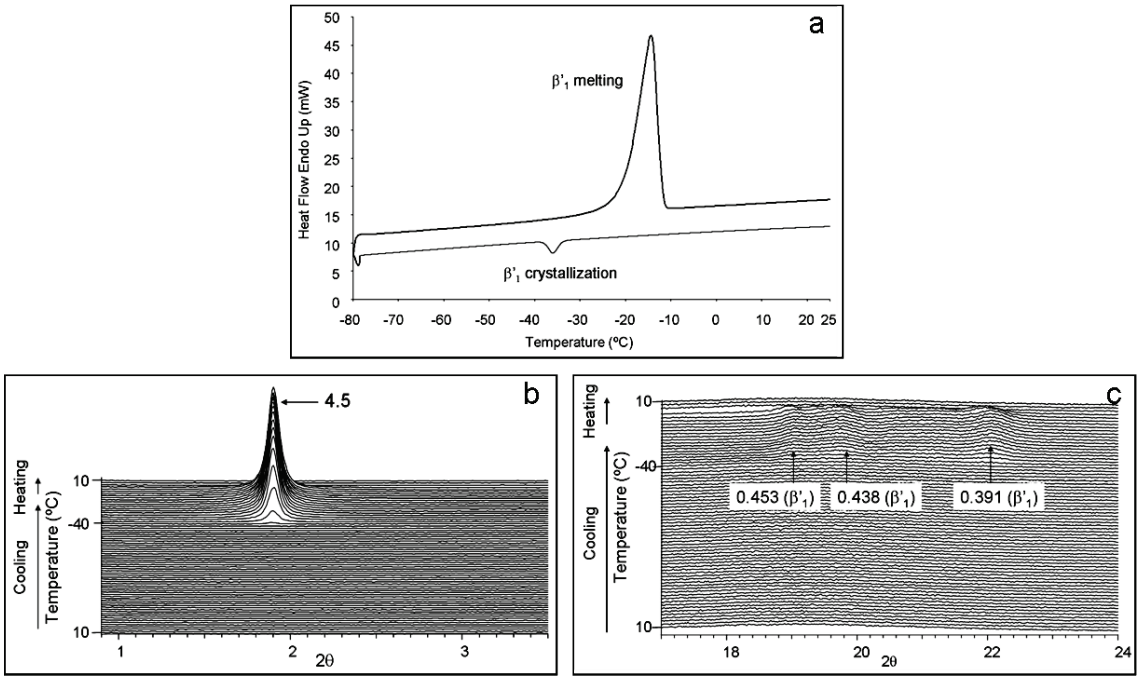

Figure 2.33. Polymorphic behavior of OOO when cooled at 0.5ºC·min^{-1} (β'$_1$ crystallization) and heated at 15ºC·min^{-1}. a) DSC thermogram. b) SR-SAXD pattern. c) SR-WAXD pattern.

When lower cooling rates were applied (2 and 0.5ºC·min^{-1}), the first-occurring form was the most stable β'$_1$. The crystallization temperatures of β'$_1$ were -41.6ºC for cooling at 2ºC·min^{-1} and -33.4ºC for cooling at 0.5ºC·min^{-1}. In both cases, the typical XRD peaks of β'$_1$ were observed, and no β'$_2$ form was present.

When β'$_1$ crystals were heated, they simply melted at -21 to -20ºC without transformation to β form.

Figure 2.34 summarizes the polymorphic characteristics of OOL observed by varying the cooling and heating rates.

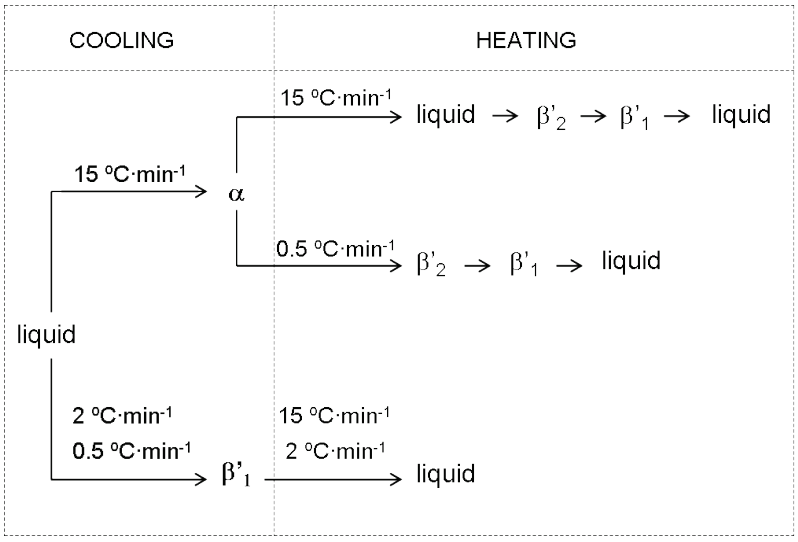

Figure 2.34. Polymorphic crystallization and transformation pathways of OOL under different cooling and heating conditions.

High cooling rates caused the crystallization of α (least stable form), while intermediate and low cooling rates led to the crystallization of the most stable β'$_1$ form. Starting from α crystals, the sequence of polymorphs of increasing stability when the heating rate was high (15ºC·min^{-1}) was α→liquid→β'$_2$→β'$_1$→liquid; however, when the heating rate was low (0.5ºC·min^{-1}), it changed to α→β'$_2$→β'$_1$→ liquid. The difference between the two pathways was apparent in the nature of the α→β'$_2$ transition: melt-mediation at 15ºC·min^{-1} and solid-state at 0.5ºC·min^{-1}. This was quite similar to that observed for the TAGs studied in the present chapter.

The present study has demonstrated the following kinetic properties of polymorphic crystallization and transformation of OOO and OOL, which were affected by different thermal treatments.

(1) Five polymorphs (α, β'_2, β'_1, β_2, and β_1) were isolated in OOO, and three polymorphs (α, β'_2 and β'_1) in OOL.
(2) The effects of varying cooling and heating rates were remarkable. More stable polymorphs were crystallized by decreasing the cooling rates, whereas less stable polymorphs were manifest at higher cooling rates.
(3) Solid-state transformations occurred more easily than melt-mediated transformation when the heating rate was decreased.

These properties were consistent with those observed for POP, OPO, POO, POL and SOO, whose crystallization and transformation properties were examined with DSC and SR-XRD at cooling and heating rates of 15ºC·min^{-1} to 0.5ºC·min^{-1} and they will be summarized in the following section.

The *in situ* study of the polymorphic behavior of OOO and OOL was submitted as a research paper to the Journal of Physical Chemistry B.

2.7.

Summary of the polymorphic behavior observed for 1,3-dipalmitoyl-2-oleoyl glycerol (POP), 1,3-dioleoyl-2-palmitoyl glycerol (OPO), 1- palmitoyl-2,3-dioleoyl glycerol (POO), 1-palmitoyl-2-oleoyl-3-linoleoyl glycerol (POL), 1-stearoyl-2,3-dioleoyl glycerol (SOO), trioleoyl glycerol (OOO) and 1,2-dioleoyl-3-linoleoyl glycerol (OOL)

Table 2.13 summarizes the crystallization and transformation pathways of POP, OPO, POO, POL, SOO, OOO and OOL at different cooling and heating rates.

For OPO, multiple polymorphic forms involving the most stable β form were obtained, demonstrating complex concurrent crystalization in most cases. For POP, however, it was dificult to obtain stable forms such as β' and β even when the cooling rate was lowered to 0.5ºC·min^{-1}; for example, γ was obtained instead of β' form. For POO, POL, SOO, OOO and OOL, α was crystallized with rapid cooling, and β' was crystallized with slow cooling.

More stable forms (e.g., β' and β) were obtained either through solid-state or melt-mediated transformation for OPO, POO, POL, SOO, OOO, and OOL even at a high rate (15ºC·min^{-1}). However, it was necessary to decrease the heating rates to 2 to 0.1ºC·min^{-1} to obtain the most stable β form for POP. Thus, we may conclude that similar characteristics of polymorphic crystallization and transformation were observed for OPO, POO, POL, SOO, OOO, and OOL; however, POP differed in the difficulty of obtaining the most stable β form.

Table 2.13. Crystallization and transformation pathways of POP, OPO, POO, POL, SOO, OOO and OOL at different cooling and heating rates, in which *mm* and *ss* mean melt-mediated and solid-state transformations.

		POP	OPO	POO	POL	SOO	OOO	OOL
Polymorphs		α-2, γ-3, β'-2[a], δ-3, β-3 [a]	α-2, β'-2[a] , β-3	sub-α-2, α-2, LC, β'-3[a]	sub-α-2, α-2, β'-3[a]	sub-α-2, α-2, LC, β'-3[a]	α-2, β'-2[a] , β-2 [a]	α-2, β'-2[a]
Crystallization on cooling	rapid	α	α	α	α	α	α	α
	slow	γ	β' + β	β'	β'	β'	β'	β'
Transformation on heating	rapid	α→(*mm*)β'→L γ→L	α→(*mm*) β'→β→L β'→β→L	α→(*mm*)β'→L β'→L	α→(*mm*)β'→L β'→L	α→(*mm*)β'→L β'→L	α→(*mm*) β'→(*mm*) β→L β'→(*mm*) β→L	α→(*mm*) β'→L β'→L
	slow	α→γ→(*ss*)δ→(*mm*) β→L γ→(*mm*) β'+δ→(*mm*) β→L	n.a[b] n.a[b]	α→LC→β'→L n.a[b]	α→(*ss*)β'→L n.a[b]	α→LC→β'→L n.a[b]	n.a[b] β'→(*ss*) β→L	α→(*ss*) β'→L β'→L

[a] For simplicity, β_2' and β_1' or β_2 and β_1 are summarized into β' or β, respectively.
[b] Not available.

We may explain these results by taking into account the activation energies of solid-state and melt-mediated transformations from one polymorphic form to another, as fully discussed for POP (see section 2.3). Figure 2.35 illustrates two typical transformations that take place from a less stable form (A) to a more stable form (B).

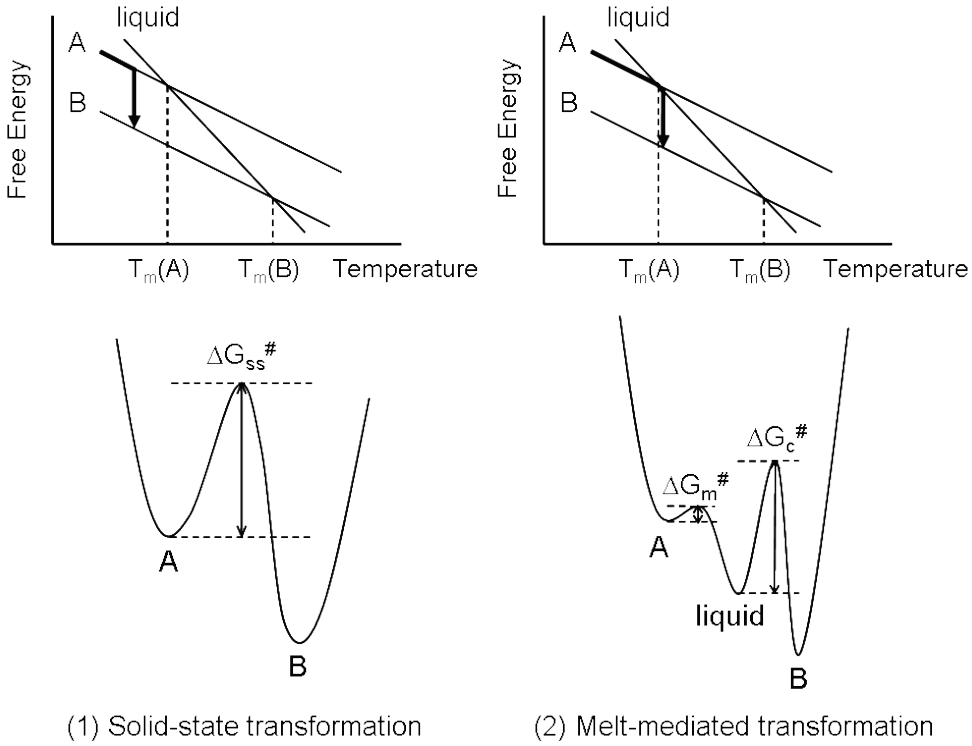

Figure 2.35. Activation free energy ($\Delta G^{\#}$) for solid-state and melt-mediated transformation from metastable A to more stable B forms.

The rates of transformation are basically determined by the magnitude of the activation free energies ($\Delta G^{\#}$) involved in each process: the larger the $\Delta G^{\#}$, the lower the transformation rate. As for solid-state transformation, $\Delta G_{ss}^{\#}$ may include excess energy to enable structural changes (e.g., subcell structure and chain-length structure) needed to cause transformation from form A to form B. The rate of the melt-mediated transformation is determined by the magnitude of $\Delta G_m^{\#}$ corresponding to the melting of form A and the subsequent crystallization ($\Delta G_c^{\#}$) of form B. However, the actual rate may be determined by $\Delta G_c^{\#}$ because of the ease of melting and the small values of $\Delta G_m^{\#}$.

We may simply assume that the values of $\Delta G_{ss}^{\#}$ for transformations involving

change from loosely packed subcell structures (e.g., hexagonal (α polymorph)) to more closely packed subcell structures of O⊥ (β') and T// (β) are larger than those from O⊥ (β') to T// (β). Also the values of $\Delta G_{ss}^{\#}$ may be lower for transformation between polymorphs having the same double chain length structures than for changes from double to triple chain length structures (Figure 2.36).

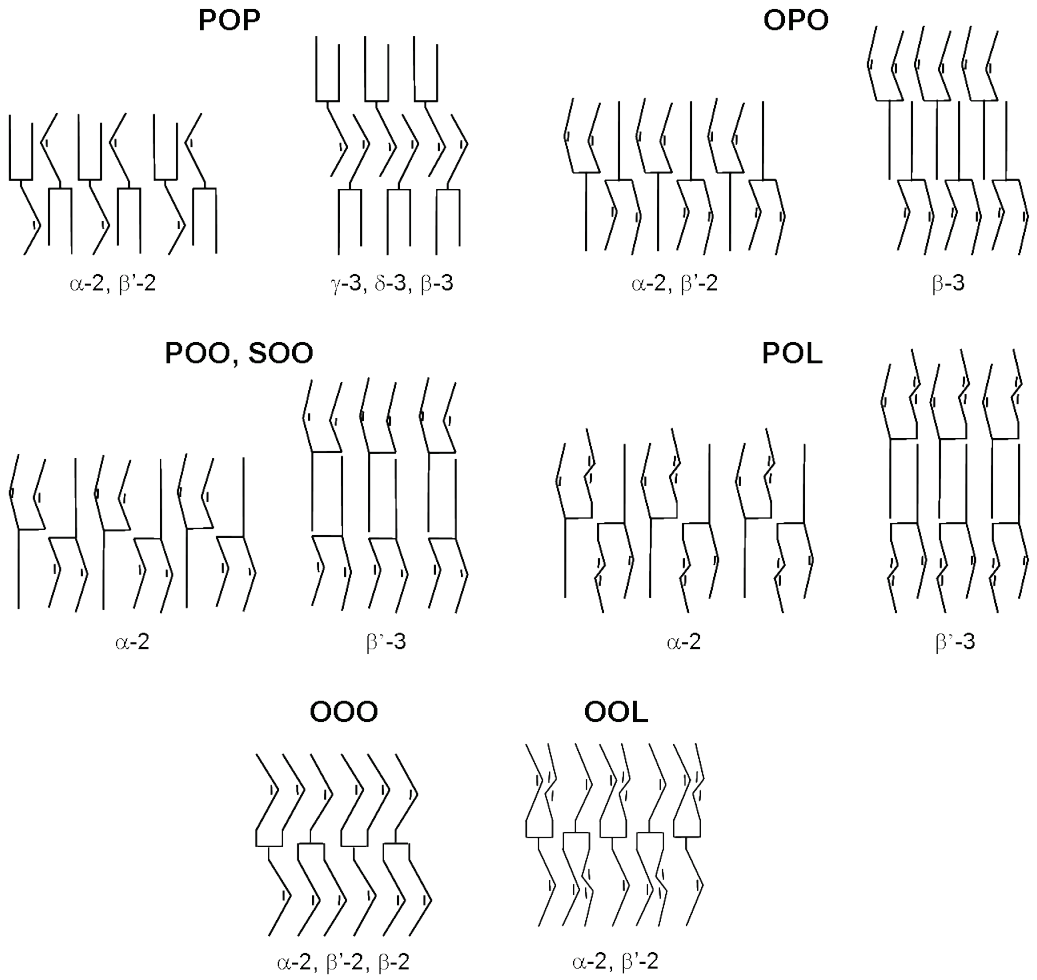

Figure 2.36. Structure models of POP, OPO, POO, SOO, POL, OOO and OOL. For simplicity, multiple β' and β forms are represented by β' and β.

The same assumption may apply to crystallization, in that the values of $\Delta G_c^{\#}$ of the polymorphs having tightly packed subcell and triple chain length structures may be larger than in the other cases. Taking into account these points, the crystallization and transformation of more stable β and β' forms of OOO and OOL occur easily, since the all polymorphic forms exhibit the same double chain length structure.

A peculiarity in the transformation pathways was observed for POP in that, even during slow heating, solid-state transformation occurred with more difficulty, compared to the OOO and OOL cases. This may be due to the fact that POP contains saturated fatty acid (palmitic acid) moiety whose transformation from less stable to more stable forms may need large activation energies ($\Delta G_{ss}^{\#}$) compared with those of oleic and linoleic acid moieties. The flexibility of the chain packing of unsaturated acids is more enhanced than that of saturated fatty acids (Small, 1984). This may decrease the value of $\Delta G_{ss}^{\#}$ for transformation into more stable forms of OOO and OOL.

2.8.
Chapter conclusions

The main conclusions of the present chapter can be summarized as follows:

- The polymorphic behavior of main TAGs of some vegetable and animal fats and oils (POP, OPO, POO, POL, SOO, OOO and OOL) has been *in situ* studied by mainly using DSC and SR-XRD with SAXD and WAXD simultaneous measurements. The combined usage of SR-XRD and DSC enabled us to monitor the occurrence and transformation behavior even at high rates, which may have a direct application in factories and cannot be attained with laboratory-scale XRD techniques. Thus, all TAG samples were cooled from the melt, in order to avoid their thermal history, and heated afterwards, by using different rates of cooling and heating.

- Some general trends were observed in the polymorphic behavior of all TAG samples when different cooling and heating rates were used. As to the polymorphic occurrence observed when cooling, more stable forms crystallized from the melt when decreasing the rate used, not following the Ostwald step rule of stages. In the sequence of polymorphic transformations observed in the heating step, the use of low heating rates also permitted obtaining higher amounts of most stables phases. Regarding to the nature of the polymorphic transformation from less stable to more stable forms, the number of solid state transitions increased at the expense of melt-mediated transformations when the heating rate was decreased. This phenomenon was explained, in this chapter, by taking into account the activation energies of solid-state transformations from one polymorphic form to another.

- A peculiar behavior was detected in POP, which becomes the most saturated TAG analyzed in the present chapter. By decreasing the cooling and heating rates, it was more difficult to obtain more stable forms of POP, compared to the OPO, POO, POL, SOO, OOO and OOL cases. As to the transformation pathways during heating, less solid state transitions were observed when the rate of heating was decreased,

compared to the other TAGs examined. This may be due to the fact that POP contains more saturated fatty acid moieties, whose transformation from less stable to more stable forms may need large activation energies ($\Delta G_{ss}^{\#}$) compared to those of oleic and linoleic acid moieties. The flexibility of the chain packing of unsaturated acids is more enhanced than that of saturated fatty acids.

- The study of the influence of kinetic factors, such as variations in the cooling and heating rates applied to TAG samples, permitted determining and characterizing a higher amount of polymorphic forms than those published until now. As an example, liquid crystalline (LC) phases were detected in POO and SOO when the samples were subjected to low heating rates. These phases could only be detected by SR-XRD experiments, not laboratory-scale XRD, due to their instability.

- The results obtained in this chapter are closely related to actual crystallization processes of edible fats and oils, in which most functional polymorphic forms can be obtained by applying the most efficient thermal treatments.

CHAPTER 3

Solid state miscibility of triacylglycerols containing palmitic and oleic fatty acids

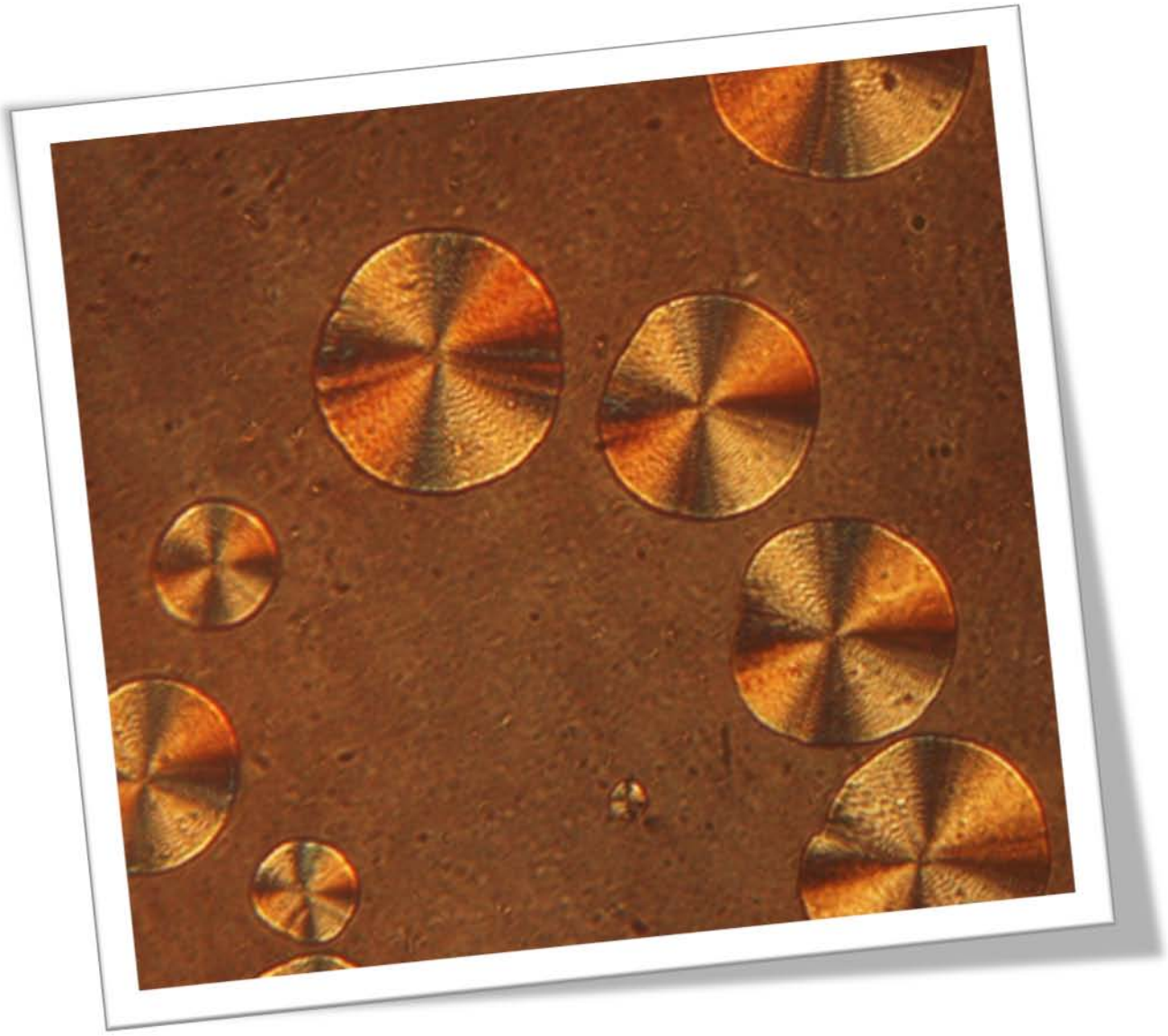

3.1.

Introduction

Many lipids, such as triacylglycerols (TAGs) and diacylglycerols (DAGs), consist of multiple components in two ways: (i) a lipid phase contains a variety of lipids differing in hydrophilic and hydrophobic structures, and (ii) each single lipid molecule involves different types of fatty acid moieties. Therefore, the physicochemical properties of lipids must be studied not only in their pure systems but also in mixed systems. In particular, studies on binary mixture systems provide valuable information about molecular interactions among different lipid materials. The same analysis is applied to TAGs, which are, as previously mentioned, the main components of natural and industrial lipids.

Diversified molecular interactions among TAGs are found in polymorphism and mixing behavior. The number of individual polymorphic forms of TAGs and their molecular structures drastically change when fatty acid compositions included in the TAGs are changed (see Chapter 2) (Larsson et al., 2006). Moreover, for the binary mixing behavior of TAGs, three situations have been confirmed: (i) solid solution phase, (ii) eutectic phase, and (iii) molecular compound (MC) formation. When two component TAG molecules exhibit structural similarity and affinitive molecular interactions, a miscible solid solution phase is formed. However, when two component molecules are immiscible due to steric hindrance, a eutectic equilibrium is obtained (Kitaigorodsky, 1984; Sato et al., 2005; Larsson et al., 2006). More unusual is the formation of MC phase, which is only formed at a concrete composition, through specific molecular interactions between two component molecules (Sato et al., 2001a).

The properties of polymorphism and mixing behavior of TAGs are strongly related because the chemical nature (saturated or unsaturated) of the component TAG molecules results in complicated polymorphism and mixing behavior.

As typical examples, we present here TAGs containing palmitic and oleic acid moieties, PPP (tripalmitoyl glycerol), OOO (trioleoyl glycerol), POP (1,3-dipalmitoyl-2-oleoyl glycerol), POO (1-palmitoyl-2,3-dioleoyl glycerol), PPO (1,2-dipalmitoyl-3-oleoyl glycerol), and OPO (1,3-dioleoyl-2-palmitoyl glycerol). The

mixtures of PPP:POP (Minato et al., 1996), PPP:OOO (Small, 1986), and POP:POO (Zhang et al., 2007) are eutectic, whereas the mixtures of POP:PPO and POP:OPO are MC-forming at ratios of POP:PPO = 50:50 and POP:OPO = 50:50 (Minato et al., 1997a; Minato et al., 1997b). The MC-forming mixtures of POP:OPO were observed in crystals formed not only from neat liquid, but also from solutions including n-dodecane as a solvent (Ikeda et al., 2010), as this binary mixture is significant for fractionation of palm oil in dry and solvent methods.

One of the aims of this study was to analyze and understand the whole mixing behavior of triacylglycerols containing palmitic and oleic acids, which could be extrapolated to other TAGs containing saturated and unsaturated fatty acid moieties. As explained above, the phase behavior of POP:POO (eutectic), POP:PPO (MC-forming) and POP:OPO (MC-forming) were already determined in other work. As to other possible TAG mixtures, in view of the results obtained by the reported studies, we expected an eutectic behavior for PPO:OPO and MC formation for PPO:POO and POO:OPO. The MC formation may be due to specific interactions between the fatty acid chains (saturated/unsaturated) of the TAG molecules and the two glycerol conformations, which will be discussed through this chapter. Thus, Figure 3.1 depicts the phase behavior of all these TAGs mixtures. The results obtained by other studies are shown in black, whereas the results we expected for the PPO:OPO, PPO:POO and POO:OPO mixtures are highlighted in red.

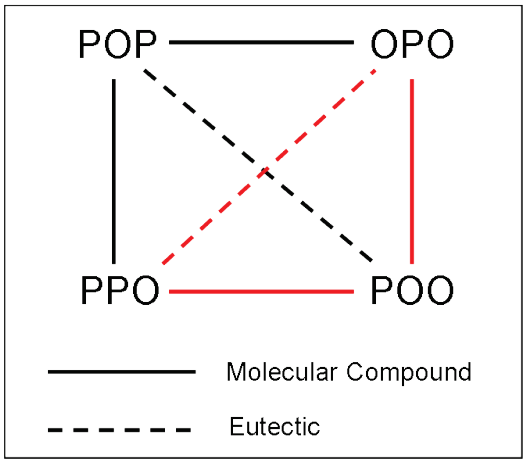

Figure 3.1. Expected diagram showing the phase behavior of TAGs containing palmitic and oleic fatty acids.

The proposed scheme, having a square shape, shows MC formation at the sides of the square and eutectic behavior in the diagonals.

Another aim of this study was to carefully analyze the crystallization behavior of some of these TAGs mixtures (more concretely, some POP:OPO compositions). Currently, most research on the binary mixing behavior of TAGs has been conducted on a thermodynamic equilibrium phase diagram. However, crystallization behavior is significant for applications: for example, fractionation of palm oil to produce high-melting, medium-melting, and low-melting fractions for multiple applications is influenced by crystallization properties of high-melting fractions such as PPP, POP, PPO, OOP, and OPO (Timms, 2005). This property is related to kinetic aspects of the binary mixing systems. However, few studies of kinetic properties of TAG mixtures have been conducted. Hence, we analyze the microstructures of spherulites of POP:OPO mixtures (with MC formation at the 50:50 composition), formed in neat liquid (Minato et al., 1997b) and solution (using n-dodecane as a solvent, Ikeda et al., 2010). Then, we wanted to examine how the microstructures of spherulites of the TAG mixtures are determined, when the MC crystals and POP or OPO component crystal can be formed competitively. For studying the microstructure of spherulites, synchrotron radiation microbeam X-ray diffraction (SR-μ-XRD) was used. Experimental details will be described further on (section 3.3).

This chapter is divided into two parts. In the first section, phase behavior of PPO:OPO (section 3.2.1), PPO:POO (section 3.2.2) and POO:OPO (section 3.2.3) mixtures are shown and discussed. The second part of this chapter is focused on the use of SR-μ-XRD to study the kinetic aspects of some POP:OPO binary mixtures.

3.2.

Binary phase behavior of 1,2-dipalmitoyl-3-oleoyl glycerol and 1,3-dioleoyl-2-palmitoyl glycerol (PPO-OPO), 1,2-dipalmitoyl-3-oleoyl glycerol and 1-palmitoyl-2,3-dioleoyl (PPO-POO), and 1-palmitoyl-2,3-dioleoyl and 1,3-dioleoyl-2-palmitoyl glycerol (POO-OPO)

As already described in Chapter 2, samples of PPO, OPO and POO (purity >99%) were purchased from Tsukishima Foods Industry (Tokyo, Japan) and used without further purification. Samples of asymmetric PPO and POO consisted of the racemic mixture of the enantiomeric compounds R-PPO and S-PPO, and R-POO and S-POO, respectively. Analyzing those racemic mixtures instead of enantiopure TAGs may arise some questions, as it will be discussed through this chapter.

In order to determine the phase behavior of PPO:OPO, PPO:OPO and POO:OPO systems, TAG mixtures (% molar) were prepared for every 10%, melted at 50ºC and mixed using a vortex.

Three independent DSC aluminium pans and three XRD capillaries were prepared for each mixture. All the DSC pans and XRD capillaries were rapidly cooled to -20ºC, and then tempered at different temperatures, in order to achieve the thermodynamic equilibration. Thus, samples were subjected to an incubation process to avoid the presence of metastable forms. For the stabilization process, we selected approximate temperatures close to the melting point, but at which all the sample was still in the solid state. Table 3.1 shows the incubation temperatures used. Samples were kept under these conditions for 17 months.

Table 3.1. Incubation temperatures of PPO:OPO, PPO:POO, POO:OPO mixtures and pure PPO, POO and OPO.

	Incubation temperature (ºC)
PPO	17
OPO	10
POO	10
PPO:OPO mixtures	10
PPO:POO mixtures	10 (from 10PPO:90POO to 50PPO:50POO) 17 (from 60PPO:40POO to 90PPO:10OPO)
POO:OPO mixtures	6

The transformation and melting behavior of the incubated mixtures were measured by DSC (Perkin-Elmer DSC Diamond, see details in Chapter 2) by heating the samples from 0ºC to 50ºC at 2ºC·min^{-1}. Shape factors ΔT_{end} (Corchinoux et al., 1989) were calculated by measuring the $|T_{onset}-T_{end}|$ of the melting signal of the TAG components, and used to obtain the characteristic temperatures of the complex phenomena of the phase behavior. Crystal forms were measured, as a function of temperature, by laboratory-scale powder XRD (PANalytical X'Pert Pro MPD powder diffractometer equipped with a Hybrid Monochromator and X'Celerator Detector, see Chapter 2).

Kinetic experiments were performed on the 50PPO:50POO and 50POO:50OPO binary mixtures in order to observe the molecular compounds occurrence in their metastable state. Moreover, they provided useful information to select the incubation temperatures of some of the binary mixtures. Isothermal processes and dynamic temperature variations were applied to the samples. As to the dynamic experiments, samples were cooled from 35ºC to -30ºC at different cooling rates and heated from -30ºC to 35ºC at 2ºC·min^{-1}. Thermal profiles were obtained by DSC (Perkin-Elmer DSC-7, see Chapter 2) and crystallization and transformation processes were identified by laboratory-scale powder XRD (PANalytical X'Pert Pro MPD). Synchrotron Radiation X-Ray Diffraction (SR-XRD) with Small-Angle X-Ray Diffraction (SAXD)

and Wide-Angle X-Ray Diffraction (WAXD) were used for some experimental condition. SR-XRD experiments were performed at BL-6A of the synchrotron radiation facility Photon Factory (PF) at the High-Energy Accelerator Research Organization (KEK) in Tsukuba (Japan). A double-focusing camera operated at a wavelength of 0.15 nm. The X-ray scattering data were simultaneously collected by a CCD camera for small-angle data, and a Pilatus detector for wide-angle data. The temperature program was controlled by a Mettler DSC-FP84 with FP99 software. A 2mm-thick sample was placed in an aluminium sample cell with Kapton film windows. SR-XRD spectra were acquired at 30s intervals.

Table 3.2 summarizes the melting temperatures and long and short spacing values of the three TAGs which configure the binary mixtures studied in this section.

Table 3.2. Melting temperatures (T_m, ºC), long spacing (LS, nm) and short spacing (SS, nm) values of PPO, OPO and POO. Melting temperatures were defined by the peak top temperatures.

PPO			
	T_m (ºC)	LS (nm)	SS (nm)
α	18.5	7.8	0.42
β’	35.2	6.5	0.46 0.44 0.42 0.40 0.38
OPO			
	T_m (ºC)	LS (nm)	SS (nm)
α*	nd	5.4 5.2	0.42
α	-18.3	5.3	0.42
β’	11.7	4.4	0.43 0.40
β_2	15.8	5.6	nd
β_1	21.9	6.7	0.48 0.38 0.37
POO			
	T_m (ºC)	LS (nm)	SS (nm)
sub-α	nd	5.8	0.42 0.38
α	-4.0	5.7	0.41
LC	nd	6.0	–
β'_2	nd	6.7	0.43 0.41
β'_1	20.3	6.7	0.47 0.46 0.45 0.43 0.41 0.40 0.39

nd. Not determined

α and β' forms were determined in PPO (Minato et al., 1997a), having long spacing values of 7.8 and 6.5nm, respectively. No β forms were present probably due to the asymmetric structure of PPO. As described in Chapter 2, more complicated polymorphism was observed in OPO, with five polymorphic forms already reported: α* (with long spacing values of 5.4 and 5.2 nm), α (5.3 nm), β' (4.4 nm), β_2 (5.6 nm) and β_1 (6.7 nm). Also five phases were detected in POO (Miura et al., 2001; present work), which are sub-α form (having a long spacing value of 5.8 nm), α form (5.7 nm), a liquid crystal (LC) phase (6.0 nm), and β'_2 and β'_1 forms (both with a long spacing of 6.7 nm).

3.2.1. Binary phase behavior of 1,2-dipalmitoyl-3-oleoyl glycerol and 1,3-dioleoyl-2-palmitoyl glycerol (PPO-OPO)

PPO was incubated at 17ºC, whereas OPO and PPO:OPO binary mixtures were kept at 10ºC. The stabilization of the samples was checked after 6, 11 and 17 months of incubation, and the eutectic behavior of the binary system was confirmed from the earliest experiments. Here we only present the data obtained after 17 months of incubation. Figure 3.2a plots the DSC thermograms obtained when PPO:OPO mixtures were heated from 0ºC to 50ºC at a rate of $2ºC \cdot min^{-1}$. In order to identify the polymorphic forms, laboratory-scale XRD experiments were carried out at 10ºC for all the compositions (Figure 3.2b).

Single endothermic DSC peaks, corresponding to the melting temperatures of β form of OPO and β' form of PPO, were observed for pure OPO and PPO. Two endothermic melting peaks were detected from the mixtures of 10PPO:90OPO to 90PPO:10OPO. The second peak increased in temperature when increasing the PPO concentration. On the contrary, the first melting peak, corresponding to the OPO fraction, appeared at a constant temperature from the mixture of 10PPO:90OPO to 90PPO:10OPO. With increasing the PPO concentration, the intensity of the second peak, corresponding to the PPO fraction, increased at the expense of the first melting DSC peak.

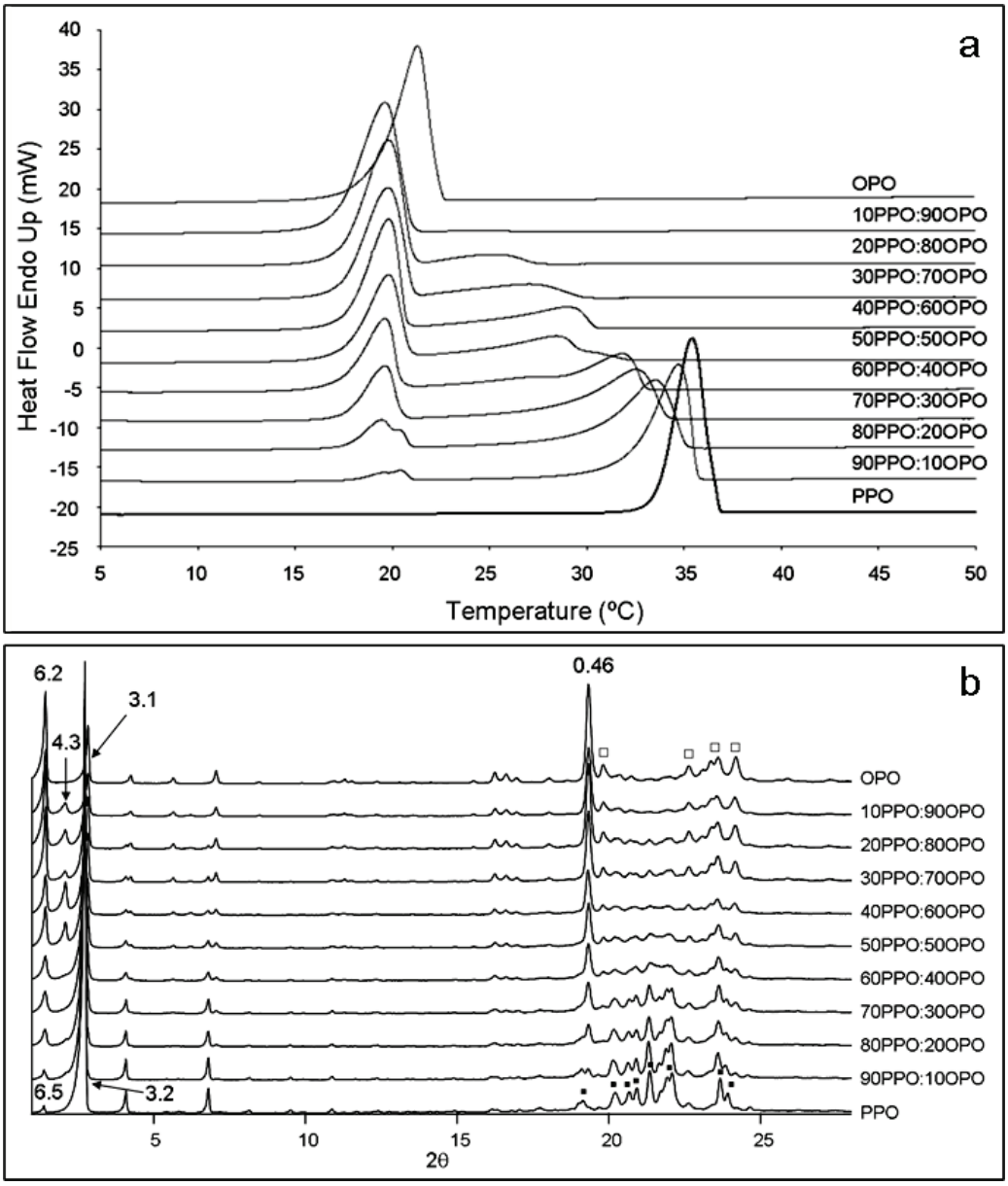

Figure 3.2. a) DSC heating thermopeaks of PPO:OPO mixtures. b) X-ray diffraction patterns of PPO:OPO mixtures at 10ºC. Data were obtained after an incubation period of 17 months.

The polymorphic forms were determined by XRD measurements (see Figure 3.2b). XRD diffraction peaks in the short and wide angle region identified single β form for pure OPO. Thus, a peak with a long spacing value of 6.2 nm was detected, whereas the typical β form peak at 0.46 nm appeared in the wide angle region. The d-spacing values of other β peaks (noted by □) were the following: 0.44 nm, 0.39 nm, 0.38 nm and 0.37 nm. The intensity of the XRD peak with short-spacing value of 0.46 progressively decreased as the PPO concentration increased. Therefore, typical XRD peaks corresponding to β' form of PPO became more important. The XRD pattern of pure

PPO exhibited triple chain length structure of β' form, having a long spacing value of 6.5 nm. The β' form XRD peaks which appeared at the wide angle region (noted by ▪) had short spacing values of 0.46 nm, 0.44 nm, 0.43 nm, 0.42 nm, 0.42 nm, 0.40 nm, 0.38 nm and 0.37 nm. Mixing the PPO and OPO samples produced no new peaks in the wide angle region of the XRD patterns at any of the PPO:OPO ratios, aside from those of the PPO and OPO fractions. However, mixtures from 10PPO:90OPO to 50PPO:50OPO (OPO rich region) exhibited a SAXD peak with a long spacing value of 4.3 nm. This XRD peak, noting a double chain length structure, may correspond to a metastable β' form of OPO (see Table 3.2). It should be noted that, during the 17 months of stabilization, when the state of samples was checked after 6 and 11 months of incubation, a decrease of the 4.3 nm intensity peak was observed for some PPO:OPO mixtures. Thus, this metastable β' form of OPO tends to disappear while samples reach their thermodynamic stabilization.

Figure 3.3 depicts the phase behavior of PPO:OPO mixtures constructed by onset and end temperatures encountered in the DSC experiments, taking into account the corresponding shape factor ΔT_{end}, as described above.

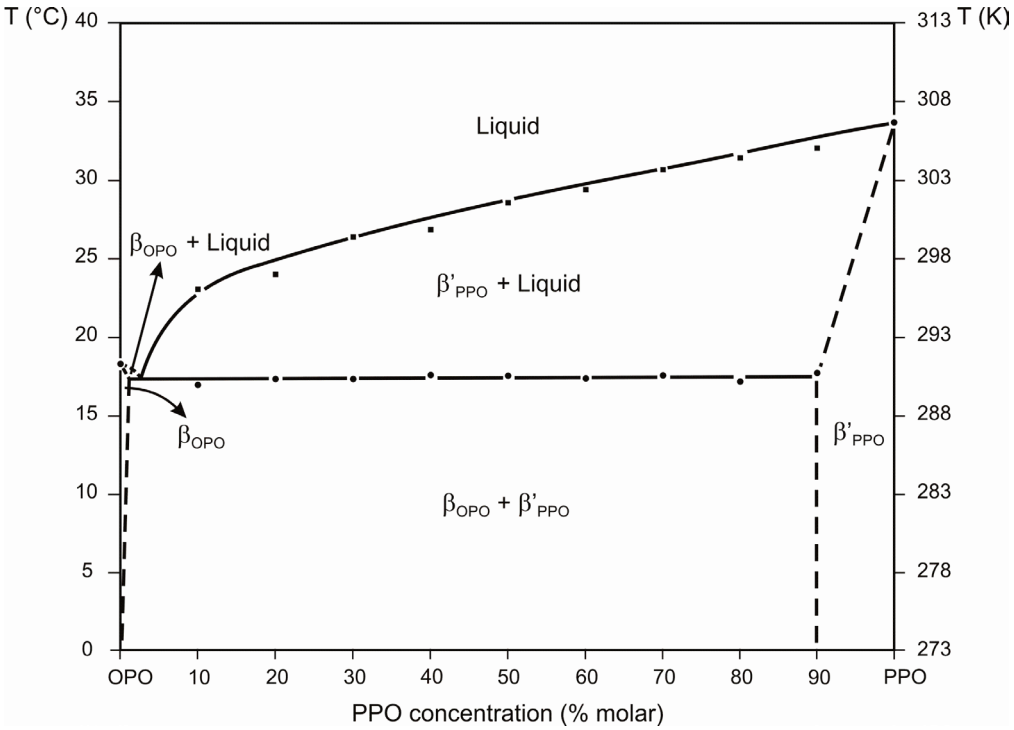

Figure 3.3. Phase behavior of PPO:OPO mixtures, based on DSC onset and end temperatures (T_{end}-ΔT_{end}).

It is clear that PPO and OPO are immiscible, revealing the eutectic mixing property. The exact position of the eutectic point could not be determined, as mixtures were prepared for every 10%. Nevertheless, it should be located at a composition between pure OPO and 10PPO:90OPO.

Hypothesis to justify why both compounds were immiscible will be given at the end of this chapter section, together with the discussion of all the binary systems studied in the present work.

3.2.2. Binary phase behavior of 1,2-dipalmitoyl-3-oleoyl glycerol and 1-palmitoyl-2,3-dioleoyl (PPO-POO)

Pure POO was incubated at 10ºC. Binary PPO:POO mixtures were kept, for 17 months, at different temperatures. The incubation of the POO rich region (from 10PPO:90POO to 40PPO:60POO) and the 50PPO:50POO composition was held at 10ºC, whereas the temperature at which the PPO rich region was kept (from 60PPO:40POO to 90PPO:10POO) was 17ºC. The state of some of the samples was checked after 6 and 11 months of incubation. However, initially some kinetic experiments were performed in order to observe the occurrence of metastable forms at the 50PPO:50POO composition and to check if a $MC_{PPO:POO}$ was formed.

3.2.2.1. Occurrence of PPO:POO molecular compound (non-incubated samples)

Figure 3.4 illustrates the occurrence of metastable forms in the 50PPO:50POO mixture when 1 hour isotherm at 10ºC and subsequent heating to 35ºC at a rate of $2ºC \cdot min^{-1}$ was applied to the sample.

A series of three endothermic DSC peaks appeared in the DSC heating profile (see Figure 3.4a). During the setting at 10ºC, a XRD peak with a long spacing value of 4.2 nm appeared in short angle region. Simultaneously, two peaks at 0.42 nm (broad) and 0.39 nm appeared in the wide angle region, corresponding to a β' form. The double chain length structure indicated by the spacing value of 4.4 nm should be due to a $MC_{PPO:POO}$ formation, as none of the polymorphic forms of pure PPO or POO had such

a long spacing value (see Table 3.2). Thus, the first occurring polymorph during the setting at 10ºC was $\beta'_{PPO:POO}$. Later on, triple chain length structure XRD peaks at 6.4 nm and 3.2 nm, accompanied by more defined β' peaks at 0.45 nm, 0.43 nm and 0.42 nm were observed in the short and wide angle region, respectively. These peaks should be due to β' forms of pure TAG components. After the setting, the sample was heated at 2ºC·min^{-1} and, at approximately 20ºC, the triple chain length peaks completely disappeared. At 35ºC, the double chain length diffraction peak also vanished. Thus, we may conclude that the first DSC endothermic peak with T_{onset} at 15.7ºC and peak top temperature at 17.8ºC may correspond to β'_{POO} melting, whereas the second melting peak with a peak top temperature at 22.9ºC should be due to the melting of $\beta'_{PPO:POO}$. A shoulder was identified at higher temperatures, which should correspond to the melting of β_{PPO}, although this phenomenon was not observed in the XRD patterns.

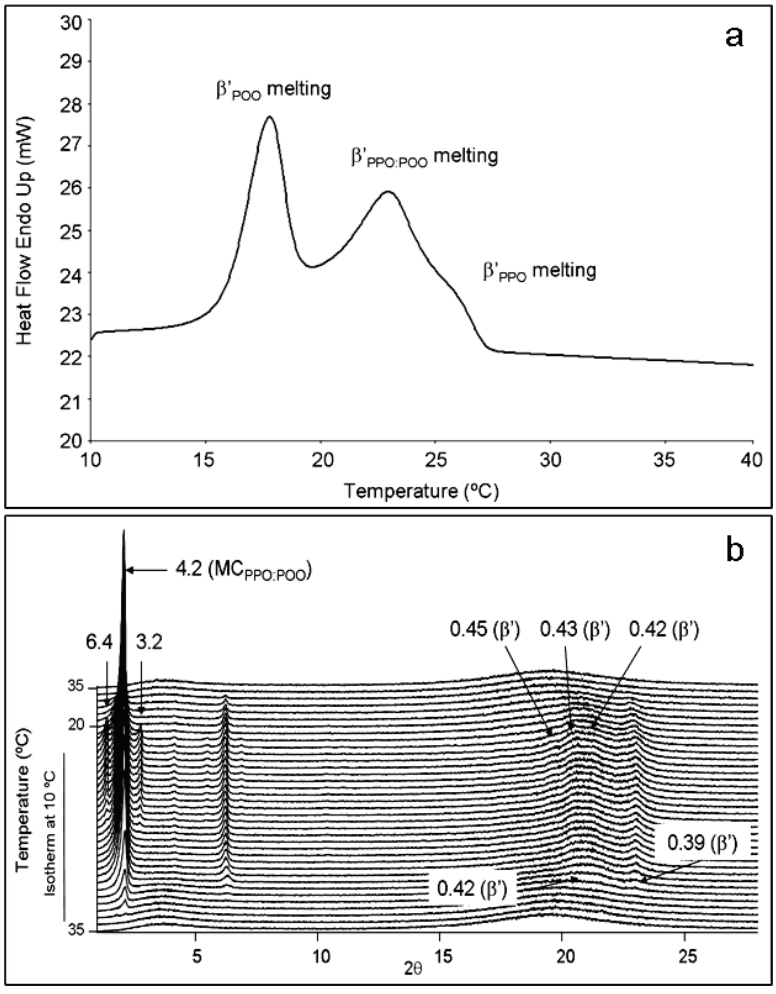

Figure 3.4. Polymorphic behavior of metastable forms of 50PPO:50POO mixture obtained when the sample was kept at 10ºC for 1 hour and heated at a rate of 2ºC·min^{-1}. a) DSC heating thermopeaks. b) XRD patterns taken during the isotherm and heating step.

A more complicated polymorphic behavior was observed when the 50PPO:50POO mixture was cooled and heated at 2ºC·min^{-1} (Figure 3.5).

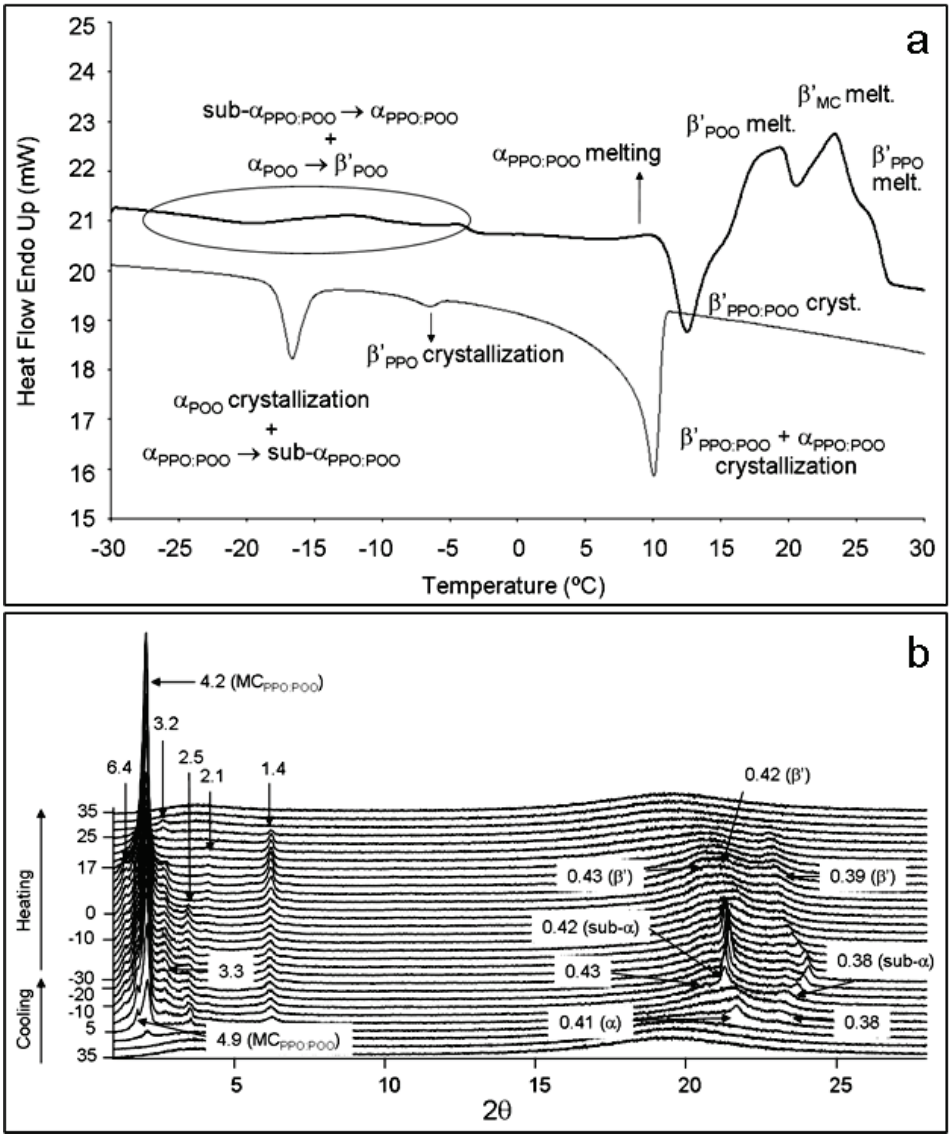

Figure 3.5. Polymorphic behavior of metastable forms of 50PPO:50POO mixture obtained during cooling and heating processes at a rate of 2ºC·min^{-1}. a) DSC heating thermopeaks. b) XRD patterns.

The XRD data revealed a first occurring XRD peak with a long spacing value of 4.2 nm. Soon after, another peak at 4.9 nm appeared in the short angle region. The wide angle region exhibited a typical α form XRD peak at 0.41nm accompanied by a broad peak at 0.38 nm. Therefore, the first crystallizing form should be $\beta'_{PPO:POO}$ and, immediately, $\alpha_{PPO:POO}$ was formed from the melt. The broad profile of the wide angle XRD region revealed the coexistence of both polymorphic forms. This complex

crystallization process appeared in the DSC thermogram (see Figure 3.5a) as a broad and exothermic peak with a T_{onset} of 10.8ºC. On further cooling, another DSC peak was observed at a T_{onset} of -4.9ºC, which should correspond to the β'_{PPO} crystallization, as triple chain structure XRD peaks at 6.4 nm and 3.3 nm and a new β' peak at 0.43 nm were observed in the XRD patterns. It should be noted that the wide angle region peaks became broader because of overlapping peaks. Another exothermic phenomenon appeared at a T_{onset} of -9.8ºC in the cooling DSC curve. The XRD data showed the presence of sharp sub-α peaks at 0.42 nm and 0.38 nm. Thus, $\alpha_{PPO:POO}$ may have transformed to sub-$\alpha_{PPO:POO}$. Furthermore, α_{POO} may have crystallized. As previously discussed, α_{POO} was crystallized from the melt at -11.3ºC (T_{onset}) when the sample was cooled at a rate of 2ºC·min^{-1}(see Figure 2.17 and Table 2.7 in Chapter 2). When the 50PPO:50POO mixture was heated from -30 to 35ºC at 2ºC·min^{-1}, the DSC curve exhibited a series of complex phenomena in the temperature range from -20 to -5ºC (see noted DSC peaks in Figure 3.5a). The corresponding XRD patterns revealed the disappearance of wide angle sub-α peaks (the peak at 0.38 nm vanished) so that sub-$\alpha_{PPO:POO}$ may have transformed to $\alpha_{PPO:POO}$, and broad β' peaks (0.43 nm, 0.42 nm and 0.39 nm) started appearing. Therefore, most probably, α_{POO} transformed to β'_{POO}. Further on, a melt-mediated transition was observed in the DSC heating thermogram, consisting of the $\alpha_{PPO:POO}$ melting (with T_{onset} at 7.2ºC) and subsequent $\beta'_{PPO:POO}$ crystallization (with T_{onset} at 10.6ºC). Simultaneously, the XRD patterns showed the disappearance of the short angle region peaks at 4.9 nm and 2.5 nm, corresponding to the $\alpha_{PPO:POO}$, and β' peaks at 0.43 nm, 0.42 nm and 0.38 nm became more defined. Finally, the DSC heating curve exhibited a complicated melting behavior consisting of, as already observed in Figure 3.4, the melting of β'_{POO}, $\beta'_{PPO:POO}$ and β'_{PPO}, with peak top temperatures of 19.4ºC, 23.4ºC and 26.1ºC, respectively. Simultaneously, the XRD patterns showed a first disappearance of triple chain length diffraction peaks at 6.4 nm and 3.3 nm. Later on, a new triple chain length at 3.2 nm could be observed in the short angle region, which vanished simultaneously to the double chain length peak at 4.2 nm. The reasons why the new peak at 3.2 nm appeared on heating at such high temperatures, just before its melting, are not clear. Probably, some additional crystallization occurred during the heating process. In any case, further studies would be needed in order to clarify the crystallization mechanisms in such a complicated system.

In order to simplify and understand more the polymorphic behavior of 50PPO:50POO, when the binary mixture was cooled and heated at 2ºC·min^{-1}, a shorter thermal treatment was performed. Thus, the sample was cooled from 35 to 0ºC (instead of -30ºC) and heated afterwards to 35ºC. The first exothermic DSC peak with T_{onset} at 10.8ºC was observed. When heating, the melt-mediated transformation, consisting of a melting process at 7.2ºC and subsequent crystallization at 10.6ºC, also occurred. However, on further heating, only one melting peak appeared. These results demonstrated that the melt-mediated transformation was related to first occurring polymorphic forms ($\alpha_{PPO:POO}$ and $\beta'_{PPO:POO}$). Hence, the melt mediated transition from $\alpha_{PPO:POO}$ to $\beta'_{PPO:POO}$ was confirmed.

As we expected, the PPO:POO binary mixtures were MC-forming and several polymorphic forms of the molecular compound (sub-$\alpha_{PPO:POO}$, $\alpha_{PPO:POO}$ and $\beta'_{PPO:POO}$) were determined by studying the metastable phases of the 50PPO:50POO composition. However, not all the sample constituted the PPO:POO molecular compound, as for both thermal treatments, there was a coexistence of MC and pure TAG components.

3.2.2.2. Phase behavior of incubated PPO:POO binary mixtures

Further DSC and XRD experiments were carried out after 17 months of stabilization of the binary mixtures. Figure 3.6 depicts the heating thermograms obtained at a rate of 2ºC·min^{-1} (Figure 3.6a) and the XRD analyses carried out at 5ºC (Figure 3.6b) of the PPO:POO mixtures at various concentration ratios.

Single endothermic peaks were observed for pure POO and PPO, corresponding to the melting of β' form of the two TAGs. The XRD data showed triple chain length peaks, with long spacing values of 6.5nm and 3.2nm. Typical β' form peaks were observed in the wide angle diffraction region. The short spacing values of β'_{POO} (noted by □ in Figure 3.6b) were the following: 0.47 nm, 0.45 nm, 0.44 nm, 0.43 nm, 0.42 nm, 0.41 nm, 0.40 nm, 0.39 nm, 0.39 nm and 0.38 nm. On the other hand, typical β'_{PPO} peaks appeared at 0.46 nm, 0.44 nm, 0.43 nm, 0.42 nm, 0.42 nm, 0.40 nm, 0.38 nm and 0.37 nm (noted by ▪) in the wide angle region. Two endothermic DSC peaks appeared in the mixtures of PPO:POO at 10:90 and 20:80 concentration ratios, although the first endothermic peak of the 20:80 composition was considerably broad, and the second one

was so weak. The DSC heating curves of the 30:70, 40:60 and 50:50 concentration ratios became highly complex, showing more than three endothermic DSC peaks in all cases. Concurrently, the XRD patterns corresponding to the POO rich region (from 10PPO:90POO to 40PPO:60POO) and the 50PPO:50POO mixture, exhibited broad diffraction peaks at the wide angle region, probably due to the overlapping of several polymorphic forms. Furthermore, from the 20PPO:80POO to the 50PPO:50POO composition, a double chain length diffraction peak appeared in the short angle region, having a spacing value of 4.2 nm.

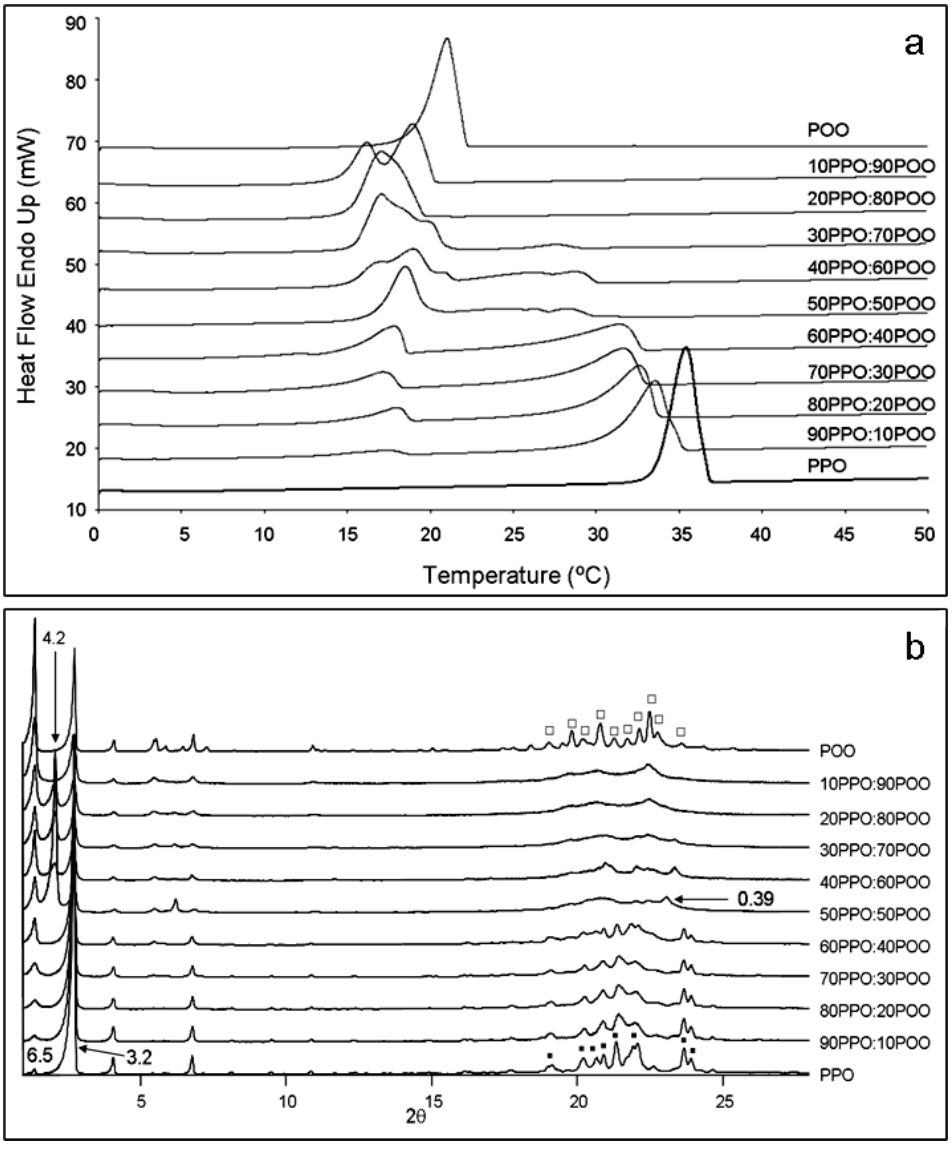

Figure 3.6. a) DSC heating thermopeaks of PPO:POO mixtures. b) X-ray diffraction patterns of PPO:POO mixtures at 5ºC. Data were obtained after an incubation period of 17 months.

Nevertheless, in the PPO rich region, two well defined melting DSC peaks were observed, where the T_{onset} of the first melting peak was maintained and the T_{end} of the second peak increased while increasing the PPO concentration. The corresponding XRD patterns exhibited clear β' diffraction peaks, and no double chain length peak at 4.2 nm was present in the whole PPO rich region.

Hence, laboratory-scale XRD was carried out as a function of temperature for some binary mixtures, in order to describe the phenomena observed in the DSC thermograms. Figure 3.7 illustrates the laboratory scale XRD patterns carried out when heating the 10:90, 20:80, 40:60 and 90:10 concentration ratios from 5ºC to 50ºC at a rate of $2ºC \cdot min^{-1}$.

The melting behavior of the 10PPO:90POO mixture is shown in Figure 3.7a. As observed, only a triple chain length structure was present at 5ºC, with long spacing values of 6.4 nm and 3.2 nm. Wide angle diffraction peaks revealed the occurrence of β' form (0.45 nm, 0.43 nm and 0.40 nm). However, the wideness of the diffraction peaks evidenced the presence of more than one β' form. This fact was confirmed upon heating, as at around 16ºC, sharper and more defined β' peaks were observed due to the melting of a β' form (β'_{POO} melted, and only β'_{PPO} was present). The XRD pattern taken at 20ºC showed no diffraction peaks, so that the remaining β' form (β'_{PPO}) had already melted.

A different behavior was observed for the 20PPO:80POO binary mixture (Figure 3.7b). At 5ºC, triple (6.4 nm and 3.2 nm) and double (4.3 nm) chain length structures were coexisting. Triple chain length structure peaks should correspond to β' forms of pure TAG components, whereas the peak at 4.2 nm may be referred to $\beta'_{PPO:POO}$ molecular compound. When heating, a slight change could be appreciated in the wide angle region: β' peaks at 0.47 nm and 0.40 nm became more defined, meaning the melting of some β' form, which should be β'_{POO}. Finally, at 19ºC, the remaining triple (β'_{PPO}) and double (β'_{MC}) chain length structure peaks vanished.

A diffraction peak at 4.2 nm, corresponding to $\beta'_{PPO:POO}$ was also present in the 40PPO:60POO composition (Figure 3.7c). Although the corresponding DSC heating curve (see Figure 3.6a) showed a highly complex thermal profile, few phenomena could be interpreted through the XRD data. At 18ºC, the β' form diffraction peaks, observable in the wide angle region, became more defined, possibly due to the melting of β'_{POO}. At 20ºC, the double chain length peak at 4.2 nm vanished ($\beta'_{PPO:POO}$ melting). Finally, at

28ºC, β'_{PPO} melted, as triple chain length peaks at 6.4 nm and 3.2 nm and the corresponding β' peaks (at 0.42 nm, 0.40 nm and 0.38 nm) disappeared.

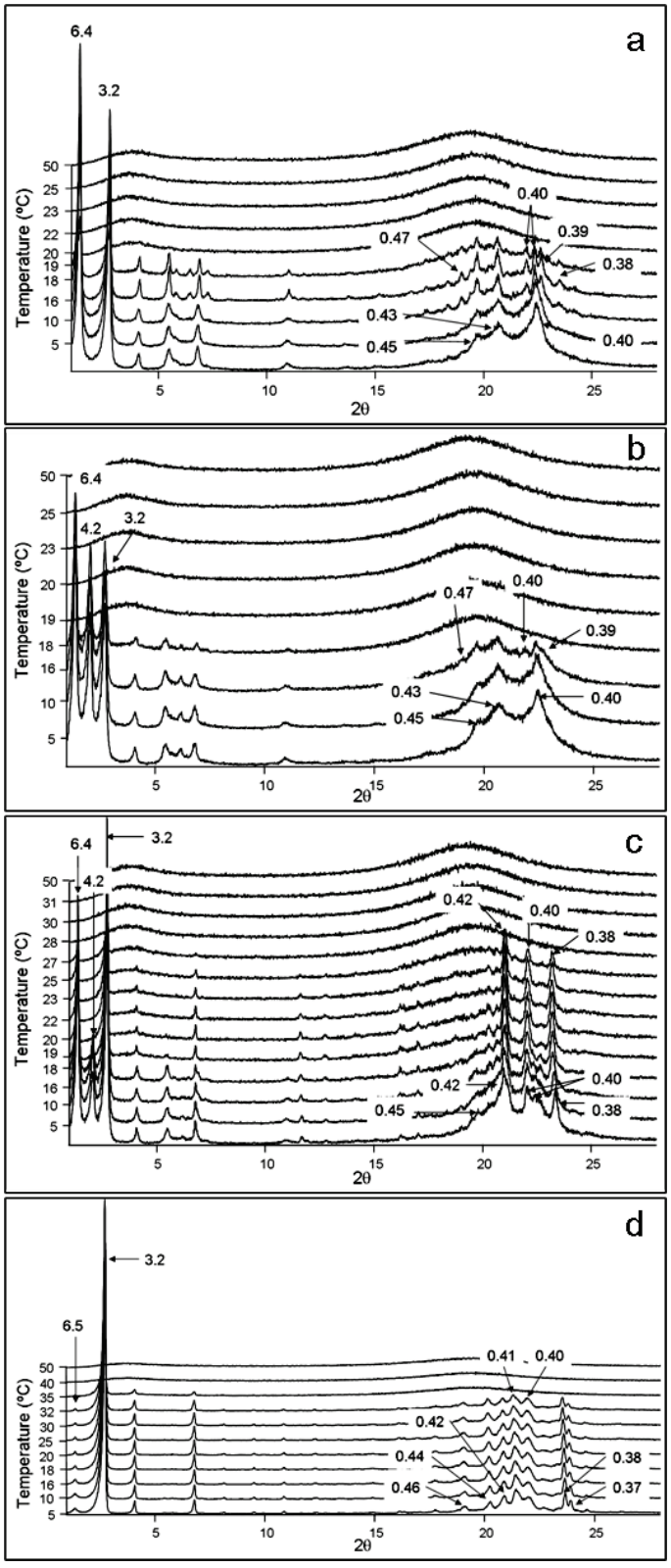

Figure 3.7. Laboratory scale XRD when incubated binary mixtures were heated at 2ºC·min^{-1} a) 10PPO:90POO. b) 20PPO:80POO. c) 40PPO:60POO. d) 90PPO:10POO.

No $\beta'_{PPO:POO}$ formation was observed in the 90PPO:10POO composition (Figure 3.7d). Instead, only β' forms having triple chain length structure were present. Upon heating, wide angle diffraction peaks became slightly sharper at around 18ºC (β'_{POO} melting) and all diffraction peaks disappeared at 40ºC (β'_{PPO} melting).

From all these results, one may notice that the behavior of the POO rich region was different to that of the PPO rich region. An equilibrium between $MC_{PPO:POO}$ and pure TAG components was not observed at all the concentration ratios of the PPO:POO mixtures. The double chain length diffraction peak at 4.2 nm corresponding to the $MC_{PPO:POO}$ (β' form) was only detected in the binary mixtures from 20PPO:80POO to 50PPO:50POO, being more intense at the last mentioned ratio. As to the DSC heating profiles, a more complicated melting behavior was observed in the POO rich region (due to the presence of metastable phases), whereas the thermograms of the PPO rich region only consisted of two endothermic peaks. In other words, the mixing behavior of the POO rich region seemed to be MC-forming, while the PPO rich region followed an immiscible eutectic pattern. At this point, one question may arise: what is the reason of such a different behavior in the two compositional regions? Samples were kept, for 17 months, at different incubation temperatures: mixtures from 10PPO:90POO to 50PPO:50POO were incubated at 10ºC, whereas concentration ratios from 60PPO:40POO to 90PPO:10POO were incubated at 17ºC. Therefore, we incubated new samples of pure PPO and binary mixtures from 60PPO:40POO to 90PPO:10POO at 10ºC for three months, and the same DSC heating curves were obtained, meaning that the incubation temperature was not the responsible for the different behavior observed. Moreover, as some XRD experiments were carried out after 6 and 11 months of incubation, we could compare the data obtained with that of 17 months of incubation. Then, we realized that the triple chain length diffraction peaks at 6.5 nm and 3.2 nm (corresponding to β'_{POO} and β'_{PPO}) were increasing with the time at the expense of the double chain length diffraction peak at 4.2 nm (corresponding to $\beta'_{PPO:POO}$). Thus, we may conclude that the MC formed ($\beta'_{PPO:POO}$) was metastable and tended to disappear, being separated into two β' TAG components during the thermodynamic stabilization of the samples. In other words, initially, MC was formed, but due to its metastable nature, it decomposed into two β' TAG components, revealing the eutectic mixing property. The melting point of $\beta'_{PPO:POO}$ was approximately 19ºC.

Figure 3.8 illustrates the phase domains of PPO:POO mixtures.

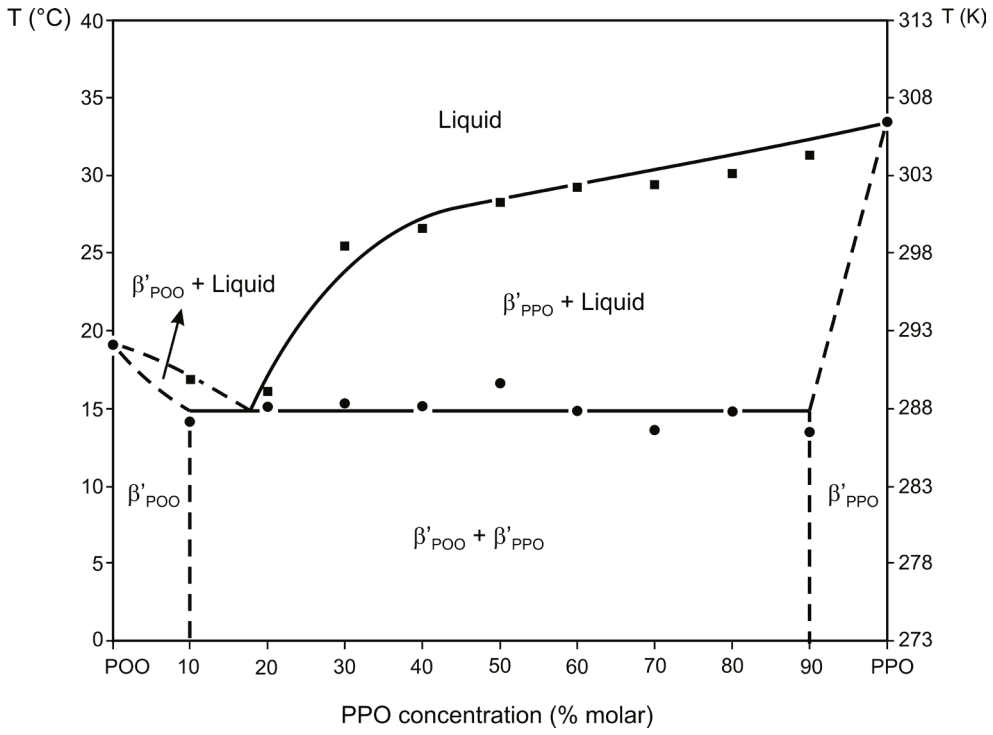

Figure 3.8. Phase behavior of PPO:POO mixtures, based on DSC onset and end temperatures (T_{end}-ΔT_{end}).

The eutectic point should be located between the 10PPO:90POO and 20PPO:80POO compositions.

3.2.3. Binary phase behavior of 1-palmitoyl-2,3-dioleoyl glycerol and 1,3-dioleoyl-2-palmitoyl glycerol (POO-OPO)

All samples, including pure TAG components and binary mixtures, were kept at 10ºC for 17 months, as shown in Table 3.1. Some binary mixtures were analyzed after 6 and 11 months of incubation to follow the thermodynamic stabilization of the samples.

3.2.3.1. Occurrence of POO:OPO molecular compound (non-incubated samples)

In order to check the molecular compound formation at the ratio of 50POO:50OPO, different thermal treatments, consisting of applying isothermal processes or changing the cooling rates (15, 2 and 0.5ºC·min^{-1}), were conducted. Thus, the polymorphic occurrence of metastable forms of the 50POO:50POO binary mixture was analyzed.

Figure 3.9 depicts the polymorphic behavior of 50POO:50OPO, when the sample was set at 0ºC for 1 hour and, afterwards, heated to 35ºC at a rate of 2ºC·min^{-1}.

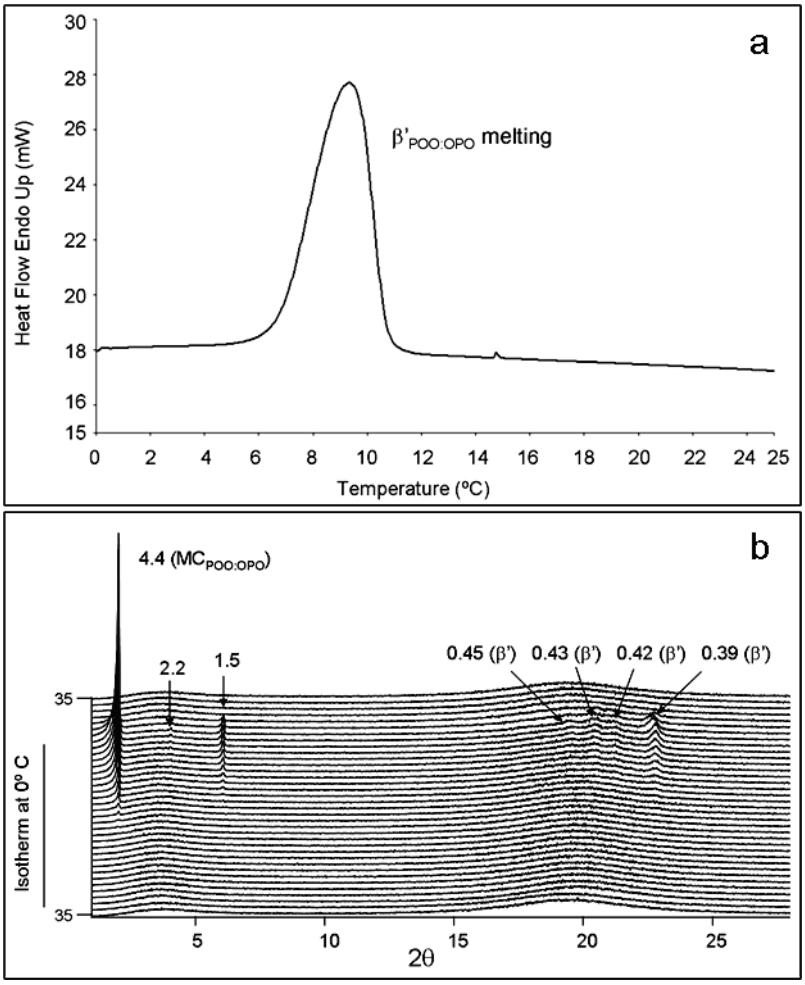

Figure 3.9. Polymorphic behavior of metastable forms of 50POO:50OPO mixture obtained when the sample was kept at 0ºC for 1 hour and heated at a rate of 2ºC·min^{-1}. a) DSC heating thermopeaks. b) XRD patterns taken during the isotherm and heating step.

The XRD data showed the occurrence of a double chain length structure, having a long spacing value of 4.4 nm (see Figure 3.9b). Simultaneously, the wide angle region revealed the typical diffraction peaks corresponding to a β' form (at 0.45 nm, 0.43 nm,

0.42 nm and 0.39 nm). When heating at 2ºC·min^{-1}, a broad DSC endothermic peak, with T_{onset} at 6.7ºC and peak top temperature at 9.3ºC, was observed in the DSC heating curve. One may conclude that, when the 50POO:50OPO binary mixture was kept for 1 hour at 0ºC, a $\beta'_{POO:OPO}$ molecular compound was formed.

Dynamic experiments by changing the rates of cooling were also carried out. Figure 3.10 depicts the polymorphic crystallization and transformation when 50POO:50OPO was rapidly cooled at 15ºC·min^{-1} and heated at 2ºC·min^{-1}.

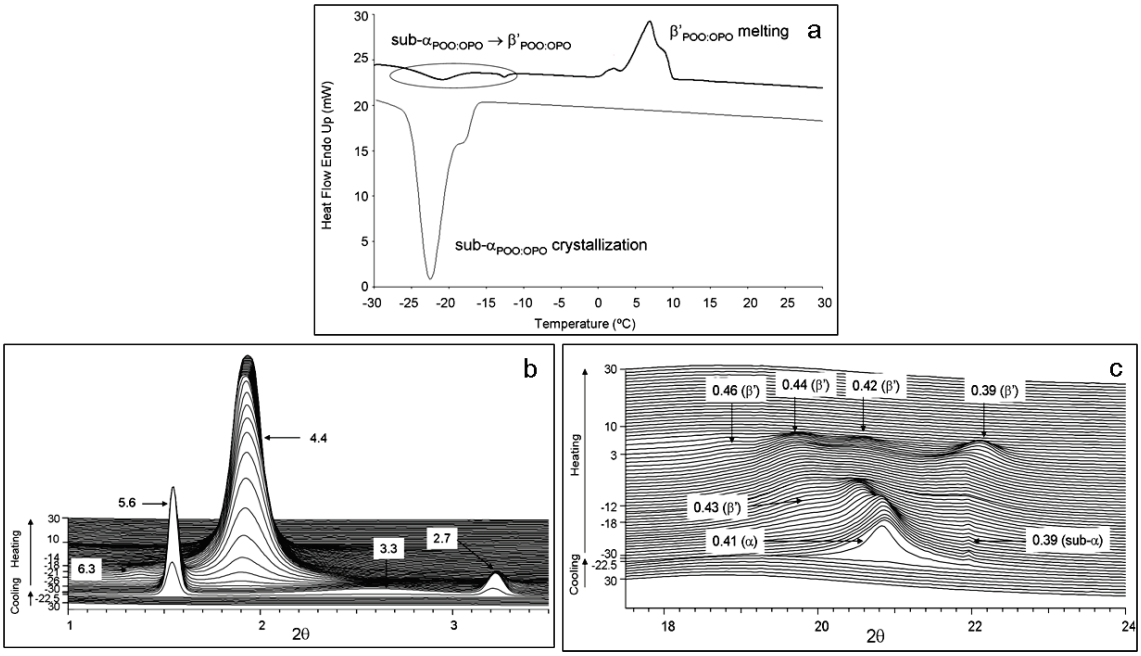

Figure 3.10. Polymorphic behavior of metastable forms of 50PPO:50POO mixture when cooled at 15ºC·min^{-1} and heated at 2ºC·min^{-1}. a) DSC cooling and heating curves. b) SR-SAXD pattern. c) SR-WAXD pattern.

To explain the highly complex thermal profile observed in the DSC thermograms (Figure 3.10a), SR-XRD experiments were carried out (see Figure 3.10b). A double exothermic DSC peak, with T_{onset} at -16.3 ºC, appeared in the DSC cooling curve. Two SAXD peaks at 5.6 nm and 2.7 nm and an intense WAXD peak at 0.41 nm accompanied by a small peak at 0.39 nm were observed in the 50POO:50OPO SR-XRD patterns, which should be due to the occurrence of a sub-α form of the POO:OPO molecular compound (sub-$\alpha_{POO:OPO}$). Also a broad SAXD peak was observed at 3.3 nm, probably due to some disordered form which took place for a short time. When the sample was heated from -30ºC to 35ºC, a complex set of thermal phenomena appeared

in the DSC heating step from -30ºC to -10ºC. According to the SR-XRD data, a double chain SAXD peak at 4.4 nm appeared at around -26ºC, at the expense of the peaks with long spacing values of 5.6 nm and 2.7 nm, which vanished at approximately -18ºC. Concurrently, a β' WAXD peak at 0.43 nm appeared. Thus, the set of thermal phenomena from -30ºC to -10ºC was caused by the sub-$\alpha_{POO:OPO} \rightarrow \beta'_{POO:OPO}$ transformation. No α_{POO} formation was detected between the occurrence of sub-$\alpha_{POO:OPO}$ and $\beta'_{POO:OPO}$. The SAXD pattern also showed the presence of a SAXD peak at 6.3 nm, which could be firstly observed at -21ºC and disappeared at -14ºC. This peak probably may be caused by an intermediate polymorphic form which could not be identified. At -14ºC, the only SAXD peak observable was the one with a spacing value of 4.4 nm ($\beta'_{POO:OPO}$). On further heating, the WAXD pattern clearly revealed well-defined β' form peaks at 0.46 nm, 0.44 nm, 0.42 nm and 0.39 nm. Finally, at a T_{onset} of 0.2ºC, the DSC heating curve showed a set of three endothermic peaks, with peak top temperatures of 1.9ºC, 6.9ºC and 9.0ºC. However, the SR-XRD data only disclosed the $\beta'_{POO:OPO}$ melting process.

Further kinetic experiments were carried out by changing the rate of cooling, and keeping the same rate of heating (2ºC·min^{-1}). Figure 3.11 illustrates the polymorphic behavior of 50POO:50OPO when it was cooled at intermediate (2ºC·min^{-1}) and low (0.5ºC·min^{-1}) cooling rates and heated at 2ºC·min^{-1}.

The laboratory-scale XRD patterns of the two thermal treatments (Figure 3.11(a)B and Figure 3.11(b)B) were identical, whereas the two DSC thermograms (Figure 3.11(a)A and Figure 3.11(b)A) became slightly different.

When 50POO:50OPO was cooled at 2ºC·min^{-1} (Figure 3.11(a)), a complex and broad exothermic peak with T_{onset} at -9.4ºC, caused by the $\beta'_{POO:OPO}$ crystallization, was observed in the DSC cooling curve. The XRD patterns showed the occurrence of a double chain length peak at 4.4 nm and typical β' peaks at 0.45 nm, 0.43 nm, 0.42 nm and 0.39 nm, in the short and wide angle regions, respectively. When heating, a small exothermic DSC peak appeared at around -14ºC, but no changes were detected in the XRD patterns. Finally, a set of three endothermic DSC peaks, with T_{onset} at 0.3ºC and T_{end} at 9.8ºC, was observed. The XRD data only showed the melting of $\beta'_{POO:OPO}$.

When the cooling rate applied to the 50POO:50OPO binary mixture was lower (0.5ºC·min^{-1}, Figure 3.11(b)), a single exothermic DSC peak with T_{onset} at -5.4ºC appeared in the cooling curve. According to the XRD data, this peak should be due to

the $\beta'_{POO:OPO}$ crystallization, as a SAXD peak at 4.4 nm and WAXD peaks at 0.45 nm, 0.43 nm, 0.42 nm and 0.39 nm were identified. When heating, only one broad endothermic DSC peak appeared, with a T_{onset} of 3.4ºC and a T_{end} of 10.0ºC, which corresponded to the $\beta'_{POO:OPO}$ melting.

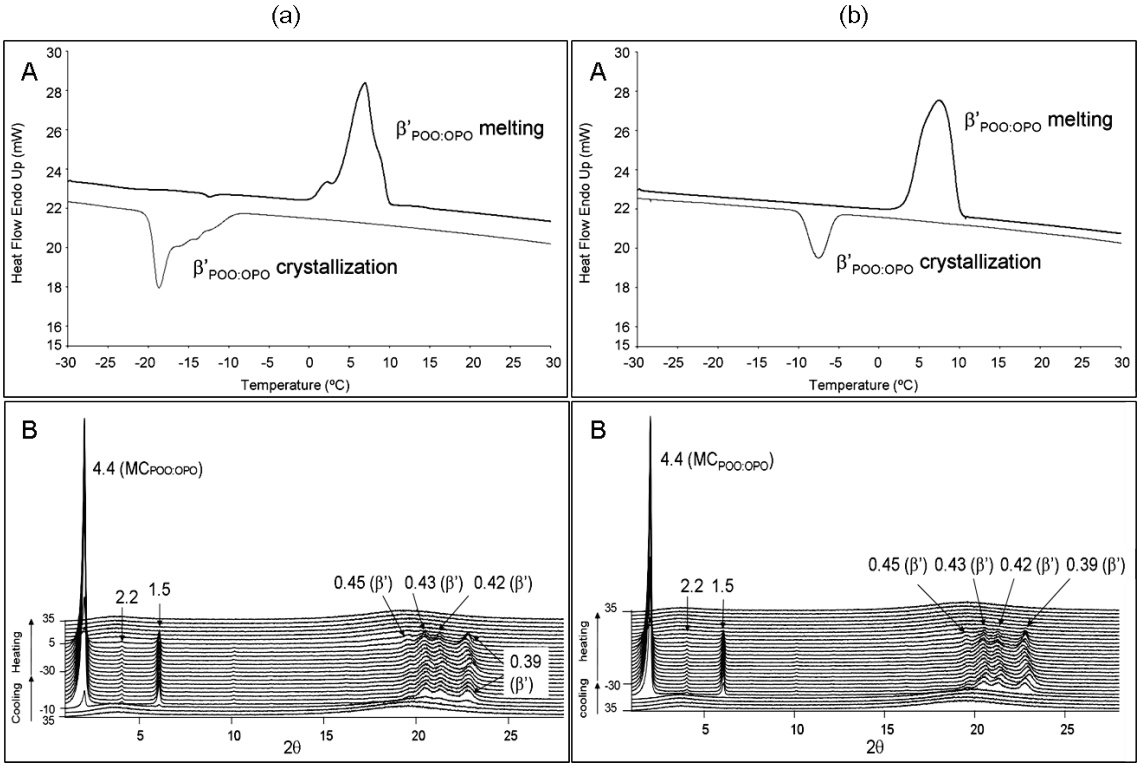

Figure 3.11. Polymorphic behavior of metastable forms of 50PPO:50POO. (a) Cooling at 2ºC·min^{-1} and heated at 2ºC·min^{-1}. A. DSC thermogram. B. XRD patterns. (b) Cooling at 0.5ºC·min^{-1} and heated at 2ºC·min^{-1}. A. DSC thermogram. B. XRD patterns.

The formation of a POO:OPO molecular compound at the ratio 50:50 was confirmed and two polymorphic forms (sub-$\alpha_{POO:OPO}$ and $\beta'_{POO:OPO}$) were detected by applying different thermal treatments to the 50POO:50OPO binary mixture. Differently to the PPO:POO case, all the sample constituted the POO:OPO molecular compound, and there was no coexistence with the pure TAG components (POO and OPO).

3.2.3.2. Phase behavior of incubated POO:OPO binary mixtures

To analyze the phase behavior in the most stable state of the POO:OPO mixtures, DSC and laboratory-scale experiments were performed after 17 months of incubation of the samples. Figure 3.12 illustrates the DSC and XRD data obtained at the different concentration ratios. DSC thermograms were registered while heating from 0ºC to 50ºC at a rate of 2ºC·min^{-1}, whereas XRD experiments were performed at 5ºC.

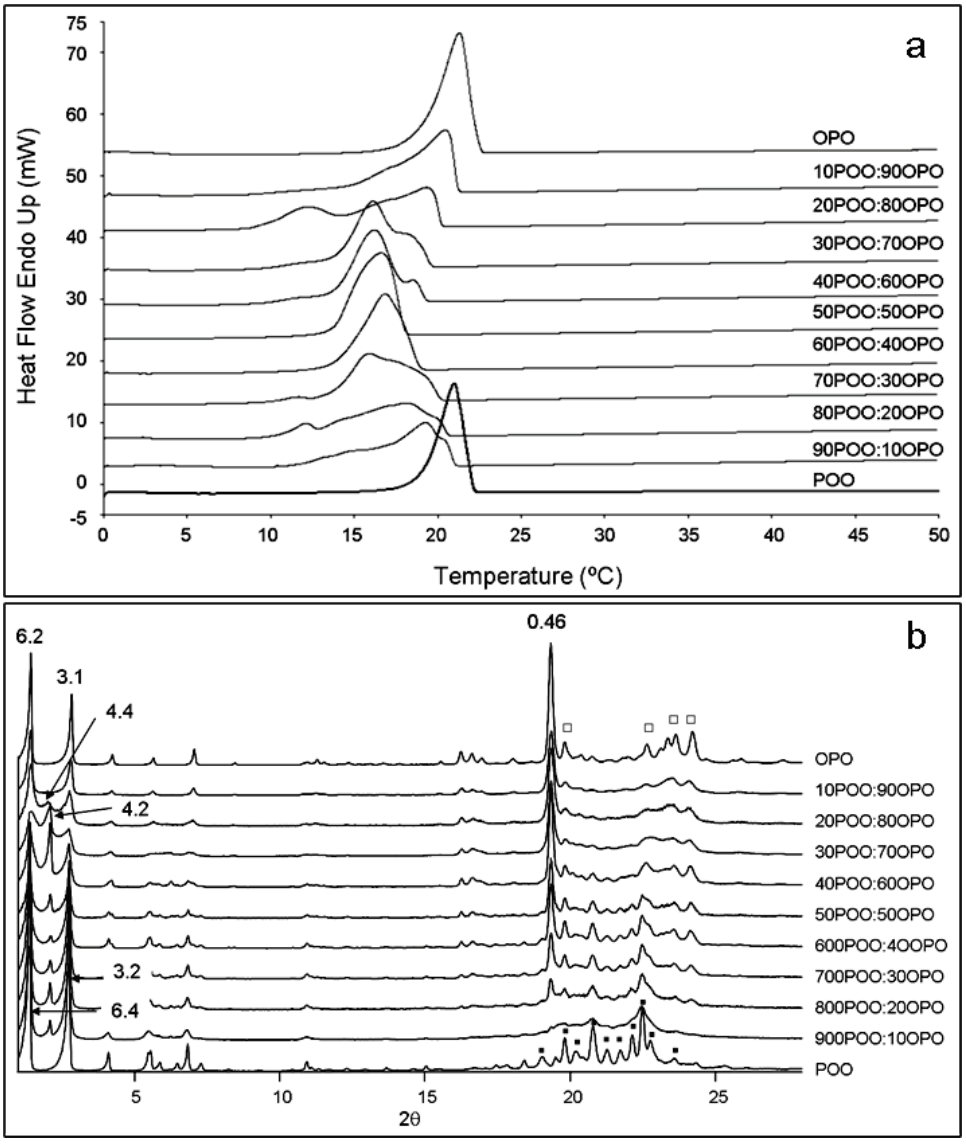

Figure 3.12. a) DSC heating thermopeaks of POO:OPO mixtures. b) X-ray diffraction patterns of POO:OPO mixtures at 5ºC. Data were obtained after an incubation period of 17 months.

The DSC heating curves of the two TAG components only showed the melting peak of their most stable form. The corresponding XRD patterns showed clear patterns of β_{OPO} and β'_{POO}. β_{OPO}, having a triple chain length structure (6.2 nm and 3.1 nm) was identified by the typical β form intense peak at 0.46 nm and other wide angle diffraction peaks at 0.44 nm, 0.39 nm, 0.38 nm and 0.37 nm (noted by □ in Figure 3.12b). The XRD pattern of incubated POO exhibited triple chain length peaks, with long spacing values of 6.4 nm and 3.2 nm, and wide angle diffraction peaks at 0.47 nm, 0.45 nm, 0.44 nm, 0.43 nm, 0.42 nm, 0.41 nm, 0.40 nm, two peaks at 0.39 nm, and 0.38 nm (noted by ▪ in Figure 3.12b).

At least two endothermic peaks were observed in the DSC heating curves of the mixtures from the 10:90 to the 40:60 concentration ratios. In some cases, another endothermic peak appeared around 9ºC (T_{onset}), becoming stronger in the 20:80 composition. A single broad endothermic peak with a T_{onset} around 14ºC appeared at the 50:50 and 60:40 compositions, and more than two melting peaks were observed in the DSC thermograms from the 70:30 to the 90:10 concentration ratios. Similarly, to the 20:80 composition case, one may notice the presence of an endothermic peak at a T_{onset} around 9ºC in the 70:30 and 80:20 concentration ratios. XRD patterns revealed the presence of triple chain length structure at all the concentration ratios. Moreover, double chain length peaks were observed in the short angle regions from the 20:80 to the 90:10 concentration ratios. In almost all cases, the corresponding long spacing value was 4.2 nm, except for the 20:80 binary mixture, where a spacing value of 4.4 nm was detected. The intensity of the β diffraction peak at 0.46 nm decreased as the POO composition increased.

To try to understand the complicated phase behavior of the incubated POO:OPO binary mixtures, laboratory-scale XRD experiments were performed as a function of the temperature for some of the incubated compositions. Figure 3.13 depicts the XRD patterns obtained by heating the 20POO:80OPO, 50POO:50OPO and 80POO:20OPO binary mixtures from 5ºC to 50ºC at $2ºC \cdot min^{-1}$.

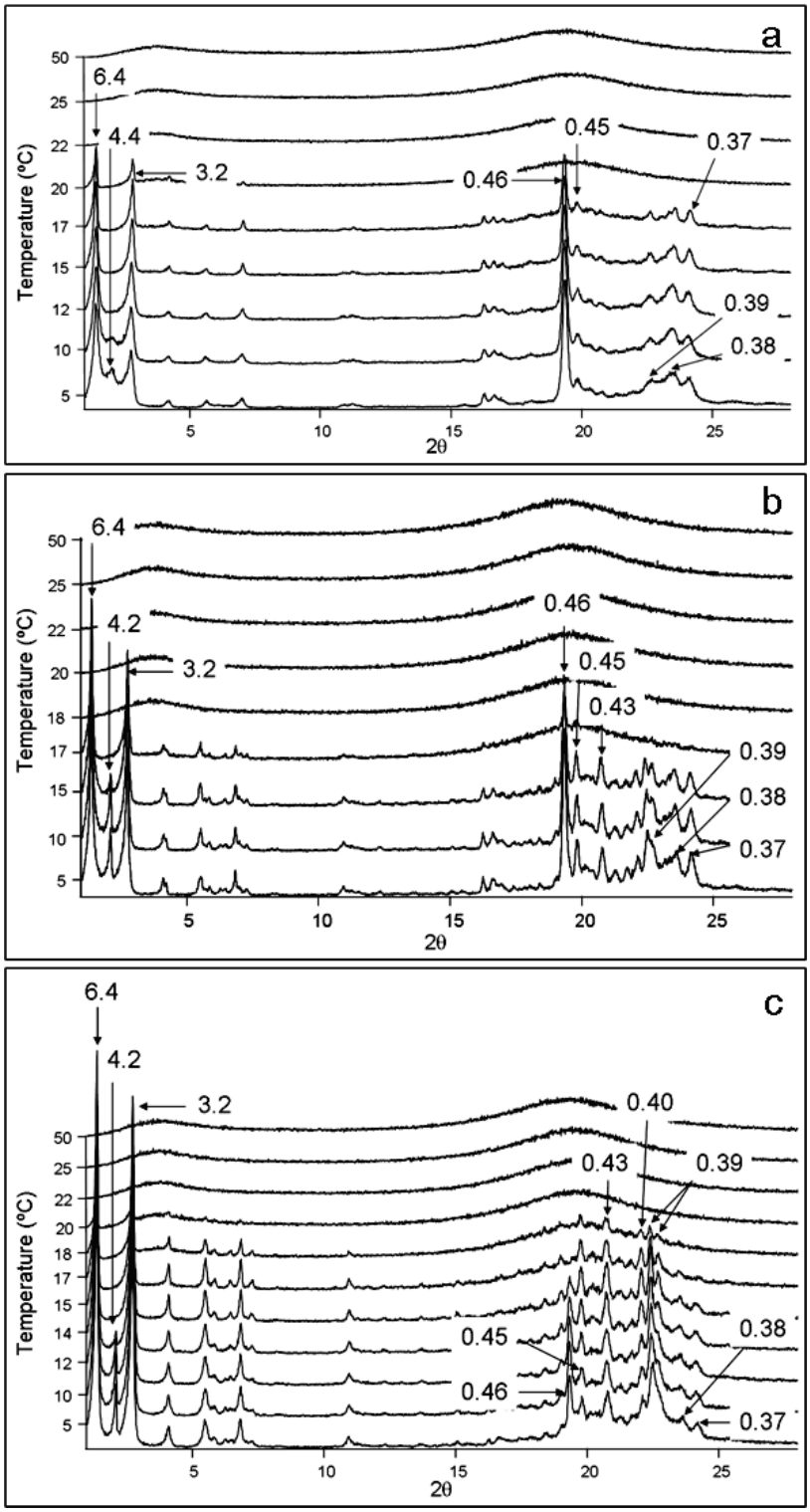

Figure 3.13. Laboratory scale XRD when incubated binary mixtures were heated at 2ºC·min^{-1} a) 20POO:80OPO. b) 50POO:50OPO. c) 80POO:20OPO.

The XRD diffraction patterns of the 20POO:80POO binary mixture, obtained when heated at 2ºC·min^{-1}, are shown in Figure 3.13a. Both triple (6.4 nm and 3.2 nm) and double (4.4 nm) chain length structures were present at 5ºC. The wide angle region

showed a coexistence of β and β' forms. β form was clearly noticeable by the presence of the typical sharp peak at 0.46 nm, whereas broad peaks at 0.39 nm, 0.38nm and 0.37 nm revealed the presence of coexisting β' form. Upon heating, at 12ºC, the double chain length structure vanished, and the wide angle peaks became more defined. The long spacing value of this form corresponds to that of $\beta'_{POO:OPO}$ (molecular compound), as already explained in the section 3.2.3.1 of the present chapter. Thus, we may conclude that the first melting peak which appears in the DSC thermogram of the 20:80 composition should be due to the melting of $\beta'_{POO:OPO}$. Moreover, we should also consider that this peak was inexistent or, at least, weaker at the other concentration ratios. On further heating, at 17ºC, XRD peaks corresponding to β form were more defined and, finally at 22ºC, no diffraction peaks were present.

As to the 50POO:50OPO binary mixture, we expected to only observe a double chain length structure, corresponding to the POO:OPO molecular compound. Nevertheless, triple chain length structure XRD peaks at 6.4 nm and 3.2 nm were also detected, being more intense than that of the double chain length structure (Figure 3.13b). The kinetic experiments performed to study the occurrence of POO:OPO molecular compound demonstrated its formation but, apparently, the thermodynamic stabilization for 17 months caused, similarly to the PPO:POO case, the decomposition of the molecular compound into the two TAG components. Only one endothermic peak appeared in the corresponding DSC heating curve (see Figure 3.12a), although we should consider the wideness of the mentioned peak. The long spacing value corresponding to the double chain length structure was 4.2 nm, which became different to that of the 20:80 composition. Not surprisingly, when heating, some of the wide angle XRD peaks became more defined. At 17ºC, the double chain length peak disappeared and, simultaneously, the intensity of the XRD peak at 0.46 nm (corresponding to β form) had decreased its intensity in a 63%. In more detail, at 15ºC, the intensity of the triple chain length peaks was maintained with respect to that of 5ºC, whereas the intensity of the XRD peak at 4.2 nm had decreased together with the intensity of the peak at 0.46 nm. Thus, we may conclude that the polymorphic form of the POO:OPO molecular compound, which totally disappeared at around 17ºC was β form. Hence, the $\beta'_{PPO:POO}$ observed in the 20:80 concentration ratio became a metastable form of the molecular compound, being the $\beta_{POO:OPO}$ the most stable one.

Finally, at 18ºC, the triple chain XRD peaks disappeared, together with the peak at 0.46 nm (β_{OPO} melting).

A similar behavior was observed in the 80:20 binary mixture (Figure 3.13c). At 5ºC, the XRD pattern showed the coexistence of triple (6.4 nm and 3.2 nm) and double (4.2 nm) chain length structures. However, the wide angle region exhibited a higher predominance of β' form (corresponding to β'_{POO}) with respect to the β form. At 15ºC, the double chain length structure totally vanished, due to the $\beta_{POO:OPO}$ melting. The β form of the POO:OPO molecular compound was again confirmed by the fact that the intensity of the XRD peaks at 4.2 nm and 0.46 nm simultaneously decreased, whereas the intensities of the peaks at 6.4 nm and 3.2 nm were maintained. On further heating, at 17ºC, the typical β form peak at 0.46 nm totally disappeared, due to the β_{OPO} melting. Finally, β'_{POO} melted at around 22ºC.

After analyzing these results, one may conclude that a POO:OPO molecular compound was definitely formed, and several polymorphic forms were detected. Studying the occurrence of this molecular compound by changing the rates of cooling permitted identifying two different polymorphic forms: sub-$\alpha_{POO:OPO}$, which was obtained by applying rapid rates of cooling (15ºC·min^{-1}) and $\beta'_{POO:OPO}$, which crystallized at intermediate (2ºC·min^{-1}) and low (0.5ºC·min^{-1}) cooling rates, but also under isothermal conditions (at 0ºC for 1 hour). Moreover, thermodynamic stabilization for 17 months at 10ºC made the molecular compound evolve to most stable $\beta_{POO:OPO}$. However, we should consider the presence of still some metastable $\beta'_{POO:OPO}$, which didn't completely transformed to $\beta_{POO:OPO}$ in some of the concentration ratios after the incubation period. The most surprising fact was the presence of triple chain length structures of the pure TAG components (β'_{POO} and β_{OPO}) at the 50:50 concentration ratio, demonstrating that the molecular compound should be finally metastable and tends to decompose into the pure TAG components during the stabilization process. As already mentioned, XRD experiments were performed after 6 and 11 months of incubation, in order to monitor the binary mixtures stabilization. Similarly to the PPO:POO case, we observed a progressive increase of the intensity of the triple chain length diffraction peaks of the TAG components (β'_{POO} and β_{OPO}) at the expense of the double chain length diffraction peak, corresponding to the POO:OPO molecular compound ($\beta_{POO:OPO}$). This fact again evidenced the metastable nature of the POO:OPO

molecular compound. Thus, one may conclude that the first polymorphic form of the POO:OPO molecular compound obtained was $\beta'_{POO:OPO}$, which evolved to $\beta_{POO:OPO}$ with the time but, finally, it tended to decompose into the two TAG components. The $\beta_{POO:OPO}$ melting temperature (T_{onset}) was approximately 12ºC.

Due to the POO:OPO molecular compound metastability, the system was, therefore, approaching to the eutectic behavior. Figure 3.14 illustrates the phase behavior of PPO:POO mixtures. MC was represented with a broken line due to its metastable nature.

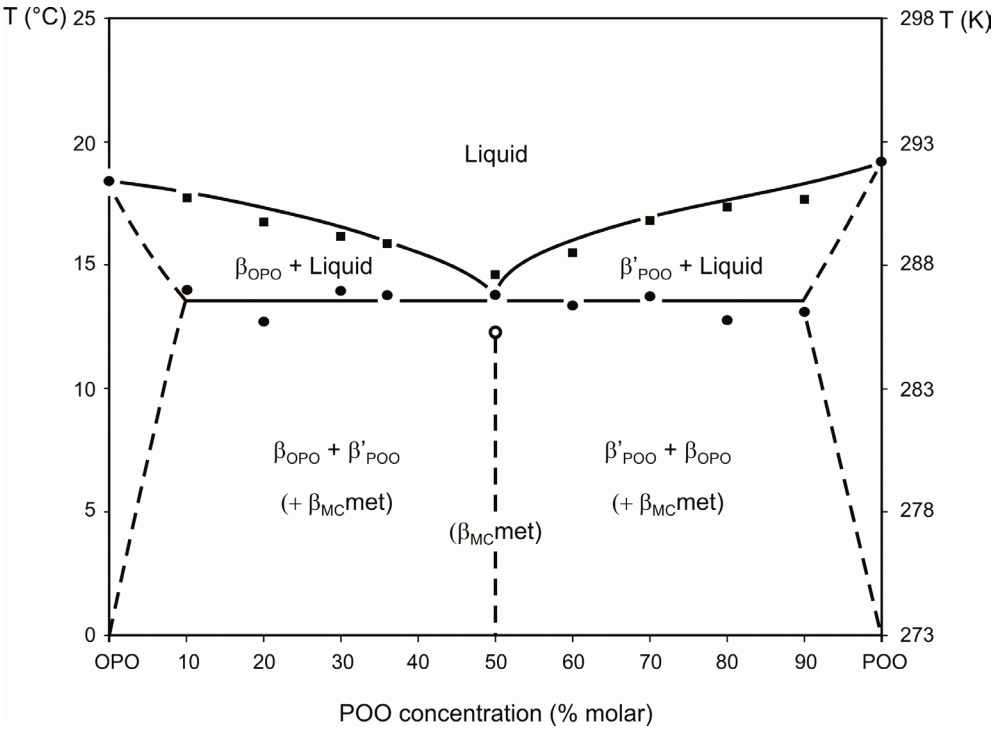

Figure 3.14. Phase behavior of POO:OPO mixtures, based on DSC onset and end temperatures (T_{end}-ΔT_{end}).

According to the DSC heating curves (Figure 4.12a), the eutectic point should be located at the 50POO:50OPO composition. However, it is still not clear whether the $\beta_{POO:OPO}$ melting should be set slightly under or about the eutectic point.

3.2.4. Factors influencing the molecular compound formation

The eutectic mixing behavior was confirmed for the PPO:OPO binary system, whereas PPO:POO and POO:OPO were metastable MC-forming. Several polymorphic forms were detected for the two molecular compounds, by applying different cooling rates to the 50:50 compositions, and by incubating the binary mixtures for 17 months. Table 3.3 summarizes the long and short spacing values of the polymorphic forms of $MC_{PPO:POO}$ and $MC_{POO:OPO}$.

Table 3.3. Long spacing (LS, nm) and short spacing (SS, nm) values of polymorphic forms of PPO:POO and POO:OPO molecular compounds.

	$MC_{PPO:POO}$			**$MC_{POO:OPO}$**		
Polymorph	sub-$\alpha_{PPO:POO}$	$\alpha_{PPO:POO}$	$\beta'_{PPO:POO}$	sub-$\alpha_{POO:OPO}$	$\beta'_{POO:OPO}$	$\beta_{POO:OPO}$
LS (nm)	4.9	4.9	4.2	5.6	4.4	4.2
SS (nm)	0.42 0.38	0.41	0.42 0.39	0.41 0.39	0.45 0.43 0.42 0.39	0.46 nd.

nd. Not determined

However, after the thermodynamic stabilization at a constant temperature, we confirmed that both molecular compounds tended to evolve into the corresponding TAG components, finally revealing the immiscible eutectic property. Such a phase behavior was never observed in the mixtures of POP:OPO and POP:PPO, in which β form of the molecular compound was stable and no evolution occurred.

Thus, the firstly showed Figure 3.2 should be modified, considering the metastability or stability of the molecular compounds obtained, as represented in Figure 3.15.

Figure 3.15 also summarizes the phase behavior of all TAGs containing palmitic and oleic fatty acids, including previous work and the present study. The upper part shows the MC-forming systems, whereas the binary mixtures revealing an eutectic behavior appear at the bottom.

The fact that PPO:OPO mixture was immiscible, not forming a molecular compound, and that PPO:POO and POO:OPO mixtures were MC-forming (although in

the two cases they finally became metastable) can be explained by taking into account the molecular interactions between the molecular TAG components.

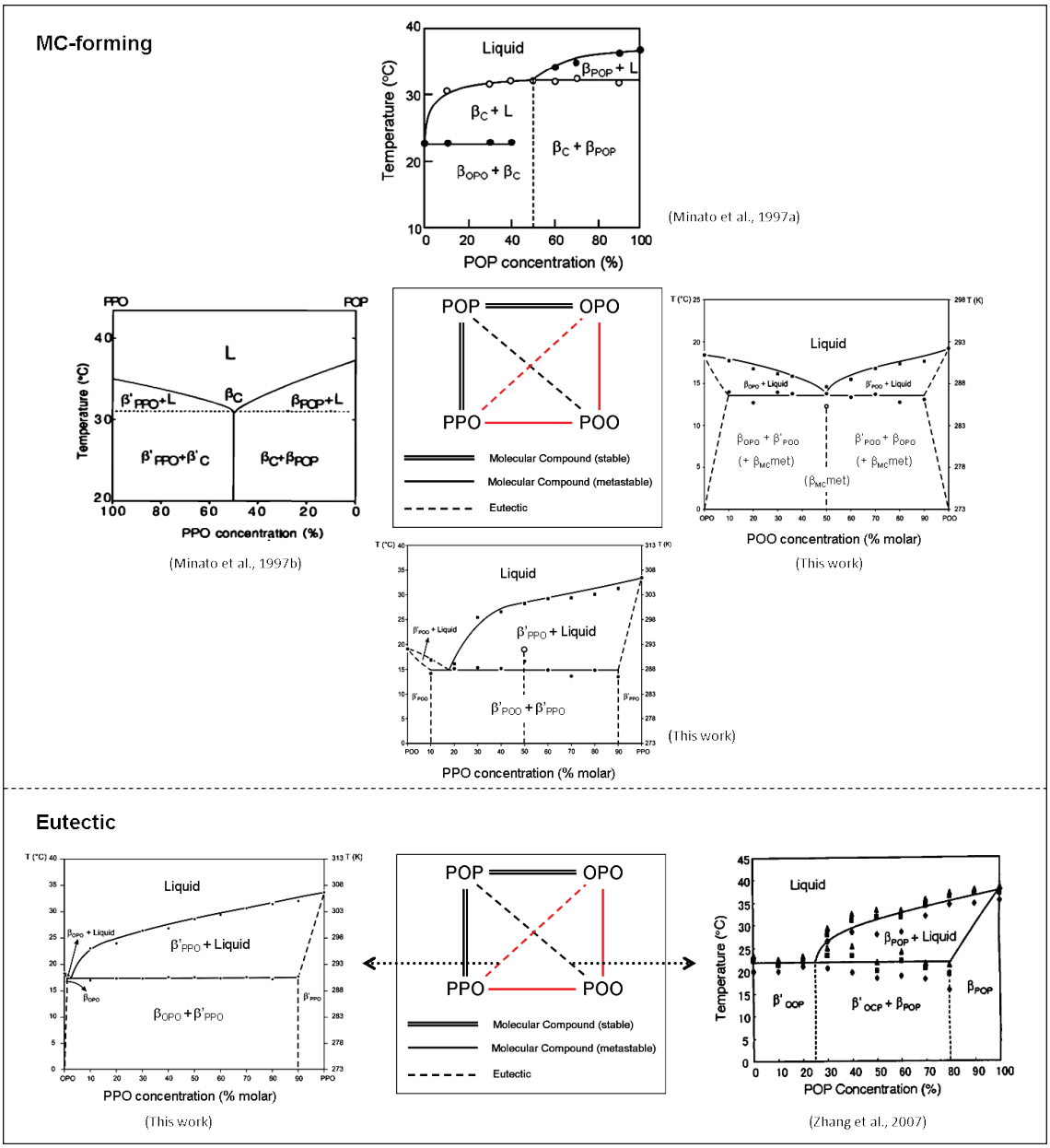

Figure 3.15. Diagram showing the phase behavior of TAGs containing palmitic and oleic fatty acids.

As already explained in the general introduction section of the present thesis, the main molecular interactions which influence stabilization of crystal structures of TAGs containing saturated and unsaturated fatty acids are the following (Larsson et al., 2006):

(i) Aliphatic chain packing, formed by the molecular interactions between saturated and unsaturated fatty acid chains.

(ii) Glycerol conformation, which determines the configuration of the whole TAG molecules.

(iii) Methyl end stacking, which determines the chain inclination and the chain length structure.

The ability or inability to form a molecular compound, having a double-chain length structure, may be explained by considering the combined effects of the before mentioned interactions.

Figure 3.16 illustrates the different glycerol conformations of two asymmetric units of TAG molecules in their most stable form.

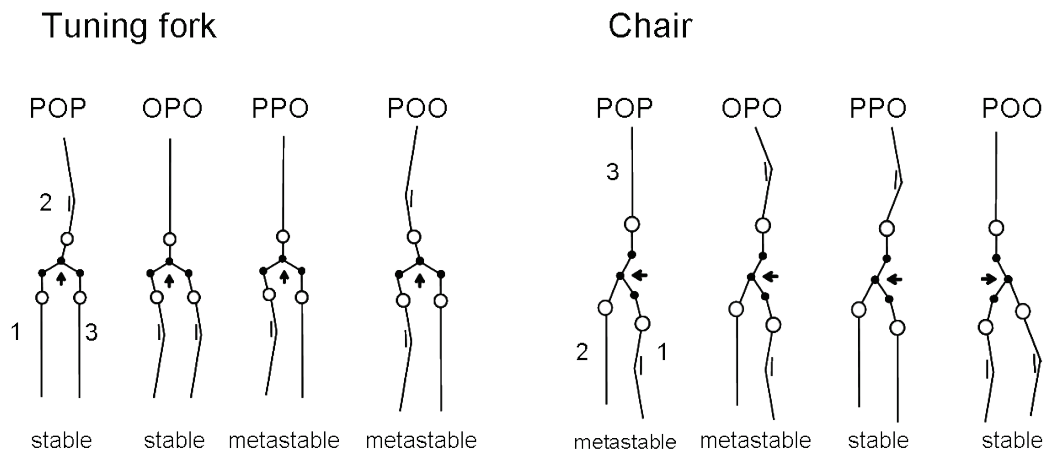

Figure 3.16. Structure models of TAGs containing palmitic and oleic fatty acids in their tuning fork and chair conformation.

The glycerol conformation is symbolized by using the direction of the glycerol group, which is indicated by an arrow and defines the direction between the middle point of the two glycerol carbon atoms at the first and third positions and the glycerol carbon atom at the second position. The glycerol conformation determines the lateral chain packing of palmitic and oleic acid moieties. It is known that, in more stable conformations, the palmitic and oleic acid chains should be packed in separated leaflets. By contrast, coexistence of palmitic and oleic acid in the same leaflet may cause steric hindrance in the aliphatic chain packing. Thus, the conformation obtained should become metastable. Taking this into account, the most stable conformation for

symmetric POP and OPO may be the tuning fork, and asymmetric PPO and POO may adapt a chair conformation.

Figure 3.17 illustrates possible structure models of molecular compounds of TAGs containing palmitic and oleic fatty acids. The three structure models shown in the upper part of Figure 3.17 had previously been reported (Minato et al., 1997b; Minato et al., 1997a; Zhang et al., 2007), whereas the three which appear at the bottom were those determined in the present work.

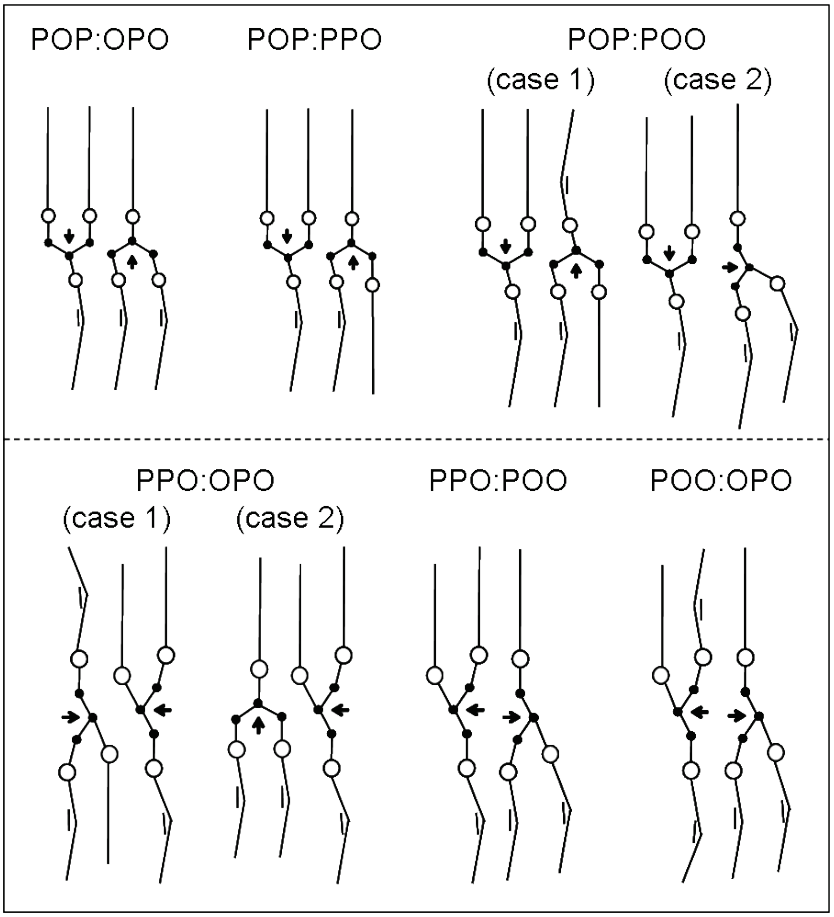

Figure 3.17. Possible structure models of molecular compounds of TAGs containing palmitic and oleic fatty acids. POP:OPO, POP:PPO and POP:POO cases were reported by Minato et al., (1997b and 1997a) and Zhang et al. (2007), respectively.

The neighbouring glycerol groups in a parallel arrangement are directed along the chain axis with an opposite turn in the POP:OPO mixture (Minato et al., 1997b). The tuning fork conformation become the most stable for both POP and OPO (see Figure 3.16), and enables the oleoyl and palmitoyl chains to make separate leaflets with stabilized aliphatic interactions. Hence, $MC_{POP:OPO}$ is stable.

As to the POP:PPO molecular compound formation, both TAGs may adapt a tuning fork conformation, so the adjacent glycerol groups should be directed along the chain axis with an opposite turn, similarly to those in the POP:OPO mixture. However, it is inevitable that palmitoyl and oleoyl chains will be located in one leaflet, and the other leaflet may be fully occupied by palmitoyl chains (Minato et al., 1997a). Although chain packing of palmitoyl-palmitoyl leaflet may be stabilized, steric hindrance may occur in palmitoyl-oleoyl leaflets, but this hindrance does not destabilize the total MC molecule. Thus, probably the glycerol group interactions and palmitoyl-palmitoyl interactions may prevail against the destabilization in the chain packing of the palmitoyl-oleoyl leaflet.

Mixtures of POP:POO exhibited an immiscible eutectic behavior, with no molecular compound formation (Zhang et al., 2007). These authors considered two possible models of $MC_{POP:POO}$. The model of case 1 assumes a parallel direction for the glycerol groups, which may be more stabilized than the unparallel direction in case 2. However, the structural model of case 1 may cause destabilization of the acyl chain packing because of the coexistence of oleoyl and palmitoyl chains in the two leaflets. In case 2, the oleoyl and palmitoyl chains are separately placed in their own leaflets. Nevertheless, they assumed that this model may cause additional destabilization of the glycerol conformation and unequal chain lengths of the neighbouring molecules of POP and POO. Consequently, neither of the two possible models of the POP:POO molecular compound may alleviate destabilization of the acyl chain packing, and no molecular compound was observed in either the metastable or stable states in the POP:POO mixture.

In the present work, an eutectic mixing behavior was also observed in the PPO:OPO binary mixtures, and no molecular compound was formed. Figure 3.17 shows two possible models of PPO:OPO molecular compound. In case 1, the two TAGs adapt a chair conformation and the adjacent glycerol groups would be parallel to each other and perpendicularly directed to the chain axis, so parallel to the lamellar plane. However, this structure model may be destabilized due to the chain packing of the two leaflets, where palmitoyl-oleoyl steric hindrance occurs. On the contrary, in case 2, no steric hindrance takes place in the aliphatic chain packing, as oleoyl and palmitoyl chains are located in different leaflets. However, the structure may be destabilized

because of steric hindrance between tuning fork (OPO) and chair (PPO) conformations, as the directions of adjacent glycerol groups would be at right angles to each other.

A molecular compound, having double chain length structure, was formed in the PPO:POO system. However, the thermal stabilization revealed that this molecular compound was metastable and tended to evolve into the two TAG components, so that the system was evolving to an eutectic behavior. The structure model of the PPO:POO molecular compound depicted in Figure 3.17, shows the stabilization of both glycerol conformations, as the two TAGs would adapt the chair conformation and adjacent glycerol groups would be parallel to each other and perpendicularly directed to the chain axis. Moreover, as to the chain packing, palmitoyl and oleoyl chains would be packed in separated leaflets, avoiding steric hindrance. Nevertheless, experimental results demonstrated the metastability of this molecular compound and, at this point, the racemic nature of both TAG molecules should be considered. Racemic compound crystals of R-PPO:S-PPO and R-POO:S-POO may become more stable than molecular compound crystals formed by the two TAGs. Thus, MC-forming mixtures may be destabilized to form eutectic mixtures of racemic compound crystals of R-PPO:S-PPO and R-POO:S-POO. Further studies would be needed in order to determine the mixing behavior of the enantiopure TAGs (R/S).

A metastable molecular compound was also form in the POO:OPO binary mixtures. In the proposed structure model, the directions of glycerol groups are parallel to the lamellar plane, and the glycerol conformations of POO and OPO are chair-type. The chain packing of oleoyl-oleoyl leaflet may be also stabilized, yet steric hindrance in palmitoyl-oleoyl leaflet may occur. However, this hindrance did not destabilize the total MC structures in its metastable state. Thermodynamic stabilization made the binary mixtures evolve to an eutectic behavior. Probably the glycerol conformation of OPO was converted from chair-type to tuning fork-type (more stable) during this stabilization, causing a higher steric hindrance in the palmitoyl-oleoyl leaflet.

With this work, the study of the mixing behavior of TAGs containing palmitic and oleic fatty acids was fully completed. The results shown may be also useful to understand the phase behavior of binary systems of other mixed saturated/unsaturated TAGs, such as those containing stearic acid instead of palmitic acid as saturated fatty acid.

Furthermore, it would be interesting to examine the effect of the racemicity of asymmetric TAGs (PPO and POO) on the phase behavior of binary mixtures. Thus, further studies are needed in order to analyze the mixing behavior of enantiopure TAGs (R and S).

3.3.

Heterogeneous microstructures of spherulites of 1,3-dipalmitoyl-2-oleoyl glycerol and 1,3-dioleoyl-2-palmitoyl glycerol ((POP-OPO) mixtures characterized with synchrotron radiation microbeam X-ray diffraction

Samples of POP and OPO (purity >99%) were purchased from Tsukishima Foods Industry (Tokyo, Japan). The solvent, n-dodecane (99% pure), was purchased from Nakalai Tesque (Kyoto, Japan).

As mentioned in the introduction section of the present chapter, microstructures of spherulites of POP and OPO (both in the neat liquid system and in n-dodecane solution) were analyzed with SR-μ-XRD. Firstly, to prepare the binary mixtures of OPO and POP, two TAG samples were melted at 50ºC and mixed using a vortex. When n-dodecane was added to the POP:OPO mixtures, the ratio of n-dodecane/(POP:OPO) was 1/1 (50% solution).

The SR-μ-XRD experiments were carried out at beamline BL-4A of the synchrotron radiation facility Photon Factory (PF) at the High-Energy Accelerator Research Organization (KEK) in Tsukuba, Japan. The details of the experiment set-up are reported elsewhere (Ueno et al., 2008). The sample set was placed in a temperature-controlled furnace, Linkam LK-600. Using an Olympus CX31 microscope system, polarized optical-microscope observations and SR-μ-XRD measurements were carried out. A microbeam was prepared by reflecting a synchrotron X-ray beam onto a K-B mirror and focusing the reflected beam on the sample position. The X-ray microbeam wavelength was 0.11 nm, and the beam area was 5x5μm^2. The position of the microbeam was detected by moving a wire (40 μm diameter) perpendicular to beam direction, and always pointed on a monitor image on which the sample subjected to microbeam diffraction was shown using the optical microscope (magnification 100 to 200×). The sample was moved by an x-y-z stepping motor (1 μm step) while being observed by the optical microscope. The

length between the sample and the detector was around 110 cm. The X-ray data was detected by a CCD camera to produce two-dimensional (2D) patterns. Figure 3.18 shows an image of BL-4A of the synchrotron facility PF at KEK in Tsukuba (Japan).

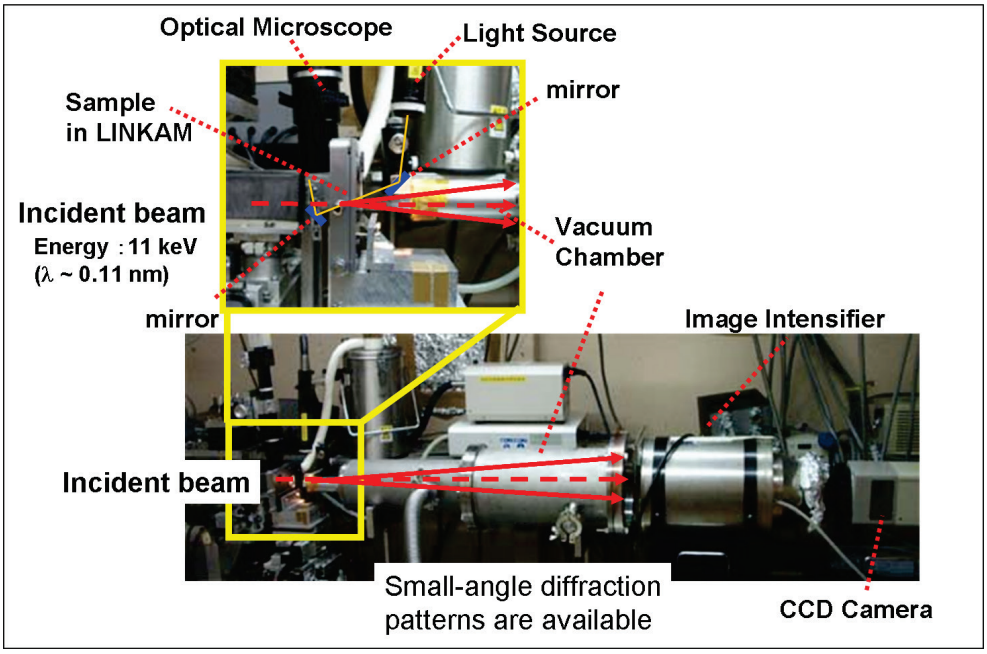

Figure 3.18. Details of BL-4A of the synchrotron facility Photon Factory at the High-Energy Accelerator Research Organization (KEK) in Tsukuba (Japan) (Figure provided by Prof. Satoru Ueno, Hiroshima University).

Basically, it is possible to observe small-angle and wide-angle diffraction patterns simultaneously in the SR-μ-XRD experiments, as examined in O/W emulsion (Shinohara et al., 2008). In the present study, however, we only focused on small-angle SR-μ-XRD patterns, so that diffraction peaks corresponding to long spacing values (lamellar distances) could be observed with high resolution by expanding the 2D patterns at the small diffraction angle regions.

In order to determine the temperature at which spherulites that were large enough to be examined with the SR-μ-XRD were grown, crystallization experiments were performed using a Linkam LK-600 PM stage (Tadworth, UK) mounted on an Olympus BX51 microscope (Tokyo, Japan). The system also consisted of an LNP liquid nitrogen cooling system and an L-600A temperature controller. Optical micrograph images were taken with an Olympus DP12 Digital Camera.

After determining the optimal crystallization conditions, we prepared

spherulites for the SR-μ-XRD experiments by the following process. A sample of molten mixture was placed between two Mylar films to obtain thin layers in which crystallization occurred. The films were set on a temperature-controlled Linkam stage and quickly cooled from 50ºC to crystallization temperature (T_c), at which the SR-μ-XRD experiments were carried out. The values of T_c are presented in Table 3.4.

Table 3.4. Melting temperatures (T_m, ºC), crystallization temperatures (T_c, ºC) and supercooling values ($\Delta T=T_m-T_c$, ºC).

	Neat liquid system				Solution system (50% n-dodecane)			
	75POP:25OPO		25POP:75OPO		75POP:25OPO		25POP:75OPO	
	β_{POP}	β_{MC}	β_{OPO}	β_{MC}	β_{POP}	β_{MC}	β_{OPO}	β_{MC}
T_m	35	32	22	31	27	17	6	20
T_c (ΔT)	16 (19)	16 (16)	6 (16)	6 (25)	7 (20)	7 (10)	2 (4)	2 (18)
			9 (13)	9 (22)				

At least two different spherulites were measured in every case.

In order to confirm the polymorphic forms of TAGs, laboratory-scale X-ray diffraction (XRD) was also performed (RINT-TTR, Rigaku Co., Tokyo, Japan, λ=0.154 nm) using a rotator-anode X-ray beam generator.

In this study, we seek to analyze the microstructures of spherulites of the binary mixtures of POP and OPO formed from neat liquid and solution including n-dodecane. Spherulites are the most typical crystal morphology of TAGs during cooling from neat liquid and solution (Boerrigter et al., 2002; Marangoni, 2004). Instead of growth of single crystal pieces separately, fat crystals tend to grow in the form of spherulites at ambient temperatures and moderate cooling rates (Acebedo et al., 2010a; Acebedo et al. 2010b). The morphology and microstructures of spherulites are determined by crystallization kinetics, since the central region of a spherulite is formed by the nucleation of many tiny crystals, and post-nucleation

crystal growth occurs toward the external region. Thus, the microstructures of the spherulites of the mixture samples are determined by relative rates of nucleation and crystal growth of component materials. Therefore, detailed analysis of microstructures of spherulites provides deep insight into crystallization kinetics of long-chain soft materials, as reported in polymer (Nozue et al., 2003) and TAG crystals (Ueno et al., 2008).

Our particular concern in this work was to examine how the microstructures of spherulites of the TAG mixtures are determined, when the MC crystals and POP or OPO component crystal can be formed competitively. The polymorphic structures of POP, OPO, and $MC_{POP:OPO}$ are summarized in Table 3.5.

Table 3.5. Polymorphic structures of POP and OPO grown from neat liquid.

TAGs	Polymorphs	T_m (°C)[a]	Chain length structure	Long spacing value (nm)
POP (Sato et al., 1989)	α γ β'_2 β'_1 β_2 β_1	15.2 27.0 30.3 33.5 35.1 36.7	Double Triple Double Double Triple Triple	4.7 6.5 4.2 4.2 6.1 6.1
OPO (Minato et al., 1997b)	α β' β_2 β_1	-18.3 11.7 15.8 21.9	Double Double n. d. Triple	4.8 4.4 5.6 6.4
$MC_{POP/OPO}$ (Minato et al., 1997b)	α β	n.d[b] 32.0	Double Double	4.7 4.2

[a] Melting temperature [b] Not determined

Figure 3.19 depicts phase diagrams of POP:OPO mixtures in neat liquid (Figure 3.19(a), Minato et al., 1997b) and n-dodecane (50%) solution (Figure 3.19(b), Ikeda et al., 2011).

At a concentration ratio of POP:OPO=75:25, POP and $MC_{POP:OPO}$ are formed at an equal ratio; at a concentration ratio of POP:OPO=25:75, $MC_{POP:OPO}$ and OPO are formed at an equal ratio. The molecular structures of POP, OPO, and $MC_{POP:OPO}$ are largely different, as seen in the triple-chain-length structures of POP and OPO, and the double-chain-length structure of $MC_{POP:OPO}$ (Figure 3.19(c)).

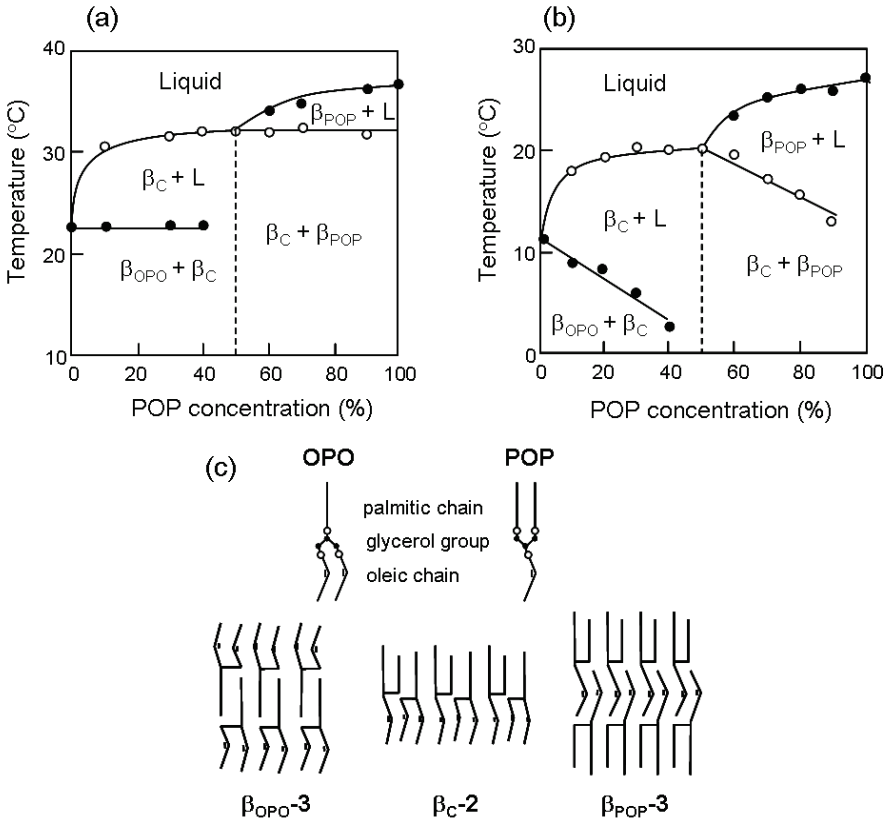

Figure 3.19. Phase behaviour of POP : OPO mixtures: (a) in neat liquid and (b) in 50% solution of n-dodecane. (c) Model of β_{MC} (double chain length structure) compared to β_{POP} and β_{OPO} (triple chain length structure).

Thus, observation of microstructures of spherulites may provide information about the relative crystallization rates of $MC_{POP:OPO}$, POP, and OPO. For this purpose, we employed synchrotron radiation microbeam X-ray diffraction (SR-μ-XRD).

The principle of SR-μ-XRD relies on X-ray focusing optics and a synchrotron radiation X-ray source, and it enables scanning in two dimensions of the sample, with steps on the order of the beam size. SR-μ-XRD has been used to examine many soft materials (e.g., biological tissues (Kuckzumow et al., 2000; Müller et al., 2000; Nakano et al., 2002; Stock et al., 2002; Paris et al., 2003; Drakopoulos et al., 2005; Kajiura et al., 2006; Fratzl et al., 2007; Seidel et al., 2008; Yagi et al., 2009), starch (Chanzy et al., 2006), proteins, and synthetic polymers (Nozue et al., 2003; Riekel et al., 2005; Kikuzuki et al., 2010; Kajioka et al., 2010)). For example, Kajiura et al. (2006) studied the keratin fibre arrangement of different types of human hair by SR-μ-XRD to determine the origin of curliness. Also, Seidel

et al. (2008) studied the orientation of chitin fibres of the airflow sensors of crickets. SR-μ-XRD analysis of spherulites revealed different types of microstructures on a micrometer scale, which traditional diffraction techniques had not detected (Riekel et al., 1996).

SR-μ-XRD has also been applied to lipid samples, such as spherulite of trilaurin (Ueno et al., 2008), oil-in-water emulsion (Shinohara et al., 2008; Arima et al., 2009), granular crystals of palm-oil-based water-in-oil emulsion (Tanaka et al., 2009), and interfacial fat crystals in water-in-oil emulsions (Wassell et al., 2012). SR-μ-XRD analysis of trilaurin spherulites indicated that the lamellar planes of tiny crystals are aligned parallel to the radial direction from the central and peripheral directions of the spherulite. Furthermore, the same study showed that the lamellar directions are not randomized after solid-state polymorphic transformation from β' to β forms.

In the present work, scanning SR-μ-XRD experiments of spherulites of the binary mixtures of POP and OPO clarified the details of heterogeneous structures.

3.3.1. Optical characterization of spherulites

Figure 3.20 depicts polarized microscopic images of the spherulites of the mixtures of 75POP:25OPO and 25POP:75OPO grown from neat liquid and 50% n-dodecane solution.

In Figure 3.20(a) of 75POP:25OPO, large and many small spherulites coexisted when grown from neat liquid. The diameters of the large spherulites were 150μm, and those of the small spherulites were less than 20μm. We observe aggregation of small spherulites between the large spherulites.

One may reasonably expect that the large spherulites started growing later than the small spherulites. Although not shown here, we performed SR-μ-XRD analysis on the aggregated small spherulites. In these spherulites, the polymorphic occurrence and lamellar direction were quite random, and not every spherulite was distinguished from the others. Therefore, SR-μ-XRD analysis was performed on only the large spherulites. It is evident that in every typical large spherulite of 75POP:25OPO depicted in Figure 3.20(a), morphology in the central part differs

from that in the peripheral part: a compact pattern is observed in the central area and needle patterns appear in the peripheral areas. In contrast, for 25POP:75OPO grown from neat liquid (Figure 3.20(c)), every spherulite has a uniform pattern of polarized-crossing without any separated inner textures.

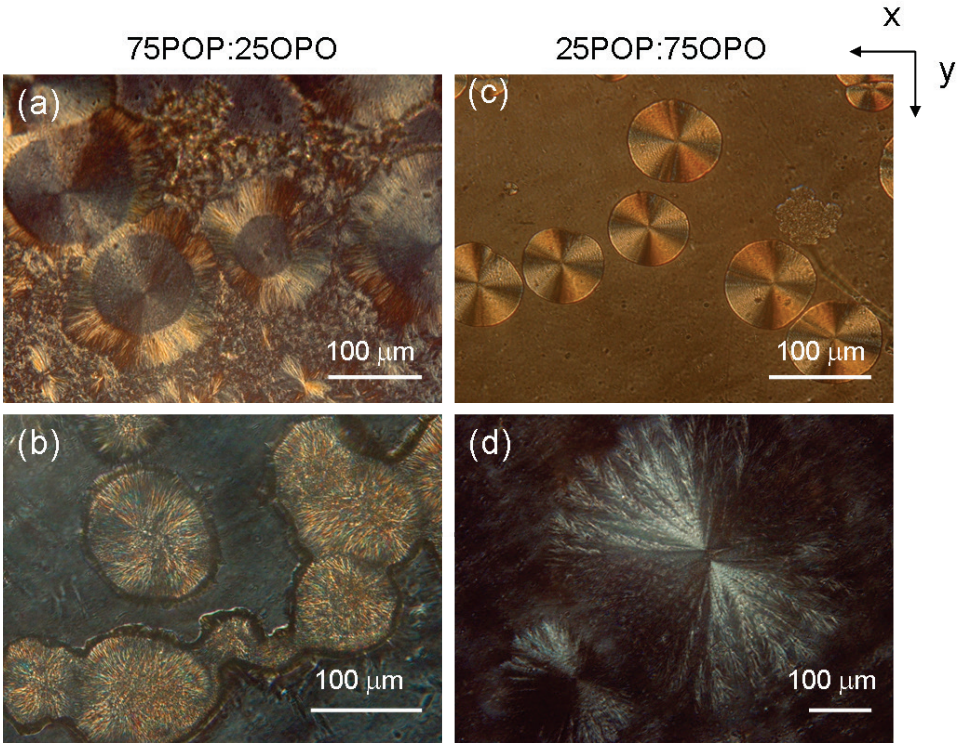

Figure 3.20 Polarized microscopic images of spherulites of POP:OPO binary mixtures. (a) 75POP:25OPO (neat liquid) grown at 16ºC, (b) 75POP:25OPO (50% n-dodecane) grown at 7ºC, (c) 25POP:75OPO (neat liquid) grown at 6ºC and (d) 25POP:75OPO (50% n-dodecane) grown at 2ºC. X and Y directions in the spherulites are shown.

The spherulites grown from 50% n-dodecane solution have uniform morphology in which needle patterns are arranged parallel to the radial direction from the central to the outer regions of the spherulites.

3.3.2. SR-μ-XRD analysis

3.3.2.1. Spherulites grown from neat liquid

The samples were cooled from 50ºC to 16ºC for the 75POP:25OPO mixture, and 6ºC or 9ºC for the 25POP:75OPO mixture (see Table 3.4), where isothermal stabilization was applied to grow large spherulites before the SR-μ-XRD experiments.

Figure 3.21 depicts scanning SR-μ-XRD patterns taken at 204 individual positions in an 80μm-diameter spherulite of the 75POP:25OPO mixture.

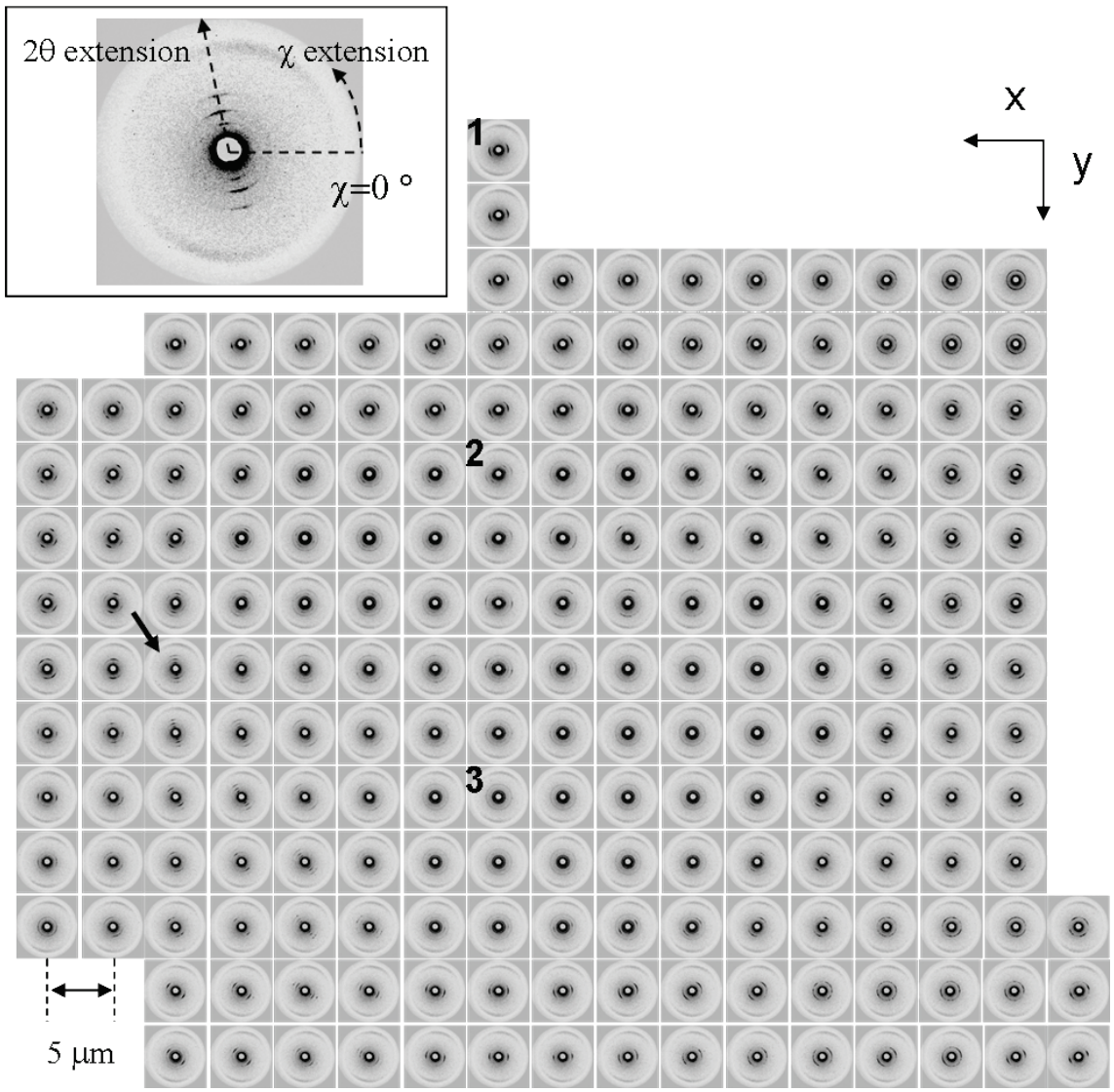

Figure 3.21. Scanning SR-μ-XRD patterns taken at all positions of a spherulite of the mixture of 75POP:25OPO grown from neat liquid, and an enlarged 2D pattern of the position noted by an arrow (inset).

Microbeam scanning was performed at a distance of 5 μm, and all the patterns indicated clear diffraction peaks from the crystals in the areas where the microbeam was irradiated.

As a typical example, an enlarged 2D diffraction pattern at a position is denoted by the arrow in the inset box in Figure 3.21, where the diffraction angle (2θ) and the azymuthal angle (χ) extensions are indicated. The detailed analysis of 2θ and χ extensions is reported elsewhere (Ueno et al., 2008). The pair of white and black patterns at the central position corresponds to the beam stopper and direct beam, and the broad grey circle at the periphery position corresponds to Mylar film. Two sets of three sharp arc peaks are identified, indicating the presence of two different types of crystals having well-ordered lamellar orientations. These sharp peaks were analyzed in two ways: the 2θ extension provides information on the long spacing of crystals, and the χ extension indicates the lamellar direction of the crystals.

To precisely analyze the spatial distribution of $MC_{POP:OPO}$ and POP crystals within the spherulite, Figure 3.22 depicts enlarged 2D patterns and corresponding 2θ and χ extension patterns taken at three positions along the radial direction from the central to outer regions of the spherulite (denoted as positions 1, 2, and 3 in Figure 3.21).

The 2θ extension pattern of position 1 indicates a single peak (denoted by ■) at 2θ=2.0°, which corresponds to the 002 reflection of the 6.4 nm long spacing. This value corresponds to the long spacing of β_{POP}-3 (Minato et al., 1997b). The χ extension has two sharp peaks at χ=5° and 185°, although each peak is split into two. No peak is observed at any χ value except for these two peaks; therefore, we conclude that the lamellar planes of the crystals at this position are aligned along the direction denoted by broken lines in the figure. In this way, we can interpret the 2D diffraction patterns of the other two positions.

Position 2 indicates two sets of arc peaks, providing three peaks in the 2θ extension (denoted by ■). The peaks at 2θ=1.3° and 2.7° correspond to the 001 and 002 reflections of the 4.6 nm long spacing, which corresponds to β_{MC}-2. The peak at 2θ =2.0° corresponds to the 002 reflection of the 6.4 nm long spacing of β_{POP}-3. From these results, we can conclude that two kinds of crystals (β_{MC}-2 and

β_{POP}-3) exist at this position. Interesting results are indicated for the χ extension, since the arrangements of lamellar planes of the β_{MC}-2 and β_{POP}-3 crystals differ. In the χ extension patterns of the β_{MC}-2 crystals, broad peaks appear at maximum χ values of 15° and 195°; however, sharp peaks appear at 45° and 225° for the β_{POP}-3 crystals. This result indicates that the lamellar directions of the β_{MC}-2 and β_{POP}-3 crystals differ by 30° at this position.

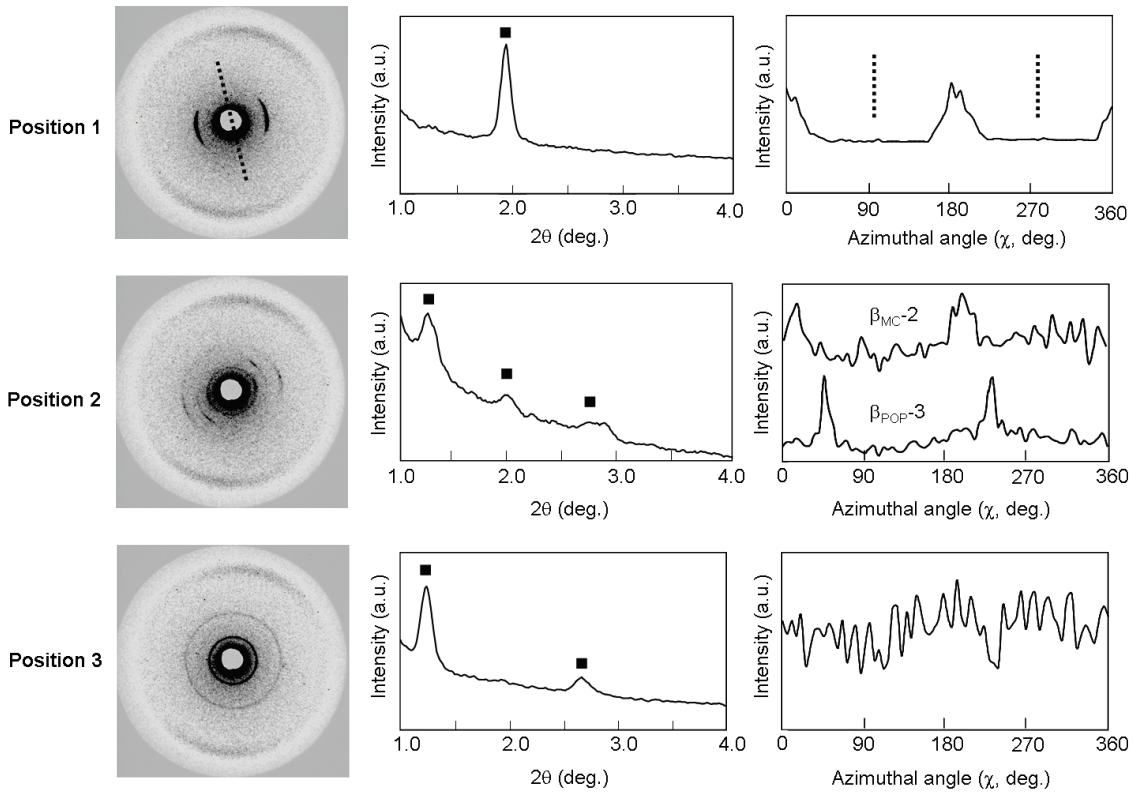

Figure 3.22. Enlarged patterns taken at three positions noted by 1, 2 and 3 in Figure 4.4. 2D diffraction patterns (left), 2θ extension (middle) and χ extension (right).

Finally, at position 3, which is near the central part of the spherulite, only β_{MC}-2 crystals exist and have a randomly oriented lamellar arrangement. This conclusion could be drawn by observing that the peaks at $2\theta = 1.3°$ and 2.7° correspond to the 4.6 nm long spacing and that the diffraction peaks have almost the same intensity at all the azymuthal angles, although the patterns were highly noisy. From the results presented in Figure 3.22, it was evident that the predominant TAG crystals varied from β_{MC}-2 to β_{POP}-3 when the microbeam scanning positions changed from the central regions to the outer regions in the same

spherulite.

Figure 3.23 illustrates the spatial distribution of β_{POP}-3 and β_{MC}-2 crystals in the spherulite depicted in Figure 3.21 and indicates their lamellar directions.

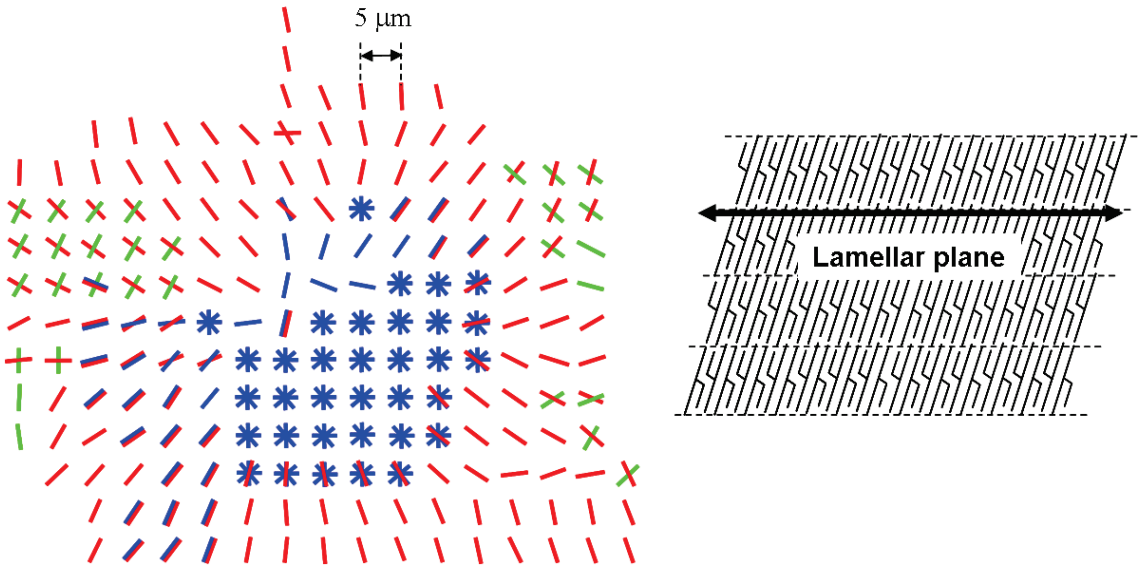

Figure 3.23. Lamellar plane directions of the crystals at all positions examined of the spherulite of 75POP:25OPO shown in Figure 4.4. Red and blue lines correspond to β_{POP}-3 and β_{MC}-2, respectively. Green lines correspond to the crystals of neighbouring spherulites. Star-like pattern means random orientation of the lamellar plane.

The β_{MC}-2 crystals with random lamellar orientation occupy the central part of the spherulite (area of 30 x 40 μm^2). However, predominant crystals vary from β_{MC}-2 to β_{POP}-3 when the position moves from the central to the peripheral areas of the spherulite, as explained above. In addition, the lamellar plane directions of the β_{POP}-3 crystals are arranged parallel to the radial direction of the spherulite. Between the periphery and the central areas of the spherulite, there are some areas where β_{MC}-2 and β_{POP}-3 crystals co-exist. The lamellar directions of the β_{MC}-2 and β_{POP}-3 crystals are almost parallel, with some exceptions (e. g., position 2 in Figure 3.22).

Figure 3.23 also depicts many crystals whose lamellar planes make right angles at the peripheral areas of the spherulite (green lines). These areas overlap with the neighbouring spherulites (see Figure 3.20(a)). Interestingly, the crystals of the neighbouring spherulites are all β_{POP}-3. This result indicates that perhaps the heterogeneous structure of the spherulite examined in Figures 3.21-3.23 also exists

in the neighbouring spherulites that have β_{POP}-3 crystal in their peripheral zones.

Figure 3.24 presents the results of SR-μ-XRD experiments of the spherulites of the 25POP:75OPO mixture grown from neat liquid at 9°C and 6°C.

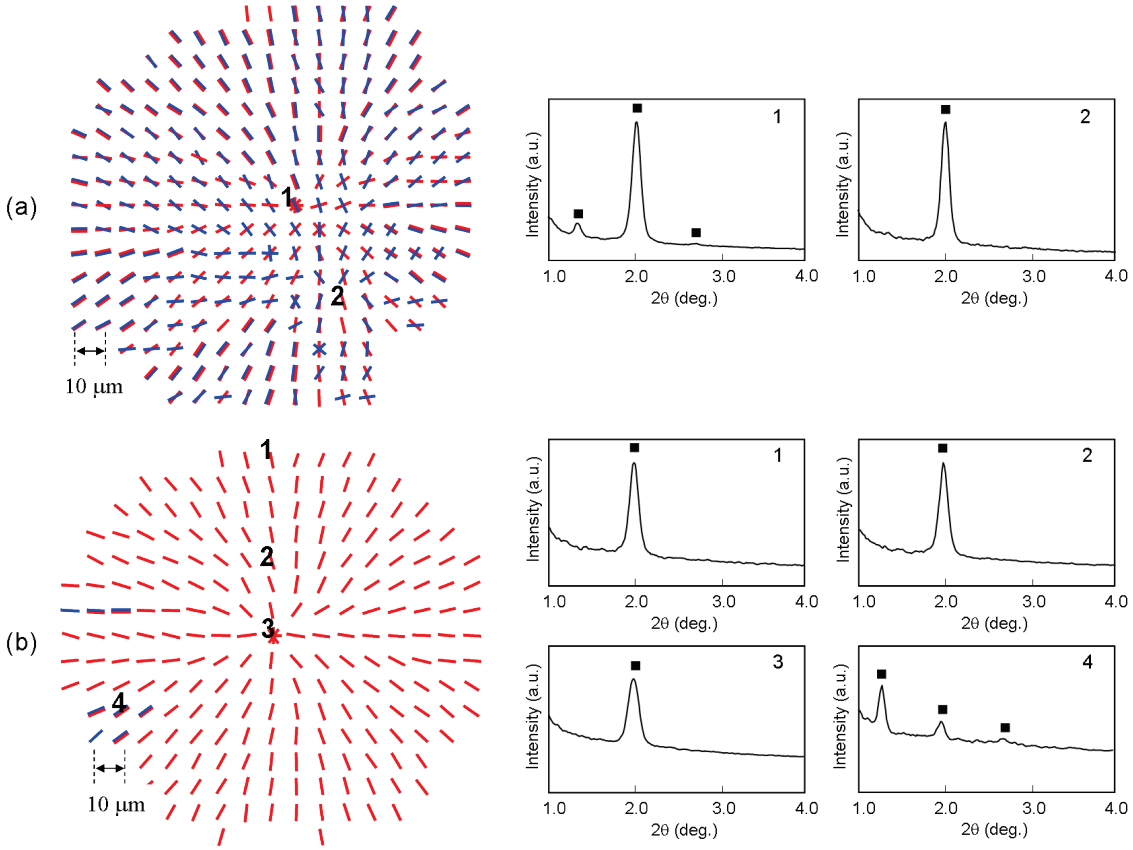

Figure 3.24. SR-μ-XRD data of spherulites of 25POP:75OPO mixtures grown from neat liquid (a) at 9ºC and (b) at 6ºC. Left: lamellar plane directions, right: 2θ extension patterns. Blue and red lines correspond to β_{MC}-2 and β_{OPO}-3, respectively.

Two spherulites were analyzed, following the same methodology than in the case before, over the whole area by scanning SR-μ-XRD studies at each temperature, and the same results were obtained. It must be noted that microbeam X-ray scanning was performed at 10 μm distance in both cases. The corresponding SR-μ-XRD patterns taken at the all positions of the spherulites are depicted in the Appendix of the present thesis (Figure A.1).

For spherulites grown at 9°C (Figure 3.24(a)), concurrent crystallization of β_{MC}-2 and β_{OPO}-3 was observed at almost every position. However, the concentration of β_{OPO}-3 crystals was always higher than that of β_{MC}-2 at the

positions where the two crystals co-existed. Furthermore, only β_{OPO}-3 crystals were observed at some places. Two typical examples are the 2θ extension patterns at positions 1 and 2 in Figure 3.24(a). There are three peaks at position 1 (denoted by ■). The peaks at 2θ=1.3° and 2.7° correspond to the 001 and 002 reflections of the 4.6 nm long spacing of β_{MC}-2, whereas the peak at 2θ=2.0 ° corresponds to the 002 reflection of the 6.4 nm long spacing of β_{OPO}-3. The relative concentration ratio of the β_{OPO}-3 and β_{MC}-2 crystals should be compared by considering the peak intensity of the 002 reflections. It is clear that the peak intensity of β_{OPO}-3 is much higher than that of β_{MC}-2. As an extreme case, position 2 has only one peak of β_{OPO}-3. Thus, the predominant crystallization of β_{OPO}-3 over β_{MC}-2 was confirmed at 231 of the 241 positions in Figure 3.24(a). At the other positions, either β_{OPO}-3 and β_{MC}-2 or only β_{MC}-2 was predominant, but this feature was not common to all the positions of this spherulite. The predominant crystallization of β_{OPO}-3 thus covered 95% of the area in this spherulite.

The lamellar directions of the β_{OPO}-3 and β_{MC}-2 crystals in Figure 3.24(a) were parallel to the radial direction of the spherulite at the outer regions. However, the lamellar directions were more or less random in the central region.

Figure 3.24(b) depicts the SR-μ-XRD patterns taken at 225 positions of the spherulite of the 25POP:75OPO mixture grown at 6°C. In this case, only β_{OPO}-3 was observed at 217 positions, concurrent crystallization of β_{OPO}-3 and β_{MC}-2 was observed at six positions, and β_{MC}-2 appeared without β_{OPO}-3 at two positions. The lamellar directions of all the crystals were parallel to the radial direction of the spherulite in almost all the regions, except the central position.

From analysis of the spherulites of the 25POP:75OPO mixture grown at two temperatures (Figure 3.24), we conclude that the rate of crystallization of β_{OPO}-3 crystals was higher than that of β_{MC}-2 crystals in the range of growth temperatures examined.

3.3.2.2. Spherulites grown from n-dodecane solution

When n-dodecane was added to the binary mixtures of POP and OPO, the SR-μ-XRD intensity decreased compared to that of the neat liquid system. Nevertheless, the behavior of the samples and the results obtained were the same as for those grown from neat liquid for the mixtures of both 75POP:25OPO and 25POP:75OPO.

Figure 3.25(a) illustrates the lamellar plane directions of the crystals at 79 positions indicating clear SR-μ-XRD patterns for the 167 positions examined at 10 μm distance in the spherulite of the 75POP:25OPO mixture grown at 7°C in 50% solution.

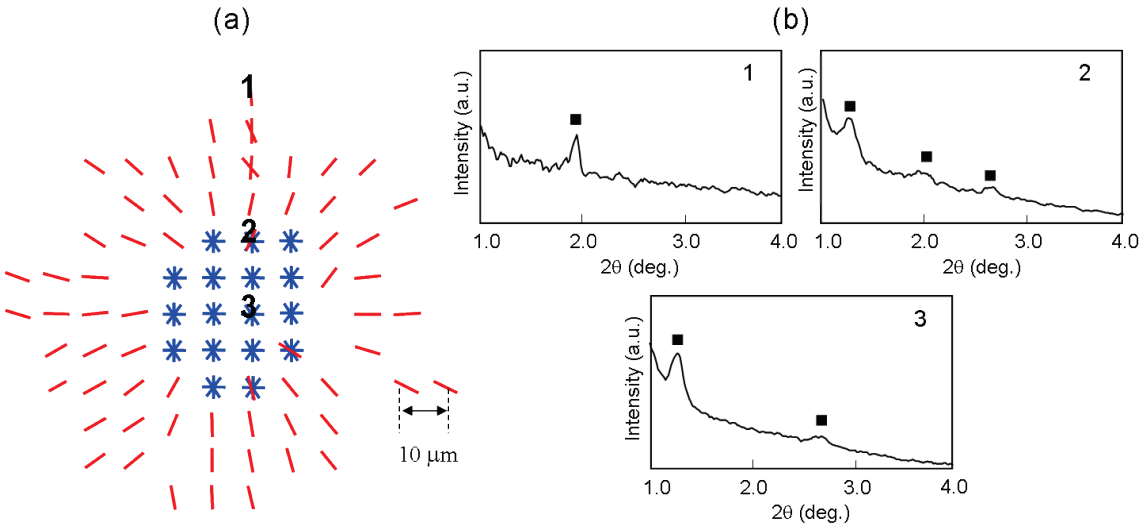

Figure 3.25. SR-μ-XRD data of spherulites of 75POP:25OPO mixtures grown from n-dodecane solution at 7ºC. (a) Lamellar plane directions and (b) 2θ extension patterns taken at the positions noted in (a). Blue and red lines correspond to β_{MC}-2 and β_{OPO}-3, respectively.

Having performed the same analyses as for Figures 3.21-3.24, we can draw the following conclusions about the heterogeneous microstructure of the spherulite depicted in Figure 3.25. The central part of the spherulite is occupied by β_{MC}-2 and β_{POP}-3 concurrently crystallized in the intermediate area, and β_{POP}-3 is predominant in the outer zone. The lamellar plane directions of β_{MC}-2 crystals in the central region are random, whereas a well-ordered lamellar arrangement parallel to the radial direction is observed in the peripheral regions where β_{POP}-3 crystals

predominate. These properties are basically the same as those of the spherulites of the 75POP:25OPO mixture grown from neat liquid in Figures 3.21-3.23.

Finally, SR-μ-XRD patterns were taken at 107 positions of the spherulite of the 25POP:75OPO mixture grown at 2ºC, and the lamellar plane directions at 48 positions are presented in Figure 3.26(a), with a 5 μm distance between consecutive positions.

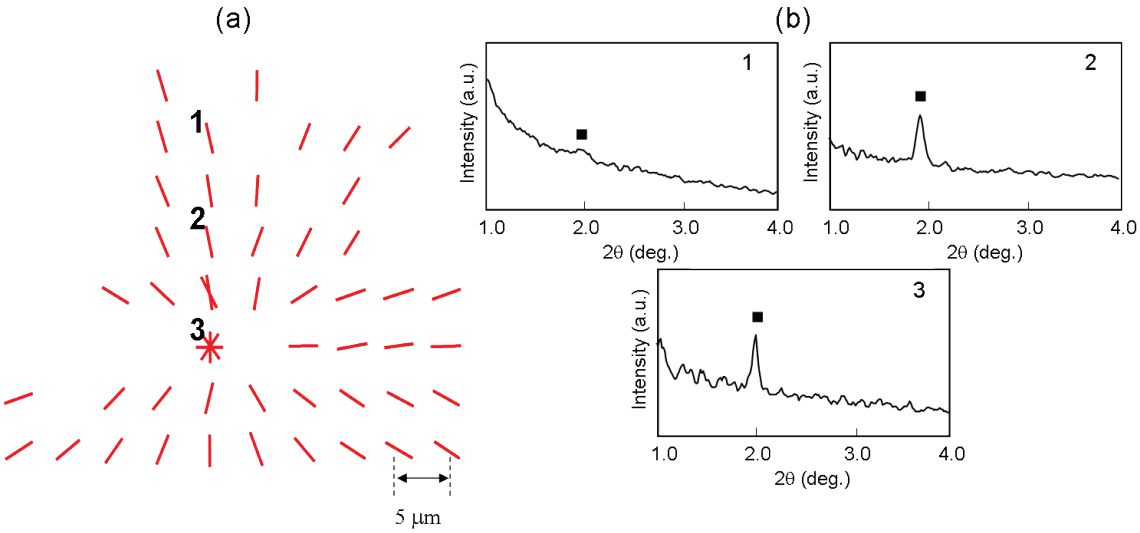

Figure 3.26. SR-μ-XRD data of spherulites of 25POP:75OPO mixtures grown from n-dodecane solution at 2ºC. (a) Lamellar plane directions and (b) 2θ extension patterns taken at the positions noted in (a).

The results were the same as those observed in 25POP:75OPO mixture grown from neat liquid: β_{OPO}-3 predominated over β_{MC}-2. Namely, β_{OPO}-3 was always observed, and no β_{MC}-2 crystals appeared. The lamellar plane directions of the β_{OPO}-3 crystals were parallel to the radial direction of the spherulites in all the regions except the central position.

The corresponding SR-μ-XRD patterns taken at the all positions of the spherulites of 75POP:25OPO and 25POP:75OPO grown from n-dodecane solution are shown in Figures A.2 and A.3 (Appendix), respectively.

3.3.3. SAXD and WAXD patterns

We have presented the SR-μ-XRD results of the spherulites of 75POP:25OPO and 25POP:75OPO mixtures grown from neat liquid and n-dodecane solutions, and we examined them with small-angle X-ray diffraction (SAXD). The long spacing values of the POP, OPO, and $MC_{POP:OPO}$ crystals examined in the present SR-μ-XRD study are summarized in Table 3.6, compared with those reported in previous analysis with conventional synchrotron radiation X-ray diffraction (SR-XRD).

Table 3.6. Long spacing (LS) values of β_{POP}, β_{OPO} and β_{MC} crystals obtained with synchrotron radiation microbeam X-ray diffraction (SR-μ-XRD) and synchrotron radiation macrobeam X-ray diffraction (SR-XRD).

	SR-μ-XRD			SR-XRD (neat liquid) (Minato et al., 1997b)			SR-XRD (50 % n-dodecane solution) (Ikeda et al., 2010)		
	β_{POP}	β_{OPO}	β_{MC}	β_{POP}	β_{OPO}	β_{MC}	β_{POP}	β_{OPO}	β_{MC}
LS (nm)	6.4	6.4	4.6	6.4	6.4	4.2	6.1	6.4	4.3
Chain Length Structure	Triple	Triple	Double	Triple	Triple	Double	Triple	Triple	Double

The chain-length structures of the POP, OPO, and $MC_{POP:OPO}$ crystals are all the same in the three studies: $MC_{POP:OPO}$ crystals have a double-chain-length structure, and the other two components have triple-chain-length structures. Although the precise long spacing values differ slightly (by 0.1~0.3 nm) among the studies with SR-μ-XRD and SR-XRD, this uncertainty is within experimental error. However, in order to confirm the polymorphic forms of TAG crystals, we observed the wide-angle X-ray diffraction (WAXD) peaks using RINT because WAXD patterns are more sensitive to subcell structures, such as tricilinic parallel ($T_{//}$) for β polymorph or orthorhombic perpendicular ($O_{\perp}$) for β' polymorph.

For this purpose, we performed laboratory-scale XRD using a RINT apparatus (laboratory scale X-ray diffraction). Figure 3.27 depicts the WAXD and SAXD patterns of the crystals of 75POP:25OPO mixtures grown from neat liquid at

16°C and for 25POP:75OPO mixtures grown from neat liquid at 6°C.

The SAXD patterns of the two mixtures are the same as those observed with SR-μ-XRD. The WAXD patterns were typical of β polymorph, since a strong peak of 0.46 nm at 2θ=19° was observed in the two mixtures (denoted by ■). Having confirmed the presence of β forms for POP, OPO, and $MC_{POP:OPO}$ in the 75POP:25OPO and 25POP:75OPO mixture samples with the RINT XRD, we performed the SR-μ-XRD experiments.

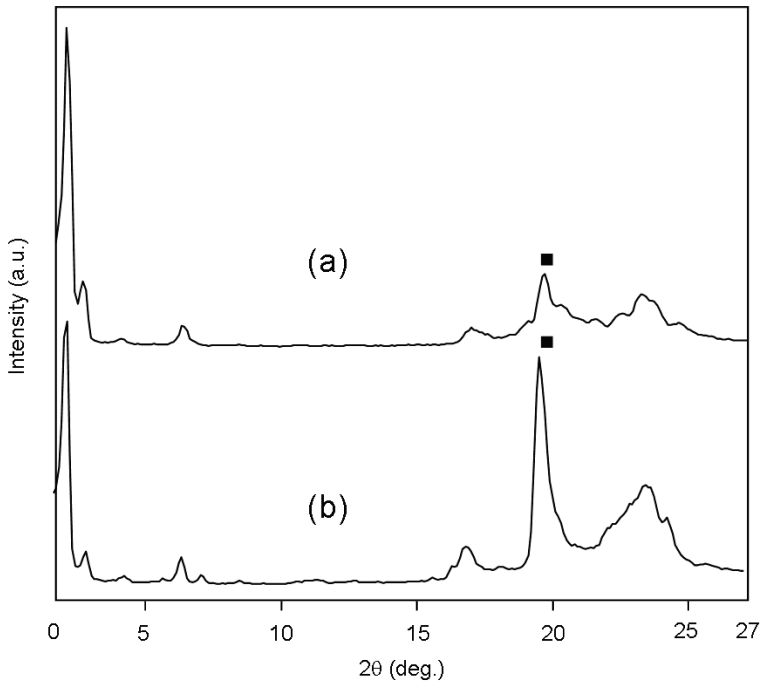

Figure 3.27. SAXD and WAXD patterns of (a) 75POP:25OPO mixture and (b) 25POP:75OPO mixture grown from neat liquid.

As with XRD studies of crystals grown from n-dodecane solutions containing 50% of fat samples, it was quite difficult to obtain clear diffraction patterns with RINT because the diffraction peaks from the solution samples were too weak. However, the mixing behavior of POP:OPO in n-dodecane solution examined with SR-XRD demonstrated that the equilibrium states contained β forms of POP, OPO, and $MC_{POP:OPO}$ (Ikeda et al., 2010). As equilibration from metastable to most stable forms occurs much faster in the solution system than in neat liquid systems, we conclude that the spherulites of the mixtures of POP:OPO grown from n-dodecane solution are all β forms.

In the present study, we observed the microstuctures of spherulites of 75POP:25OPO and 25POP:75OPO with SR-μ-XRD. Mixtures having these two ratios were chosen because previous studies indicated that the averaged concentration ratios of POP:$MC_{POP:OPO}$ and OPO:$MC_{POP:OPO}$ are 50:50 in the mixtures of 75POP:25OPO and 25POP:75OPO, due to the fact that POP and OPO form $MC_{POP:OPO}$ crystals at the ratio of 50:50. Therefore, we expected that the microstructures of spherulites might not be homogeneous, due to differences in the rates of crystallization of POP, $MC_{POP:OPO}$, and OPO, and that such heterogeneous structures can be analyzed solely with SR-μ-XRD experiments, as reported in previous studies of spherulites of a simple TAG system (Ueno et al., 2008), granular crystals in fat spreads (Tanaka et al., 2009), and oil-in-water emulsion droplets (Shinohara et al., 2008; Arima et al., 2009).

The results obtained by the present experiments are summarized in the following:

(1) For mixtures of 75POP:25OPO, large spherulites grown from both neat liquid and n-dodecane solution were dominated by $MC_{POP:OPO}$ in the inner regions, whereas the outer region was dominated by POP. From this result, we conclude that the relative crystallization rate of $MC_{POP:OPO}$ was higher than that of POP because we can reasonably assume that crystals having higher rates of nucleation may first occur in the central part of the spherulite, and successive nucleation and crystal growth having lower rates of nucleation may occur afterward and extend to the outer part of the spherulite at the T_c examined.

(2) For mixtures of 25POP:75OPO, the entire area was homogeneously occupied either with almost exclusively OPO or with coexisting $MC_{POP:OPO}$ and OPO (Table 3.7). This result indicates that the relative nucleation rate of OPO is higher than, or at least similar to that of $MC_{POP:OPO}$ at the T_c examined. SR-μ-XRD patterns corresponding to a horizontal scanning over many small spherulites of 25POP:75OPO grown from neat liquid are shown in Figure A.4 (Appendix).

Table 3.7. Occurrence frequency of β_{OPO} and β_{MC} in the 25POP:75OPO mixture grown from neat liquid examined by scanning SR-μ-XRD at different positions over many small spherulites at two crystallization temperatures (T_cs).

	T_c=9 ºC (82 positions)	T_c=6 ºC (45 positions)
$\beta_{OPO} > \beta_{MC}$	82	43
$\beta_{OPO} \sim \beta_{MC}$	0	1
$\beta_{OPO} < \beta_{MC}$	0	1

Based on these results, we may determine relative rates of crystallization of POP and $MC_{POP:OPO}$ in the 75POP:25OPO mixture, and OPO and $MC_{POP:OPO}$ in the 25POP:75OPO mixture, based on the following considerations:

(a) Spherulite formation starts from the inner regions and continues to the outer regions.

(b) As crystallization is performed during rapid cooling, no difference exists between crystallization temperatures at different positions of the spherulite, and the crystallization temperature is quickly reached.

(c) Heterogeneity in the occurrence of different crystal fractions is caused by relative rates of nucleation: the higher the nucleation rate, more dominated is the inner region of the spherulite.

As the nucleation rate of crystals largely increases with increased supercooling (ΔT) (Aquilano et al., 2001), it is necessary to take into account the effects of ΔT on crystal nucleation when we compare the relative nucleation rates of POP, OPO, and $MC_{POP:OPO}$. Table 3.4 presents the following ΔT values: in the 75POP:25OPO mixtures, 19°C for POP and 16°C for $MC_{POP:OPO}$ at T_c=16°C from neat liquid, and 20°C for POP and 10°C for $MC_{POP:OPO}$ at T_c=7°C from 50% solution; in the mixtures of 25POP:75OPO, 16°C for OPO and 25°C for $MC_{POP:OPO}$ at T_c=6°C, 13°C for OPO and 22°C for $MC_{POP:OPO}$ at T_c=9°C from neat liquid, and 4°C for OPO and 18°C for $MC_{POP:OPO}$ at T_c=2°C from 50% solution. It is evident that ΔT is larger for the crystals having higher T_m values at all T_c. However, differences in ΔT between the crystals decrease when T_c increases.

Taking into account the effects of ΔT discussed above, we may reasonably assume the relative rates of nucleation of β forms of POP, OPO, and $MC_{POP:OPO}$ at different T_c as shown in Figure 3.28.

Thus, the nucleation rate of β_{MC} may be higher than that of β_{POP} at large ΔT values in the mixtures of 75POP:25OPO (Figure 3.28(a)). In this case, T_c may be below the temperature where the nucleation rate of β_{MC} exceeds that of β_{POP}. In contrast, the nucleation rate of β_{OPO} may be slightly higher than, or similar to, that of β_{MC} in the mixtures of 25POP:75OPO at the crystallization temperatures examined in the experiments (Figure 3.28(b)).

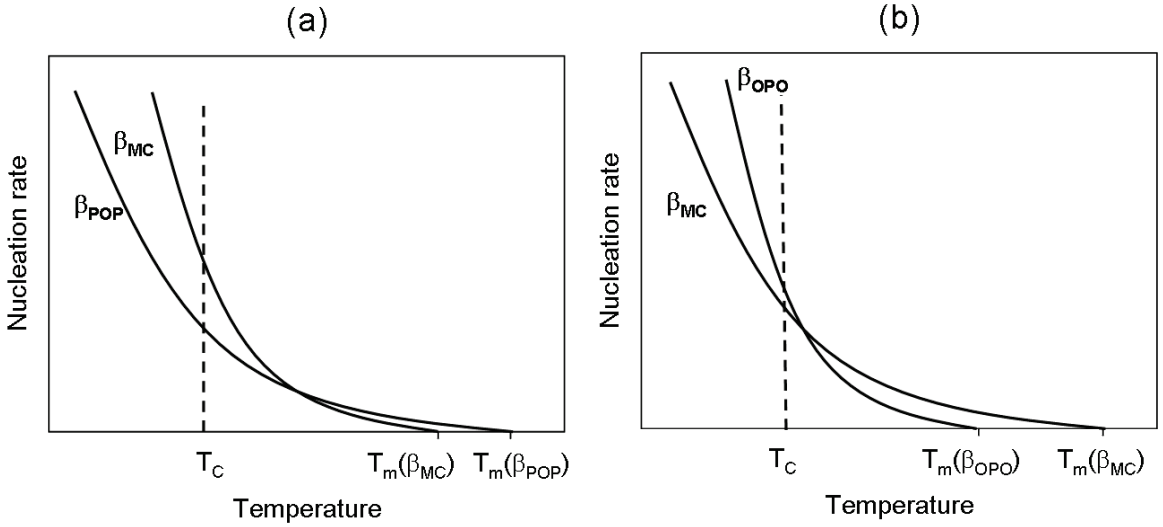

Figure 3.28. Schematic figures of the nucleation rate of β_{POP}, β_{MC} and β_{OPO} as a function of temperature in the mixtures of (a) 75POP:25OPO and (b) 25POP:75OPO. T_c, crystallization temperature.

It is highly significant to observe directly the relative nucleation rates of β forms of POP, OPO, and $MC_{POP:OPO,}$ by *on-site* observation, as has been performed on different polymorphic forms of POP and OPO using a synchrotron radiation X-ray beam (Bayés-García et al., 2013; Bayés-García et al., 2011a).

Microstructural studies of spherulites of the mixtures of POP:OPO were examined at 75POP:25OPO and 25POP:75OPO in a neat liquid system and with 50% n-dodecane by using SR-μ-XRD. This technique enabled the scanning of samples in two dimensions to determine the exact composition at each point, with a

difference in distance of 5 μm or 10 μm. The results indicated that at 75POP:25OPO a β_{MC} is located in the inner part of the spherulite and β_{POP} appears near the outer part. In contrast, for 25POP:75OPO, β_{OPO} predominates over β_{MC} at the crystallization temperatures examined. These heterogeneous distributions were due to the different crystallization rates of $MC_{POP:OPO}$ and component POP and OPO crystals, which were also confirmed by polarized microscopy: the morphology of spherulites of 75POP:25OPO grown from 50% n-dodecane and 25POP:75OPO grown from neat liquid and 50% n-dodecane were homogeneous, whereas those of 75POP:25OPO grown from neat liquid were heterogeneous (see Figure 3.29).

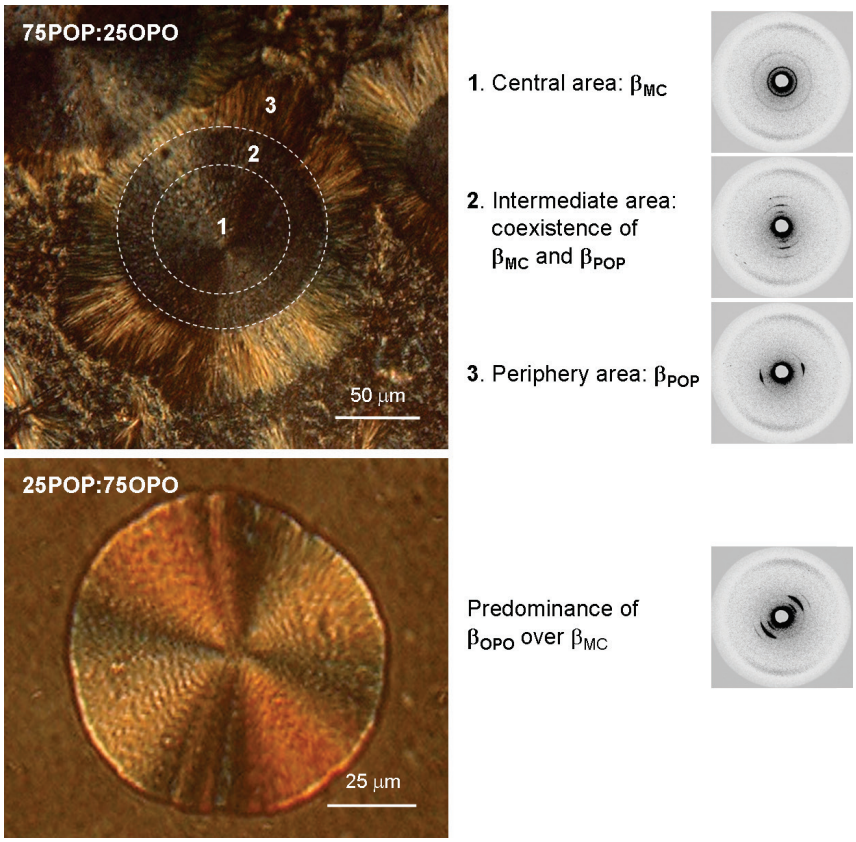

Figure 3.29. Schematic figure showing the heterogeneous components distribution in the 75POP:25OPO and 25POP:75OPO mixtures.

Although further study of the relative nucleation rates of these polymorphic forms is required, knowing the compound distribution in the spherulitic system aids in the comprehension and prediction of growth mechanisms. This study was published as a research paper (Bayés-García et al., 2011b).

3.4.

Chapter conclusions

The conclusions which can be extracted from the present chapter can be summarized as follows:

- The phase behavior of PPO:OPO, PPO:POO and POO:OPO binary mixtures were determined. PPO:OPO system revealed an eutectic behavior whereas PPO:POO and POO:OPO were MC-forming in the metastable state. Long incubation periods were needed in order to thermodynamically stabilize the binary mixtures, and the results demonstrated that $MC_{PPO:POO}$ and $MC_{POO:OPO}$ were metastable and tended to decompose into the pure TAG components.

- The non formation of molecular compound in PPO:OPO and metastabilities of $MC_{PPO:POO}$ and $MC_{POO:OPO}$ were discussed taking into account the main molecular interactions which influence stabilization of crystal structures of TAGs containing saturated and unsaturated fatty acids. Mainly, these interactions consist of aliphatic chain packing, glycerol conformation of the TAG components and methyl end stacking.

- With the determination of the phase behavior of PPO:OPO, PPO:POO and POO:OPO mixtures, the study of the mixing behavior of TAGs containing palmitic and oleic fatty acids was fully completed. The results shown may be also useful to understand and predict the phase behavior of binary systems of other mixed saturated/unsaturated TAGs, such as those containing stearic acid instead of palmitic acid as saturated fatty acid.

- Further studies are needed in order to examine the effect of racemicity of asymmetric TAGs on the phase behavior of binary mixtures. It could be interesting to analyze the mixing behavior of enantiopure TAGs (R and S).

- Microstructures of spherulites of POP:OPO binary mixtures were analyzed in neat liquid and solution (50% n-dodecane) systems by using SR-μ-XRD. Due to the $MC_{POP:OPO}$ formation at the 50:50 concentration ratio, 75POP:25OPO and 25POP:75OPO compositions were characterized to study how the microstructures of spherulites of the TAG mixtures are determined when the MC crystals and POP or OPO component crystals can be formed competitively.

- Microstructural results revealed that at 75POP:25OPO a β_{MC} was located in the inner part of the spherulite and β_{POP} appeared near the outer part. In contrast, for 25POP:75OPO, β_{OPO} predominated over β_{MC} at the crystallization temperatures examined. These heterogeneous distributions were due to the different crystallization rates of $MC_{POP:OPO}$ and component POP and OPO crystals. Thus, the nucleation rate of β_{MC} may be higher than that of β_{POP} at large ΔT values in the mixtures of 75POP:25OPO. In contrast, the nucleation rate of β_{OPO} may be slightly higher than, or similar to, that of β_{MC} in the mixtures of 25POP:75OPO at the crystallization temperatures examined.

- Polarized microscopy results confirmed the different behavior of the 75POP:25OPO and 25POP:75OPO mixtures: the morphology of spherulites of 75POP:25OPO grown from 50% n-dodecane and 25POP:75OPO grown from neat liquid and 50% n-dodecane were homogeneous, whereas those of 75POP:25OPO grown from neat liquid were heterogeneous.

- Studies of heterogeneous microstructures of POP:OPO mixtures in neat liquid and solution are applicable to palm oil fractionation processes by dry and solvent methods.

CHAPTER 4

Polymorphism for food authentication: edible fats and oils

"Descobrir el món de la Ciència ens permet ser més cults, aprendre a raonar i jutjar millor"

Prof. Miquel Àngel Cuevas-Diarte, Barcelona, 2011

4.1.
Introduction

After characterizing the polymorphic behavior of the main TAGs present in some vegetable and animal fats and oils (Chapter 2), and some of their binary mixtures (Chapter 3), we made an attempt to understand the polymorphic behavior of natural fats and oils.

Could polymorphism be used as a tool to determine the quality of a food product or to detect adulterations? The problem of food adulteration is by no means a contemporary phenomenon and is likely to be as old as the food processing and production systems themselves (Ellis et al., 2012). Authentication of food products is of primary importance for both consumers and industries, at all levels of the production process. Food adulteration normally becomes a means for fraudulent economic gain, as fraudulent actions are commonly applied to high-commercial-value products and/or produced in high tonnage. Alimentary products, such as jam, fruit juice, meat, honey, milk, spirit, wine, soy or vegetable oils are often adulterated with the addition of cheaper products, dilution processes or mislabelling (Cordella et al., 2002).

However, the detection of adulterations becomes a very complicated issue when the chemical compositions of both the food product and the adulterant have a very similar chemical composition.

Several methods have been used in foods authentication and detection of adulteration. Mainly, these techniques can be classified in the following: spectroscopic methods, techniques based on mass spectrometry, chromatography, and calorimetric techniques.

Spectroscopic techniques (NMR, Raman, FT-IR, and particularly near-IR and mid-IR) are characterized by their rapidity and portability, and they can provide the fingerprint of a food product. On the other hand, calorimetric techniques, such as DSC, also become rapid and highly sensible, and they can show the authenticity of a food product or the effect of an adulteration on the physicochemical properties of the sample.

This chapter is divided into two main parts. In the first section, the polymorphic behavior of multicomponent TAG mixtures is shown and discussed. After characterizing single TAGs and some of their binary mixtures, the study of more

complex systems is required in order to try to understand natural samples, such as olive oil. Thus, mixtures from the 2 to the 6 main TAGs present in an extra virgin olive oil from the Arbequina variety were prepared and analyzed.

The second part of the present chapter is focused on the use of the polymorphic behavior of edible fats and oils as a tool to determine their authentication. On the one hand, we tried to determine fraudulent additions of hazelnut oil in virgin and extra virgin olive oils (section 4.4.1). On the other hand, the physico-chemical properties of Iberian ham permitted to discriminate between hams coming from pigs produced with different systems of animal nutrition (section 4.4.2).

4.2.
Materials and methods

Specific experimental details will be given in the corresponding sections of the present chapter. However, the general and common procedures can be described as follows.

All samples were kept in purged (N_2) dark vials, which were stored in the freezer, in order to avoid oxidation.

TAG and fatty acid compositions of the samples were determined by High Performance Liquid Chromatography (HPLC) and Gas Chromatography (GC), respectively.

The chromatograph used for HPLC was an Agilent-1100 with thermostatic control of column temperature and equipped with a differential refractometry detector. A Kinetex column (250 mm long x 4.6 mm i.d.) with C18 reverse phase (particle size 5mm) (Phenomenex) was used. TAGs were eluted using a gradient according to the following procedure: mobile phase A acetonitrile and B acetone (50:50), with isocratic gradient during the full analysis. The flow rate was 1 $ml \cdot min^{-1}$. TAGs were identified by their equivalent carbon number (ECN) calculated as follows: ECN=CN–2NDB, where CN is the carbon number and NDB is the number of double bonds of the TAG.

Fatty acid (FA) methyl esters were analyzed on an Agilent 4890D model gas chromatograph, fitted with a flame-ionization detector and a split-splitless injector, set at 300ºC and 270ºC, respectively. The split ratio was 1:30. Chromatographic separation of fatty acid methyl esters was performed on a fused-silica capillary column (60 m x 0.25 mm i.d.) coated with 0.2 μm of a stationary phase of 90% biscyanopropil and 10% cyanopropylphenyl-polysiloxane (SP-2380 from Supelco). Helium, at 30 psi, was used as a carrier gas. The oven was programmed as follows: firstly, 2 min at 150ºC, then the temperature was increased by 1.5ºC$\cdot min^{-1}$ to 180ºC, then by 7.5ºC$\cdot min^{-1}$ to 220ºC, where it was held for 6 min, and finally the temperature was increased by 5ºC$\cdot min^{-1}$ to 250ºC and held for 20 min. The sample volume injected was 1 μl. The quantification of each analytical signal was carried out by evaluating the corresponding relative percentage according to the normalization area procedure, assuming an equal response for any species.

Crystallization, transformation and melting behavior of the samples were studied by DSC (Perkin-Elmer DSC-7 and Perkin Elmer DSC Diamond, see details in Chapter 2) by cooling the melted samples and heating them afterwards at $2ºC \cdot min^{-1}$. Three independent measurements were performed in each case.

The information given by the DSC was complemented by laboratory-scale powder XRD (PANalytical X'Pert Pro MPD powder diffractometer equipped with a Hybrid Monochromator and X'Celerator Detector, see Chapter 2). XRD patterns were obtained as a function of temperature.

For some of the samples, Synchrotron Radiation X-Ray Diffraction (SR-XRD) with Small-Angle X-Ray Diffraction (SAXD) and Wide-Angle X-Ray Diffraction (WAXD) was also used. SR-XRD experiments were performed at BL-6A of the synchrotron radiation facility Photon Factory (PF) at the High-Energy Accelerator Research Organization (KEK) in Tsukuba (Japan). The details of the mentioned beamline were described in Chapter 3. SR-XRD spectra were acquired at 60s intervals.

Thermo-Optical Microscopy (TOM) experiments allowed the observation of the crystallization, transformation and melting behavior of some of the samples. A Linkam THMSF-600 stage mounted to a Nikon Eclipse 50iPol Microscope was used (see Chapter 2 for further details). Linksys32 software permitted controlling the thermal treatments and image captures (QImaging QICAM FAST 1394 camera).

Preliminary chemometric analyses were carried out for Iberian ham fat, and olive oil and blends of olive and hazelnut oil samples, by the research group of Prof. Josep Boatella and Dr. Francesc Guardiola of the Nutrition and Food Science Department of the Pharmacy Faculty of the University of Barcelona. The responsible for performing the chemometric calculations was Dr. Alba Tres, from the same research group. PCA (Principal Component Analysis) calculations were made by using the software Pirouette 4.5 from Infometrix, Inc (USA). PCA becomes the main exploratory data analysis (EDA) technique, which is often the first step of the data analysis in order to detect patterns in a measured data. This visualization technique permits observing similarities or differences between samples (Massart et al., 2005). By the reduction of the data dimensionality, PCA allows their visualization retaining as much as possible the information present in the original data. So, PCA transforms the original measured variables into new uncorrelated variables called principal components (PC). Each principal component is a linear combination of the original measured variables. This technique affords a group of orthogonal axes that represent the directions of greatest

variance in the data. The first principal component (PC1) accounts for the maximum of the total variance, the second (PC2) is uncorrelated with the first and accounts for the maximum of the residual variance, and so on, until the total variance is accounted for. For practical reasons, it is sufficient to retain only those components that account for a large percentage of the total variance (Berrueta et al., 2007). Before the data analysis, data pre-treatments, such as the derivative determination and auto-scaled were applied.

4.3.

Multicomponent TAG mixtures: an approach to extra virgin olive oil

TAG samples (OOO, POO, OOL, POL, PPO and SOO) were all purchased from Tsukishima Foods Industry (Tokyo, Japan) and used without further purification (purity >99%). Extra virgin olive oil, from the Arbequina variety, was obtained from Coselva (cooperative from La Selva del Camp) and harvested on December 2010. This sample will be named O2 in section 4.4.

To prepare the multicomponent TAG mixtures, TAG samples were melted at 50ºC and mixed using a vortex. Jiménez et al. (2003, 2007) determined the TAGs composition of olive oils obtained from different olive varieties. Following the data presented by Jiménez et al. (2003, 2007), we prepared mixtures from the 2 to the 6 main TAGs present in olive oil of the Arbequina variety. In order to determine the percentage (wt/wt) of each TAG, mean values of the concentration ratios extracted from the literature were calculated and extrapolated to the total 100%. Table 4.1 shows the concentration values (% wt/wt) used to prepare the TAG mixtures, and they are compared to those already reported.

Table 4.1. Concentration ratios (% wt/wt) of TAGs constituting multicomponent TAG mixtures. Previously reported data is also shown.

	Multicomponent TAG mixtures					Arbequina virgin olive oil	
	2 TAGs	3 TAGs	4 TAGs	5 TAGs	6 TAGs	Jiménez et al. (2003)	Jiménez et al. (2007)
OOO	58	47	41	39	38	38.1	32.4
POO	42	31	27	26	25	22.9	24.6
OOL		22	20	19	19	17.6	16.8
POL			12	11	11	9.3	10.6
PPO				5	4	3.2	5.1
SOO					3	3.1	2.7

HPLC experiments were performed in order to qualitatively observe the compositional changes occurred in the sample when component TAGs were progressively added to the mixtures (Figure 4.1).

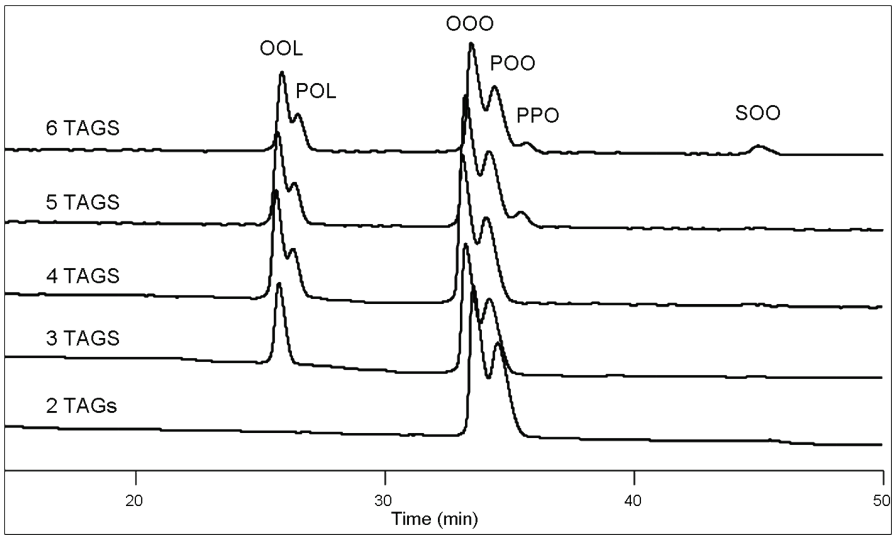

Figure 4.1. HPLC chromatograms of multicomponent TAG mixtures containing from 2 to 6 TAGs.

HPLC results confirmed the TAG concentrations, although slight differences were detected in some cases, which are within the experimental error. Table 4.2 summarizes the TAG composition of the prepared mixtures, determined by HPLC.

Table 4.2. TAG composition (% wt/wt) of multicomponent mixtures determined by HPLC.

	2 TAGs	3 TAGs	4 TAGs	5 TAGs	6 TAGs
OOO	54	44	37	36	35
POO	46	33	29	28	26
OOL		23	21	21	21
POL			12	10	10
PPO				5	4
SOO					4

All samples were subjected to the same thermal treatment, which consisted of cooling the melted samples from 25ºC to -80ºC at a rate of 2ºC·min^{-1} and heating them afterwards from -80ºC to 25ºC at the same mentioned rate. The DSC thermograms

obtained for the systems from 1 to 6 TAGs components are depicted in Figure 4.2. The thermal profile of an extra virgin olive oil of the Arbequina variety is also included.

Table 4.3 summarizes temperature (T_{onset}) and enthalpy (ΔH) values associated at each thermal phenomenon.

Figure 4.3 depicts the laboratory-scale XRD patterns, obtained as a function of temperature, corresponding to mixtures from 2 to 5 TAG components.

The DSC thermal profile of OOO (main TAG of olive oil), which is shown in Figure 4.2a was already discussed in Chapter 2 (section 2.7) and can be summarized as follows. XRD data revealed that, when OOO was cooled from the melt at 2ºC·min^{-1}, the crystallizing polymorph was β'_2. However, the DSC cooling curve showed a complex phenomenon consisting of a main exothermic peak with T_{onset} at -33.4ºC having a shoulder at -26.6ºC, which revealed the beginning of the crystallization process (see Table 4.3). When the sample was heated at 2ºC·min^{-1}, two consecutive transitions occurred: β'_2 form transformed into β_2 form at around -25.0ºC and, on further heating, a solid-state transformation took place from β_2 to β_1 form at -11.3ºC. Finally, two slightly separated melting phenomena were observed, corresponding to the melting of some remaining β_2 form (T_{onset}=-2.2ºC) and β_1 form (T_{onset}=2.9ºC).

By adding more TAG components to OOO, the complexity of the polymorphic behavior increased considerably, being unable to strictly explain the polymorphic transformations observed in the DSC profiles.

When POO was added to OOO (2 TAGs mixture composed by 58% OOO and 42% POO) and the mixture was cooled at 2ºC·min^{-1}, a broad exothermic peak with two onset temperatures at -18.6ºC and -26.8ºC, respectively (corresponding to peak 1 in Figure 4.3b and Table 4.3), appeared in the cooling DSC curve (Figure 4.3b). Therefore, the addition of POO caused a shifting of the crystallization peak to higher temperatures. The corresponding XRD pattern (Figure 4.3a) revealed the occurrence of a β' form (short spacing values of 0.45 nm, 0.43 nm, 0.40 nm and 0.39 nm) having a double chain length structure (long spacing value of 4.5 nm). No additional XRD peaks were observed during the cooling process. Thus, we may think that OOO and POO did not crystallized separately. Probably, an alloy between the two TAG components may have been formed.

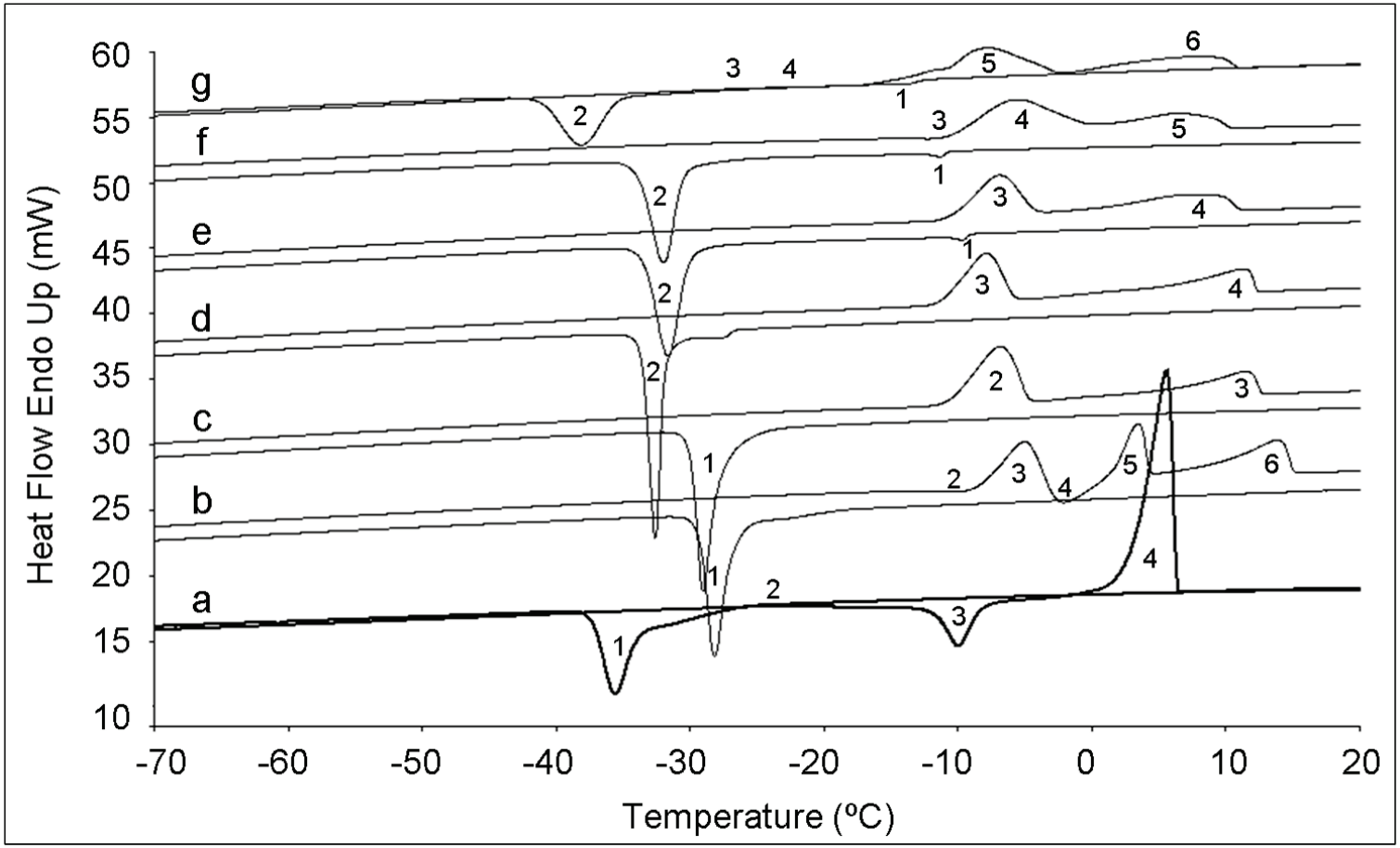

Figure 4.2. DSC (cooling and heating curves) plot of multicomponent TAG mixtures and extra virgin olive oil (Arbequina variety). a) 1 TAG (100% OOO). b) 2 TAGs (58% OOO + 42% POO). c) 3 TAGs (47% OOO + 31% POO + 22% OOL). d) 4 TAGs (41% OOO + 27% POO + 20% OOL + 12% POL). e) 5 TAGs (39% OOO + 26% POO + 19% OOL + 11% POL + 5% PPO). f) 6 TAGs (38% OOO + 25% POO + 19% OOL + 11% POL + 4% PPO + 3% SOO). g) Olive oil sample (Extra virgin olive oil, Arbequina variety).

Table 4.3. DSC data of the crystallization and transformation of OOO (1 TAG), TAG mixtures from 2 to 6 TAGs and extra virgin olive oil (Arbequina variety) obtained when the samples were cooled and heated at 2ºC·min^{-1}. The letters *c* and *m* mean crystallization and melting, respectively. DSC peaks are labelled according to their exothermic (*exo*) or endothermic (*endo*) nature.

		Cooling (2ºC·min^{-1})		**Heating (2ºC·min^{-1})**				
1 TAG		*1 (β'_2 (c))*		*2 ($\beta'_2 \rightarrow \beta_2$)*	*3 ($\beta_2 \rightarrow \beta_1$)*	*4 ($\beta_2 + \beta_1$ (m))*		
	T_{onset} (ºC)	-26.6 ± 1.2	-33.4 ± 0.7	-25.0 ± 1.7	-11.3 ± 1.7	-2.2 ± 0.7	2.9 ± 1.3	
	ΔH (J/g)	-70 ± 1		n.d.	-27 ± 4	128 ± 5**		
2 TAGs		*1 (exo)*		*2 (exo)*	*3 (endo)*	*4 (exo)*	*5 (endo)*	*6 (endo)*
	T_{onset} (ºC)	-18.6 ± 1.7	-26.8 ± 0.2	-13.3 ± 0.5	-8.1 ± 0.7	-3.3 ± 0.7	1.4 ± 0.5	6.3 ± 1.0
	ΔH (J/g)	-76 ± 3		-3 ± 1	31 ± 3	-11 ± 7	69 ± 9**	
3 TAGs		*1 (exo)*		*2 (endo)*	*3 (endo)*			
	T_{onset} (ºC)	-25.1 ± 1.4		-10.6 ± 0.4	-4.7 ± 1	3.4 ± 0.8		
	ΔH (J/g)	-76 ± 3		90 ± 3**				
4 TAGs		*1 (exo)*		*3 (endo)*	*4 (endo)*			
	T_{onset} (ºC)	-26.6 ± 0.4	-31.9 ± 0.3	-11.4 ± 0.5	-6.6 ± 1.6	1.6 ± 0.8		
	ΔH (J/g)	-70 ± 2		88 ± 4**				
5 TAGs		*1 (exo)*	*2 (exo)*	*3 (endo)*	*4 (endo)*			
	T_{onset} (ºC)	-9.0 ± 0.4	-30.0 ± 0.3	-10.3 ± 0.5	-2.8 ± 0.5			
	ΔH (J/g)	-70 ± 3**		85 ± 2**				
6 TAGs		*1 (exo)*	*2 (exo)*	*3 (exo)*	*4 (endo)*	*5 (endo)*		
	T_{onset} (ºC)	-10.6 ± 0.5	-30.5 ± 0.3	-14.0 ± 0.6	-10.2 ± 0.5	-1.6 ± 0.5		
	ΔH (J/g)	-70 ± 3**		-1 ± 1	85 ± 3**			
Oil Sample		*1 (exo)*	*2 (exo)*	*3 (endo)*	*4 (exo)*	*5 (endo)*		*6 (endo)*
	T_{onset} (ºC)	-12.4 ± 0.4	-35.4 ± 0.3	-28.5 ± 0.8*	-25.2 ± 1.3	-17.2± 0.3	-11.5±0.7	-3.7 ± 0.6
	ΔH (J/g)	-65 ± 8**		---	-4 ± 1	77 ± 4**		

n.d. Not determined

Two T_{onset} values were assigned to some DSC peaks due to the presence of shoulders, although some of them can not be clearly appreciated through Figure 4.2.

* The peak top temperature was determined in this case. No ΔH value was given for this peak, as the onset and end temperatures could not be clearly defined.

** These enthalpy values correspond to the global enthalpy of the overlapped peaks.

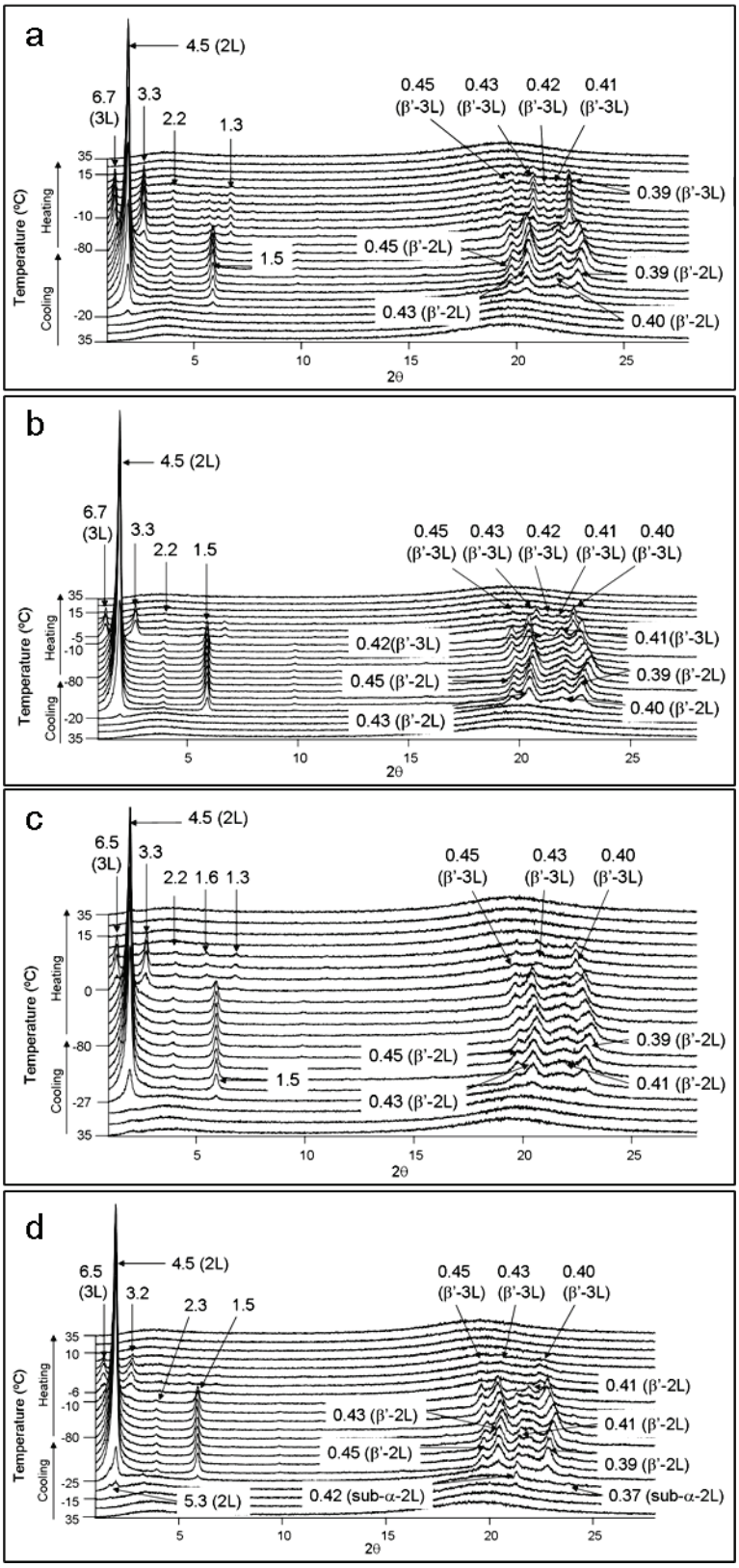

Figure 4.3. Laboratory-scale XRD patterns of multicomponent TAG mixtures from two to five TAG components. a) 2 TAGs (58% OOO + 42% POO). b) 3 TAGs (47% OOO + 31% POO + 22% OOL). c) 4 TAGs (41% OOO + 27% POO + 20% OOL + 12% POL). d) 5 TAGs (39% OOO + 26% POO + 19% OOL + 11% POL + 5% PPO).

As to the heating step, complicated transformation processes appeared in the DSC curve. A small exothermic DSC peak, with an enthalpy value of -3 $J \cdot g^{-1}$, was observed at a T_{onset} of -13.3ºC. This peak was followed by an endothermic peak at -8.1ºC (peak 3 in Figure 4.3b), another exothermic phenomenon with T_{onset} at -3.3ºC (peak 4), and two consecutive endothermic peaks at 1.4ºC and 6.3ºC (peaks 5 and 6), respectively. The XRD data only showed, at approximately -10ºC, the occurrence of a triple chain length structure (long spacing value of 6.7 nm) corresponding to a β' form (new wide angle region peaks appeared at 0.45 nm, 0.43 nm, 0.42 nm, 0.41 nm and 0.39 nm). On further heating, the double chain length peak at 4.5 nm totally vanished at 2ºC (corresponding to the β'-2L form melting), and the β'-3L peaks disappeared at around 15ºC (β'-3L melting). One may consider that the long spacing value of the last melting form could correspond to a β'_{POO} form (see Chapter 2). As to OOO, chain length structures of all the polymorphic forms of OOO are double, having a long spacing value of 4.5 or 4.4 nm, so judging from the short spacing values, some β'_{OOO} should be present. However, only one crystallizing polymorph was obtained from the melt by cooling the 2 TAGs mixture at $2ºC \cdot min^{-1}$. A possible explanation of the phenomena observed is the crystallization of a metastable alloy of the two TAG components. When heating, this alloy probably melted and individual TAGs crystallized (melt-mediated transformation). Finally, β'_{OOO} melted at around 1.4ºC (peak 5), followed by the melting of β'_{POO} at 6.3ºC (peak 6) (T_{onset} values).

By adding OOL, the DSC heating curve became simpler than that of the 2 TAGs mixture, and more similar to that of extra virgin olive oil (Arbequina variety). As to the laboratory-scale XRD patterns, they became almost identical to that of the 2 TAGs mixture. Thus, by cooling the 3 TAGs mixture at $2ºC \cdot min^{-1}$, a clear exothermic peak (peak 1 in Figure 4.3c), with a single onset temperature at -25.1ºC, appeared in the DSC cooling curve. Simultaneously, laboratory-scale XRD data showed the occurrence of a β'-2L form, which was identified by a double chain length peak at 4.5 nm and short angle diffraction peaks at 0.45 nm, 0.43 nm, 0.40 nm and 0.39 nm. When the sample was heated, an endothermic peak appeared at around -10.6ºC (peak 2) and it was followed by a broader one (peak 3) characterized by two onset temperatures at -4.7ºC and 3.4ºC, respectively. XRD data revealed, at approximately -5ºC, the occurrence of a new β'-3L form at the expense of β'-2L form. The newly formed β'-3L phase was detected by the presence of a triple chain length peak at 6.7 nm and short angle

diffraction peaks at 0.45 nm, 0.43 nm, 0.41 nm at 0.40 nm. XRD peaks of this β'-3L form totally vanished at 15ºC. Similarly to the 2 TAGs mixture case, when the sample was cooled, probably some molecular alloy of the three TAG components (OOO, POO and OOL) was formed. When heating, single TAG components may have occurred from the alloy, and they finally melted. However, in the 2 TAGs mixture thermogram, three endothermic peaks were observed in the heating curve, whereas only two appeared in the 3 TAGs mixture DSC profile. Considering the melting points of β' forms of OOO (around -15ºC), POO (14ºC) and OOL (-20ºC) (see Chapter 2), most probably a shifting to higher temperatures took place, due to the coexistence of the three TAGs in the system, and overlapping phenomena occurred. Moreover, it was not possible to distinguish β'_{OOO} and β'_{OOL}, as their long spacing values become identical (4.5 nm, Chapter 2).

No important changes were observed when POL was added. Figure 4.2d and Figure 4.3c depict the DSC thermogram of the 4 TAGs mixture and the corresponding XRD patterns, respectively.

When the 4 TAGs mixture was cooled at 2ºC·min^{-1}, again a β'-2L form was detected by the corresponding XRD peaks at 4.5 nm, and 0.45 nm, 0.43 nm, 0.41 nm and 0.39 nm in the wide and short angle regions, respectively. The corresponding exothermic DSC peak became different from that of the 3 TAGs mixture, as it consisted of a double crystallization peak with two clear onset temperatures (at -26.6ºC and -31.9ºC). Moreover, the addition of POL caused a shifting of the main crystallization peak to lower temperatures (see Figure 4.3). As to the heating process, again only two endothermic peaks appeared in the DSC curve. The first one appeared at a T_{onset} of -11.4ºC, and two different onset temperatures (-6.6ºC and 1.6ºC) were determined for the second endothermic peak (peak 3 in Figure 4.3d). Similarly to all the previous mixtures discussed in this section, the XRD data revealed the occurrence of a β'-3L form at the expense of β'-2L form, at around 0ºC. In this case, the long spacing value of the triple chain length structure was 6.5, instead of 6.7, but β' peaks at 0.45 nm, 0.43 nm and 0.40 nm were also present. Finally, the β'-3L XRD peaks vanished at 10ºC.

By comparing the DSC thermograms of multicomponent TAG mixtures containing from 2 to 4 TAGs, one may notice progressive changes as TAGs were successively added. The most important variations were observed when OOL was included in the system, as three endothermic peaks appeared in the DSC heating curve

of the 2 TAGs mixture, whereas only two were observed in the 3 TAGs mixture case. However, all the XRD patterns (for mixtures from 2 to 4 TAG components) became almost identical. At this point, one may take into account the structural similarity between some of the TAG components. As previously shown in Chapter 2, a similar polymorphic behavior was observed, on the one hand, in triunsaturated TAGs (such as OOO and OOL) and, on the other hand, in saturated-unsaturated-unsaturated TAGs (like POO and POL). Thus, in general, with the addition of new TAGs to the mixtures, no considerable changes were appreciated, especially in the XRD patterns. Only β'-2L and β'-3L forms were detected in the laboratory scale XRD data, due to different polymorphic behavior caused by two groups of TAGs: triunsaturated OOO and OOL and saturated-unsaturated-unsaturated POO and POL.

More appreciable changes were noted when a saturated-saturated-unsaturated (PPO) TAG was added. Figures 4.2e and 4.3d respectively show the DSC thermogram and the corresponding XRD patterns of the 5 TAGs mixture (composed by OOO, POO, OOL, POL and PPO). Two crystallization processes were observed in the DSC cooling curve. The first one took place at -9.0ºC, which is at higher temperatures than in the cases described above. Simultaneously, the XRD wide angle region exhibited a double chain length peak at 5.3 nm, whereas typical sub-α form peaks appeared in the wide angle region, at 0.42 nm and 0.37 nm. This sub-α form may be caused by the presence of PPO. However, previous work which reported on the polymorphism of PPO (Minato et al., 1997a) did not describe any sub-α form for this TAG. On further cooling, at -30.0ºC, an additional β'-2L crystallization took place, as XRD data revealed by the occurrence of a double chain length peak at 4.5 nm and short angle peaks at 0.45 nm, 0.43 nm, 0.41 nm and 0.39 nm. When heating, at -10ºC, the typical sub-α peak at 0.41 nm vanished, due to its melting or some polymorphic transformation. Right after, at -6ºC, new β'-3L XRD peaks appeared, at the expense of β'-2L peaks, at 6.5nm in the wide angle region, and at 0.45 nm, 0.43 nm and 0.40 nm in the short angle region. No XRD peaks were present at 10ºC, revealing the melting of β'-3L form. As to the DSC results, only two broad endothermic peaks with T_{onset} at -10.3ºC (peak 2 in Figure 4.2e) and -2.8ºC (peak 3), respectively, appeared in the DSC heating curve. Thus, complex phenomena took place within the same temperature ranges, obtaining broad responses by the DSC. One may pay attention to the flatness of the DSC signals if they are compared to those of the 4 TAGs mixture.

As to the 6 TAGs mixture, no considerable differences were observed when SOO was added. We should remind the saturated-unsaturated-unsaturated structure of this TAG, which may display a similar polymorphic behavior to that of POO and POL. Figure 4.2f shows the corresponding DSC thermogram, while XRD patterns taken as a function of temperature are depicted in Figure 4.4. For this sample, SR-XRD with SAXD and WAXD measurements were carried out, and the results obtained could be compared with the laboratory-scale XRD data.

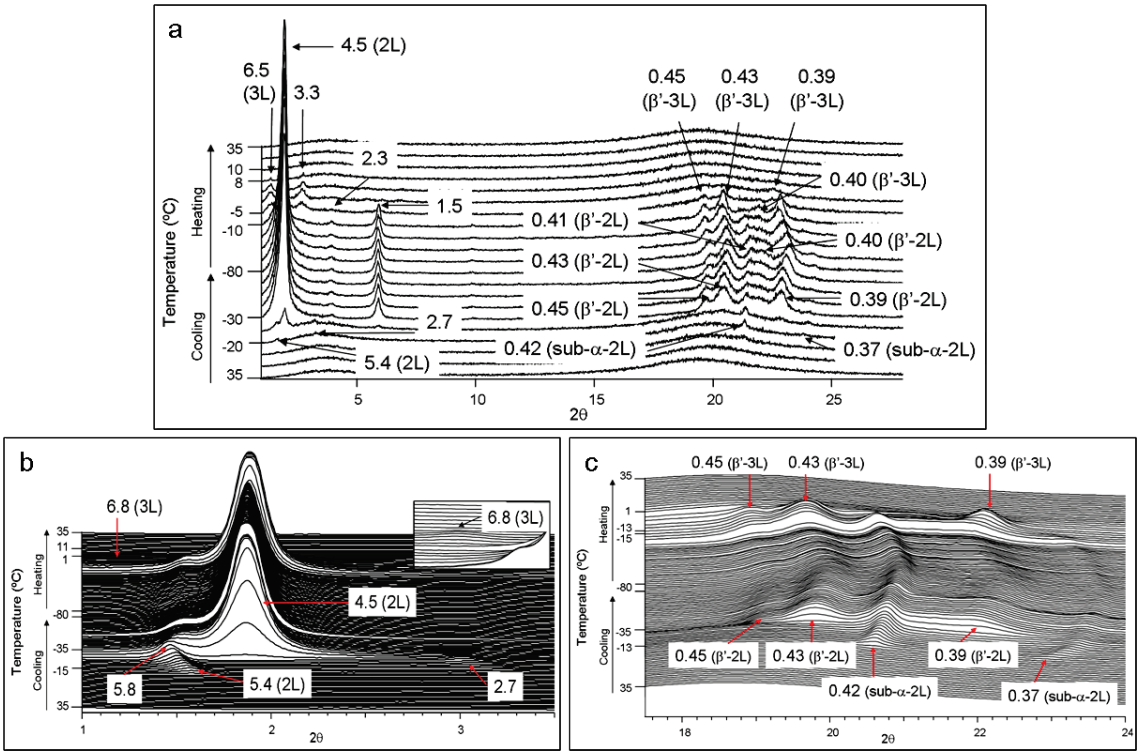

Figure 4.4. XRD patterns of multicomponent TAG mixture of 6 TAG components (38% OOO + 25% POO + 19% OOL + 11% POL + 4% PPO + 3% SOO). a) Laboratory-scale XRD. b) SR-SAXD pattern. c) SR-WAXD pattern.

Similarly to the 5 TAGs case, by cooling the 6 TAGs mixture at 2ºC·min^{-1}, a sub-α-2L crystallization occurred at -10.6ºC. Both laboratory-scale XRD and SR-XRD results revealed the corresponding double chain length structure by a peak at 5.4 nm, and the short angle region showed the typical sub-α form peaks at 0.42 nm and 0.37 nm. Later on, another exothermic peak at -30.5ºC was detected in the DSC cooling curve, corresponding to an additional crystallization of β'-2L form. The long and short spacing values of this form, obtained by both laboratory-scale XRD and SR-XRD were also identical (4.5nm, and 0.45 nm, 0.43 nm and 0.39 nm). As to the heating step, and

differently from the previous TAGs mixtures examined, an exothermic DSC peak (peak 2 in Figure 4.2f), having an onset temperature at -14.0ºC, preceded the first broad endothermic peak, which appeared at -10.2ºC. However, XRD results were the same than those of the 5 TAGs mixture. Within this temperature range, at -13ºC, SR-XRD data clearly revealed the extinction of sub-α peaks at 0.42 nm and 0.37 nm. Moreover, at approximately -5ºC, a triple chain length peak at 6.5 nm, corresponding to β'-3L form, appeared at the expense of the double chain length peak at 4.5 nm. It should be noted that, according to the SR-XRD data, the long-spacing value of this β'-3L form was slightly higher (6.8 nm) than that of the laboratory-scale XRD (6.5 nm). The broad endothermic DSC signal, labelled as peak 5 in Figure 4.2f, had a T_{onset} of -1.6ºC. XRD data revealed the total extinction of β'-2L peaks at around 1ºC, whereas β'-3L peaks disappeared at approximately 11ºC.

Finally, an extra virgin olive oil sample, coming from the Arbequina olive variety was examined, following the same procedure. Surprisingly, not important differences were appreciated in the DSC cooling and heating curves (Figure 4.2g) compared to the thermal response of the 6 TAGs mixture sample (Figure 4.2f), and the respective XRD patterns were almost identical (compare Figures 4.4 and 4.5). This fact revealed a weak influence of the minor compounds present in the olive oil sample, as it will be discussed later.

By cooling the olive oil sample, a sub-α-2L form crystallized from the melt at -12.4ºC (peak 1 in Figure 4.2g). Short spacing values of this sub-α-2L form were the same as those of the 6 TAGs mixture (0.42 nm and 0.37 nm), whereas the long spacing value became higher (5.8 nm), as confirmed by both laboratory-scale XRD and SR-XRD. On further cooling, the main crystallization peak, corresponding to β'-2L form (4.5nm, and 0.45 nm, 0.43 and 0.39 nm) appeared at lower temperatures (T_{onset}= -35.4ºC), compared to that of the mixture of 6 TAG components. Afterwards, when olive oil was heated at 2ºC·min^{-1}, a very broad endothermic peak, whose peak top temperature was -28.3ºC, was present. Its onset temperature could not be defined, due to its broadness. No variations appeared in the XRD pattern at this point. Soon after, an exothermic peak was present in the DSC heating curve, but at lower temperatures compared to that of the 6 TAGs mixture, and its onset temperature was -25.2ºC. The DSC profile also showed an endothermic signal with a shoulder, which defined two onset temperatures at -15.5ºC and -11.3ºC, respectively. Within this temperature range,

at -13ºC, XRD peaks corresponding to sub-α-2L form (5.8 nm, 2.9 nm, and 0.42 nm, 0.37 nm) vanished. Later, at -5ºC, triple a chain length peak at 6.6 nm (β'-3L) appeared while the intensity of the double chain length peak at 4.5 nm decreased. Simultaneously, the SR-XRD data clearly showed, through the WAXD pattern, the occurrence of a new β' peak at 0.40 nm. Finally, at the end of the DSC heating curve, a broad DSC signal with T_{onset} at -3.7ºC (peak 5 in Figure 4.2g) was observed. At the same time, XRD results revealed the total disappearance of β'-2L form at 1ºC, and the melting of β'-3L at around 11ºC.

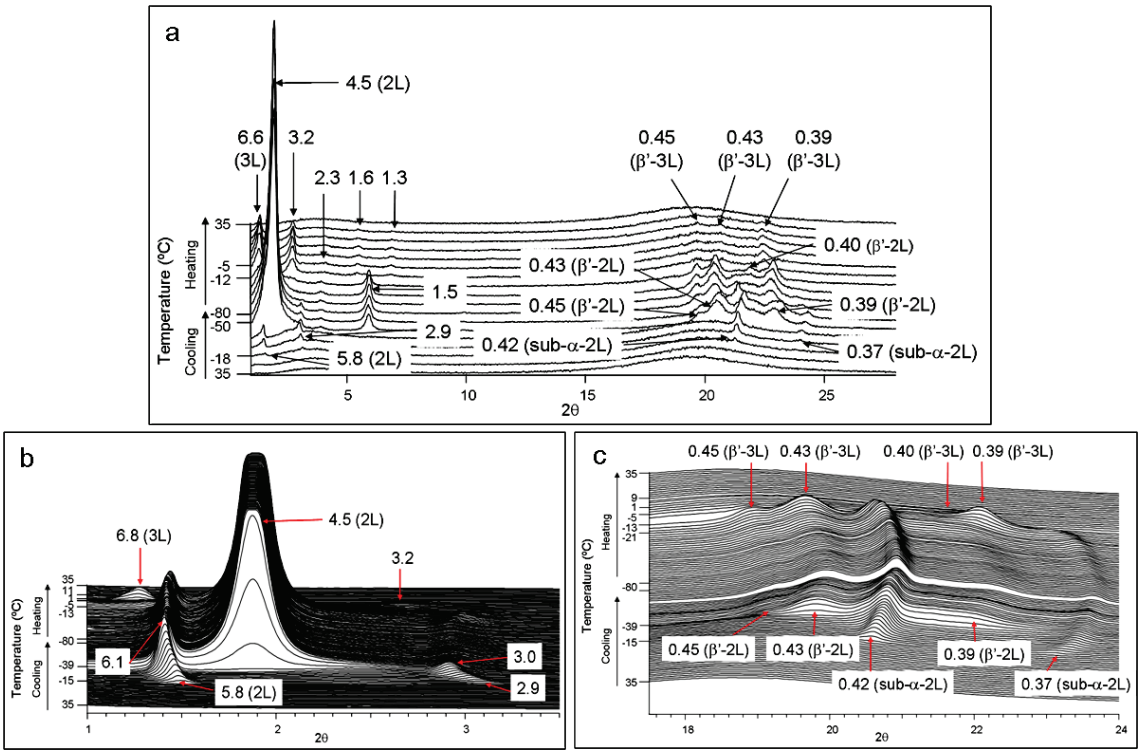

Figure 4.5. XRD patterns of extra virgin olive oil (Arbequina variety). a) Laboratory-scale XRD. b) SR-SAXD pattern. c) SR-WAXD pattern.

Very recently, Barba et al. (2012) reported on the crystallization and melting behavior of extra virgin olive oil by using DSC and SR-XRD. However, only very approximate conclusions could be extracted from the experimental results. The results showed in the present study are in discordance with those discussed by Barba et al. (2012). The authors described the crystallization of β' form when an extra virgin olive oil sample was cooled at 2ºC·min^{-1}, which partly transformed to most stable β form when heating. However, in the present work, we firstly observed the occurrence of a

sub-α form (2L), accompanied by a β' (2L) crystallization, and no β formation was detected during the heating step. The study of multicomponent TAG mixtures by using the main TAGs of olive oil permitted to understand in more detail the polymorphic behavior of such a complex sample.

The DSC results plotted in Figure 4.2 graphically showed the influence of every TAG component. Most important differences were observed when OOL was added to the 2 TAGs mixture (OOO and POO), as the complex DSC heating curve including exothermic and endothermic peaks (see Table 4.3) changed to a DSC profile only having two broad endothermic peaks. More variations were detected in the general polymorphic behavior when PPO (a saturated-unsaturated-unsaturated TAG) was added to the 4 TAGs mixture (OOO, POO, OOL and POL). At this point, a new exothermic DSC peak appeared at around -30ºC, which was due to the crystallization of a sub-α-2L form, as laboratory-scale XRD and SR-XRD data confirmed. The increasing complexity of the multicomponent TAG mixtures was reflected in the DSC thermograms, as broader and flatter signals appeared while increasing the number of TAGs.

However, the highly complex polymorphic behavior observed in the multicomponent TAG mixtures can be approximately understood by considering three main groups of TAG components: triunsaturated TAGs (OOO and OOL), saturated-unsaturated-unsaturated TAGs (POO, POL, SOO) and saturated-saturated-unsaturated TAGs (PPO). As shown in Chapter 2, the TAGs belonging to the same structural group display a very similar polymorphic behavior.

Finally, by comparing the results obtained after analyzing the mixture of 6 TAG components and extra virgin olive oil, one may realize that, despite of some differences, the general response, determined by DSC and XRD experiments, became considerably similar. Thus we may conclude that the 6 main TAGs present in olive oil, which are OOO, POO, OOL, POL, PPO and SOO, and approximately configure the 92% of its composition, mostly determine their polymorphic behavior. As to minor components, the may not have a strong influence.

4.4.

Edible fats and oils authentication

4.4.1. Determination of adulteration of extra virgin olive oil with hazelnut oil

Virgin olive oil becomes a high-value agricultural product, which is typical of the Mediterranean basin, and whose market has expanded to North Europe, USA, China and Japan. The increasing popularity of this product has been mainly attributed to its unique sensory, health and nutritional properties (Harwood et al., 2002).

For the reasons explained above, cheaper vegetable oils with similar chemical compositions to those of virgin and extra virgin olive oils are commonly employed as adulterants, leading to significant economic benefits. In particular, fraudulent small amounts of hazelnut oil are often added to virgin olive oil, due to the similar chemical composition of both major (fatty acids and triacylglycerols) and minor components. These similarities complicate the detection of small amounts of hazelnut oil in olive oil, especially at concentrations below the 10%. Moreover, some factors, such as climate and genotype, have a strong influence on the chemical composition of both kinds of oils (Shaw et al., 1997), making it more difficult to detect fraudulent additions of hazelnut oil in olive oil.

Therefore, several attempts to detect the presence of hazelnut oil in virgin or extra virgin olive oils, by using different techniques, have been reported.

As to methods based on chromatographic techniques, Parcerisa et al. (2000) detected from 10% to 50% of hazelnut oil in olive oil by applying high-performance liquid chromatography (HPLC)-atmospheric pressure chemical ionisation mass spectrometry for the TAGs determination and gas-liquid chromatography for tocopherols and sterols. The analysis of polar components, by solid phase extraction (SPE)-based isolation of the polar fraction, followed by reverse phase (RP)-HPLC analysis with UV detection, permitted detecting virgin olive oil adulterated with pressed hazelnut oil at levels as low as 5% (Zabaras et al., 2004). Less than a 4% of hazelnut oil was detected by Damirchi et al. (2005), applying gas chromatography-mass spectrometry (GC-MS) by using sterol fractions as potential markers. On the other hand,

Flores et al. (2006) detected adulterations of olive oil of different varieties with virgin hazelnut oils in percentages of up to 7% with the use of solid phase micro-extraction and multidimensional gas chromatography (SPME-MDGC) (Frankel, et al., 2010). Also several methods of analysis of volatile compounds, with subsequent chemometric treatments of data, allowed detection of olive oil adulteration with different contents of hazelnut oil ranging from 5% to 50% (v/v) (Mildner-Szkudlarz et al., 2008). Hazelnut oil additions of 6% and 15% (v/v) were detected, when direct analysis in real time (DART) coupled to a high-resolution time-of-flight mass spectrometer (TOFMS) was employed (Vaclavik et al., 2009).

Most of the methods mentioned above become expensive and time-consuming, so that spectroscopic techniques have been proposed as an alternative. Adulteration of virgin olive oil with hazelnut oil could be detected only at levels of 25% and higher, by using FT-IR spectroscopy (Ozen et al., 2002). Baeten et al. (2005) applied FT-Raman and FT-Mid-IR to detect more than 8% of hazelnut oil in olive oil. They stated that this determination was possible if both oils were Turkish, and that the detection limit became higher when the blends came from edible oils from diverse geographical origins. As to nuclear magnetic resonance (NMR) techniques, ^{1}H NMR allowed detections between 5% and 10% adulteration of olive oils with refined hazelnut oils (Mannina et al., 2009; Agiomyrgianaki et al., 2010), whereas ^{13}C NMR spectroscopy permitted detecting adulterated olive oils, extracted from different cultivars, with 5% and 20% of cold-pressed hazelnut oil (Vlahov et al., 2009). Spectrofluorimetric methods joined to multivariate analysis permitted detecting concentrations of 5%, 10%, 15%, 20%, 25% and 30% of raw and refined hazelnut oil in virgin olive oil. (Sayago et al., 2004).

As to the use of DSC as a detection method, it becomes a rapid and sensible technique and does not require the use of solvents. DSC has been applied to the characterization of olive oil as a function of their olive varieties and chemical composition (Jiménez et al., 2003; Jiménez et al., 2007; Chiavaro et al., 2007; Chiavaro et al., 2008a) their different commercial categories (Chiavaro et al., 2008b), their quality (Angiuli et al., 2006; Ferrari et al., 2007) and the influence of seasonal changes (Ilyasoglu et al., 2011). However, Chiavaro et al. (2008c) used DSC to verify adulteration of extra virgin olive oil with refined hazelnut oil, by analyzing both the cooling and heating DSC thermal profiles. They were capable of detecting fraudulent additions of 5% and higher.

The aim of this study was to detect adulterations of different kinds of hazelnut oil in virgin and extra virgin olive oils obtained from different olive varieties, by using DSC and complementing the thermal data with XRD, and make an approach to the polymorphic behavior of the samples. Moreover, a first step in chemometric calculations was also carried out. In view of the reported percentages (approximately until 5%) of hazelnut oil detected in adulterated olive oil samples, our purpose was to try to detect lower additions than 5%.

Samples of hazelnut oil and virgin and extra virgin olive oil were obtained from different Catalan producers and cooperatives. Thus, origin and nature of samples were properly known and controlled. Details of the olive and hazelnut oil samples are given in Tables 4.4 and 4.5, respectively.

Table 4.4. Description of the olive oil samples used, including its type, olive variety, origin and production period.

Sample name	Type	Olive variety	Origin	Production
O1	Virgin	65% Vera 24% Blanquilla 10% small Corbella 1% Verdal	Molí Roch del Bages (Sant Fruitós de Bages)	December 2010
O2	Extra virgin	100% Arbequina	Coselva (La Selva del Camp)	December 2010
O3	Virgin	90% Vera 5% Blanquilla 2% big Corbella 1% small Corbella	Molí Roch del Bages (Sant Fruitós de Bages)	January 2011
O4	Virgin	80% Arbequina 20% Blanquilla	Molí de cal Nasi (Piera)	November 2010
O5	Extra virgin	100% Arbequina	Molí Roch del Bages (Sant Fuitós de Bages)	n.d.

n.d. Not determined

Table 4.5. Description of hazelnut oil samples used, including its type and origin. Variety and production period could be determined in some case.

Sample name	Type	Hazelnut variety	Origin
H1	Raw pressed	n.d.	Vom Fass (France)
H2	Refined	n.d.	Afruse (Reus)
H3	Raw pressed in lab	Negreta (Selva del Camp) (production on September 2011)	Obtained by using a pilot plant press
H4	Refined	n.d.	France
H5	Refined	n.d.	Turkey

n.d. Not determined

Total fatty acid compositions were determined by GC for all olive oil and hazelnut samples. As an example, here we present the fatty acid composition of samples O2 (olive oil) and H1 (hazelnut oil) (see Table 4.6). However, it should be noted that some differences were detected between the different olive and hazelnut oils. These variations in the fatty acid compositions could be due to several determining factors, such as the olive variety used, the production and harvest periods, the climate, the geographical area and the quality of the soil (Sánchez et al., 2009).

Table 4.6. Fatty acids compositions of O2 and H1 samples (% of total fatty acid).

	O2	H1
Palmitic (16:0)	13.96	5.64
Palmitoleic (16:1n7)	1.37	0.21
Stearic (18:0)	1.77	2.60
Oleic (18:1n9)	69.90	79.58
Vaccenic (18:1n7)	3.16	1.09
Linoleic (18:2n6)	8.72	10.56
Linolenic (18:3n3)	0.56	0.11
Eicosenoic (20:1n9)	0.33	0.16
Behenic (22:0)	0.13	0.02
Arachidonic (20:4n6)	0.01	n.d.
Lignoceric (24:0)	0.06	0.01

n.d. Not detected

The results obtained are in good agreement with those reported in previous work (Chiavaro et al. 2008c). The main fatty acid present in sample O2 was oleic acid (69.90%), which was followed by palmitic (13.96%) and linoleic (8.72%) acids. The three main fatty acids of H1 sample were the same, being oleic acid the main one (79.58%), but followed by linoleic (10.56%) and palmitic (5.64%) acids. By comparing the fatty acid compositions of O2 and H1, one may notice that H1 showed significantly higher amounts of oleic and linoleic acids than did O2, whereas the latter had significantly higher contents of palmitic and palmitoleic acids.

TAG compositions have not been determined yet for the samples analyzed in this study. However, previous studies showed very similar TAG profiles in olive and hazelnut oils (Chiavaro et al., 2008c). This fact makes it difficult to differentiate between the oils and, even more challenging, to identify the presence of small amounts of hazelnut oil in olive oil.

Blends of hazelnut oil (from H1 to H5) and olive oil (from O1 to O5) samples were prepared, as summarized in Table 4.7. In this table, the percentages (wt/wt) of hazelnut oil, which were added to olive oil samples, are shown.

Table 4.7. Amounts (%, wt/wt) of hazelnut oils added to each olive oil sample.

	H1	**H2**	**H3**	**H4**	**H5**
O1	1% 2% 5% 10% 20%				
O2	1% 2% 5% 10% 20%	1% 2% 5%	1% 2% 5%	1% 2% 5%	1% 2% 5%
O3	1% 2% 5% 10% 20%	1% 2% 5%	1% 2% 5%	1% 2% 5%	1% 2% 5%
O4	1% 2% 5%				
O5	1% 2% 5%				

At first, we analyzed mixtures containing 1%, 2%, 5%, 10% and 20% of hazelnut oil (H1) in O1, O2 and O3. However, later we focused on the mixtures containing, at most, a 5% of hazelnut oil, as 10% and 20% became too high, and several methods are able to detect higher amounts than a 5% of hazelnut oil in olive oil (see introduction of this section).

As shown in Table 4.7, not all the possible mixtures between all olive and hazelnut oils were prepared and analyzed. H1 was added to all the olive oil samples (from O1 to O5). Later we focused on O2 and O3, to which all hazelnut oils were added. The reason why these olive oil samples were selected is related to the olive variety. As summarized in Table 4.4, O2 is a monovarietal olive oil, from the Arbequina variety, whereas O3 becomes multivarietal, mainly constituted by Vera (90%), but also formed by Blanquilla (5%), big Corbella (2%) and small Corbella (1%). Thus, we wanted to observe the effects caused by fraudulent additions of hazelnut oils in monovarietal and multivarietal olive oils.

Nevertheless, to describe one example, in this section we will only show those results obtained for mixtures of O2 and H1, as the polymorphic behavior of O2 (Arbequina) was more deeply characterized (see section 4.3 of this chapter).

By using DSC, olive and hazelnut oil, and their blends were all cooled from 35ºC to -80ºC and heated afterwards to 35ºC. The cooling and heating rates used were 2ºC·min^{-1} in all cases. Figure 4.6 depicts the cooling (Figure 4.6a) and heating (Figure 4.6b) thermal behavior of sample O2 and its mixtures with H1, where hazelnut oil was present in a 1%, 2%, 5%, 10% and 20%.

One may notice that, as H1 was added to the O2 sample, the main crystallization peak that appeared at around -35ºC (T_{onset}) in the DSC cooling curve of O2, became sharper and shifted to higher temperatures (having a T_{onset} at -32ºC in the mixture containing 20% of H1). The wideness of the peak changed approximately from 6ºC to 3ºC, when a 20% of H1 was included in O2.

Clearer differences were observed in the DSC heating curve. The shoulder, which appeared at a T_{onset} of around -17ºC in the O2 heating thermogram, was transformed into a clear peak that became sharper when the amount of H1 increased. Moreover, the last melting peak with a T_{onset} at -4ºC became narrower (the T_{end} of the peak moved to lower temperatures). Thus, significant variations were detected by only looking at the DSC cooling and heating profiles when H1 was added to O2, even when the fraudulent additions were lower than the 5%. Laboratory-scale XRD experiments

were also carried out to determine if those differences were also reflected in the corresponding XRD patterns (see below).

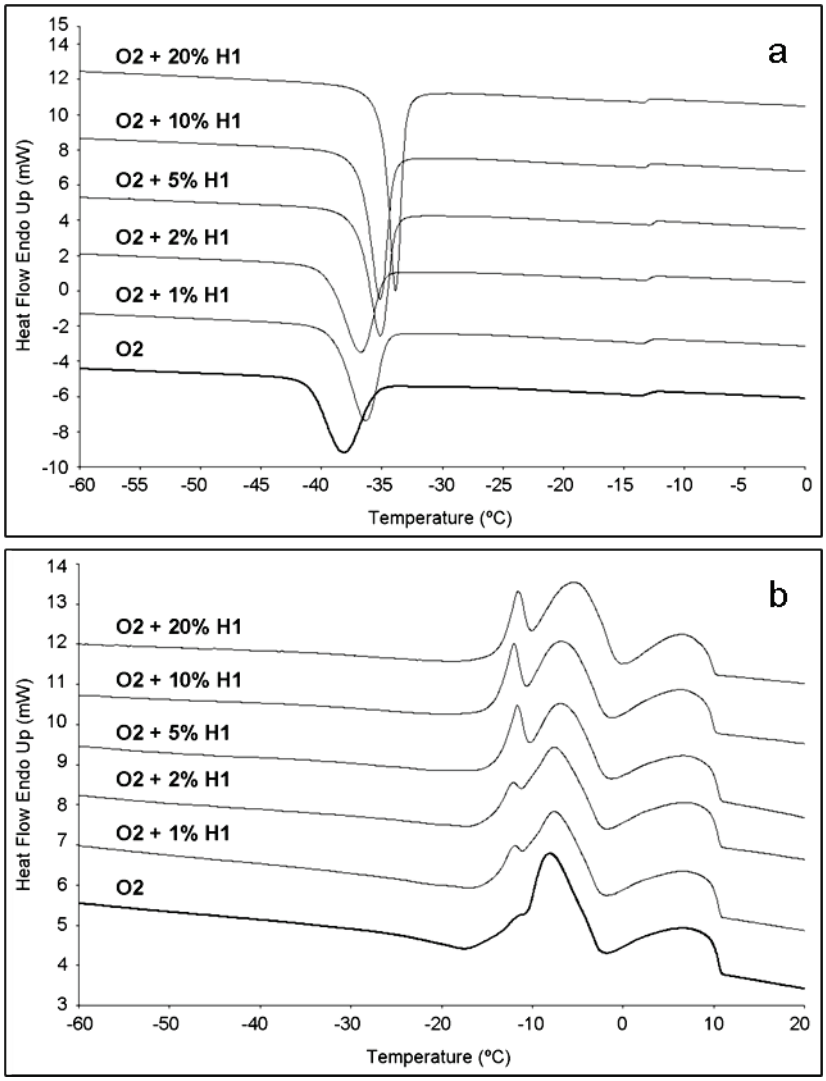

Figure 4.6. Thermal behavior of sample O2 (extra virgin olive oil, Arbequina variety), and 1, 2, 5, 10 and 20% (wt/wt) mixtures of H1 (hazelnut oil, pressed raw material) in O2 and. a) Cooling DSC curves. b) Heating DSC curves.

Figure 4.7 depicts the DSC cooling and heating curves of O2 (Figure 4.7a), a mixture of O2 and 5% of H1 (Figure 4.7b) and H1 (Figure 4.7c), including all the onset and end temperatures of the phenomena observed. It should be noted that the error bars associated at each temperature were comprised between 0.3 and 1.0ºC.

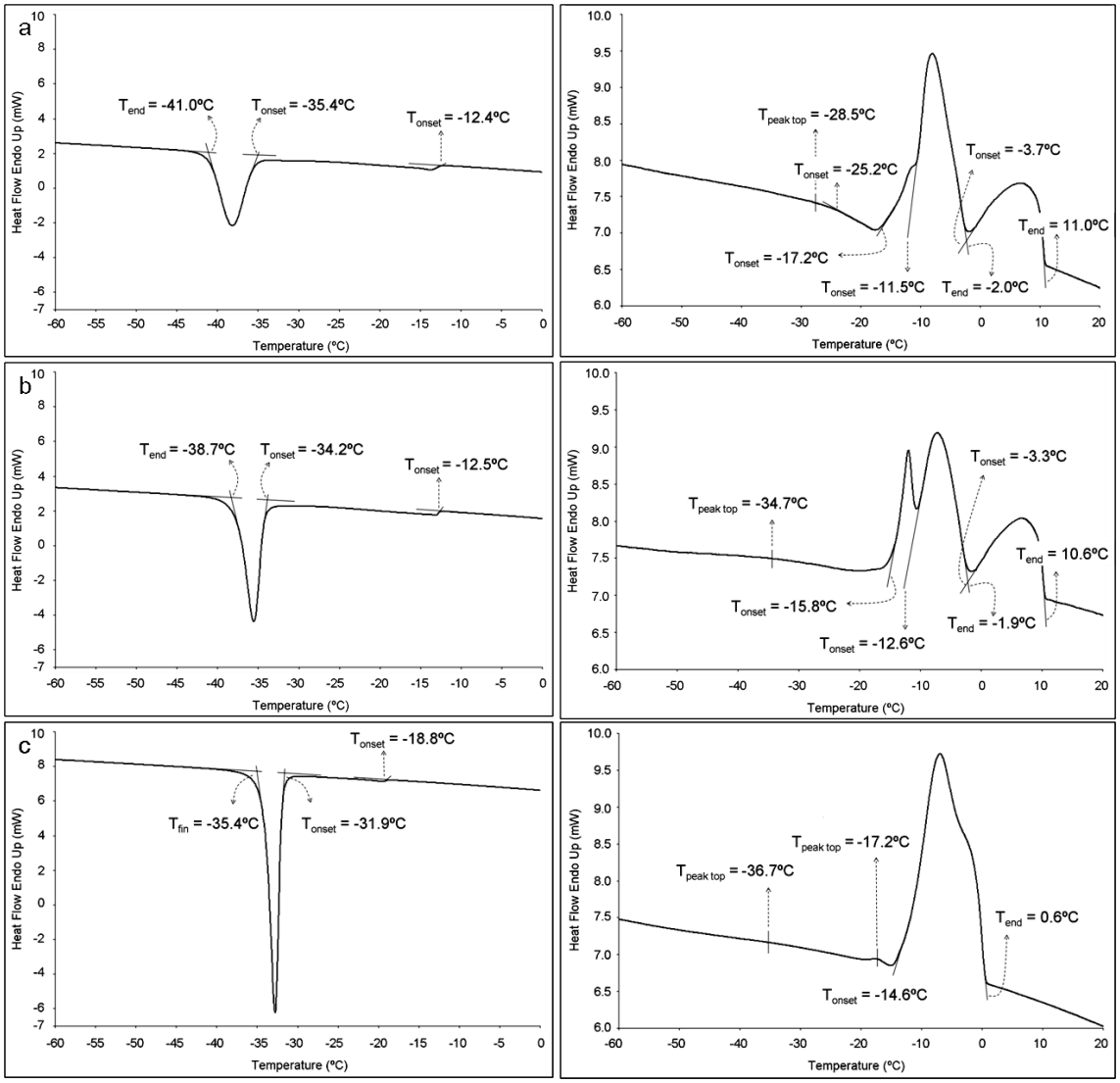

Figure 4.7. DSC cooling and heating curves. a) Sample O2. a) 5% (wt/wt) mixture of H1 in O2. c) Sample H1.

Figure 4.8 shows the corresponding XRD patterns of O2, O2 containing a 5% of H1, and H1.

The polymorphic behavior of O2 (extra virgin olive oil of the Arbequina olive variety) was already discussed in section 4.3 of the present chapter, but it can be summarized as follows. When O2 was cooled at a rate of 2ºC·min^{-1}, a sub-α-2L form crystallized from the melt at -12.4ºC. This sub-α-2L form could be identified by two wide angle diffraction peaks at 0.42 nm and 0.37 nm, and its double chain length structure was deduced by the presence of a peak at 5.8 nm in the short angle region. On further cooling, another crystallization (β'-2L, in this case) occurred at around -35.4ºC. The newly formed β'-2L crystals had a long spacing value of 4.5 nm and short spacing

values of 0.45 nm, 0.43 nm and 0.39 nm. As to the heating step, the DSC heating curve showed a very broad peak, whose onset temperature could not be properly defined, so that the peak top temperature was determined and its value was -28.5ºC. No variations appeared in the XRD pattern at this point. Soon after, an exothermic peak appeared at -25.2ºC, followed by two endothermic signals. Two different onset temperatures were defined for the first endothermic peak (-17.2ºC and -11.5ºC). At -13ºC, the XRD peaks corresponding to sub-α-2L form disappeared due to its melting or polymorphic transformation. Later, at -5ºC, the XRD data showed that the intensity of β'-2L peaks decreased while new peaks, corresponding to a β'-3L form (6.6 nm, and 0.45 nm, 0.43 nm and 0.39 nm) appeared. The last endothermic peak present in the DSC heating curve had a T_{onset} value of -3.7ºC, and corresponded to the total disappearance of β'-2L form at 1ºC and the β'-3L melting at around 11ºC.

DSC and XRD data of O2 containing a 5% of H1 are displayed in Figures 4.7b and 4.8b, respectively. Although clear differences were observed in the DSC cooling and heating curves compared to those of sample O2, no variations were detected in the XRD patterns. When the blend of O2 and H1 was cooled, the first crystallizing form was a sub-α-2L form, with a long spacing value of 5.8 nm and short spacing values of 0.42 nm and 0.37 nm. On further cooling, at -34.2ºC a new exothermic peak appeared, which corresponded to a β'-2L crystallization, defined by a double chain length peak at 4.5 nm and short angle diffraction peaks at 0.45 nm, 0.43nm and 0.39 nm. In the heating process, again a very broad endothermic peak, with a peak top temperature of -34.7ºC was present. This peak appeared at lower temperatures, compared to that of O2, and no variations were observed in the corresponding XRD patterns. Later, a series of three endothermic peaks with T_{onset} at -15.8ºC, -12.6ºC and -3.3ºC, respectively, were detected in the DSC heating curve. According to the XRD data, at -12ºC sub-α-2L form vanished and, at -5ºC, the intensity of the peaks corresponding to β'-2L form decreased, while new peaks of a β'-3L form appeared at 6.5 nm and 0.45 nm, 0.43 nm and 0.40 nm. Finally, the last DSC signal was due to the total disappearance of β'-2L form and the melting of β'-3L form.

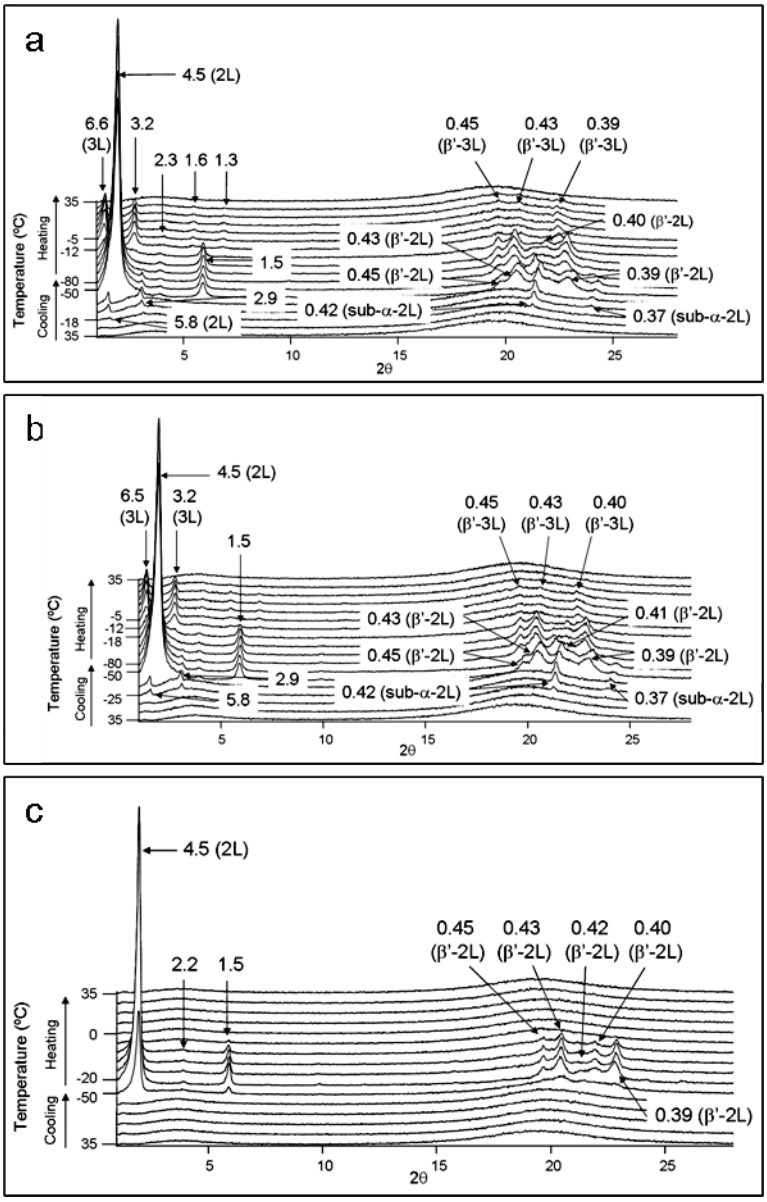

Figure 4.8. Laboratory-scale XRD patterns. a) Sample O2. a) 5% (wt/wt) mixture of H1 in O2. c) Sample H1.

Despite the similar TAG composition of olive oils and hazelnut oils (Chiavaro et al., 2008c), in this study we observed that both the DSC thermograms and XRD patterns of H1 (hazelnut oil) became highly different to those of O2 (olive oil). Although the H1 DSC cooling curve also showed two exothermic phenomena (at -18.8ºC and -31.9ºC, respectively), the XRD data only revealed one crystallization process. This crystallization corresponded to a β'-2L form, having a long spacing value of 4.5 nm and short spacing values of 0.45 nm, 0.43 nm, 0.42 nm, 0.40 nm and 0.39 nm. In the DSC heating curve, again a very broad endothermic peak was present, with a peak top

temperature of -36.7ºC in this case. This peak became flatter than the equivalent observed in the O2 thermogram, and it was followed by other two endothermic peaks: a smaller one with a peak top temperature of -17.2ºC, and a more intense one (with shoulder) that appeared at -14.6ºC. The only information given by the laboratory-scale XRD pattern was the melting of the β'-2L form, as XRD peaks disappeared at 0ºC.

Referring to the XRD results, no significant differences were detected between O2, and O2 containing a 5% of H1. Although the XRD pattern of O2 became highly different to that of H1, the results obtained for O2, and O2 containing 5% of H1 were indistinguishable.

By contrast, very clear differences were observed in the DSC thermograms, especially in the DSC heating curve, even when H1 was added to O2 in percentages lower than 5%. In order to use the DSC profile as a fingerprint to detect adulterations of olive oil with hazelnut oil, the variations observed in the DSC profiles needed to be quantified. Some authors have deconvolutionated the DSC curves by using specific software (Chiavaro et al., 2007). Nevertheless, one may consider that thermal peaks do not follow any specific mathematic function, such as Gaussian or Lorentzian. In addition, in most of cases, overlapping of several signals occurred, so that it is difficult to know what phenomena are there and the deconvolution of DSC signals should not be applied. Thus, we decided to carry out two different determinations, which are the following:

i) Partial areas determination of the DSC signals that appeared in the heating profiles.
ii) Difference between the peak heights values of two endothermic peaks present in the DSC heating curves.

As to the partial areas determination, we focused on the endothermic peaks which appeared between -20ºC and 15ºC, defining three different partial areas (one for each DSC peak). As when hazelnut oil was added the intensity of the first endothermic peak increased and the third peak became narrower, the partial areas determination should demonstrate such differences. Figure 4.9 illustrates an example of the three partial areas commented above.

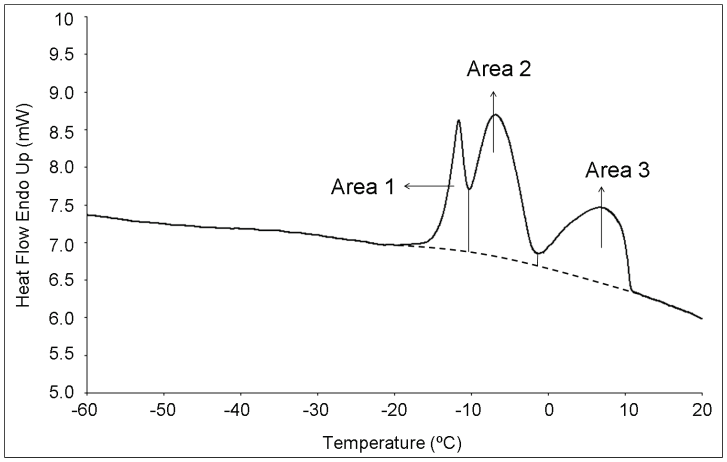

Figure 4.9. Partial areas taken from the DSC heating curve of a blend of O2 and a 5% of H1.

Results of the partial areas determination for mixtures of O2 and H1 (from 1 to 20%) are shown in Table 4.8.

Table 4.8. Partial areas of O2 and blends of O2 and H1.

	Blends of O2 and H1					
Partial areas	0% H1	1% H1	2% H1	5% H1	10% H1	20% H1
1	10 ± 1	10 ± 1	12 ± 5	16 ± 3	16 ± 1	15 ± 2
2	45 ± 2	42 ± 5	40 ± 5	38 ± 3	40 ± 3	46 ± 3
3	45 ± 1	48 ± 5	48 ± 4	46 ± 6	45 ± 4	40 ± 2

One may notice a progressive increase of the partial area of peak 1, and a decrease of that of peak 3, when the amount of H1 increased in the blends. However, taking into account the error bars associated at each value, we must conclude that a clear tendency can not be defined. Here we should mention the difficulties that arose in the partial areas determination, as the complexity of DSC signals and the baseline complicated the selection of the temperatures that defined the limits of the partial areas.

Regarding the calculation of the difference in peak heights, we considered the second main endothermic peak (peak top temperature at around -7ºC) and the first endothermic peak, whose intensity became higher when the amount of H1 increased in

the blends (peak top temperature at approximately -11ºC). Table 4.9 shows the difference in peak heights of samples O2 and its blends with H1.

Table 4.9. Differences in peak height for O2 and its blends with H1.

Blends of O2 and H1					
0% H1	1% H1	2% H1	5% H1	10% H1	20% H1
1.6 ± 0.2	1.0 ± 0.2	0.7 ± 0.2	0.2 ± 0.1	0 ± < 0	0.1 ± 0.1

By determining the differences between the peak heights, the error bars associated were lower and the tendency became clearer: when the amount of H1 contained in O2 increased, the calculated parameter decreased. However, this parameter was not representative for all the samples and blends analyzed in this study.

Therefore, the analysis and comparison of the DSC curves needed to be performed by taking into account more than one parameter. For this reason we decided to consider the DSC curves (cooling and heating) as a whole, by using chemometric analyses.

Figure 4.10 displays the PCA data corresponding to the DSC cooling curves of sample O2 and its blends with H1 (from 1% to 20%). The corresponding scores plot is depicted in Figure 5.10a, whereas Figures 5.10b and 5.10c show the loadings on factor 2 and 3, respectively. Loadings represent the weights of the variables on the factors (factors 2 and 3, in this case). Hence, while scores give information about the samples, loadings give information about the variables. The interpretation of the loadings is essentially done by looking at what variables have the higher loadings on a certain PC and are, therefore, important for scores on that PC (Massart et al., 2005). Factors 2 and 3 explained the 27.8% and 13.1% of the original variance, respectively. The use on these two factors permitted observing more differences between adulterated samples, compared to other calculations where other factors were used.

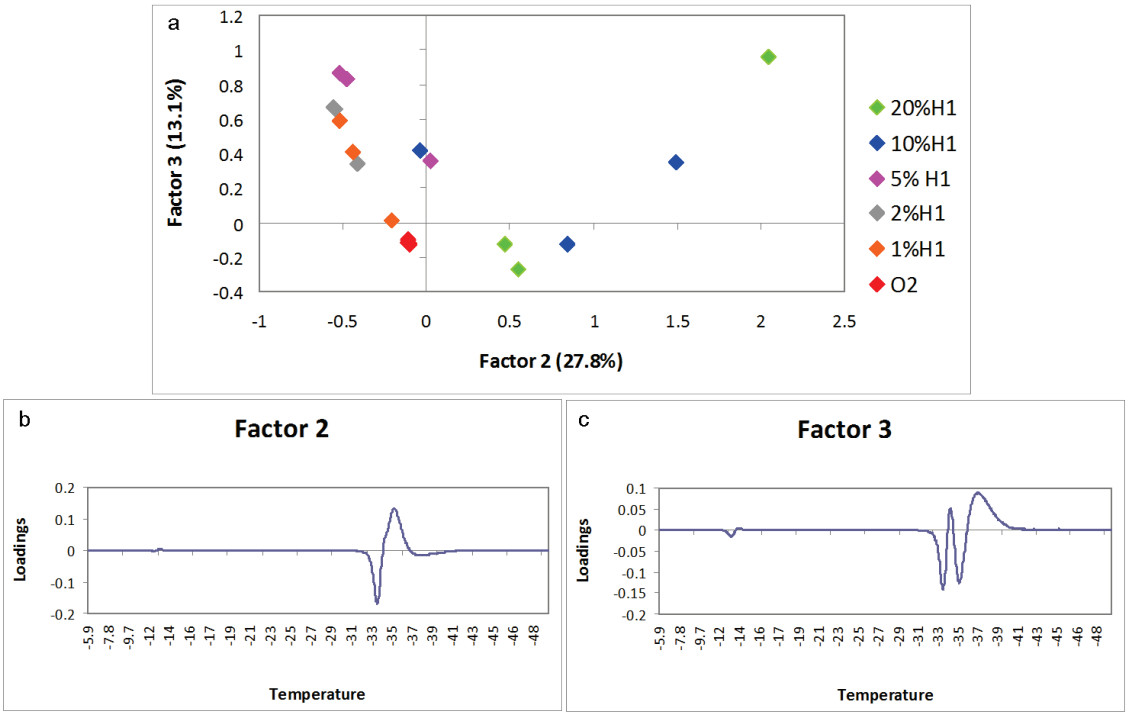

Figure 4.10. PCA data for DSC cooling curves of O2 and its blends with H1. a) Score plot in the space factors (PCs) 2 and 3. b) Loadings on factor 2 or PC2 of the variables. c) Loadings on factor 3 or PC3 of the variables.

Some dispersion was observed in the score plot based on the DSC cooling curves (Figure 4.10a), especially for higher adulterations (10% and 20% of H1). However, it was possible to distinguish O2 from adulterated samples, and it seemed that factor 2 became the most differentiating factor for the additions of H1 to O2. Referring to the loading of the variables in factors 2 and 3, factor 2 could discriminate among low and high adulteration (Figure 4.10b), whereas factor 3 became more important to differentiate between non-adulterated and slightly adulterated samples (Figure 4.10c). Hence, in the loading of the variables in factor 2, areas with high loadings (temperature range from -34.1ºC to -36.0ºC) indicated a high adulteration, while negative loadings (from -33.0ºC to -34.0ºC) indicated low or non-existent adulteration. These results are in agreement with the DSC cooling curves depicted in Figure 4.6, as the main crystallization peak became sharper and shifted to higher temperatures when high amounts of H1 were added to O2, so that the temperature range from -34.1ºC to -36.0ºC was more important for highly adulterated samples. As to the loading of the variables in factor 3, high loading areas (from -33.9ºC to -34.5ºC, and from -35.9ºC to -38.8ºC) indicated an adulteration until 5%. Again, these results are related to the sharpening and shifting to higher temperatures of the main exothermic DSC peak.

Clearer differences were observed between O2 and its blends with H1 when the data extracted from the DSC heating curves were processed. The corresponding score plot (considering factors 2 and 3) and the loadings of the variables in factor 2 are displayed in Figures 4.11a and 4.11b, respectively.

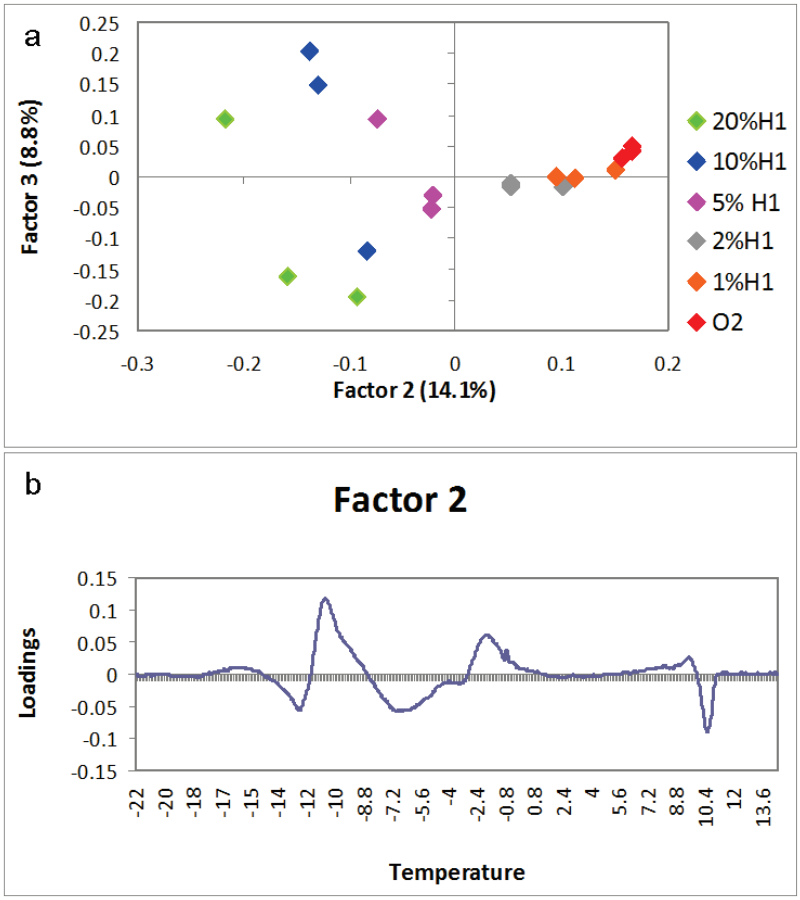

Figure 4.11. PCA data for DSC heating curves of O2 and its blends with H1. a) Score plot in the space factors 2 and 3. b) Loadings on factor 2 or PC2 of the variables.

The score plot showed defined different positions through factor 2 for O2 and adulterated O2 with H1 (from 1% to 20%). Factors 2 and 3 explained the 14.1% and 8.8% of the original variance, respectively, being factor 2 the most relevant factor to discriminate among the different samples. In this case, high loadings (from -11.5ºC to -10.4ºC, and from -2.7ºC to -0.1ºC) indicated slightly adulterated or non-adulterated samples, whereas low loadings (from -13.0ºC to -11.9ºC, from -8.1ºC to -5.3ºC, and from 10.1ºC to 10.8ºC) indicated the addition of H1. These temperature ranges are strongly related with the changes observed in the DSC heating thermograms when H1

was added to O2: the endothermic peak located between -15ºC and -10ºC became more pronounced and sharper and the last endothermic peak (between 9ºC and 11ºC) became narrower.

Thus, chemometric calculations permitted quantifying the differences observed by the DSC thermograms. However, not evident differences were observed for all the blends of olive and hazelnut oils analyzed. Many factors, such as the quality of olive oil (virgin, extra virgin), the olive varieties or the geographical areas may play important roles on their chemical composition and polymorphic behavior. Some of the chemometric results obtained for the moment showed that the quality (virgin or extra virgin olive oil) may have a strong influence, so that important differences could be observed between the two categories.

On the whole, although XRD data were not capable of detecting fraudulent additions of hazelnut oil (H1) in an extra virgin olive oil (O2), DSC permitted detecting adulterations in lower percentages than the 5%. The quantification of the differences observed in the DSC thermograms could be performed through chemometric calculations. However, depending on the nature (quality, variety, geographical area, etc.) of the oils used, the difficulty in detecting fraudulent additions is increased. Further studies are needed to analyze a higher number of samples in order to try to define some general trends taking into account those determining factors.

4.4.2. Differentiation of Iberian ham fat from pigs produced with different systems of animal nutrition

Iberian ham becomes the most appreciated cured ham produced in Spain, because of their particular and intense sensorial properties. Iberian pigs are mainly produced in the southwest regions of Spain, and the existence of different product categories arise from the different production procedures used. These production systems are closely related to the diet of the animal, and they become determining factors for the prices in the market. Until now, three different producing systems have been used, which depend on the feeding of the pig in the fattening phase. The pigs which extensively only consume acorns and grass during the fattening period are known as *bellota*, whereas those in confinement whose fattening is based on the consumption of concentrate feed are called *cebo*. The third method, named *recebo*, becomes a combination of the two commented above, so that the consumption of acorns and grass includes a supplementation with concentrate feeds. Iberico hams obtained from pigs which were produced by using the first method described (*bellota*) are those of highest commercial value. Hence, in order to regulate the market, objective measurements are needed in order to determine the feeding received by Iberian pigs.

Several methods have been used to try to define differences between hams obtained from Iberian pigs of different categories. Almost all the procedures are based on fat properties, such as melting and slip point, or fatty acid profiles. These methods focus on the fact that, in *bellota*, higher amounts of oleic acid are found, compared to *recebo* and *cebo* (Ruiz et al., 1998). Other methods include the determination of hydrocarbons (Narváez-Rivas et al., 2008) and volatile compounds (Timón et al., 2001; Narváez-Rivas et al., 2011) profiles. Moreover, isotope analyses on the adipose tissue of the animals have also been applied to characterize and differentiate Iberian pork meat as a function of the diet of the animal (González-Martín et al., 1999). As to spectrometric techniques, near-infrared spectrometry (NIR) has also been applied with the same purpose (Arce et al., 2009), although this method could not perfectly discriminate among the different pig categories.

Recently, more attention has been paid to the determination of the TAGs composition, as analyses become easier and faster, avoiding the use of saponification and the formation of methyl esters (Díaz et al., 1996; Narváez-Rivas et al. 2009;

Gallardo et al. 2012,). The TAGs composition has also been used to elucidate the effect of genotype (Tejeda et al., 2002; Petrón et al., 2004; Viera-Alcaide et al., 2008).

However, in order to regulate the market, there is still a lack of a normalized method capable of preventing the wrongful use of the commercial name of higher quality products. This fact is caused by the existence of some ambiguities in the results obtained by the methods used until now to differentiate Iberian hams produced with different fattening systems, when high amounts of samples have been analyzed.

Furthermore, nowadays the Spanish government is planning to establish, in the near future, new regulations to fix quality standards of Iberian pig products. The purpose of the new regulation consists of protecting the purity of Iberian pig, controlling the breeding and feeding, and properly labelling the final product. The genotype will be also more controlled, so that the labelling will include the percentage of Iberian purity. Hence, in the current context, there is a huge necessity of finding and establishing a universal method to discriminate among different Iberian ham categories.

Some studies have focused on the characterization of physical properties of pork fat. Svenstrup et al. (2005) analyzed the influence of changing the cooling and reheating rates applied to pork fat. By using DSC and XRD techniques, they characterized samples of lard (pork dorsal fat) and leaf pork fat (surrounding the kidneys) in their raw state, their extracted fat fraction, and in liver pâté. The crystallization behavior observed permitted defining the textural properties obtained when pork fats were used in liver pâté. Campos et al (2002) also applied different cooling rates to lard samples, but in order to observe the effects of such variations on the hardness of the fat crystal networks. On the other hand, Davenel et al. (1999) studied the Solid Fat Content (SFC) variations of pig adipose tissues in relation to their lipid composition. Raman spectrometry was applied to *in situ* analyze the crystalline states of fat in porcine adipose tissue (Motoyama et al., 2013). Their purpose was to use the method described as a tool for routine monitoring of the physical conditions of meat carcasses in refrigerators. The same technique was also proposed to discriminate between pork and beef fat, by analyzing the polymorphic features of the characterized samples (Motoyama et al., 2010).

The aim of the present study was to analyze the physical properties of Iberian ham fat samples, from the *cebo* and *bellota* categories, and try to differentiate them by characterizing their polymorphic behavior. For this purpose, DSC, XRD (with both conventional and synchrotron radiation) and Thermo-optical polarized microscopy were

used. To the best of our knowledge, this is the first work where the polymorphic behavior is used to discriminate among different Iberian ham fat categories.

Iberian ham fat samples were supplied by the Instituto Comunitario de Certificación (ICC), which assured a known and controlled origin and nature of the samples.

All Iberian ham fat samples were subjected to an extraction of the lipid fraction. Thus, samples were grinded, and the lipid fraction was extracted with petroleum ether by using a Polytron mixer. The water phase was eliminated with the addition of saline solution (1% NaCl) and a subsequent centrifugation. The lipid fraction was dried on anhydrous Na_2SO_4 and the solvent was eliminated by rotoevaporation.

Samples of extracted Iberian ham fat were subjected to DSC, XRD and TOM experiments. However, DSC and XRD were also applied to some grinded ham fat, instead of the extracted fraction. The results obtained demonstrated the heterogeneity of the samples, so that they were not completely reproducible. Thus, we decided to analyze the extracted fat fraction of the samples.

Fatty acid compositions of *cebo* and *bellota* samples were determined by HPLC, and the results obtained are displayed in Table 4.10. The values shown become the mean value of all the samples belonging to the same category, and standard deviations are also included.

One may notice a higher amount of oleic acid (C18:1n9) in *bellota* samples (52.08% with a s.d. of 1.38), compared to that of *cebo* samples (44.89% with a s.d. of 0.44).

To quantify the differences in the fatty acid compositions of the two categories, chemometric calculations were carried out. Figure 4.12 depicts the PCA data obtained for the fatty acid compositions of the two categories. The scores plot is displayed in Figure 4.12a, whereas Figure 4.12b shows the loading plot on factors 1 and 2.

Table 4.10. Fatty acids compositions (%) of *bellota* and *cebo* samples. Mean values of all samples belonging to the same category were calculated. Standard deviation values are included between parentheses.

	bellota	***cebo***
C10:0	0.03 (<0.01)	0.05 (<0.01)
C12:0	0.06 (0.01)	0.07 (<0.01)
C14:0	1.22 (0.10)	1.46 (0.06)
C15:0	0.05 (0.01)	0.06 (0.01)
C16:0	20.67 (0.83)	23.47 (0.52)
C16:1n9	0.42 (0.02)	0.34 (0.02)
C16:1n7	1.89 (0.25)	2.55 (0.18)
C17:0	0.29 (0.04)	0.34 (0.03)
C17:1	0.27 (0.05)	0.35 (0.03)
C18:0	9.64 (0.71)	10.88 (0.50)
C18:1 (trans)	0.39 (0.08)	0.59 (0.09)
C18:1n9	52.08 (1.38)	44.89 (0.44)
C18:1n7	2.74 (0.34)	3.59 (0.17)
C18:2n6	7.42 (0.41)	8.40 (0.47)
C18:3n3	0.45 (0.05)	0.55 (0.04)
C20:0	0.18 (0.01)	0.18 (0.02)
C20:1n9	1.36 (0.13)	1.20 (0.11)
C20:2n6	0.48 (0.05)	0.56 (0.05)
C20:3n6	0.06 (0.01)	0.07 (0.01)
C20:3n3	0.10 (0.02)	0.12 (0.02)
C20:4n6	0.10 (0.01)	0.12 (0.01)
C20:5n3	0.02 (0.01)	0.02 (0.01)
C24:0	0.04 (0.01)	0.07 (0.02)
C24:1n9	0.04 (0.02)	0.07 (0.01)

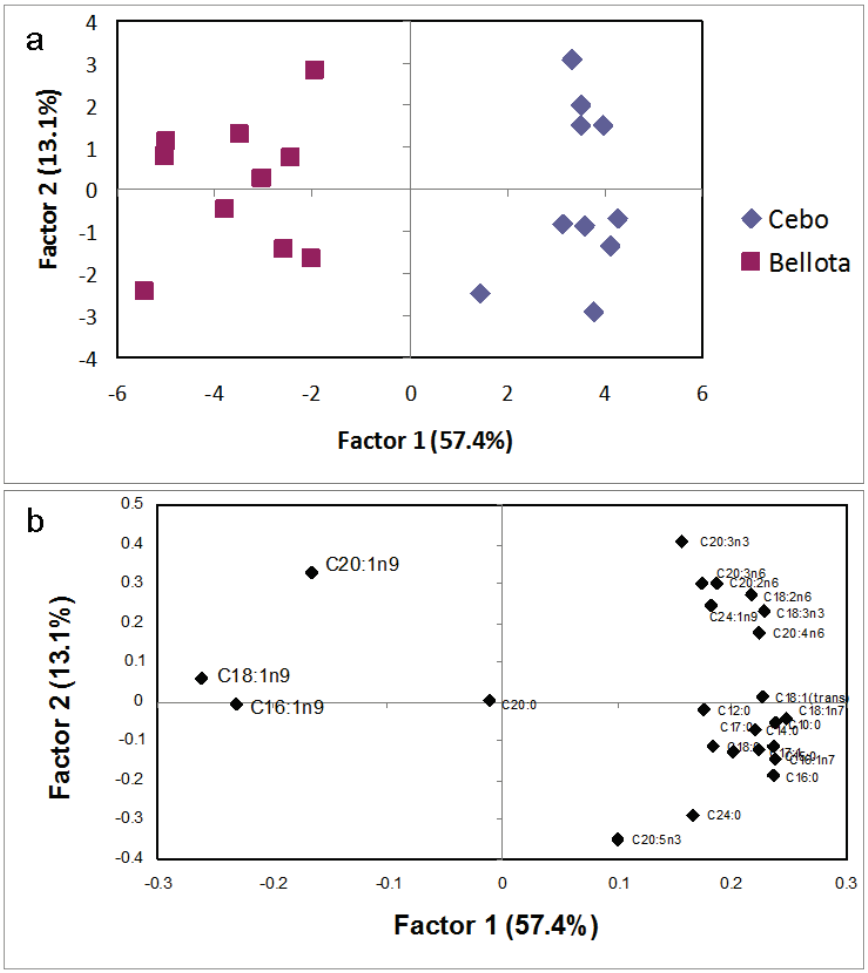

Figure 4.12. PCA data for the fatty acids compositions of *cebo* and *bellota* sample. a) Score plot in the space of the two first factors (PCs). b) Loading plot on the two first factors of the variables.

The first two factors explained the 57.4% and 13.1% of the original variance, respectively. The two figures are complementary in the sense that, as the plot score presents the *bellota* category on the left side (Figure 4.12a), the fatty acids which become important for *bellota* are those which appear on the left side of the loading plot (Figure 4.12b). On the contrary, more relevant fatty acids for the *cebo* category appear on the right side of the loading plot. Therefore, C18:1n9, C16:1n9 and C20:1n9 became important for *bellota*. C20:0 was very close to the origin, so its weight was small and it was not important, and the rest of fatty acids were more relevant for the *cebo* category. Thus, the fatty acid compositions showed clear differences between the two analyzed categories.

TAGs compositions of the samples analyzed in this study were not determined. However, as already explained above, some studies have reported on the TAGs

composition of Iberian ham fat obtained from pigs with different fattening systems. As an example, Table 4.11 presents the main data obtained by Díaz et al. (1996) and Gallardo et al. (2012).

Table 4.11. Mean values of TAG percentages in ham fat of Iberian pigs.

	Bellota		***Cebo***	
	Diaz et al., 1996	Gallardo et al., 2012	Diaz et al., 1996	Gallardo et al., 2012
POO	33.0	31.93	31.7	35.26
OOO	17.7	10.62	7.2	4.66
POL	15.1	10.36	17.3	9.00
POS	10.0	13.81	19.1	20.18
OOL	9.1	5.66	3.5	2.04
SOO	7.2	6.64	6.8	5.45
POP	3.8	5.11	8.2	8.06

Although some differences were detected between the results reported in the two studies, general trends can be described as follows. Higher amounts of triunsaturated TAGs (OOO and OOL) were found in *bellota*, compared to *cebo*. As to diunsaturated TAGs (POO, POL, SOO), no significant differences were detected between the two categories. On the other hand, *cebo* presented higher amounts of monounsaturated TAGs (POS, POP) than *bellota*. Therefore, as confirmed by the determination of the fatty acids compositions, a more unsaturated nature was detected in *bellota* Iberian ham fats.

Furthermore, one may notice some similarities in the main TAGs compositions of Iberian ham fat and virgin olive oil (see section 4.4.1).

As to the characterization of the physical properties, at first, preliminary analyses were performed with only two different fat samples coming from pigs produced with different systems of animal nutrition (*cebo* and *bellota*). DSC experiments were carried out by cooling the melted sample from 65ºC to -80ºC at $2ºC \cdot min^{-1}$ and heating it afterwards to 65ºC at the same rate. The two samples were labelled C1 (*cebo*) and B1 (*bellota*). The DSC cooling and heating curves obtained for C1 and B1 are depicted in Figure 4.13.

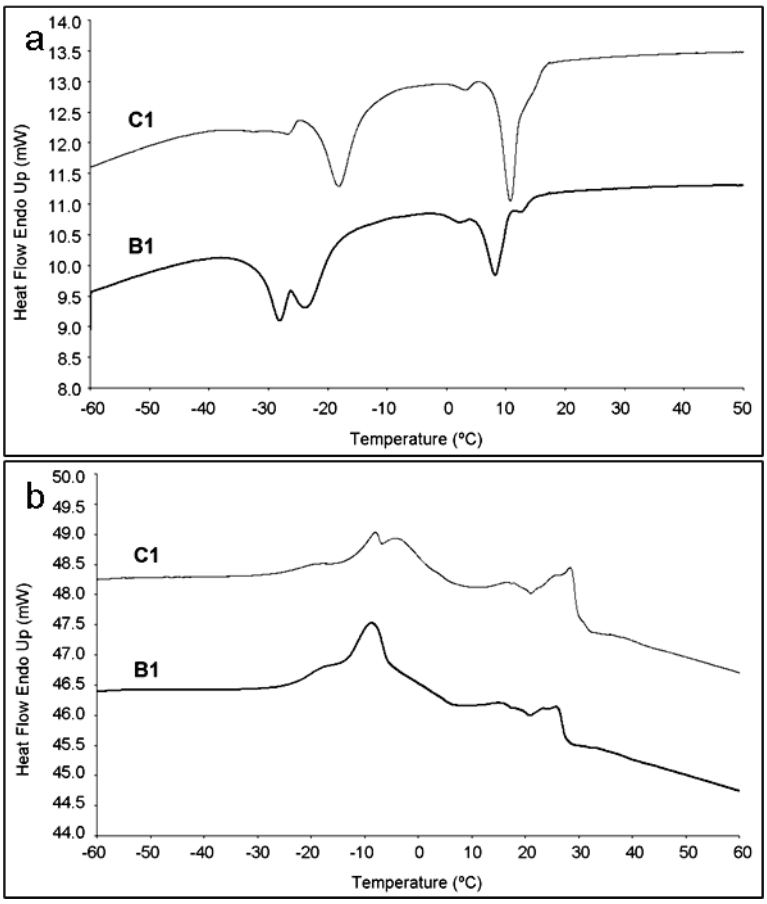

Figure 4.13. C1 and B1 DSC thermograms obtained when cooled and heated at 2ºC·min^{-1}. a) DSC cooling curves. b) DSC heating curves.

At first sight, by looking at both DSC cooling and heating thermograms of C1 and B1, several differences may be appreciated. Regarding the cooling curves, two exothermic DSC peaks appeared in the temperature range from 20ºC to 0ºC when C1 was cooled at 2ºC·min^{-1}. On the contrary, three well defined peaks were present in the interval from 20ºC to -5ºC of the B1 DSC cooling thermogram. The main difference between the two set of phenomena was the intensity of the main exothermic peak. The one with a peak top temperature of 12.3ºC in C1 became significantly more intense than that of B1, which appeared at 8.5ºC. From -10ºC to -40ºC, another set of exothermic peaks were detected in both cases. However, in C1, a strong signal (-15.6ºC) was accompanied by a weaker one (-29.2ºC), whereas two peaks (at -20.2ºC and -25.8ºC) of approximately the same intensity were found in the cooling thermogram of B1. Moreover, the two peaks were more separated in C1.

More variations were found in the heating profiles. A broad endothermic peak appeared at -18.7ºC in C1, and it was followed by a double endothermic signal, with

peak top temperatures at -8.5ºC and -2.3ºC, respectively. On the contrary, a main endothermic peak at -6.8ºC, having two shoulders, was appreciable in the first stage of the heating process of B1. From 0ºC to 40ºC, no significant differences were observed between C1 and B1 heating curves.

In view of the promising results obtained, a higher amount of samples was studied in order to confirm if the behavior observed could be extrapolated to other *cebo* and *bellota* samples. Hence, we used the following methodology. The ICC supplied 20 new Iberian ham fat samples, 5 of which were included in the *cebo* category, 5 more were *bellota*, and natures of the 10 remaining samples were unknown (they were only known by the ICC staff). The aim of the study was to determine if we were able to classify the unknown samples in one of the two categories: *cebo* or *bellota*. After performing the corresponding DSC experiments of the 5 known *cebo* and the 5 known *bellota* samples, we confirmed that, within each group of samples, the thermal behavior was the same, whereas it differed from one group to the other. Moreover, after carrying out the DSC experiments of the unknown samples, we could successfully classify them all in one of the two categories. By taking a quick look at the DSC thermal profile, one could easily attribute the *cebo* or *bellota* category at each of the unknown samples.

Figure 4.14 plots the DSC cooling and heating curves for all the *cebo* (Figure 4.14a) and *bellota* (Figure 4.14b) samples, including the samples which were unknown at the beginning. C1 and B1 corresponded to the fat samples that were analyzed as preliminary experiments (see above).

One may notice that all *cebo* samples exhibited the same thermal behavior, and the same happened in the case of *bellota* samples. The two typical DSC profiles are totally comparable to those already discussed for C1 and B1 samples.

Tables 4.12 and 4.13 summarize first onset, last end temperatures and enthalpy value of the whole thermogram (for both cooling and heating curves), and peak top temperatures of the most representative peaks (labelled peaks in Figure 4.14) of *cebo* (Table 4.12) and *bellota* (Table 4.13) samples. Although no error bars were included for the values given in Table 4.10, we should point out that three independent DSC measurements were carried out for all samples and the thermal curves were almost identical in all cases.

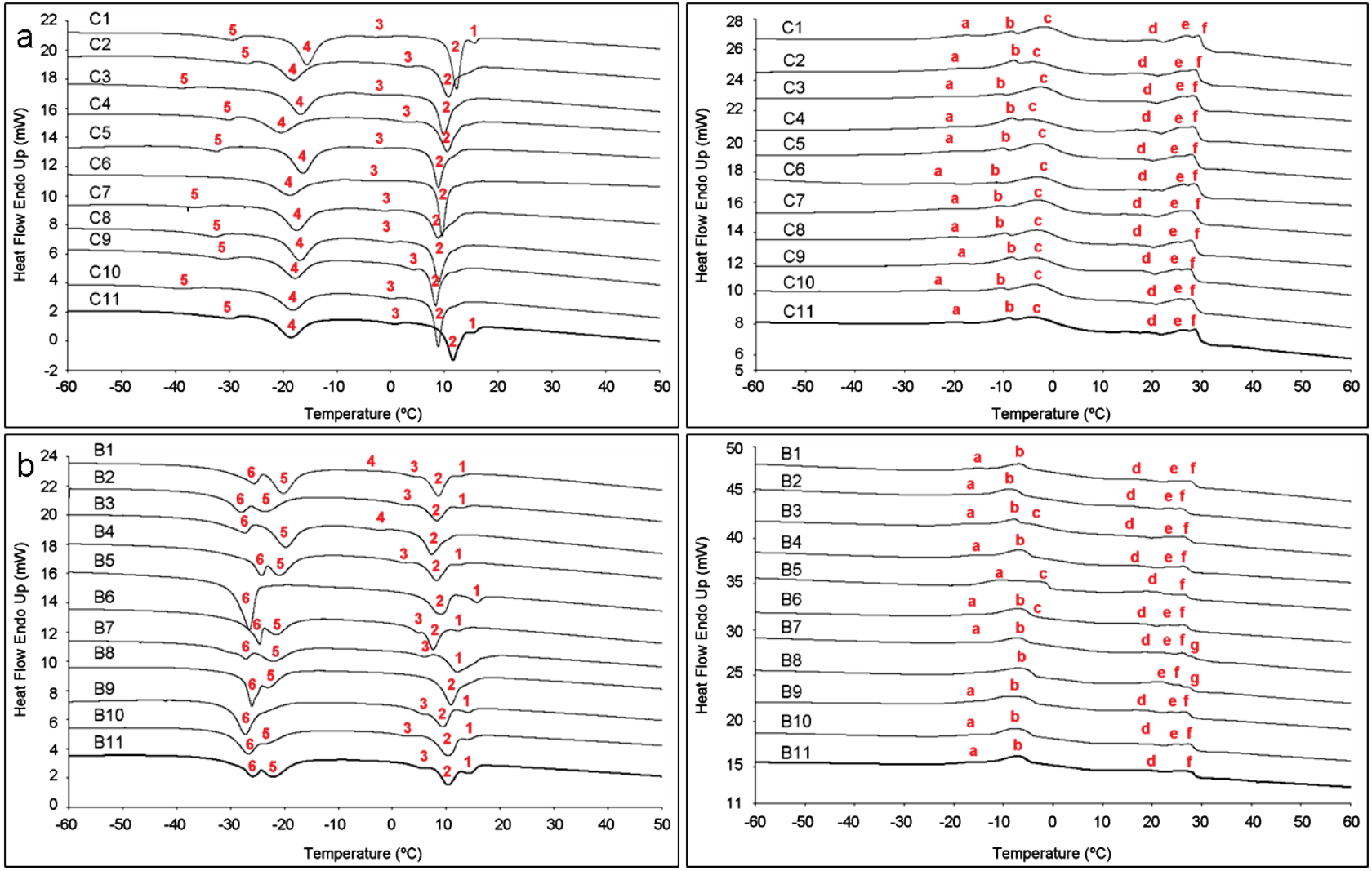

Figure 4.14. DSC thermograms of Iberian ham fat. a) Cooling and heating curves of *cebo* samples. b) Cooling and heating curves of *bellota* samples.

Table 4.12. T_{onset} (ºC), T_{end} (ºC) and ΔH ($J \cdot g^{-1}$) values of the cooling and heating curves, and peak top temperatures of *cebo* samples.

	Cooling (2ºC·min^{-1})								
	T_{onset} (ºC)	T_{end} (ºC)	ΔH (J/g)	Peak 1 (ºC)	Peak 2 (ºC)	Peak 3 (ºC)	Peak 4 (ºC)	Peak 5 (ºC)	
C1	16.5	-38.1	-68	15.7	12.3	-2.8	-15.6	-29.2	
C2	16.5	-39.2	-63	shoulder	10.8	3.2	-18.1	-26.7	
C3	14.9	-44.6	-59	shoulder	9.8	-2.8	-16.7	-39.2	
C4	16.3	-39.7	-60	shoulder	10.5	2.7	-20.4	-30.0	
C5	13.6	-38.1	-61	shoulder	8.9	-2.3	-16.3	-32.6	
C6	15.7	-25.5	-55	shoulder	9.6	-3.6	-18.7	shoulder	
C7	13.9	-42.2	-56	shoulder	8.8	-1.2	-17.5	-36.1	
C8	13.8	-39.5	-61	shoulder	8.9	-0.2	-16.9	-32.8	
C9	13.8	-36.8	-60	shoulder	8.4	4.0	-17.8	-31.0	
C10	13.8	-45.2	-54	shoulder	8.8	-0.1	-18.2	-38.6	
C11	16.8	-38.8	-58	15.6	11.7	0.8	-18.5	-29.9	
	Heating (2ºC·min^{-1})								
	T_{onset} (ºC)	T_{end} (ºC)	ΔH (J/g)	Peak a (ºC)	Peak b (ºC)	Peak c (ºC)	Peak d (ºC)	Peak e (ºC)	Peak f (ºC)
C1	-30.1	45.2	95	-18.7	-8.5	-2.3	20.0	26.8	29.2
C2	-31.9	42.5	95	-19.5	-7.8	-3.1	17.2	25.3	28.5
C3	-35.4	43.1	103	-22.5	-10.5	-2.5	18.1	26.2	28.2
C4	-32.9	43.6	100	-19.7	-8.3	-3.3	17.1	26.0	28.2
C5	-32.6	42.1	107	-20.8	-10.0	-2.9	17.1	24.5	28.0
C6	-35.0	42.7	106	-25.3	-11.2	-2.9	18.7	26.5	28.7
C7	-38.9	40.4	110	-21.9	-10.1	-2.9	18.4	24.9	27.6
C8	-32.1	42.4	103	-21.4	-9.5	-3.3	17.2	24.4	27.7
C9	-33.6	41.2	91	-19.8	-8.2	-3.8	17.2	24.4	27.3
C10	-35.6	41.5	112	-23.9	-10.2	-3.5	15.1	25.7	27.6
C11	-32.1	43.9	117	-20.5	-8.7	-3.9	19.6	25.6	28.6

Table 4.13. T_{onset} (ºC), T_{end} (ºC) and ΔH ($J \cdot g^{-1}$) values of the cooling and heating curves, and peak top temperatures of *bellota* samples.

	Cooling (2ºC·min^{-1})									
	T_{onset} (ºC)	T_{end} (ºC)	ΔH (J/g)	Peak 1 (ºC)	Peak 2 (ºC)	Peak 3 (ºC)	Peak 4 (ºC)	Peak 5 (ºC)	Peak 6 (ºC)	
B1	14.2	-38.1	-69	12.4	8.5	4.3	-7.3	-20.2	-25.8	
B2	14.6	-33.2	-63	12.6	8.3	2.1	shoulder	-24.0	-28.0	
B3	11.8	-35.2	-64	shoulder	7.3	shoulder	-2.5	-19.8	-27.3	
B4	13.4	-29.7	-68	12.2	8.2	2.2	shoulder	-21.1	-24.2	
B5	17.4	-31.5	-66	15.6	8.7	shoulder	shoulder	shoulder	-26.5	
B6	13.9	-30.9	-65	11.9	7.6	4.8	shoulder	-21.7	-24.6	
B7	19.9	-35.3	-59	11.9	shoulder	5.8	shoulder	-22.1	-27.3	
B8	16.7	-30.0	-67	shoulder	10.9	shoulder	shoulder	-23.3	-26.1	
B9	15.8	-32.5	-64	13.9	9.4	5.6	shoulder	shoulder	-27.3	
B10	16.3	-33.7	-64	14.0	10.3	2.2	shoulder	-22.8	-26.6	
B11	16.3	-33.0	-66	14.2	10.4	5.5	shoulder	-22.0	-26.0	
	Heating (2ºC·min^{-1})									
	T_{onset} (ºC)	T_{end} (ºC)	ΔH (J/g)	Peak a (ºC)	Peak b (ºC)	Peak c (ºC)	Peak d (ºC)	Peak e (ºC)	Peak f (ºC)	Peak g (ºC)
B1	-25.4	42.1	111	-15.1	-6.8	shoulder	17.3	24.7	27.3	shoulder
B2	-27.6	39.6	112	-18.1	-8.5	shoulder	15.7	23.0	26.1	shoulder
B3	-26.1	42.1	101	-17.5	-7.7	-4.8	17.2	22.7	26.3	shoulder
B4	-25.5	41.3	104	-15.7	-6.6	shoulder	17.2	23.2	26.5	shoulder
B5	-19.5	27.8	92	-10.0	shoulder	-2.7	19.7	shoulder	26.5	shoulder
B6	-27.8	39.5	119	-15.7	-6.9	shoulder	17.1	23.1	26.4	Shoulder
B7	-29.6	44.6	117	-17.9	-7.0	shoulder	18.4	23.3	26.2	27.9
B8	-24.3	42.3	103	shoulder	-6.4	3.5	shoulder	22.2	25.2	27.2
B9	-28.7	44.0	106	-18.0	-7.0	shoulder	18.7	24.1	26.6	shoulder
B10	-26.5	42.4	105	-16.9	-7.5	shoulder	16.2	24.4	27.4	shoulder
B11	-26.6	41.7	109	-16.6	-6.9	shoulder	19.0	shoulder	27.2	shoulder

Some dispersion was observed in the peak temperatures for samples belonging to the same category, as shown in Tables 4.12 and 4.13. Moreover, some peaks became more intense in some cases, whereas they were described as shoulders in others. However, all samples belonging to the same Iberian ham fat category followed the same trends.

The mean value of the first onset temperature that appeared in the DSC cooling curve of *cebo* samples was 15.0ºC, with a standard deviation (s.d.) of 1.3ºC. No significant differences were observed, compared to that of *bellota* samples (15.5(s.d. 2.2) ºC). The T_{end} of the whole crystallization process in *cebo* was about -38.9ºC with a high standard deviation between samples (5.2ºC), whereas in the case of *bellota* this T_{end} became higher (-33.0(s.d. 2.5) ºC). The lower T_{end} observed in *cebo* samples should be due to the shape of the last crystallization peak, which became broad and extended, while the ending of last crystallization peaks of *bellota* samples were more defined. The mean enthalpy value of the cooling process of *cebo* samples (-59(s.d. 4) $J \cdot g^{-1}$) was comparable to that of *bellota* samples (-65(s.d. 3) $J \cdot g^{-1}$), if the standard deviation values were considered. As to the crystallization peaks of *cebo*, peak 1 only appeared in C1 and C11, becoming a shoulder in the other samples (see Figure 4.14a). The corresponding mean value of the peak top temperature was 15.6ºC with a standard deviation of 0.1ºC. Peak top temperatures of peaks 2, 3, 4 and 5 were 9.9(s.d. 1.3) ºC, -0.2(s.d. 2.6) ºC, -17.7(s.d. 1.3) ºC, and -32.6(s.d. 4.1) ºC, respectively. In the DSC cooling curve of *bellota* samples, six crystallization peaks were detected. The mean values of peaks 1, 2 and 3 (and their standard deviations) were 13.2(s.d. 1.3) ºC, 8.9(s.d. 1.2) ºC, and 4.0(s.d. 1.6) ºC. Only in samples B1 and B3, peak 4 appeared (see Figure 4.14b) with a mean peak top temperature of -4.9ºC and a high standard deviation of 3.4ºC. As an average, peaks 5 and 6 were detected at -21.9(s.d. 1.4) ºC and -26.3(s.d. 1.2) ºC, respectively.

Regarding the heating process, the mean value of the first onset temperature observed in *cebo* samples was -33.7(s.d. 2.4) ºC, being lower than that of the *bellota* samples (-26.1(s.d. 2.7) ºC). The lower T_{onset} detected in *cebo* samples again should be due to the broad shoulder that appeared in peak *a*, which differed from the more defined peak found in *bellota* samples. No significant differences were observed in both the T_{end} and enthalpy values of the heating process of *cebo* and *bellota*. The mean values of T_{end} were 42.6(s.d. 1.3) ºC and 40.7(s.d. 4.5) ºC, respectively, whereas enthalpy values were 104(s.d. 8) $J \cdot g^{-1}$ and 107(s.d. 8) $J \cdot g^{-1}$. It should be noted that the standard deviation of *bellota* was higher than that of *cebo* samples, noting a more dispersed behavior at the end of the fat melting. Six endothermic peaks appeared in the DSC heating curves of *cebo* samples, the mean peak top temperatures of which were (from peak *a* to *f*): -21.3(s.d. 2.0) ºC, -9.4(s.d. 1.1) ºC, -3.1(s.d. 0.5) ºC, 17.8(s.d. 1.4) ºC, 25.5(s.d. 0.8) ºC, and 28.1(s.d. 0.6) ºC. In general, standard deviation values of the heating peaks were

lower than that of the cooling peaks, demonstrating a more common behavior in the heating process. As to the *bellota* samples, seven endothermic signals were present, but not all samples exhibited the seven DSC signals, as they were considered shoulders in some cases. The peak top temperatures of peaks *a* and *b* were -16.1(s.d. 2.4) ºC and -7.1(s.d. 0.6) ºC, respectively. Peak *c* (-1.3(s.d. 4.3) ºC) was only present in samples B3, B5 and B8, being considered a shoulder in the other samples. Peaks *d*, *e* and *f* appeared at 17.6(s.d. 1.3) ºC, 23.4(s.d. 0.8) ºC, and 26.5(s.d. 0.6)ºC, respectively. Referring to peak *g*, it only appeared in samples B7 and B8 (see Figure 4.14b), having a peak top temperature at 27.6ºC and a standard deviation of 0.5ºC.

As already shown, very similar thermograms were observed in both the cooling and heating processes for all samples belonging to the same category (*cebo* and *bellota*). On the other hand, the two categories became highly different.

Although the differences between Iberian ham fat samples belonging to different categories could be easily detected by only looking at the DSC profiles, we wanted to quantify such differences. For this reason, chemometric calculations were applied to the DSC cooling and heating curves. The analyzed DSC data included the three repetitions (n=3) performed for each sample.

Figure 4.15 displays the PCA data obtained by analyzing the DSC cooling curves of all *cebo* and *bellota* samples. The corresponding scores plot is shown in Figure 4.15a, and Figure 4.15b depicts the loadings on factor 1. The first two factors explained the 22.9% and 13.8% of the original variance, respectively.

Through Figure 4.15a, it could be observed that samples belonging to different fattening (*cebo* and *bellota*) appeared quite separated in this space, with factor 1 being the most differentiating factor. As to the loading of the variables in factor 1 (Figure 4.15b), areas with high loadings (temperature ranges from -10.0ºC to -16.8ºC, and from -27.9ºC to -33.7ºC) were important for the *bellota* category, whereas lower loadings (from 9.3ºC to 7.1ºC, and from -17.0ºC to -26.3ºC) became more relevant for the *cebo* category. This temperature ranges corresponded to the beginning of peak 5 and to peak 6 for the *bellota* category and to the end of peak 2 and to peak 4 for the *cebo* category.

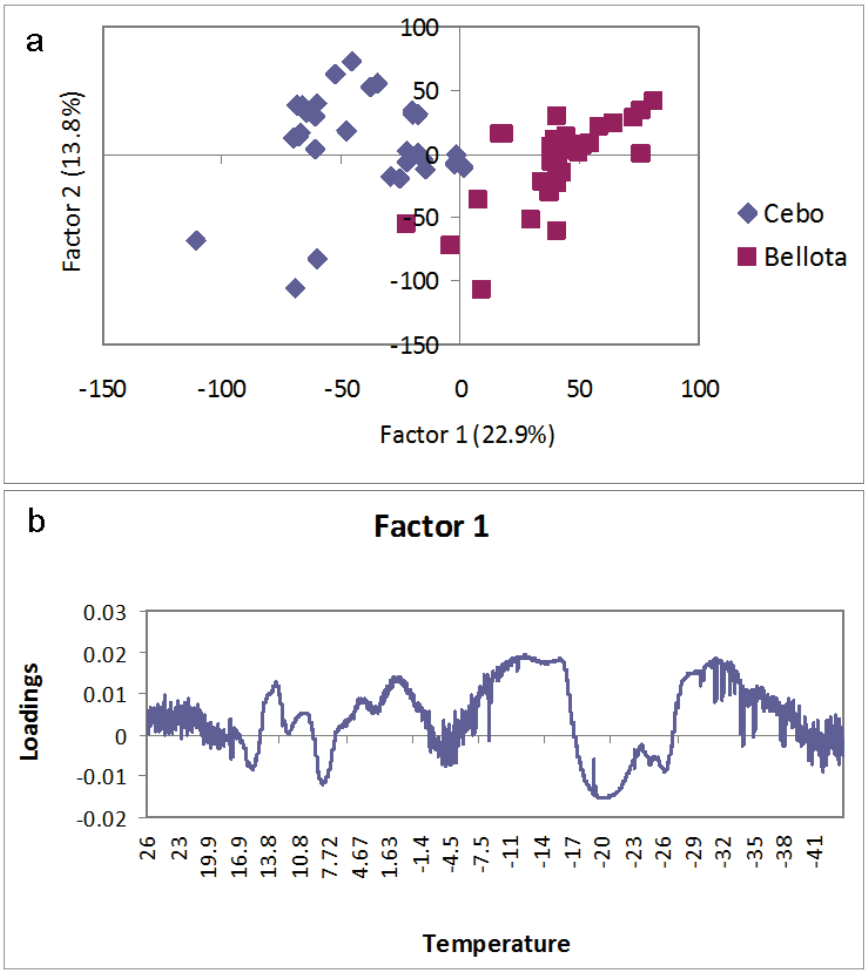

Figure 4.15. PCA data for DSC cooling curves of *cebo* and *bellota* samples. a) Score plot in the space of the two first factors (PCs). b) Loadings on factor 1 or PC1 of the variables.

As to the heating DSC curve, the corresponding score plots and the loadings of the variables in factor 1 are shown in Figure 4.16. Higher differences were detected by processing the data extracted from the DSC heating thermograms, compared to those of the DSC cooling curves (see Figure 4.16a).

The two factors explained the 50.9% (factor 1) and the 20.5% (factor 2) of the original variance. In this case, factor 2 became the most differentiating factor. Thus, the loading of the variables were represented on factor 2 (Figure 4.16b). Again, high loadings (temperature range from 30.2ºC to 31.7ºC) were more relevant for *bellota* samples, whereas lower loadings (from -5.7ºC to -1.9ºC and from 28.2ºC to 29.7ºC) became more important for *cebo*. This temperature ranges determined that most important differences between the two samples were detected in the peak *c* appreciable in the DSC heating curve of *cebo* and in the last melting peaks for the two samples.

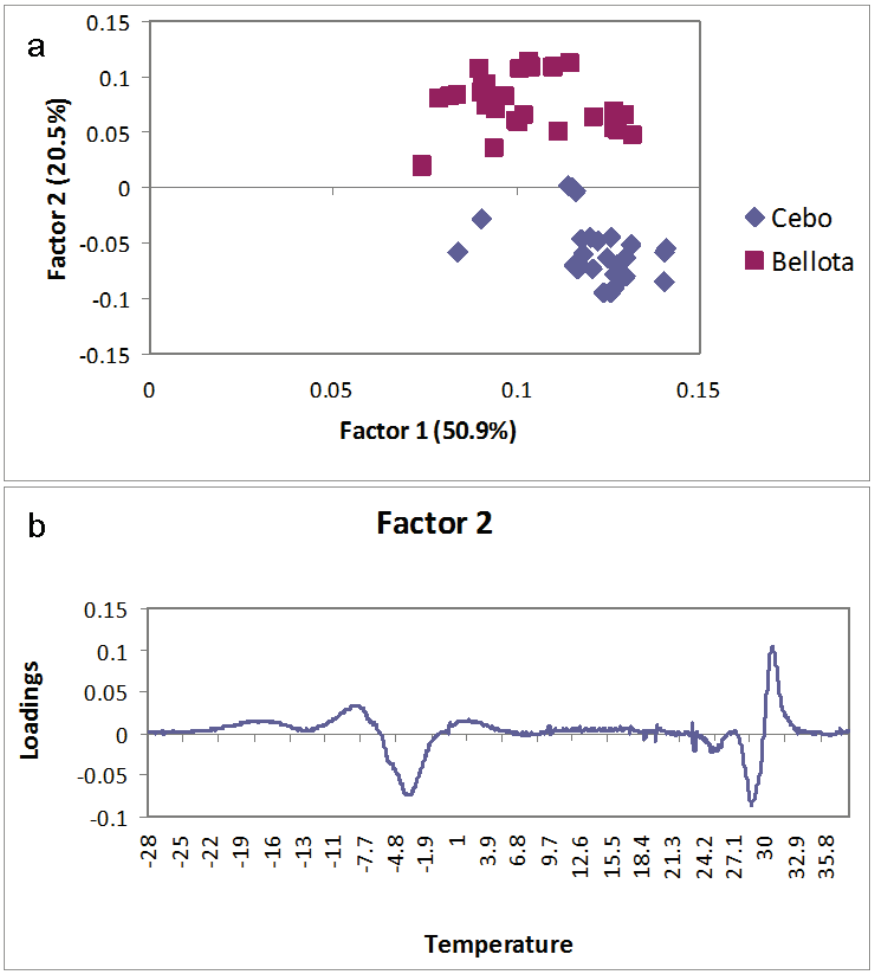

Figure 4.16. PCA data for DSC heating curves of *cebo* and *bellota* samples. a) Score plot in the space of the two first factors (PCs). b) Loadings on factor 2 or PC2of the variables.

Laboratory-scale XRD and SR-XRD experiments were performed for some *cebo* and *bellota* samples, to determine if differences between the two categories were also detected by using these techniques.

Figure 4.17 displays laboratory-scale XRD (Figure 4.17a) and SR-XRD (Figure 4.17b) data, taken as a function of temperature, of sample C1 (*cebo*). The results revealed by the two techniques were totally comparable.

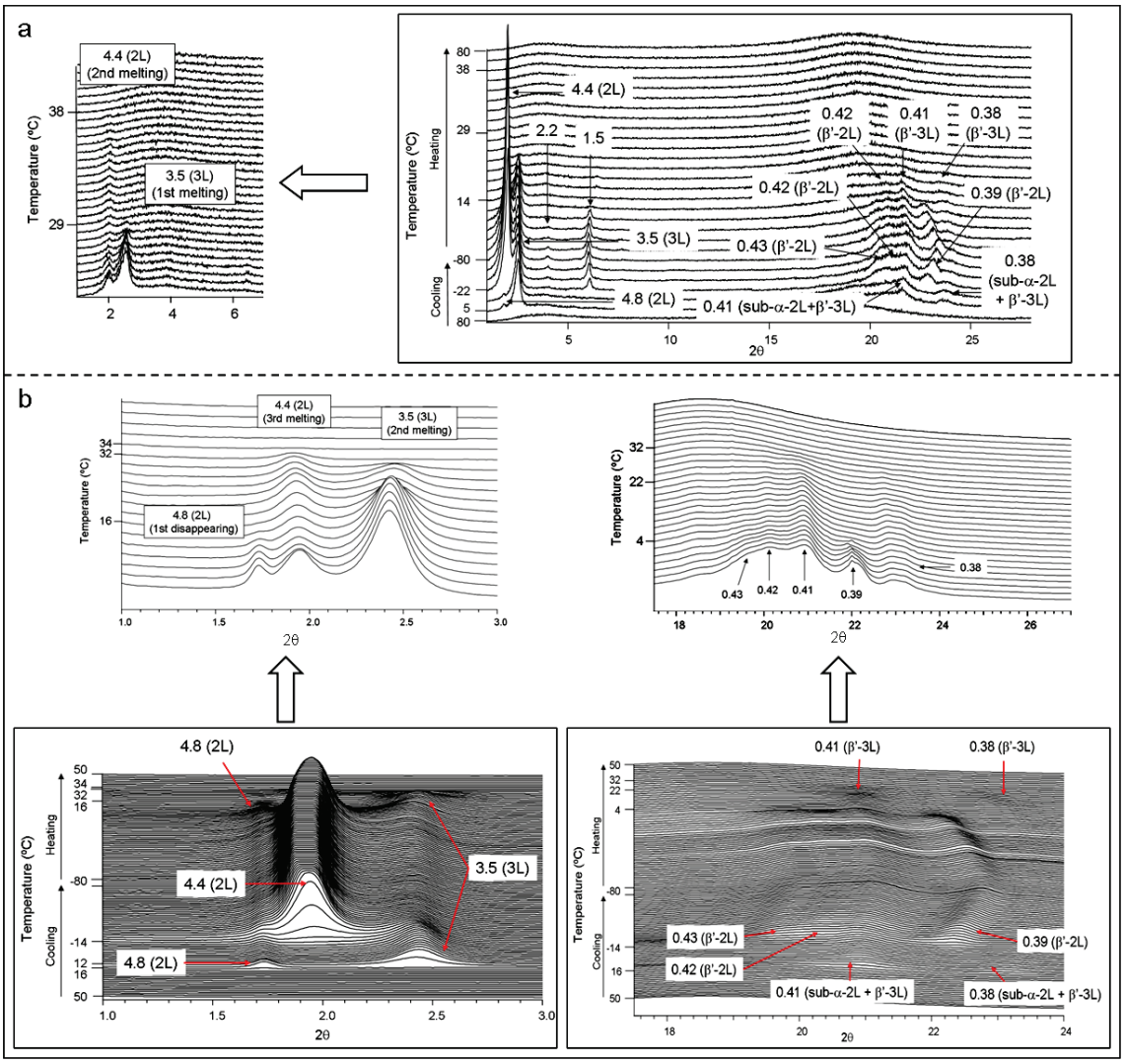

Figure 4.17. XRD patterns of C1 sample. a) Laboratory-scale XRD. b) SR-XRD (SR-SAXD and SR-WAXD patterns). Enlarged figures depict the melting behavior of the sample.

When the C1 sample was cooled from 65ºC to -80ºC at 2ºC·min^{-1}, SR-XRD showed a first occurring sub-α-2L form, which crystallized at 16ºC. The double chain length structure was confirmed by the presence of a weak SAXD peak at 4.8 nm, whereas the sub-α polymorphic form was identified by WAXD peaks at 0.41 nm and 0.38 nm. A sub-α crystallization from the melt at such high temperatures is unusual. However, similarly to the case of olive oil, here we considered that this sub-α form may have occurred from some alloy of more saturated TAGs present in Iberian ham fat. Soon after, at 14ºC, the SR-SAXD pattern revealed the occurrence of a triple chain length peak at 6.5 nm (also present in the laboratory-scale XRD patterns). This triple chain length peak should be due to the crystallization of a β'-3L form. Although not

clear β' WAXD peaks could be observed, the wideness of sub-α WAXD peaks could be an indicative of the coexistence of overlapped β' peaks with those of sub-α form. These two crystallizations (sub-α-2L and β'-3L) corresponded to the first set of exothermic peaks that appeared from 20ºC to -5ºC in the DSC cooling thermogram of Figure 4.13a. On further cooling, at around -14ºC according to the SR-XRD data (at -22ºC in the laboratory-scale XRD patterns), a new β'-2L form crystallized. This form was identified by diffraction peaks at 4.4 nm (double chain length), and 0.43 nm, 0.42 nm and 0.39 nm in the SAXD and WAXD patterns, respectively. The last β'-2L crystallization should correspond to the second set of crystallization peaks that could be observed from -10ºC to -40ºC in the cooling curve of C1 present in Figure 4.13a. As to the heating treatment, enlarged images, showing the melting behavior observed in the laboratory-scale XRD and SR-XRD patterns, are inserted in Figure 4.17. SR-XRD data revealed, at 4ºC, the disappearance of the WAXD peak at 0.39 nm, probably due to some β' form which was overlapped with other existing β' forms. At 16ºC, the SAXD peak at 4.8 nm, corresponding to sub-α-2L form, vanished because of its melting or polymorphic transformation. According to the SR-XRD data, on further heating, the triple (3.5 nm) and double (4.4 nm) chain length peaks disappeared almost simultaneously, at 32ºC and 34ºC, due to β'-3L and β'-2L melting, respectively. The melting behavior shown in the enlarged figured of the SR-SAXD pattern gave more details than that of the laboratory-scale XRD patterns, as it is easier to distinguish the peaks at 4.8 nm and 4.4 nm through the synchrotron data.

Laboratory-scale XRD and SR-XRD patterns corresponding to sample B1 (*bellota* variety) are depicted in Figure 4.18.

Similarly to C1, when B1was cooled, a double chain length peak (4.8 nm) firstly appeared in the SAXD pattern at 12ºC and a triple chain length peak (3.5 nm) occurred at around 8ºC. Simultaneously, the WAXD pattern showed two peaks at 0.41 nm and 0.38 nm, which may correspond, also considering the long spacing values, to a concurrent crystallization of a sub-α-2L form (of more saturated TAGs) and a β'-3L form, whose peaks were overlapping.

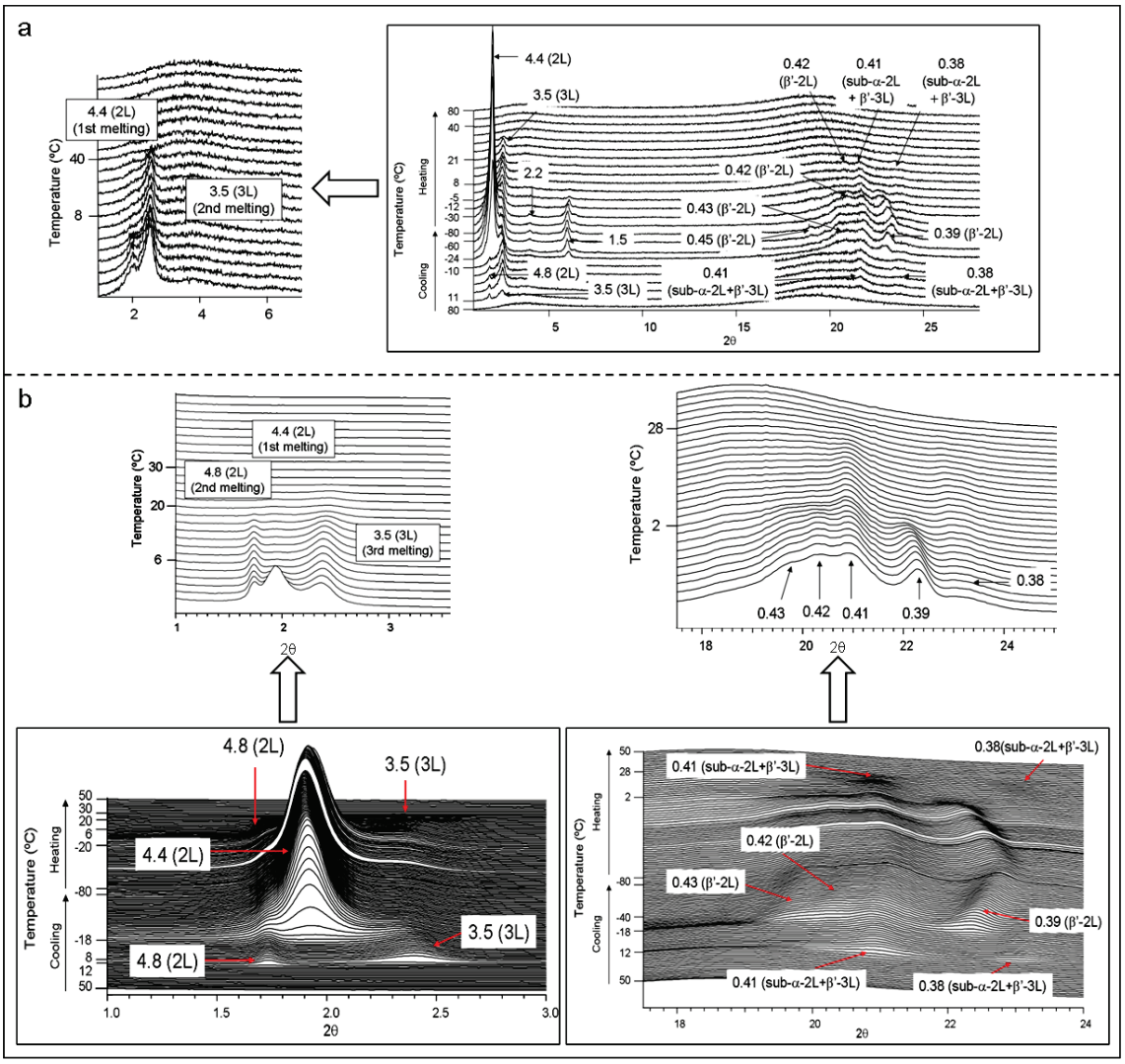

Figure 4.18. XRD patterns of B1 sample. a) Laboratory-scale XRD. b) SR-XRD (SR-SAXD and SR-WAXD patterns). Enlarged figures depict the melting behavior of the sample.

Upon cooling, a new β'-2L form crystallized from the melt at approximately -18ºC. This form could be identified by a double chain length peak at 4.4 nm and WAXD peaks at 0.43 nm, 0.42 nm and 0.39 nm. Afterwards, when B1 was heated at a rate of 2ºC·min^{-1}, the SR-XRD revealed that, around 6ºC, the form having a double chain length peak at 4.4 nm vanished. Moreover, WAXD peaks at 0.43 nm, 0.42 nm and 0.39 nm (β'-2L) also disappeared. This phenomenon corresponded to the first set of endothermic peaks that could be observed, in the temperature range from -30ºC to 5ºC, in the corresponding DSC heating curve of B1 sample (see Figure 4.13b). Enlarged images, inserted in Figure 4.15, also showed that polymorphic forms having long spacing values of 4.8 nm (sub-α-2L form) and 3.5 nm (β'-3L form) coexisted until 20ºC,

temperature at which sub-α-2L form melted. Finally, at approximately 30ºC, the diffraction peaks of the remaining β'-3L disappeared, so that β'-3L form melted.

Highly complex polymorphic behavior was observed in both Iberian ham fat samples. The XRD patterns of the two varieties studied (*cebo* and *bellota*) became very similar, but some differences, referred to their melting behavior, could be detected. SR-XRD patterns of B1 exhibited a first disappearing SAXD peak at 4.8 nm, followed by the peaks at 3.5 nm and 4.4 nm. However, in the case of C1, at first the peak at 4.4 nm vanished and, later, those at 4.8 nm and 3.5 nm also disappeared. We could not extract such detailed information from the laboratory-scale XRD data. Nevertheless, results showed that in B1, the peak at 3.5 nm disappeared before the one at 4.4 nm, whereas in B1, the sequence was the opposite (firstly the peak at 4.4 nm disappeared, followed by the peak at 3.5 nm). The sequence of melting forms observed for the two samples may be related to the TAG compositions of both kinds of ham fat.

As shown in Chapter 2, when a TAG exhibits double and triple chain length structure polymorphic forms, triple chain length forms use to present a higher melting point than double chain length polymorphs. If a double chain length (2L) polymorph melts at higher temperatures than a triple chain length (3L) polymorph, it may indicate that the 2L form comes from a more saturated TAG than that with 3L structure. The results obtained in the present study showed that in B1 (*bellota*), the last melting form exhibited a triple chain length structure, whereas in C1 (*cebo*) the chain length structure of the last melting form was double. Hence, we may reasonably think that 2L forms present in *cebo* came from more saturated TAGs than the 3L forms. Moreover, in the *cebo* sample, TAGs with 2L structure may be more saturated than those with 2L structure of *bellota*, so that *cebo* may contain more saturated TAGs than *bellota*.

Thus, some differences were also detected in the XRD patterns of *cebo* and *bellota* samples. However, similarly to the olive oil case (Section 4.4.1), the DSC data revealed more differences than the XRD data. The corresponding DSC results provided characteristic cooling and heating curves for the two analyzed categories.

Thermo-optical polarized microscopy (TOM) experiments were also performed for C1 and B1. The thermal treatment applied to samples was the same than that used in the DSC and XRD experiments. Figure 4.19 illustrates some TOM images obtained when cooling and heating the samples at $2ºC \cdot min^{-1}$.

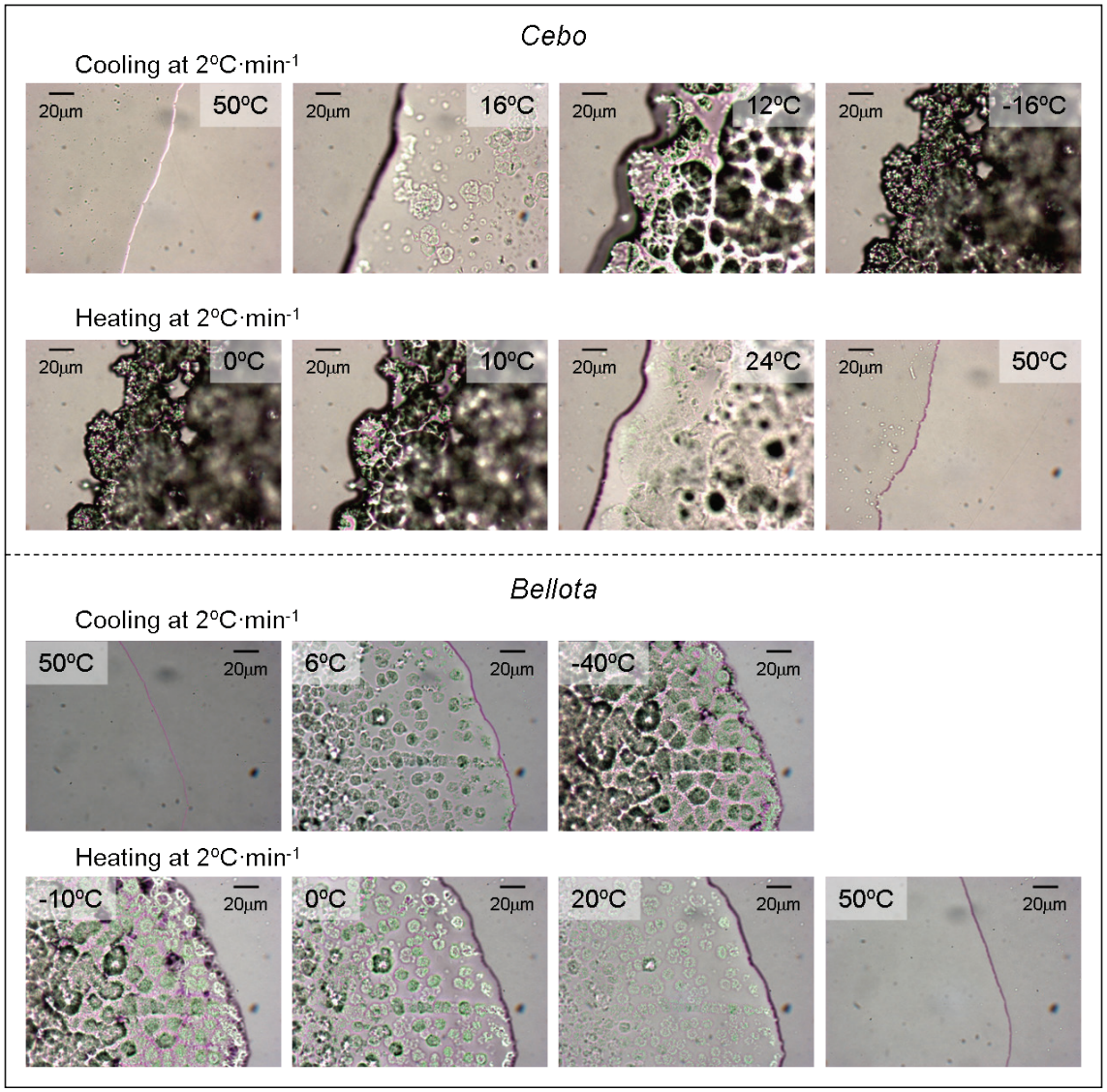

Figure 4.19. Thermo-optical polarized microscopy images obtained when C1 (*cebo*) and B1 (*bellota*) samples were cooled and heated at 2ºC·min^{-1}.

When C1 was cooled, first crystals were observed at around 16ºC, and further crystals grew until 12ºC. This crystallization process corresponded to the first set of exothermic peaks that appeared in the corresponding DSC cooling curve of Figure 4.13a. More crystals were observed at -16ºC (corresponding to the second set of exothermic peaks observable in the DSC cooling curve) and no more changes took place until -80ºC. Therefore, two different crystallization processes could be easily distinguished in the cooling process of C1. As to the heating step, the beginning of the melting was firstly appreciated at around 0ºC. In Figure 4.19, TOM images taken at 10ºC, 24ºC and 50ºC show the progressive melting of C1.

The crystallization behavior of B1 became different to that of C1. Crystals gradually grew from the melted sample, and not distinguished crystallization processes were observed by TOM experiments. At -40ºC, the whole sample had crystallized. When a heating rate of 2ºC·min^{-1} was applied, B1 progressively melted. Figure 4.19 shows the state of the sample at -10ºC, 0ºC, 20ºC and 50ºC.

By looking at the TOM images, one may notice some differences in the crystal morphologies of the two samples. More aggregated and bigger crystals were obtained in C1, while separated spherulites, having an average diameter of around 10 μm, could be easily noted in the TOM micrographs of B1.

To sum up, high differences were observed in the fatty acid compositions and the polymorphic behavior of Iberian ham fat samples obtained from pigs produced with different fattening systems (*cebo* and *bellota*).

DSC results showed important variations in both the DSC cooling and heating curves, which were corroborated by the PCA calculations. Regarding the XRD data, most important differences appeared in the melting sequence of the polymorphic forms (double or triple chain length structures), which was also confirmed by PCA (temperature ranges defined by the loadings on factor 2). As to thermo-optical polarized microscopy, we also observed a different crystallization behavior in the two samples. *Cebo* crystals became bigger, thicker and more aggregated than those of *bellota*, and they crystallized in two different steps. On the contrary, *bellota* crystals gradually grew from the melt, and they were smaller and spreader.

The most important differences were detected by using DSC. DSC is a rapid and sensible technique that could be used to obtain a fingerprint of Iberian ham fat samples from different categories. However, more samples are needed to be analyzed in order to obtain more data and extrapolate the results obtained to more ham categories (also including *recebo* samples), hams coming from different geographical areas, and also including the genotype factor. The analysis of a higher amount of samples will permit further chemometric calculations by using classification methods (pattern recognition) with the purpose of fingerprinting and, therefore, authenticating the samples.

4.5.

Chapter conclusions

Following are the conclusions which can be extracted from this chapter:

- The characterization of the polymorphic behavior of multicomponent TAG mixtures, formed by 2, 3, 4, 5 and 6 TAGs permitted to make an approach to the understanding of a complex natural oil, such as olive oil. We observed that the polymorphic behavior of an extra virgin olive oil obtained from the Arbequina olive variety was mainly influenced by its main TAGs, whereas apparently minor components did not develop a crucial role.

- We used the polymorphic behavior of natural fats and oils (virgin and extra virgin olive oil, and Iberian ham fat) as a tool to determine authenticity (ham categories depending of the fattening system used) and adulteration practices (fraudulent additions of hazelnut oil to olive oil).

- The combined use of DSC and preliminary chemometric calculations permitted determining fraudulent additions of raw hazelnut oil in an extra virgin olive oil from the Arbequina variety at concentrations below 5%. However, more difficulties arise in adulteration detections due to the complexity of these samples and the influence of external factors, such as the olive variety, geographical region, climate, etc. Further work is needed to analyze a higher number of samples and try to define some general trends, considering these determining factors.

- Highly significant differences were detected in the polymorphic behavior of Iberian ham fat obtained from pigs with different fattening systems (*cebo* and *bellota*). The DSC data showed important differences in the cooling and heating thermograms of the two categories, which were corroborated by the PCA chemometric calculations. XRD patterns (with both conventional and synchrotron radiation) showed different melting sequences of the polymorphic forms of *cebo* and *bellota*, which are strongly related to the chemical composition of the samples.

Moreover, variations in the crystallization behavior and crystal morphology were also observed by thermo-optical polarized microscopy: *cebo* crystals grew in two different steps, and they became bigger and more aggregated, while more dispersed and smaller spherulites were progressively formed when *bellota* fat sample was subjected to a cooling process. It would be interesting to analyze a higher amount of Iberian ham fat samples, including more categories (*recebo*), different geographical areas, producers, and genotypes.

- Due to its rapidity and high sensibility, the use of the DSC could become a useful tool to obtain a fingerprint of food products for their authentication and adulteration detection.

CHAPTER 5

General conclusions

The work presented in this PhD thesis focused on the *in situ* polymorphic study of main TAGs present in some vegetable and animal fats and oils, the phase behavior of some of their binary mixtures, and the use of polymorphism as a tool for food authentication.

Some general conclusions can be extracted from the work performed, which can be summarized as follows:

- By mainly using a combination of DSC and SR-XRD (simultaneous SAXD and WAXD measurements), we monitored the polymorphic occurrence and transformation pathways of POP, OPO, POO, POL, SOO, OOO and OOL, which become the main triacylglycerols present in some edible fats and oils, such as olive oil and Iberian ham fat. The results indicated that more stable forms were formed in a higher quantity when fatty samples were slowly cooled and heated, whereas less stable forms occurred at higher rates of cooling and heating. The polymorphic transitions took place either in solid state or melt-mediation and were largely influenced by the heating rates. We discussed the results obtained by considering the differences in activation free energies for the polymorphic transformations from less to more stable forms.

  A particular behavior was observed in POP, which becomes the most saturated TAG analyzed in the first section of the present PhD thesis. By decreasing the cooling and heating rates, it was more difficult to obtain more stable forms of POP, compared to the OPO, POO, POL, SOO, OOO and OOL cases. As to the heating process, less solid state transformations were detected when the rate of heating decreased, compared to the other TAGs examined. This may be related to the more saturated nature of POP, whose transformation from less stable to more stable forms may need large activation energies compared to those TAGs containing more unsaturated acid moieties. The flexibility of the chain packing of unsaturated acids is more enhanced than that of saturated fatty acids.

  The results obtained are directly applicable to crystallization processes of edible fats and oils to obtain the desired product characteristics by using the most efficient temperature programs.

- In order to understand the molecular interactions between TAG components, we determined the phase domains of some binary mixtures of TAGs containing palmitic

and oleic fatty acids, which are the following: PPO-OPO, PPO-POO and POO-OPO. PPO-OPO system revealed an eutectic behavior, whereas PPO-POO and POO-OPO were MC-forming in the metastable state and tended to decompose into the pure TAG components. The non formation or metastability of the molecular compounds observed were discussed taking into account the main molecular interactions between the TAG molecules, which basically consist of aliphatic chain packing, glycerol conformation of the TAG components and methyl end stacking. The results obtained may be also useful to understand and predict the phase behavior of binary systems of other mixed saturated/unsaturated TAGs. Nevertheless, in the future it would be interesting to examine the effect of racemicity of asymmetric TAGs on the phase behavior of these binary mixtures.

□ Heterogeneous microstructures of spherulites of POP-OPO binary mixtures were analyzed in neat liquid and solution (50% n-dodecane) systems by using SR-μ-XRD. Two different compositions were characterized to establish how the microstructures of spherulites of the TAG mixtures are formed when MC crystals (formed at the 50:50 concentration ratio) and POP or OPO component crystals can be formed competitively. The results obtained permitted defining the relative nucleation rates of MC and component POP and OPO crystals at the crystallization temperatures examined. In the two analyzed compositions, a different behavior on the relative nucleation rates of MC and component TAG crystals was observed. This study may have a direct implication to palm oil fractionation processes by dry and solvent methods.

□ In order to make an approach to more complex fatty samples, such as olive oil, we characterized the complicated polymorphic behavior of multicomponent TAG mixtures (containing from 2 to 6 TAG components). The results revealed that, in the particular case of olive oil, the polymorphic behavior is basically governed by its main TAGs, whereas minor component may not be determining. The polymorphic behavior of the multicomponent mixture containing 5 TAGs (OOO, POO, OOL, POL, and PPO) became almost identical to that of an extra virgin olive oil obtained from the Arbequina olive variety.

- Finally, we used the polymorphic behavior as a tool for food authentication and the detection of adulteration practices. In particular, we determined fraudulent additions of raw hazelnut oil in extra virgin olive oil at concentrations below 5%, and we could easily distinguish Iberian ham fats obtained from pigs with different fattening systems (*cebo* and *bellota*). For the two cases, most evident differences were detected in the DSC cooling and heating thermograms, revealing that this technique could become a useful tool to obtain a fingerprint of food products for their authentication and detection of adulterations. However, further work is needed to analyze a higher amount of samples and try to define some general trends, considering some determining factors, like the olive variety and geographical region in the case of olive oil, or the genotype in the case of Iberian ham fat.

APPENDIX

Complementary scanning synchrotron radiation microbeam X-ray diffraction patterns of POP-OPO binary mixtures

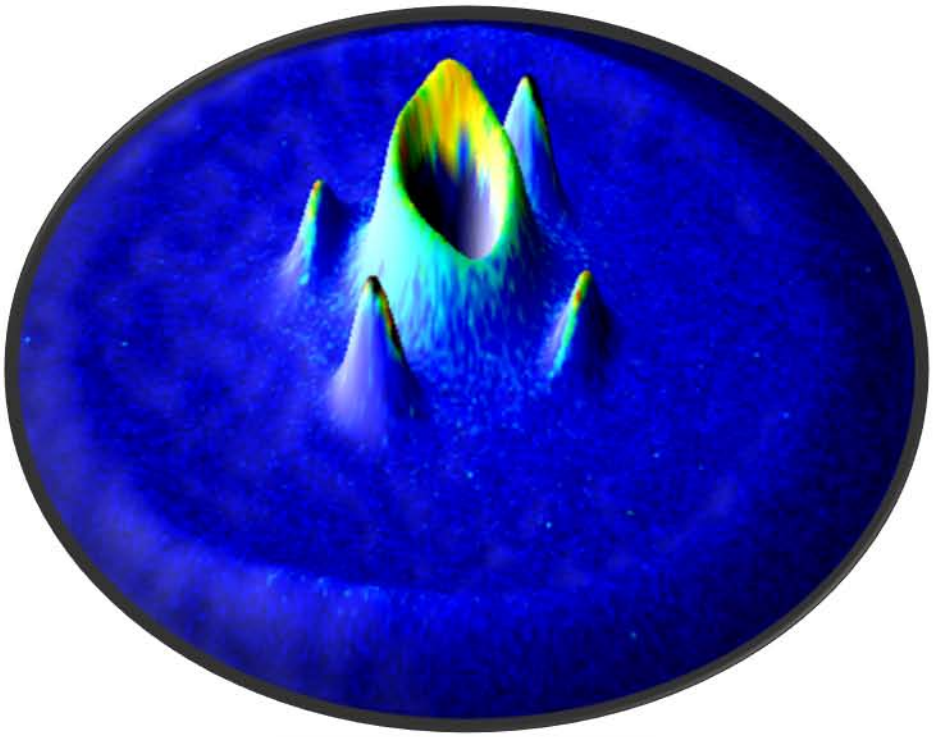

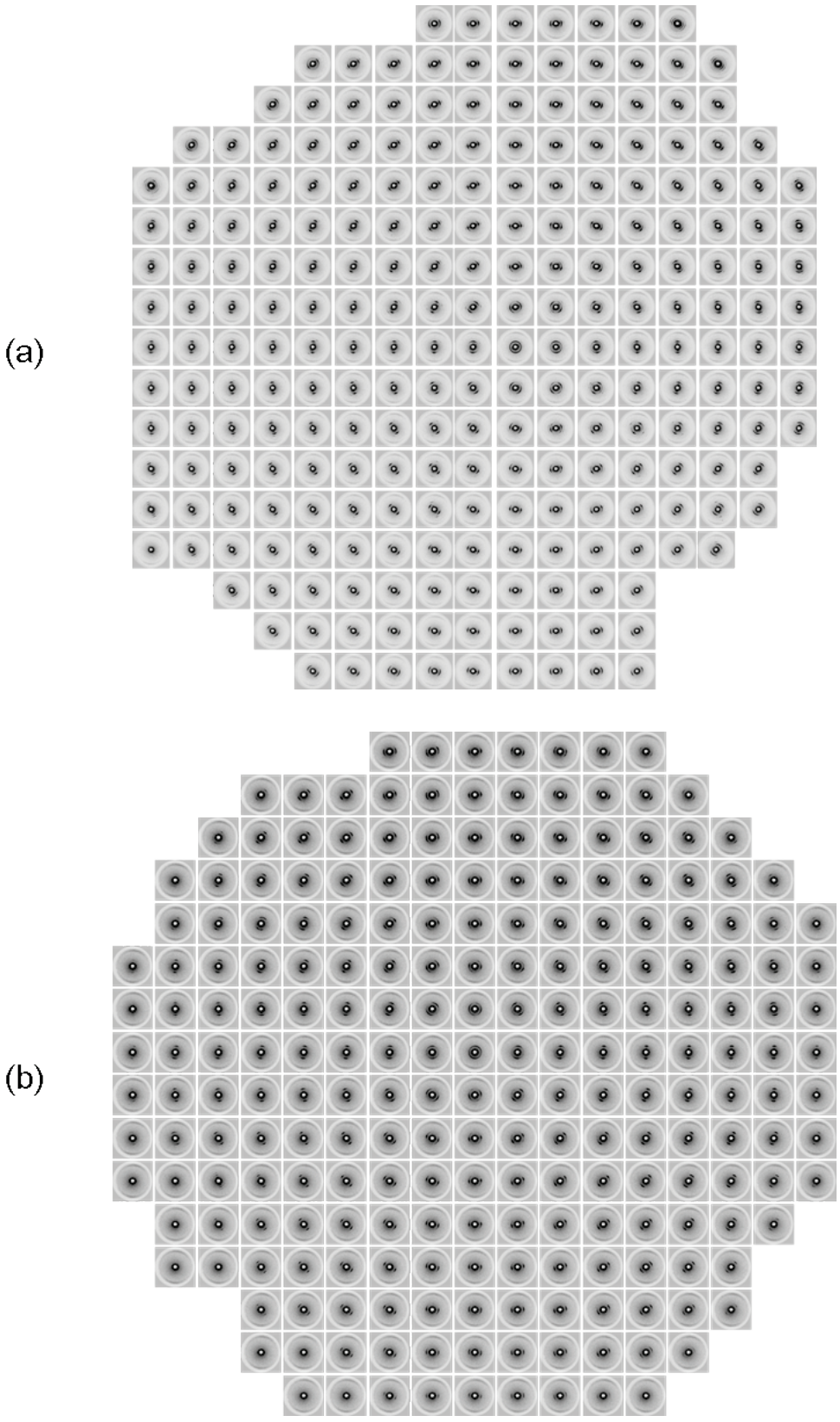

Figure A.1. Scanning SR-μ-XRD patterns taken at the all positions of a spherulite of the mixture of 25POP:75OPO grown from neat liquid (a) at 9 ºC and (b) at 6º C

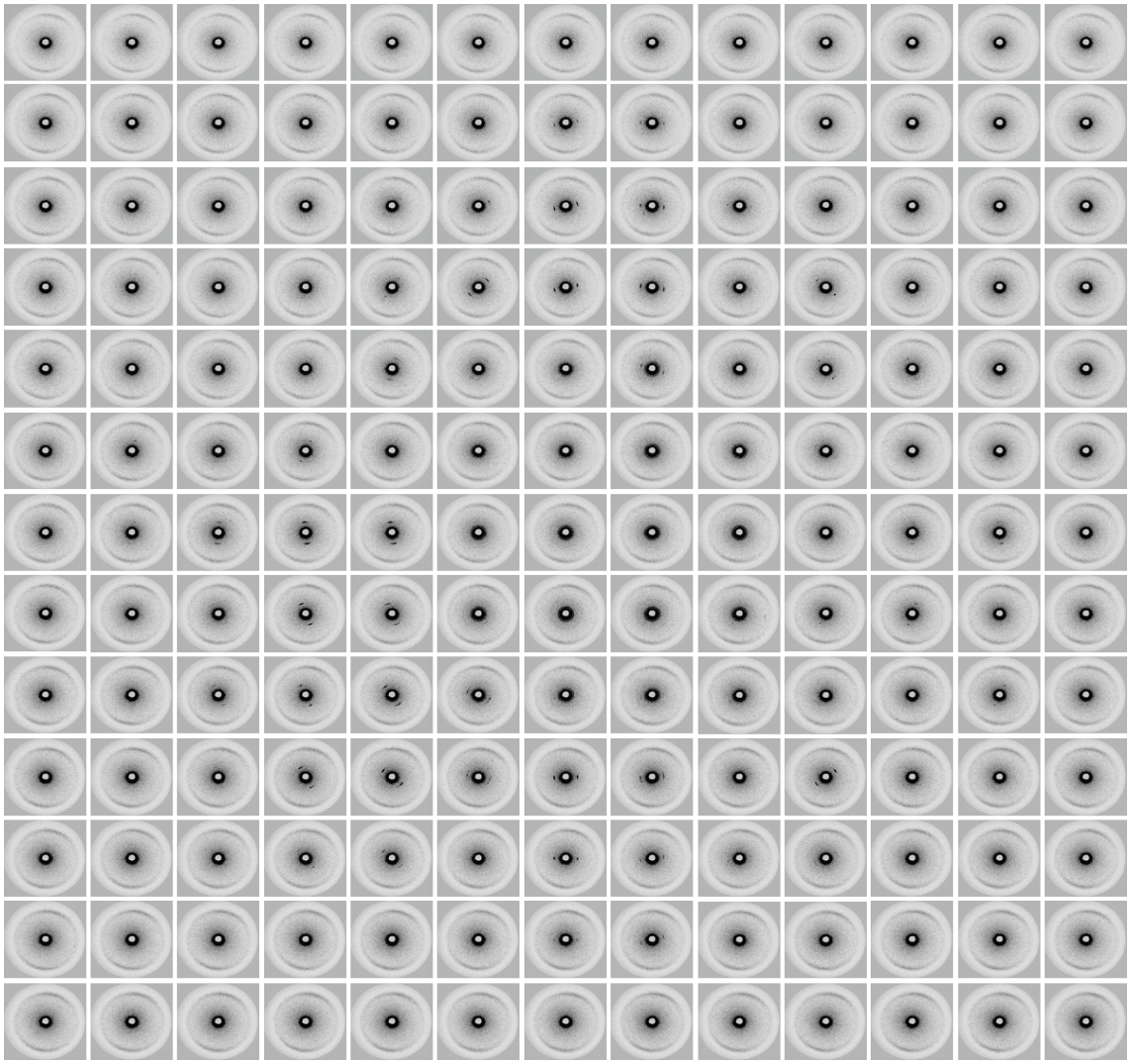

Figure A.2. Scanning SR-μ-XRD patterns of a spherulite of the mixture of 75POP:25OPO grown from n-dodecane solution at 7 ºC

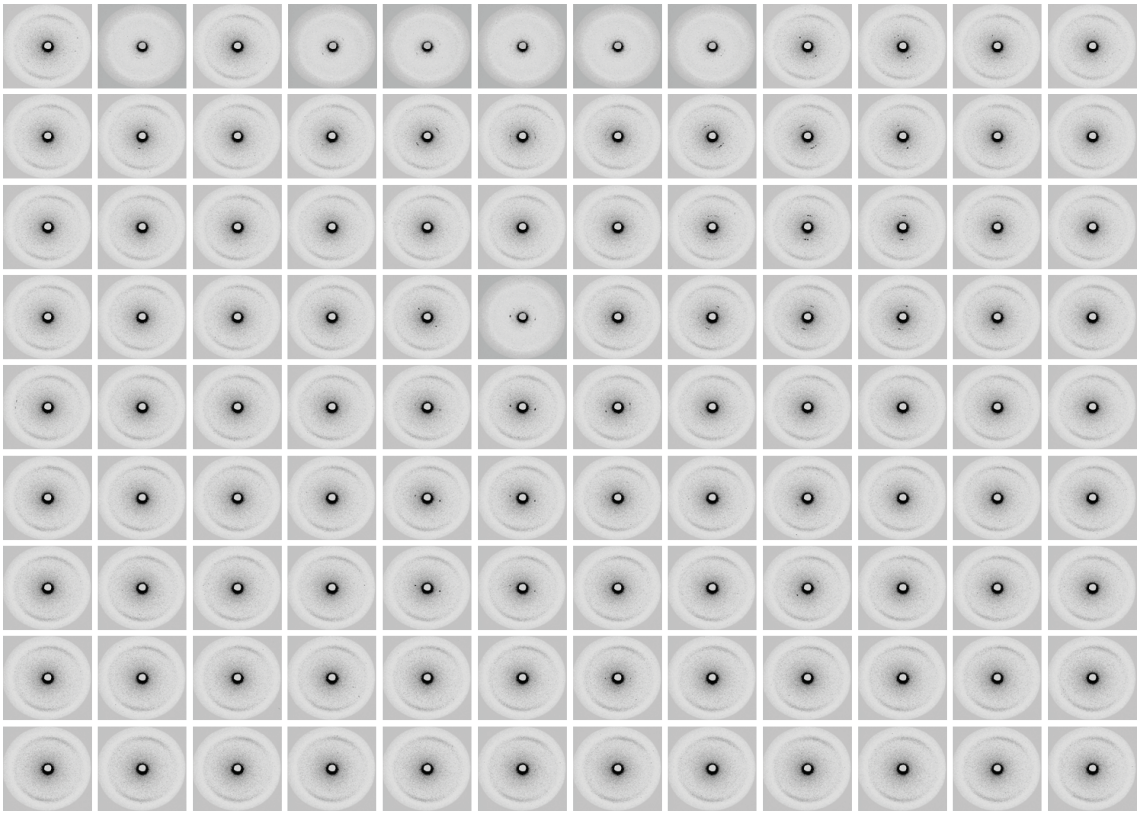

Figure A.3. Scanning SR-μ-XRD patterns of a spherulite of 25POP:75OPO grown from n-dodecane solution at 2 ºC

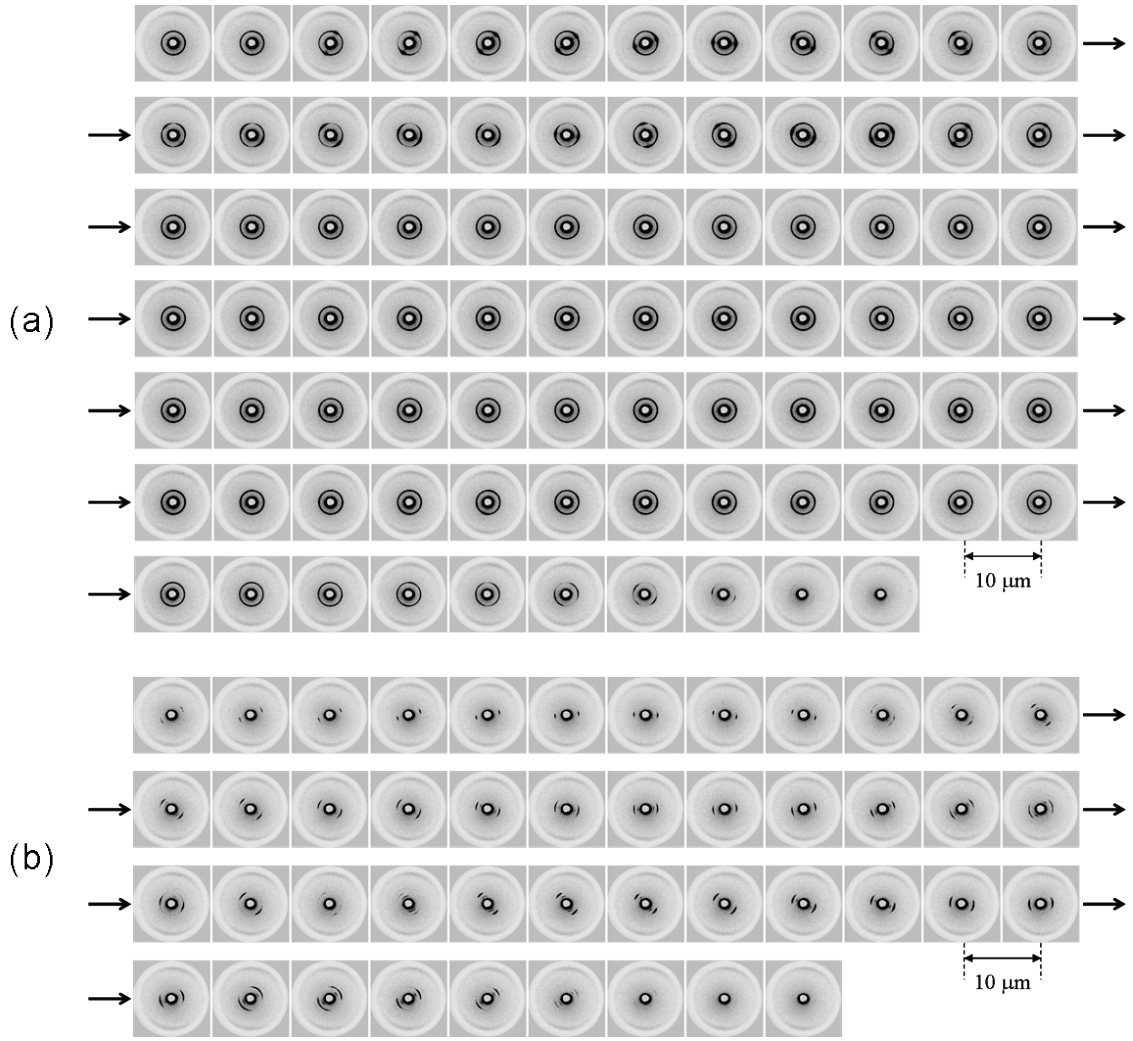

Figure A.4. Scanning SR-μ-XRD patterns through the horizontal direction over many small spherulites of 25POP:75OPO mixture grown from neat liquid (a) at 9 ºC and (b) at 6 ºC**.**

REFERENCES

A

Acevedo, N. C.; Marangoni, A. G. *Cryst. Growth Des.* **2010a**, 10 (8), 3327.

Acevedo, N. C.; Marangoni, A. G. *Cryst. Growth Des.* **2010b**, 10 (8), 3334.

Agiomyrgianaki, A.; Petrakis, P.V.; Dais, P. *Talanta* **2010**, 80, 2165.

Akita, C.; Kawaguchi, T.; Kaneko, F. *J. Phys. Chem. B* **2006**, 110 (9), 4346.

Aquilano, D.; Squaldino, G. in Crystallization Processes in Fats and Lipid Systems, ed. Garti, N.; Sato, K. Marcel Dekker, New York, USA, 2001, pp. 1–51.

Angiuli, M.; Ferrari, C.; Lepori, L.; Matteoli, E.; Salvetti, G.; Tombari, E.; Banti, A.; Minnaja, N. *J. Therm. Anal. Calorim.* **2006**, 84 (1), 105.

Arce, L.; Domínguez-Vidal, A.; Rodríguez-Estévez, V.; López-Vidal, S.; Ayora-Cañada, M. J.; Valcárcel, M. *Anal. Chim. Acta* **2009**, 636, 183.

Aree, T.; Chaichit, N.; Engkakul, C. *Carbohyd. Res.* **2008**, 343, 2451.

Arima, S.; Ueno, S.; Ogawa, A.; Sato, K. *Langmuir* **2009**, 25 (17), 9777.

B

Baeten, V.; Fernández Pierna, J. A.; Dardenne, P.; Meurens, M.; García-González, D. L.; Aparicio-Ruiz, R. *J. Agric. Food Chem.* **2005**, 53, 6201.

Barba, L.; Arrigheti, G.; Calligaris, S. *Eur. J. Lipid Sci. Technol.* **2013**, 15, 322.

Bayés-García, L.; Calvet, T.; Cuevas-Diarte, M. A.; Ueno, S.; Sato, K. *CrystEngComm.* **2011a**, 13, 3592.

Bayés-García, L.; Calvet, T.; Cuevas-Diarte, M. A.; Ueno, S.; Sato, K. *CrystEngComm*. **2011b**, 13, 6694.

Bayés-García, L.; Calvet, T.; Cuevas-Diarte, M. A.; Ueno, S.; Sato, K. *CrystEngComm*. **2013**, 15, 302.

Bennema, P.; Meekes, H.; Boerrigter, S. X. M.; Cuppen, H. M.; Deij, M. A.; van Eupen, J.; Verwer, P.; Vlieg, E. *Cryst. Growth Des.* **2004**, 4 (5), 905.

Bernstein, J. Polymorphism in Molecular Crystals, Oxford University Press, New York, USA, 2002.

Berrueta, L. A.; Alonso-Salces, R. M.; Héberger, K. *J. Chromatogr. A* **2007**, 1158, 196.

Boerrigter, S. X. M.; Hollander, F. F. A.; van de Streek, J.; Bennema, P.; Meekes, H. *Cryst. Growth Des.* **2002**, 2 (1), 51.

Boodhoo, M. V.; Kutek, T.; Filip, V.; Narine, S. S. *Chem. Phys. Lipids* **2008**, 154 (1), 7.

Bouzidi, L.; Narine, S. S. *Langmuir* **2010**, 26 (6), 4311.

Bouzidi, L.; Narine, S. S. *Chem. Phys. Lipids* **2012**, 165, 105.

C

Calliauw, G.; Gibon, V.; de Greyt, W.; Plees, L.; Foubert, I.; Dewettinck, K. *J. Am. Oil Chem. Soc.* **2007**, 84, 885.

Campos, R.; Narine, S. S.; Marangoni, A. G. *Food Res. Int.* **2002**, 35 (10), 971.

Campos, R.; Ollivon, M.; Marangoni, A. G. *Cryst. Growth Des.* **2010**, 10 (1), 205.

Cebula, D. J.; Smith, K. W. *J. Am. Oil Chem. Soc.* **1991**, 68 (8), 591.

Chanzy, H.; Putaux, J. L.; Dupeyre, D.; Davies, R.; Burghammer, M.; Montanari, S.; Riekel, C. *J. Struct. Biol.* **2006**, 154, 100.

Chapman, D. *Chem. Rev.* **1962**, 62 (5), 433.

Chiavaro, E.; Vittadini, E.; Rodriguez-Estrada, M. T.; Cerretani, L.; Bonoli, M.; Bendini, A.; Lercker, G. *J. Agric. Food Chem.* **2007**, 55, 10779.

Chiavaro, E.; Vittadini, E.; Rodriguez-Estrada, M. T.; Cerretani, L.; Bendini, A. *J. Agric. Food Chem.* **2008a**, 56, 496.

Chiavaro, E.; Rodriguez-Estrada, M. T.; Barnaba, C.; Vittadini, E.; Cerretani, L.; Bendini, A. *Anal. Chim. Acta* **2008b**, 625, 215.

Chiavaro, E.; Vittadini, E.; Rodriguez-Estrada, M. T.; Cerretani, L.; Bendini, A. *Food Chem.* **2008c**, 110, 248.

Chiavaro, E.; Rodríguez-Estrada, M. T.; Bendini, A.; Cerretani, L. *Eur. J. Lipid Sci. Technol.* **2010**, 112, 580.

Chong, C. L.; Kamarudin, Z.; Lesieur, P.; Marangoni, A.; Borgaux. C.; Ollivon, M. *Eur. J. Lipid Sci. Technol.* **2007**, 109, 410.

Corchinoux, R.; Chanh, N. B.; Haget, Y.; Calvet, T.; Estop, E.; Cuevas-Diarte, M. A. *J. Chim. Phys.* **1989**, 86, 561.

Cordella, C.; Moussa, I.; Martel, A. C.; Sbirrazzuoli, N.; Lizzani-Cuvelier, L. *J. Agric. Food Chem.* **2002**, 50, 1751.

D

Damirchi, S. A.; Savage, G. P.; Dutta, P. C. *J. Amer. Chem. Soc.* **2005**, 82 (10), 717.

Davenel, A.; Riaublanc, A.; Marchal, P.; Gandemer, G. *Meat Sci.* **1999**, 51, 73.

Dhonsi, D.; Stapley, A. G. F. *J. Food Eng.* **2006**, 77 (4), 936.

Díaz, I.; García Regueiro, J. A.; Casillas, M.; De Pedro, E. *Food Chem.* **1996**, 55 (4), 383.

Drakopoulos, M.; Sergienko, P. M.; Snigireva, I.; Snigirev, A.; Vazina, A. A. *Nucl. Instrum. Meth. A* **2005**, 543, 161.

E

Ellis, D. I.; Brewster, V. L.; Dunn, W. B.; Allwood, J. W.; Golovanov, A. P.; Goodacre, R. *Chem. Soc. Rev.* **2012**, 41, 5706.

Engstrom, L. J. *Fat Sci. Technol.* **1992**, 94, 173.

F

Falini, G.; Fermani, S.; Gazzano, M.; Ripamonti, A. *Chem. Eur. J.* **1998**, 4 (6), 1048.

Ferguson, R. H.; Lutton, E. S. *J. Am. Chem. Soc.* **1947**, 69, 1445.

Ferrari, C.; Angiuli, M.; Tombari, E.; Righetti, M. C.; Matteoli, E.; Salvetti, G. *Thermochim. Acta* **2007**, 459, 58.

Flores, G.; Ruiz del Castillo, M. L.; Blanch, G. P.; Herraiz, M. *Food Chem.* **2006**, 97, 336.

Foubert, I.; Fredrick, E.; Vereecken, J.; Sichien, M.; Dewettinck, K. *Termochim. Acta* **2008**, 471, 7.

Frankel, E. N. *J. Agric. Food Chem.* **2010**, 58, 5991.

Fratzl, P.; Weinkamer, R. *Prog. Mater. Sci.* **2007**, 52, 1263.

G

Gallardo, E.; Narváez-Rivas, M.; Pablos, F.; Jurado, J. M.; León-Camacho, M. *J. Agric. Food Chem.* **2012**, 60, 1645.

Gliguem, H.; Ghorbel, D.; Lopez, C.; Michon, C.; Ollivon, M.; Lesieur, P. *J. Agric. Food Chem.* **2009**, 57 (8), 3195.

Goto, M.; Kodali, D. R.; Small, D. M.; Honda, K.; Kozawa, K.; Uchida, T. *Proc. Natl. Acad. Sci.* **1992**, 89, 8083.

H

Hagemann, J. W.; Tallent, W. H.; Kolb, K. E. *J. Am. Oil Chem. Soc.* **1972**, 49 (2), 118.

Harwood, J. L.; Yaqoob, P. *Eur. J. Lipid Sci. Technol.* **2002**, 104, 685.

Himawan, C.; Starov, V. M.; Stapley, A. G. F. *Adv. Colloid Interfac.* **2006**, 122, 3.

Hodge, S. M.; Rousseau, D. *J. Am. Oil Chem. Soc.* **2002**, 79 (11), 1115.

Hollander, F. F. A.; Boerrigter, S. X. M.; van de Streek, J.; Bennema, P.; Meekes, H.; Yano, J.; Sato, K. *J. Phys. Chem. B* **2003**, 107, 5680.

Humphrey, K. L.; Narine, S. S. *J. Am. Oil Chem. Soc.* **2007**, 84 (8), 709.

I

Ikeda, E.; Ueno, S.; Miyamoto, R.; Sato, K. *J. Phys. Chem. B* **2010**, 114 (34), 10961.

Ilyasoglu, H.; Ozcelik, B. *J. Am. Oil Chem. Soc.* **2011**, 88, 907.

J

Jensen, L. H.; Mabis, A. J. *Acta Crystallogr.* **1966**, 21, 770.

Jiménez Márquez, A.; Beltrán Maza, G. *Grasas Aceites* **2003**, 54 (4), 403.

Jiménez Márquez, A.; Beltrán Maza, G.; Aguilera Herrera, M. P.; Uceda Ojeda, M. *Grasas Aceites* **2007**, 58 (2), 122.

K

Kajioka, H.; Yoshimoto, S.; Gosh, R. C.; Taguchi, K.; Tanaka, S.; Toda, A. *Polymer* **2010**, 51, 1837.

Kajiura, Y.; Watanabe, S.; Itou, T.; Nakamura, K.; Iida, A.; Inoue, K.; Yagi, N.; Shinohara, Y.; Amemiya, Y. *J. Struct. Biol.* **2006**, 155, 438.

Kaneko, F. in Crystallization Processes in Fats and Lipid Systems, ed. Garti, N.; Sato, K. Marcel Dekker, New York, USA, 2001, pp. 53–97.

Kashchiev, D.; Sato, K. *J. Chem. Phys.* **1998**, 109, 8530.

Kellens, M.; Meeussen, W.; Hammersley, A.; Riekel, C. H. *Chem. Phys. Lipids* **1990**, 52, 79.

Kikuzuki, T.; Shinohara, Y.; Nozue, Y.; Kazuki, I.; Amemiya, Y. *Polymer* **2010**, 51, 1632.

Kitaigorodsky, A. I. Mixed Crystals, Springer Series in Solid-State Sciences, Springer-Verlag, Berlin Heidelberg, Germany, 1984, vol. 33.

Kodali, D. R.; Atkinson, D.; Redgrave, T. G.; Small, D. M. *J. Lipid Res.* **1987**, 28, 403.

Kodali, D. R.; Atkinson, D.; Small, D. M. *J. Lipid Res.* **1990**, 31, 1853.

Koyano, T.; Hachiya, I.; Arishima, T.; Sagi, N.; Sato, K. *J. Am. Oil Chem. Soc.* **1991**, 68, 716.

Koyano, T.; Hachiya, I.; Sato, K., *J, Phys. Chem.* **1992**, 96, 10514.

Kuckzumow, A.; Chevallier, P.; Dillmann, P.; Wajnberg, P.; Rudas, M. *Spectrochim. Acta* B **2000**, 55, 1623.

Kulkarni, C. V.; Tang, T. Y.; Seddon, A.; Seddon, J. M.; Ces, O.; Templer, R. *Soft Matter* **2010**, 6, 3191.

Kulkarni, C.; Wachter, W.; Iglesias-Salto, G.; Engelskirchen, S.; Ahualli, S. *Phys. Chem. Chem. Phys.* **2011**, 13, 3004.

L

Lam, R.; Quaroni, L.; Pederson, T.; Rogers, M. A. *Soft Matter* **2010**, 6, 404.

Larsson, K. *Proc. Chem. Soc.* **1963**, 87.

Larsson, K. *Ark. Kemi*. **1964**, 23, 1.

Larsson, K. *Acta Chem. Scand.* **1966**, 20, 2255.

Larsson, K.; Quinn, P.; Sato, K.; Tiberg, F. Lipids: structure, physical properties and functionality, The Oily Press, Bridgewater, USA, 2006, pp. 9-71.

Lopez, C. ; Lesieur, P. ; Bourgaux, C.; Ollivon, M. *J. Dairy Sci.* **2005a**, 88 (2), 511.

Lopez, C.; Karray, N.; Lesieur, P.; Ollivon, M. *Eur. J. Lipid Sci. Technol.* **2005b**, 107, 673.

Lutton, E. S. *J. Am. Oil Chem. Soc.* **1950**, 27, 276.

M

MacMillan, S. D.; Roberts, K. J.; Rossi, A.; Wells, M. A.; Polgreen, M. C.; Smith, I. H. *Cryst. Growth Des.* **2002**, 2 (3), 221.

Mannina, L.; D'Imperio, M.; Capitani, D.; Rezzi, S.; Guillou, C.; Mavromoustakos, T.; Molero Vilchez, M. D.; Herrera Fernández, A.; Thomas, F.; Aparicio, R. *J. Agric. Food Chem.* **2009**, 57, 11550.

Marangoni, A. G.; Narine, S. S. Ed. Physical Properties of Lipids, Marcel Dekker, New York, USA, 2002, pp. 63-217.

Marangoni, A. G. Fat Crystal Networks, Marcel Dekker, New York, USA 2004.

Marangoni, A. G.; Aurand, T. C.; Martini, S.; Ollivon, M. *Cryst. Growth Des.* **2006**, 6 (5), 1199.

Marangoni, A. G.; Ollivon, M. *Chem. Phys. Lett.* **2007**, 442, 360.

Martini, S.; Suzuki, A. H.; Hartel, R. W. *J. Am. Oil Chem. Soc.* **2008**, 85, 621.

Massart, D. L.; Vander Heyden, Y. *LC GC Eur.* **2005**, 18 (2), 84.

Mazzanti, G.; Guthrie, S. E.; Sirota, E. B.; Marangoni, A. G.; Idziak, S. H. J. *Cryst. Growth Des.* **2003**, 3, 721.

Mazzanti, G.; Li, M.; Marangoni, A. G.; Idziak, S. H. J. *Cryst. Growth Des.* **2011**, 11, 4544.

McClements, D. J. *Adv. Colloid Interfac.* **2012**, 174, 1.

Mildner-Szkudlarz, S.; Jelén, H. H. *Food Chem.* **2008**, 110, 751.

Minato, A.; Ueno, S.; Yano, J.; Wang, Z. H.; Seto, H.; Amemiya, Y.; Sato, K. *J. Am. Oil Chem. Soc.* **1996**, 73(11), 1567.

Minato, A.; Ueno, S.; Smith, K.; Amemiya, Y.; Sato, K. *J. Phys. Chem. B* **1997a**, 101(18), 3498.

Minato, A.; Ueno, S.; Yano, J.; Smith, K.; Seto, H.; Amemiya, Y.; Sato, K. *J. Am. Oil Chem. Soc.* **1997b**, 74 (10), 1213.

Minato, A.; Yano, J.; Ueno, S.; Smith, K.; Sato, K. *Chem. Phys. Lipids* **1997c**, 88, 63.

Miskandar, M. S.; Man, Y. B. C.; Yusoff, M. S. A.; Rahman, R. A. *J. Food Lipids* **2004**, 11 (1), 1.

Miura, S.; Konishi, H. *Eur. J. Lipid Sci. Technol.* **2001**, 103, 804.

Mortimer, R. G. Mathematics for Physical Chemistry, Elsevier Academic Press, San Diego, USA, 2005, pp. 326.

Motoyama, M.; Ando, M.; Sasaki, K.; Hamaguchi, H. *Appl.Spectrosc.* **2010**, 64 (11), 1244.

Motoyama, M.; Chikuni, K.; Narita, T.; Aikawa, K.; Sasaki, K. *J. Agr.Food Chem.* **2013**, 61, 69.

Müller, M.; Riekel, C.; Vuong, R.; Chanzy, H. *Polymer* **2000**, 41, 2627.

N

Nakano, T.; Kaibara, K.; Tabata, Y.; Nagata, N.; Enomoto, S.; Marukawa, K.; Umakoshi, Y. *Bone* **2002**, 31(4), 479.

Narváez-Rivas, M.; Rios, J. J.; Arteaga, J. F.; Quilez, J. F.; Barrero, A. F.; León-Camacho, M. *Anal. Chim. Acta* **2008**, 624, 107.

Narváez-Rivas, M.; Pablos, F.; Jurado, J. M.; León-Camacho, M. *Anal. Bioanal. Chem* **2011**, 399, 2115.

Nozue, Y.; Kurita, R.; Hirano, S.; Kawasaki, S.; Ueno, S.; Iida, A.; Nishi, T.; Amemiya, Y. *Polymer* **2003**, 44, 6397.

O

Ostwald, W. *Z. Phys. Chem*. **1897**, 22, 289.

Ozen, B. F.; Mauer, L. J. *J. Agric. Food Chem.* **2002**, 50, 3898.

P

Parcerisa, J.; Casals, I.; Boatella, J.; Codony, R.; Rafecas, M. *J. Chromatogr. A* **2000**, 881, 149.

Paris, O.; Müller, M. *Nucl. Instrum. Meth. B* **2003**, 200, 390.

Perez-Martinez, D.; Alvarez-Salas, C.; Charo-Alonso, M.; Dibildox-Alvarado, E.; Toro-Vazquez, J. F. *Food Res. Int.* **2007**, 40 (1), 47.

Petrón, M. J.; Muriel, E.; Timón, M. L.; Martín, L.; Antequera, T. *Meat Sci.* **2004**, 68, 71.

Perkin Elmer. Instructions Model DSC-4. Norwalk, Connecticut, USA, 1982.

R

Riekel, C.; Bösecke, P.; Diat, O.; Engström, P. *J. Mol. Struct.* **1996**, 383, 291.

Riekel, C.; Davies, R. J. *Curr. Opin. Colloid Interface Sci.* **2005**, 9, 396.

Ross, Y. H. Phase Transitions in Foods, Academic Press, London, UK, 1995.

Rossel, J. B., *Adv. Lipid Res.*, 1967, 5, 353.

Rossel, J. B. (1967) in Advances in Lipid Research, ed. Paoletti, R.; Krichevsky, D. Academic Press, New York, USA, 1967, Vol. V, pp. 353-408.

Rousseau, D.; Sonwai, S. *Food Biophys.* **2008**, 3, 273.

Rousset, P.; Rappaz, M.; Minner, E. *J. Am. Oil Chem. Soc.* **1998**, 75(7), 857.

Ruiz, J.; Cava, R.; Antequera, T.; Martín, L.; Ventanas, J.; López-Bote, J. *Meat Sci.* **1998**, 49 (2), 155.

S

Sánchez Casas, L.; De Miguel Gordillo, D.; Osorio Bueno, E.; Marín Expósito, J.; Fuentes Mendoza, M.; Ardilla Hierro, T.; Gallardo González, L.; Martínez Cano, M. *J. Am. Oil Chem. Soc.* **2009**, 86, 933.

Sato, K.; Arishima, T.; Wang, Z. H.; Ojima, K.; Sagi, N.; Mori, H. *J. Am. Oil Chem. Soc.* **1989**, 66, 664.

Sato, N. in Advances in Applied Lipid Research. ed. Padley, F. JAI Press, 1996, pp. 213-268.

Sato, K.; Ueno, S.; Yano, J. *Prog. Lipid Res.* **1999**, 38, 91.

Sato, K.; Ueno, S. in Crystallization Processes in Fats and Lipid Systems, ed. Garti, N.; Sato, K. Marcel Dekker, New York, USA, 2001a, pp. 177–209.

Sato, K. in Crystallization and Solidification Properties of Lipids, ed. Widlak, N.; Hartel, R.; Narine, S. S. AOCS Press, Champaign, USA, 2001b, pp. 1–33.

Sato, K.; Goto, M.; Yano, J.; Honda, K.; Kodali, D. R.; Small, D. M. *J. Lipid Res.* **2001c**, 42, 338.

Sato, K.; Ueno, S. in Bailey's Industrial Oil and Fat Products, ed. Shahidi, F. John Wiley & Sons Inc., Hoboken, New Jersey, USA, 2005, vol. 1, pp. 77–120.

Sato, K.; Ueno, S. *Curr. Opin. Colloid In.* **2011**, 16, 384.

Sayago, A.; Morales, M. T.; Aparicio, R. *Eur. Food Res. Technol.* **2004**, 218, 480.

Seddon, J. M.; Templer, R. H.; Warrender, N. A.; Huang, Z.; Cevc, G.; Marsh, D. *BBA-Biomembranes* **1997**, 1327, 131.

Seidel, R.; Gourrier, A.; Burghammer, M.; Riekel, C.; Jeronimidis, G.; Paris, O. *Micron* **2008**, 39, 198.

Shaw, A. D.; di Camillo, A.; Vlahov, G.; Jones, A.; Bianchi, G.; Rowland, J.; Kell, D. B. *Anal. Chim. Acta* **1997**, 348, 357.

Shinohara, Y.; Takamizawa, T.; Ueno, S.; Sato, K.; Kobayashi, I.; Nakajima, M.; Amemiya, Y. *Cryst. Growth Des.* **2008**, 8 (9), 3123.

Small, D. M. The Physical Chemistry of Lipids, Plenum, New York, USA, 1986, pp. 345–394.

Small, D. M. *J. Lipid Res.* **1984**, 25, 1490.

Smith, K. W. in Crystallization Processes in Fats and Lipid Systems, ed. Garti, N.; Sato, K. Marcel Dekker, New York, USA, 2001; pp 357-380.

Smith, K. W.; Cain, F. W.; Talbot, G. *Eur. J. Lipid Sci. Technol.* **2005**, 107, 583.

Smith, K. W.; Bhaggan, K.; Talbot, G.; van Malssen, K. F. *J. Am. Oil Chem. Soc.* **2011**, 88, 1085.

Stock, S. R.; Barss, J.; Dahl, T.; Veis, A.; Almer, J. D. *J. Struct. Biol.* **2002**, 139, 1.

Svenstrup, G.; Brüggemann, D.; Kristensen, L.; Risbo, J.; Skibsted, L. H. *Eur. J. Lipid Sci. Technol.* **2005**, 107 (9), 607.

T

Takeuchi, M.; Ueno, S.; Sato, K. *Food Res. Int.* **2002**, 35, 919.

Takeuchi, M.; Ueno, S.; Sato, K. *Cryst. Growth Des.* **2003**, 3 (3), 369.

Tanaka, L.; Tanaka, K.; Yamato, S.; Ueno, S.; Sato, K. *Food Biophys.* **2009**, 4, 331.

Tejeda, J. F.; Gandemer, G.; Antequera, T.; Viau, M.; García, C. *Meat Sci.* **2002**, 60, 357.

Templer, R. H.; Seddon, J. M.; Warrender, N. A.; Syrykh, A.; Huang, Z.; Winter, R.; Erbes, J. *J. Phys. Chem. B* **1998**, 102, 7251.

Threlfall, T. *Org. Process Res. Dev.* **2003**, 7, 1017.

Timms, R. E. *Eur. J. Lipid Sci. Technol.* **2005**, 107, 48.

Timón, M. L. ; Ventanas, J.; Carrapiso, A. I.; Jurado, A.; García, C. *Meat Sci.* **2001**, 58, 85.

Toro-Vazquez, J. E.; Dibildox-Alvarado, E.; Charo-Alonso, M.; Herrera-Coronado, V.; Gomez-Aldapa, C. A. *J. Am. Oil Chem. Soc.* **2002**, 79 (9), 855.

U

Ueno, S.; Minato, A.; Seto, H.; Amemiya, Y.; Sato, K. *J. Phys. Chem. B.* **1997**, 101, 6847.

Ueno, S.; Ristic, R. I.; Higaki, K.; Sato, K. *J. Phys. Chem. B* **2003**, 107, 4927.

Ueno, S.; Nishida, T.; Sato, K. *Cryst. Growth Des.* **2008**, 8 (3), 751.

V

Vaclavik, L.; Cajka, T.; Hrbek, V.; Hajslova, J. A*nal. Chim. Acta* **2009**, 645, 56.

Vand, V.; Bell, I. P. *Acta Cryst.* **1951**, 4, 465.

Van Langevelde, A.; Van Malssen, K.; Driessen, R.; Goubitz, K.; Hollander, F.; Peschar, R.; Zwart, P.; Schenk, H. *Acta Cryst. B* **2000**, 56, 1103.

Van Langevelde, A.; Peschar, R.; Schenk, H. *Acta Cryst. B* **2001a**, 57, 372.

Van Langevelde, A.; Peschar, R.; Schenk, H. *Chem. Mater.* **2001b**, 13, 1089.

Van Mechelen, J. B.; Peschar, R.; Schenk, H. *Acta Cryst. B* **2006a**, 62, 1121.

Van Mechelen, J. B.; Peschar, R.; Schenk, H. *Acta Cryst. B* **2006b**, 62, 1131.

Van Mechelen, J. B.; Peschar, R.; Schenk, H. *Acta Cryst. B* **2008a**, 64, 240.

Van Mechelen, J. B.; Peschar, R.; Schenk, H. *Acta Cryst. B* **2008b**, 64, 249.

Van Mechelen, J. B.; Goubitz, K.; Pop, M.; Peschar, R.; Schenk, H. *Acta Cryst. B* **2008c**, 64, 771.

Vereecken, J.; Foubert, I.; Smith, K. W.; Dewettinck, K. *J. Agric. Food Chem.* **2007**, 55, 7793.

Viera-Alcaide, I.; Vicario, I. M.; Escudero-Gilete, M. L.; Graciani Constante, E.; León-Camacho, M. *Grasas Aceites* **2008**, 59 (4), 327.

Vlahov, G. *J. AOAC Int.* **2009**, 92 (6), 1747.

Vuillequez, A.; Koza, L.; Youssef, B.; Bridier, M.; Saiter, J. M. *Macromol. Symp.* **2010**, 290, 137.

W

Wassell, P.; Okamura, A.; Young, N. W. G.; Bonwick, G.; Smith, C.; Sato, K.; Ueno, S. *Langmuir* **2012**, 28, 5539.

Wesdorp, L. H. PhD thesis, Liquid-Multiple Solid Phase Equilibria in Fats-theory and experiments. TU Delft, 1990.

Wheeler, D. H.; Riemenschneider, R. W.; Sando, C. E. *J. Biol. Chem.* **1940**, 132, 687.

Widlak, N.; Hartel, R.; Narine, S. Ed. Crystallization and Solidification Properties of Lipids, AOCS Press, Champaign, USA, 2001, pp 53-131.

Y

Yagi, N.; Ohta, N.; Matsuo, T. *Int. J. Biol. Macromol.* **2009**, 45, 86.

Yano, J.; Kaneko, F.; Kobayashi, M.; Sato, K. *J. Phys. Chem. B* **1997**, 101, 8112.

Yano, J.; Sato, K.; Kaneko, F.; Small, D. M.; Kodali, D. *J. Lipid Res.* **1999**, 40, 140.

Z

Zabaras, D.; Gordon, M. H. *Food Chem.* **2004**, 84, 475.

Zhang, L.; Ueno, S.; Miura, S.; Sato, K. *J. Am. Oil Chem. Soc.* **2007**, 84, 219.

Zhang, L.; Ueno, S.; Sato, K.; Adlof, R. O.; List, G. R. *J. Therm. Anal. Calorim.* **2009**, 98, 105.

Zhao, D.; Zhu, Y.; Ruan, Q.; Zhang, S.; Zhang, L.; Xu, F. *Mater. Res. Bull.* **2010**, 45, 80.

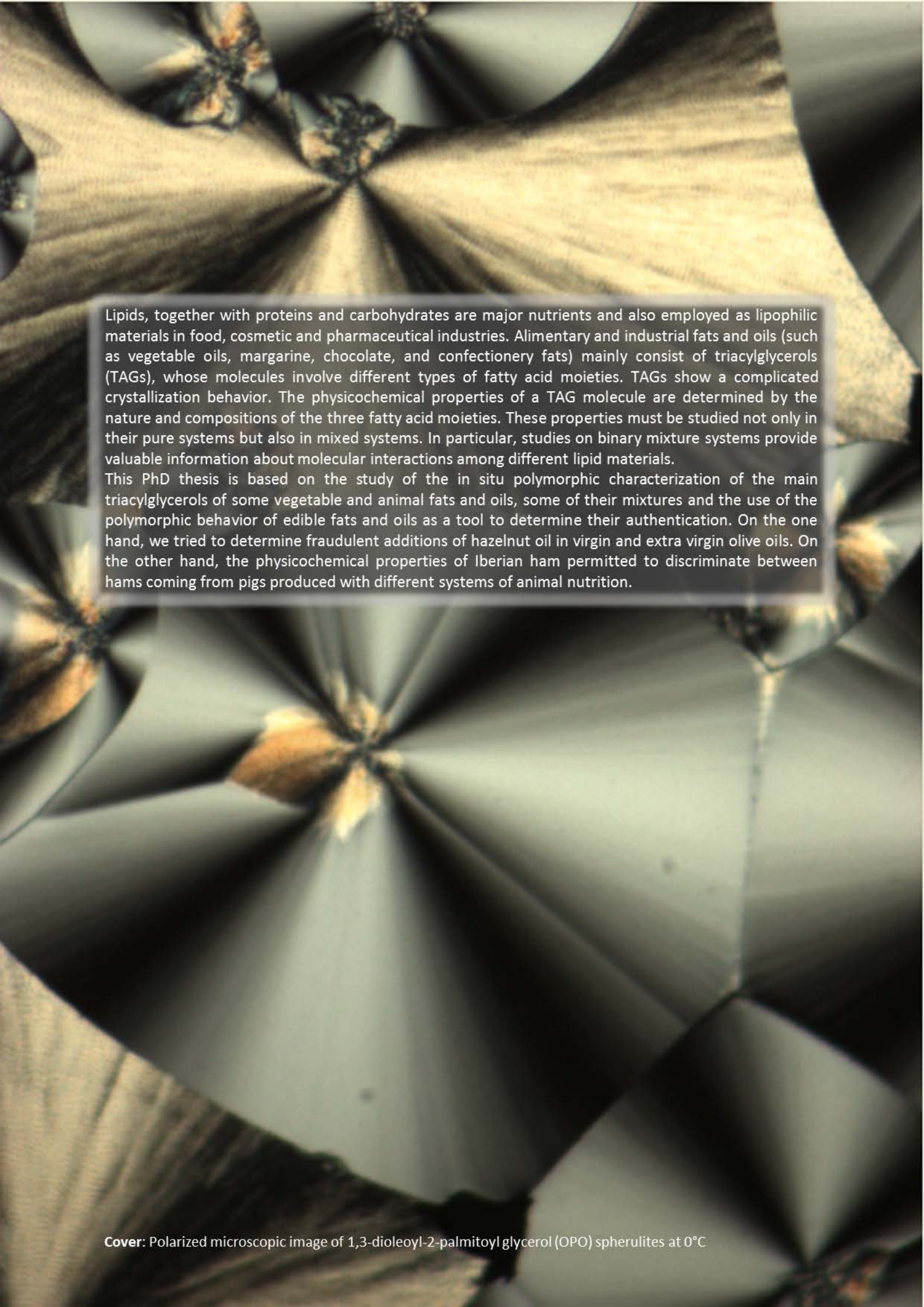

Lipids, together with proteins and carbohydrates are major nutrients and also employed as lipophilic materials in food, cosmetic and pharmaceutical industries. Alimentary and industrial fats and oils (such as vegetable oils, margarine, chocolate, and confectionery fats) mainly consist of triacylglycerols (TAGs), whose molecules involve different types of fatty acid moieties. TAGs show a complicated crystallization behavior. The physicochemical properties of a TAG molecule are determined by the nature and compositions of the three fatty acid moieties. These properties must be studied not only in their pure systems but also in mixed systems. In particular, studies on binary mixture systems provide valuable information about molecular interactions among different lipid materials.

This PhD thesis is based on the study of the in situ polymorphic characterization of the main triacylglycerols of some vegetable and animal fats and oils, some of their mixtures and the use of the polymorphic behavior of edible fats and oils as a tool to determine their authentication. On the one hand, we tried to determine fraudulent additions of hazelnut oil in virgin and extra virgin olive oils. On the other hand, the physicochemical properties of Iberian ham permitted to discriminate between hams coming from pigs produced with different systems of animal nutrition.

Cover: Polarized microscopic image of 1,3-dioleoyl-2-palmitoyl glycerol (OPO) spherulites at 0°C